

UNIVERSITY OF LIVERPOOL

Novel Ionic Liquid Based Electrolytes for Non-Aqueous Lithium-Oxygen Batteries

*Thesis submitted in accordance with the requirements of the University of Liverpool for the
Degree of Doctor in Philosophy*

Petar M. Radjenovic

November 2017

Supervisor: Laurence J. Hardwick

Abstract

Superoxide (O_2^\cdot) is the key discharge intermediary driving many non-aqueous metal-oxygen ($M-O_2$) battery chemistries.¹⁻⁴ Characteristic dioxygen (O_2^x , where $x = -2, -1, 0, +1$) stretching vibrations (ν_{O-O}) have been well documented spectroscopically in numerous chemically unique systems.⁵⁻⁸ Therefore, the O_2^\cdot intermediary can be used as a diagnostic molecule to spectroscopically probe electrolyte effects on O_2 reduction-evolution reaction (OR/ER) processes at the electrode/electrolyte interface, providing fundamental insight into non-aqueous $M-O_2$ reaction mechanisms. However, it is first important to understand the vibrational spectra of O_2^x , though a concise overview of the large amount of empirical data in different chemical environments is lacking. Herein, reviewing the spectroscopy of O_2^\cdot and other O_2^x species gave a good spectroscopic grounding that supported *in situ* spectroscopic studies of OR/ERs in novel ionic liquid (IL) based electrolytes.

Fundamental studies of OR/ERs at the roughened gold (rAu) model electrode interface in a variety of IL electrolytes using *in situ* surface enhanced Raman spectroscopy (SERS) were performed to study IL cation and anion effects on the chemical nature of O_2^\cdot . Analysis of ν_{O-O} and IL vibrational peak intensities and Stark shifts provided valuable information about electrolyte interactions. Furthermore, IL:solvent (IL:sol) blended electrolytes were studied to determine the effect of the solvent and salt additives on the properties of the IL electrolyte. Overall, four key parameters were shown to affect the chemical nature of O_2^\cdot at the electrode/electrolyte interface, the: (1) IL cation, (2) IL anion, (3) solvent additive Gutmann acceptor/donor number (AN/DN) and (4) the electrode potential. To optimise various physicochemical properties of the electrolyte, A general heuristic methodology for “tailoring”, screening and optimising the electrolyte was developed and a series of novel multi-component

heterogeneous IL:sol electrolytes (Hetblends) were formulated. These novel Hetblends showed improved O₂ reduction reaction (ORR) electrochemistry and exceptional stability in contact with lithium metal (Li-metal). Solvents that normally react with alkali metals (e.g. DMSO and MeCN) when added to an excess of ILs were found to be stable, whilst helping to greatly improve the physicochemical properties of the overall electrolyte. Our study provides valuable information for the design and tailoring of novel IL based electrolytes for Li and other M-O₂ batteries.

Many IL properties lend themselves to use as electrolytes in electrochemical systems such as their low volatility and flammability, innate conductivity and high chemical stability. Which make ILs interesting novel electrolyte environments for investigating non-aqueous lithium-O₂ (Li-O₂) cell chemistries. Non-aqueous pure IL and IL-organic solvent blend (IL:sol) electrolytes have been investigated to probe the electrolyte effects and optimise key physicochemical properties of the electrolyte. The aim of this PhD thesis was to investigate these fundamental problems with specific emphasis on anode and cathode interfacial chemistry and stability in a variety of novel IL electrolytes. This has been done using electrochemical and non-invasive *in situ* and complementary *ex-situ* spectroscopies, namely Raman and FT-IR, techniques to detect and characterise the formation of charge-discharge species as well as the flux of species at the electrode interface.

This project was part of an Innovate UK funded project called Practical Lithium-Air Batteries (PLAB) between the University of Liverpool, Queens University Belfast, Johnson Matthey, Johnson Matthey Battery Systems (formerly Axeon) and Jaguar Land Rover. Each partner contributed information to the consortium on their respective areas of expertise.

Acknowledgements

To Professor Laurence Hardwick, thank you for the opportunity to study and work in such an amazing environment with so many great people and for the academic freedom to “*brew broths.*” To Iain “*the pathfinder*” Aldous, Laura Cabo-Fernandez, Tom Galloway and Filipe Braga and the whole group thank you for your help, assistance and companionship over the past four years, it was an honour to work with such a great bunch of colleagues.

The author would like to thank collaborators at Johnson Matthey, Queen’s University Belfast Johnson Matthey battery Systems, Jaguar-Land Rover as well as Innovate UK/EPSRC and the University of Liverpool for funding and access to equipment.

In situ SEIRAS work in chapter 4 was done in collaboration with Vivek Padmanabhan and electrode films were deposited by Giorgos Papageorgiou. Thank you both for your help and expertise. Li-Li symmetrical cell and non-aqueous Li-O₂ charge-discharge cell cycling in chapter 5 were done in collaboration with Sarah Ball, Carmen Salcianu and Enrico Petrucco at Johnson Matthey, Sonning Common. Thank you for all your guidance and warm discussions. To my dear mother, thanks for always helping to bring me back to centre I feel nothing but love for you! Do moj otac, Volim te puno i hvala za sve! To my brother Ant, thanks for taking many of the burdens off my shoulders without me asking, you’re a great person and son to our parents, I truly love you bro. To Pam and Tony O’Shea my “*parents of grand age*” you have been like second parents to me, thanks for being so great! Do Baba Bosa Radjenovic, Volim te puno od zemlja do neba. To David thank you for listening and your straight-talking words, they were much appreciated. To my aunts and uncles Jenny, Chris, Jagoda, Martin, Zarko and all my family, Kum and friends that have contributed so much love, happiness, wisdom and p***

taking to my life over the years, thank you words can't express the joy you have all contributed to my life, much love! The author would like to acknowledge and thank Mohammed Iqbal, Waqas Mirza and Kabir Jhangir for their help and support. Insh'Allah I'll see you guys again soon.

To Dr. Raj Patel, Professor Mujtaba and Professor Benkreira, thank you for sparking my enthusiasm for chemical processes throughout my undergraduate studies. To Mrs. Manning and Mrs. Derby I'm truly grateful for you supporting and encouraging my interest in the sciences, even if I didn't show it at the time. To Mr Waszek and the board of St. Edwards College that admitted me into the school without needing to, I am in your debt, without a doubt you changed my life. To Mr. Burke, you are an inspiring man and great teacher, thank you. To scousers, ta for being sound, to Liverpool, ta for being a scouse. To Britain, thanks for John Locke and roast dinners. Do Srbija i Crna Gora, samo sloga Srbina spasava. To humanity thank you for peace and for working on minimising war. To life thank you for being alive. To Earth thank you for supporting life. To the universe thank you for supporting all the above. To the Creator, thank you for creating the universe and everything in it, you are truly a wondrous God worthy of praise!

Also: *Yael wow Petar bro does it rime Yes or no*

Answer () Write underneath because you cant write in it bro yo man

p.s this is so imbarising

And: *Shalom pongo is the bongo like a chongo on the pongo*

Table of Contents

Abstract	i
Acknowledgements	iv
Table of Contents	vii
List of Figures	x
List of Tables	xvii
List of Abbreviations	xix
List of Variables	xxi
List of Publications	xxii
1. Introduction and Review	1
1.1 Why is Energy Storage Important?	1
1.2 Energy Storage	3
1.2.1 Past	3
1.2.2 Present	4
1.2.3 Future	8
1.3 Metal-O ₂ Batteries	14
1.3.1 Non-Aqueous Alkali-Metal-O ₂ Overview	15
1.3.2 Aqueous Li-O ₂	20
1.3.3 Hybrid Li-O ₂	21
1.4 Non-Aqueous Li-O ₂ batteries	22
1.4.1 Discharge	23
1.4.2 Charge	40
1.4.3 Electrolyte	47
1.4.4 O ₂ -Cathode	56
1.4.5 Lithium Anode	60
1.4.6 Catalysis	68
1.4.7 Non-Aqueous Li-O ₂ Overview	82
1.5 Ionic Liquid Electrolytes	86
1.5.1 Overview	86
1.5.2 Batteries	89
1.5.3 Selecting ILs	91
1.5.4 IL Electrolyte Screening	95
2. Experimental	97
2.1 Techniques	98
2.1.1 Electrochemistry	98

2.1.2 Surface Enhanced Raman Spectroscopy.....	105
2.1.3 Surface Enhanced Infra-Red Adsorption Spectroscopy	109
2.1.4 Karl Fischer Coulometric Titration.....	111
2.1.5 Modelling Ion Properties	112
2.1.6 Theoretical Calculations	112
2.2 Equipment and Procedure	117
2.2.1 Electrochemistry	117
2.2.2 Low-Volume Spectro/Electrochemical Cells	118
2.2.3 Coin-Cell Assembly.....	126
2.2.4 Electrochemical Au Electrode Roughening.....	127
2.2.5 Reference Electrodes	129
2.2.6 Raman	130
2.2.7 Spectral Peak Fitting	132
2.2.8 Fourier Transform Infrared spectrometer (FT-IR).....	133
2.2.9 Karl Fischer Coulometric Titration Procedure	134
2.3 Electrolytes	135
2.3.1 Ionic Liquids	135
2.3.2 Solvent and Salts.....	137
2.3.3 Drying of Gas Feed Streams	138
3. Dioxygen.....	139
3.1 Introduction.....	140
3.2 Superoxide Raman Spectroscopy	144
3.2.1 Superoxide Meta-Analysis.....	144
3.2.2 Other Superoxide Spectral Trends	159
3.3 Dioxygen Raman Spectra and Bond Parameters	176
3.3.1 Important Bond Parameters	176
3.3.2 Peroxo-Superoxyl	181
3.3.3 Superoxo-Oxyl	181
3.3.4 Oxo-Dioxygenyl	182
4. <i>In Situ</i> SERS of ILs.....	188
4.1 Overview	189
4.2 Introduction.....	190
4.3 <i>In situ</i> SERS of OR/ER in ILs	192
4.3.1 Cation Effect	192
4.3.2 Anion Effect.....	220
4.3.3 Summary	225
4.4 <i>In Situ</i> SEIRAS	227

4.5 Conclusion	228
5. Tailoring IL Electrolytes.....	230
5.1 Overview.....	231
5.2 Introduction.....	233
5.3 Solvent Effect.....	235
5.3.1 <i>In Situ</i> SERS of OR/ERs.....	235
5.3.2 <i>In Situ</i> SERS of Lithiated OR/ERs	238
5.3.3 Li-Metal Stability.....	245
5.4 Multi-Component IL:Solvent Blends	247
5.4.1 Heuristic Electrolyte Tailoring Methodology	248
5.4.2 Li-Metal Stability.....	251
5.4.3 <i>In Situ</i> SERS of OR/ERs.....	253
5.4.4 Comparing blends	257
5.5 Electrolyte Practicality	258
5.5.1 Li-Li Symmetrical Cell Cycling	258
5.5.2 Li-Metal Reference Electrode	260
5.6 Conclusion	262
6. Conclusion	263
6. Conclusion	264
7. Bibliography	266
7. References.....	267

List of Figures

- Figure 1. 1.** Li-ion battery schematic in fully charged state. Figure reproduced from ref. ¹⁷...6
- Figure 1. 2.** Non-aqueous M-O₂ battery schematic, arrows indicate general direction of M⁺, O₂ and electron movement during discharge (red) and charge (light blue).19
- Figure 1. 3.** Types of Li-O₂ batteries: (a) Aqueous electrolyte, (b) aprotic/non-aqueous electrolyte, (c) mixed (aprotic-aqueous), and (d) solid-state. Figure reproduce from ref. ¹⁰⁶.21
- Figure 1. 4.** (a) ‘Schematic of the Li⁺-ORR mechanism in an aprotic solvent containing Li⁺, showing the; surface pathway in low DN electrolytes (left), solution pathway (top-right) and second electrochemical reduction reaction (bottom-right) in high DN solvents, respectively. (b) 3D plot showing the dominant pathway as a function of DN and potential. O₂ reduction in high-DN solvents and at high potentials (low overpotentials) follows the solution pathway (blue) and at low potentials (high overpotentials) the surface pathway (red). O₂ reduction in low-DN solvents at all potentials follows the surface pathway (red) forming uniform films.’ Figures reproduced from ref. ⁴29
- Figure 1. 5.** (a) ‘Schematic of Li⁺-ORR for the growth of Li₂O₂ toroids in H₂O containing electrolyte. Solvation of intermediaries circumvents the conductivity limitations produced with surface-up film growth. (b) Quantitative chart for solvent selection for high-capacity Li-O₂ batteries. The free energy of dissolution scale (red/high, blue/low) for Li⁺...O₂^{•-} into Li⁺_(sol) and O₂^{•-}_(sol) in different solvents is a function of the Gutmann AN & DN and is normalized relative to pure Dimethoxyethane (DME). High DN solvents like DMSO are capable of stabilizing Li⁺, on the other hand, high ANs like H₂O stabilize O₂^{•-}. Solvents that fall in the top-right quadrant (black dotted-line) of this plot are predicted to favour solution-mediated deposition of Li₂O₂, which will be essential for high-capacity Li-O₂ batteries.’ Figure reproduced from ref. ⁸⁸.31
- Figure 1. 6.** Cyclic voltammograms (CVs) of OR/ERs showing thermodynamic potential shifts in various electrolytes saturated with O₂. (a) Varying ratios of TBAClO₄:LiClO₄ (ClO₄⁻ maintained at 100 mM) in Me-Im (high DN: 47) at a Au working electrode. No noticeable shift in onset reduction potentials with and without Li⁺ present implying the same solvated O₂^{•-} species is generated regardless of the cation present. (b) 1 M TBATFSI (green line) or 1 M LiTFSI (blue line) dissolved in DME (low DN: 20) at a glassy carbon (GC) electrode. Large positive shift (~250 mV) in ORR onset implies Li⁺...O₂^{•-} is more thermodynamically favourable than solvated TBA⁺...O₂^{•-}. Figure (a) and (b) reproduced from ref. ⁴ and ¹²⁰, respectively.33
- Figure 1. 7.** Schematic overview of different possible Li⁺...O₂^{•-} intermediaries generated during discharge of a non-aqueous Li-O₂ cell on a generalised continuum of increasing ionicity going from left to right. A pure LiO₂ phase at < 25 K is used as the lowest, most covalent, species in the continuum, however, this species will not be generated during discharge of a cell as it is not thermodynamically or kinetically feasible.^{76,80} From left to right as the electrolyte’s ability to solvate Li⁺ and/or O₂^{•-} increases, the Li⁺...O₂^{•-} discharge intermediary likely goes from covalent like or partially stabilised surface complexes,^{83,159} to contact ion-pairs (CIPs),^{4,67,74} solvent separated contact ion-pairs (SS-CIPs), SSIPs,^{4,67,147} to free and fully solvated ions.¹⁵⁵ The relationship between O₂^{•-} solvation, its disproportionation rate and Li₂O₂ surface morphology has also been well established. Therefore, assuming the electrolyte and O₂-cathode are stable, then the disproportionation rate will slow and the lifetime of the Li⁺...O₂^{•-} intermediary will increase from left to right. The resulting Li₂O₂ morphology (yellow structures) on the O₂-cathode surface for Li⁺...O₂^{•-} can similarly be approximated on a matching continuum: transitioning from uniform ~10 nm films⁹² to heterogenous amorphous films,¹²¹ followed by large platelet,¹⁴⁸ toroidal⁸⁸ and surface aggregates⁴ and finally to low or

no O ₂ -cathode surface passivation ¹⁵⁵ when the bulk of discharge products are solvated in solution. Any generated Li ⁺ ...O ₂ ^{·-} intermediary will likely disproportionate by transitioning down this continuum. For example, Coulombic attraction between fully solvated ions may lead to the formation of SSIP aggregates in solution which, in turn, continue to attract, eventually penetrating each other's solvation shells and forming a solvent separated contact ion pair (SSCIPs). These too will aggregate with other CIPs and penetrate each other's solvation shells enabling disproportionation to Li ₂ O ₂ . However, further work is required to support this mechanism.....	38
Figure 1. 8. CVs of O ₂ saturated electrolytes on GC electrodes at 100 mV s ⁻¹ showing the impact of cation size on OER potentials. (a) 0.25 M of various TFSI ⁻ based salts in EMITFSI. More charge dense cations (TBA ⁺ > EMI ⁺ > K ⁺ > Na ⁺ > Li ⁺ , i.e. as cation size approaches that of O ₂ ^{·-}) require larger electrode polarisations to degrade the complex formed during ORR thus overpotentials increase and OER potentials shift positive. (b) 0.1 M of TAAOTf in MeCN. When the size of the cations is increased after a point, the same shift in OER is visible and coordination strength decreases due to slower surface charge-transfer kinetics. Figure (a) and (b) reproduced from ref. ¹⁶⁹ and ⁷⁰ , respectively.....	43
Figure 1. 9. CVs of Li ⁺ -OR/ER in various electrolytes saturated with O ₂ (a) Varying concentrations of LiClO ₄ in a 100 mM TBAClO ₄ /MeCN (low DN solvent) electrolyte at a Au WE, cycled at 1,000 mV s ⁻¹ . ORR onset and OER shift to higher potentials in Li ⁺ saturated electrolytes. (b) 100 mM LiClO ₄ in DMSO (relatively high DN: 27) at a GC cathode cycled to three different reduction potentials at 100 mV s ⁻¹ . OER currents are heavily dependent on the reduction potential indicating different reduction products. (c) 25 mM LiTFSI in Pyr ₁₄ TFSI on a Au electrode. Inset CVs at various cathodic limits of 1.95 V and higher. OER similarly dependent on the reduction potential. Figure (a), (b) and (c) reproduced from ref. ⁷⁴ , ¹¹⁰ and ⁶⁹ , respectively.....	45
Figure 1. 10. Reaction scheme depicting methyl carbonate degradation mechanism during Li ⁺ -ORR forming numerous degradation products. Figure reproduced from ref: ¹⁹⁵	49
Figure 1. 11. Powder X-ray diffraction patterns of Super P/Kynar composite O ₂ -cathodes cycled in TEGDME with 1M LiPF ₆ under 1 atm. Absence of Li ₂ O ₂ on fifth scan demonstrates cyclability issues with electrolyte when fully discharged. Figure reproduced from ref: ²⁰⁰	51
Figure 1. 12. Discharge voltage profiles of non-aqueous Li-O ₂ batteries with different Li ⁺ -salts discharged at a current density of 0.05 mA cm ⁻² . Figure reproduced from ref. ²²⁴	54
Figure 1. 13. Scheme of some key Li-metal anode problem areas, from left to right: dendrite formation, highly polarised region that can induce parasitic reactions, anode structural fracturing leading to isolated (dead) regions insulated by SEI build-up and large volume changes during charge discharge. Figure reproduced from ref: ²⁷²	60
Figure 1. 14. Schematic of mosaic SEI layer structure proposed by Peled <i>et al.</i> Arrows denote Li ⁺ diffusion pathways during discharge. A = Li ₂ O, B = LiF, C = Li ₂ CO ₃ , D = polyolefins, E = semi-carbonates. Figure reproduced from ref. ²⁸⁰	63
Figure 1. 15. Schematic of Li stripping/plating (dissolution/deposition) with (a) conventional SEI and (b) carbon nano-spheres protective layer. For (a) after the first cycle surface inhomogeneity increases and dendrites nucleate, dissolve and grow on cycling leading to cell failure. For (b) carbon nano-spheres protect and allow uniform Li-deposition and volume expansion on the metal anode. Figure reproduced from ref: ²⁶⁹	66
Figure 1. 16. Annual growth of IL publications 1998 – 2013, Figure reproduced from ref. ⁴⁰⁷	86
Figure 1. 17. Mulliken charge of carbon and nitrogen atoms in (a) TMHA ⁺ (b) Pyrr ₁₄ ⁺ [BMP ⁺] (c) EMI ⁺ (d) DMPI ⁺ . Figure reproduced from ref. ¹⁵⁵	93

Figure 2. 1. Schematic representation of EDL (top) with a positive bias potential applied to the electrode surface. Anions shown in green, cations in blue and solvent molecules in orange/pink (red pointers indicate direction of negative dipole on solvent molecule). IHP, OHP and the diffuse layer are depicted and their relationship to changes in potential with distance into the bulk electrolyte (bottom).....	99
Figure 2. 2. Example CV of argon (Ar) (black dashed line) and O ₂ (orange line) saturated IL-electrolyte (Pyr ₁₄ OTf). Working electrode (WE): 1.6 mm diameter glassy carbon (GC); reference electrode (RE): Ag; counter electrode (CE): Pt; scan rate: 100 mV s ⁻¹ . Where, E = standardized potential (V vs Li/Li ⁺), i = current response measured with current density (μ A cm ⁻²), subscript ‘p’ = peak, superscripts ‘r’ and ‘o’ = reduction and oxidation, respectively, $E_{1/2}$ = redox half-potential. i_p^r is measured by extrapolating a baseline as the potential for the oxidation scan is typically positive of the equilibrium potential.	102
Figure 2. 3. (a) Schematic depicting Rayleigh and inelastic scattering of light by a sample, (b) depiction of roughened coinage metal surface with regions of surface enhancement, (c) energy diagram depicting the effect of incident light on vibrating molecules. From left to right; incident photons that are absorbed by the vibrating molecules causing a noticeable shift in the vibrational energy state of the sample (IR absorption). Incident photons, which excite vibrating molecules to a virtual energy state and are reemitted on relaxation of the molecules back to their starting vibrational state, are Rayleigh scattered. Incident photons that excite molecules to a virtual energy state and are reemitted with less/more than initial energy due to molecules relaxing to a higher/lower energy vibrational state are, Stokes/anti-Stokes scattered respectively. Figure (c) reproduced from ref. ⁴³⁴	107
Figure 2. 4. (a) <i>In situ</i> SEIRAS cell schematic. EC cell built on top of Au-coated IR prism. The Au film acts as a WE whilst the IR prism facilitates reflection of the IR beam off the Au surface. (b) Close-up of reflection shows an approximate 1 μ m penetration depth of the IR laser, whilst surface enhancement factors are much smaller ~10 nm. Subtracting spectra from spectra at onset potentials removes signal from the bulk predominantly showing changes in molecular composition of the surface, see below. ⁴³⁵ Schematics by V. Padmanabhan.....	109
Figure 2. 5. Schematic comparison of (a) clear ATR-IR spectroscopy and (b) ~20 nm Au-film coated IR prism surface for SEIRAS. Penetration of IR evanescent into bulk electrolyte and photon concentration in enhancement active surface. Schematics by V. Padmanabhan.....	110
Figure 2. 6. (a) Schematic of low volume IL cell design and (b) picture of assembled cell with electrodes in 0.5 ml liquid sample (inset bottom right).	119
Figure 2. 7. (a) Low-volume SERS cell fully setup and clamped over spectrometer with rAu WE focused over Raman laser. (inset: close-up of WE) (b) Raman laser positioned directly underneath rAu WE with image of rAu surface taken from x50 microscope (10 μ m scale bar).	120
Figure 2. 8. SERS cell design for temperature-control measurements accommodating 0.4-0.8 ml electrolyte volumes. (a) (left) Top view of cone with marked inlets going clockwise: G-Out, CE, G-In, thermocouple, RE and WE in the middle. (right) Profile view of cell with WE, electrolyte reservoir and heating jacket. (b) Photo of full temperature-controlled SEC cell setup on Raman spectrometer.....	122
Figure 2. 9. (a) Assembled low-volume (0.5-1 ml) SEIRAS cell with tapped G-In and G-Out and custom Ag RE, Pt-coil CE and Au foil WE connection attached to cell with copper tape. (b) Inside of cell showing Au film coated IRE, electrolyte reservoir space and O-ring. (c) AFM image of Au film surface structure on Si showing that the layer thickness at step edge is approximately 20 nm (inset). ⁴⁰⁴ All Au films were deposited by G. Papageorgiou and AFM was provided by V. Padmanabhan.....	124
Figure 2. 10. (a) Au WE roughening CVs in 0.1 M KOH with Pt-coil CE and AgCl/Ag aqueous RE. Potentials were first cycled in the negative direction from OCP and held at -0.4 V for 40 s	

(region A). Potentials were then cycled positive and briefly held at 1.2 V for 1.2 s (region B). No current response was observed on the first cycle until after the surface had been oxidised. The first scan at 1,000 mV s⁻¹ (blue line) was followed by a scan at 500 mV s⁻¹ (red line). In this order, CVs were repeated 20 times at consecutively different scan rates. **(b)** Smooth Au WE before cycling **(c)** rAu WE after cycling, noticeably darker surface roughened film. ...128
Figure 2. 11. Example of Lorentzian peak fitted spectra from Origin 15. Example spectra taken of a rAu-WE surface in Pyr₁₄TFSI:TEGDME (60:40 vol. %) electrolyte held at -1.5 V vs Ag/Ag⁺.132
Figure 2. 12. Drying station setup. (1) Asynt temperature controller and hotplate-stirrer. (2) PTFE vacuum tap-vacuum pump connection. (3) Inhouse made glass vacuum dryer. (4) IL sample with untightened screw cap (5) Silicone-oil bath.136

Figure 3. 1. Molecular orbital diagram of dioxygen species (O₂^x) based on filled $\pi^*(2p_{xy})$ valence orbitals: O₂⁺ (black arrow only), high energy singlet (${}^1\Sigma_g^+$) O₂ (black and purple arrows only), singlet (${}^1\Delta_g$) O₂ (black and red arrows only), triplet (${}^3\Sigma_g^-$) O₂ (black, green arrows only), O₂⁻ (black, green, red arrows only) and O₂²⁻ (black, green, red, purple arrows). Figure partly reproduced from ref. ⁴⁵¹142

Figure 3. 2. vo-O Raman spectral peak positions for O₂⁻ complexes from numerous reports plotted against the Mr of the coordinating cation, references listed in Table 3. 1. A general inverse relationship is visible with heavier coordinating-cations producing complexes with lower vo-O bands indicating a less energetic O₂⁻ bond vibration and a ‘freer’ more Lewis basic species. A general fit produced an R² values of 0.757 for the overall trend. Two sub-trends are apparent; (1) single atom (blue) and (2) molecular (red) coordinating-cations. Lines of best fit for both trends (dashed lines) had R² values of 0.850 and 0.867 for single atom and molecular coordinating cations, respectively. Circled outlines (purple dashed line) are all reports of LiO₂ related species from the non-aqueous Li-O₂ battery literature. These do not match the expected trend for Li⁺ and will be discussed in section 3.2.3. Error bar refers to broad band between 1,150-1,200 cm⁻¹ observed by Xia et al.¹⁵⁹146

Figure 3. 3. **(a)** Reported vo-O spectral bands (listed in Table 3. 1) plotted against \mathbb{X}_{iv}^c of the coordinating cation. **(b)** Log₁₀ plot of \mathbb{X}_{iv}^c with line of best fit (green dashed line) and empirically derived equation in bottom left-hand corner ($R^2 = 0.952$) derived in Origin Pro 15. **(c)** Reported vo-O spectral bands plotted against \mathbb{X}_{isa}^c of the coordinating cation. **(d)** Log₁₀ plot of \mathbb{X}_{isa}^c , with line of best fit ($R^2 = 0.942$) and derived equation. \mathbb{X}^c calculated using i_v gives a slightly better approximation than i_{sa}. Cation i_v and i_{sa} values were generated in Spartan 15 using a CPK model for single atom cations (blue) and DFT (B3LYP, 6-31G*) for molecular cations (red). Only one reference reporting LiO₂ has been considered due to the ambiguity in the composition in the rest of reports. It has been long believed that LiO₂ was both thermodynamically and kinetically unstable.^{54,74-79} There have been many recent Raman studies reporting the observation of LiO₂, though they may also be other species.^{39,84,85} Due to the strength of Li⁺ as a coordinator, a pure LiO₂ species generated at room temperature would be expected to have a high vo-O shift (> 1167 cm⁻¹) similar to the broad band reported by Xia et al. centred at 1175 cm⁻¹.¹⁵⁹149

Figure 3. 4. Schematic depicting the relationship between cation interactions with O₂⁻ and the effect this has on vo-O Raman peak position in each respective system due to changes in force constant of the O-O bond vibration. Arrow sizes represent the strength and the nature of the interaction with coordinating cations i.e. small, light ions have concentrated charges with stronger electrostatic forces of attraction with O₂⁻ and may even be able to abstract electron density producing a covalent-like interaction, whilst the reverse is true for charge dispersed ions.151

Figure 3. 5. (a) Raman Spectra of an Ir-rGO cathode using PVDF binder in non-aqueous Li-O₂ cell after discharging. Spectral bands at 1,123 cm⁻¹ and 1,505 cm⁻¹ reported as the v_{O-O} of LiO₂, and the interaction between LiO₂ and the graphitic surface, respectively.¹ (b) Raman spectra of an Ir-rGO cathodes with PVDF binder. Spectral bands at 1,133 cm⁻¹ and 1,525 reported as PVDF degradation products.⁸⁴ (c) *In situ* SERS during Li⁺-OR/ER at rAu surface in 0.1 M LiClO₄ MeCN. Spectral bands 2 at 1,137 cm⁻¹ and 3 at 808 cm⁻¹ are reported as the v_{O-O} of an LiO₂ intermediate and Li₂O₂ discharge products during cycling on an rAu WE.⁷⁴

.....160
Figure 3. 6. Plot of v_{O-O} spectral bands attributed to LiO₂ in the non-aqueous Li-O₂ literature (see, Table 3. 1) against the molecular mass of Li⁺. The estimated v_{O-O} for LiO₂ based on the coordinating cation (Li⁺) is 1,167±10 cm⁻¹, calculated from derived \mathbb{K}_{iv}^c relationship, shown in red. Region (A) v_{O-O} values would fit with the expected value of a LiO₂ species. Only one value matched this and it was reported by Xia *et al.* who observed a broad v_{O-O} band (1,150-1,200 cm⁻¹) after discharging non-aqueous Li-O₂ batteries.¹⁵⁹ Region (B) v_{O-O} values would be expected to be partially stabilised Li⁺...O₂^{·-} species' or misallocated bands. Other reports of v_{O-O} in a variety of different systems (Table 3.1) are likely solvated surface/solution LiO₂ species or possibly PVDF degradation product in cases where PVDF binder is present.^{39,84,85}

Figure 3. 9. Plot of v_{O-O} of KO₂ doped alkali-metal halogen salts against the molecular mass of the anion in the salt.⁴⁶¹

.....172
Figure 3. 10. Low temperature (15-16 K) v_{O-O} spectral positions of alkali-metal O₂^{·-} in Ar matrices vs the cation Mr, see Table 3. 5 for values. Δv_{O-O} gap between thermodynamically; stable (KO₂, RbO₂, CsO₂), and unstable (LiO₂, NaO₂) M⁺...O₂^{·-} species'.

.....175
Figure 3. 11. Fitted plots of O₂^x bond parameters from Table 3. 6 against the B_o. All colour-coordinated axis labels are shown above the graph. Cubic lines of best fits are shown by dashed lines, all fits generated an R² value of 1. Fit values shown in Table 3. 7

.....178
Figure 3. 12. Fitted plots of O₂^x estimated bond parameters calculated from all previously mentioned v_{O-O} values reported in the literature (> 200 species). Light green shaded regions signify covalent O₂^x species where valence bond electrons are concentrated in the O₂^x π2px, y * orbitals. Light orange regions signify covalent O₂^x species were the outermost valence electron is shared with the coordinating environment. Colour coordinated axis labels are shown above the graph.....184

Figure 4. 1. Chemical structures of IL cations, anions used in this work as well with the associated abbreviations for each constituent are presented.....191

Figure 4. 2. Dynamic surface potential *in situ* SERS multi-dimensional (a) and (c): plots, Top: Potential (black lines)/current (blue or red lines) vs. time plots of OR/ER in O₂ saturated TESTFSI and Aze₁₄TFSI (analogous with CVs in Figure 4. 3 (b) and (d)). Bottom: contour plots of SERS data in v_{O-O} and v_{O-Surf} regions, respectively, at corresponding times with the electrochemistry. Regions of low and high v_{O-O} and v_{O-Surf} band intensities highlighted in green and red in the electrochemical top plots. (b) and (d): 3D visual plot of spectral changes with time. This data has been reproduced from previously published work, ref:⁴²¹

.....194
Figure 4. 3. Dynamic surface potential *in situ* SERS. (a) and (c): Selection of stacked SERS spectra of the rAu working electrode surface collected in rapid succession in O₂ saturated TESTFSI and Aze₁₄TFSI, respectively. Left and right are scans of v_{O-O} and v_{O-Surf} wavenumber regions, respectively. (b) Top, CVs of O₂ saturated TESTFSI at 100 mV s⁻¹ with standard OR/ER cycle (dashed line) and extended reduction cycle (blue line). Top right inset shows potential region where O₂^{·-} bands first appear with small current response due to formation of a O₂^{·-}-surface layer prior to the bulk ORR current response. Bottom, v_{O-O} (purple dashed lines and dots) and v_{O-Surf} (orange dashed lines and dots) wavenumber position/intensity vs. potential plots. There is a visible blue-Stark shift and intensity rise then decrease as the potential is

- lowered. (d) Top, CVs of O₂ saturated Aze₁₄TFSI at 20 mV s⁻¹ during normal OR/ER cycle (dashed line) and extended reduction cycle (red line). Bottom, v_{O-O} and v_{O-Surf} wavenumber positions and intensity plots vs. potential. There is a visible red-Stark shift and intensities increase with decreasing potential. Both (b) and (d): starting data points when O₂^{•-} bands appear shown in black, where possible coloured arrows are included as visual aids indicating reduction (dark red) and oxidation (dark blue) directions of potential scanning.....198
- Figure 4. 4.** Controlled electrode surface potential *in situ* SERS spectra (a) and (c): Stacked SERS spectra of rAu working electrode surface at specified held potentials, during reduction (bottom) and oxidation (top) in O₂ saturated TESTFSI (a) and Aze₁₄TFSI (c), respectively. (b) and (d): Top: Selected CVs of O₂ saturated TESTFSI (b) and Aze₁₄TFSI (c), respectively. Where potential is held a current drop is visible on the CV. Bottom: v_{O-O} and v_{O-Surf} wavenumber position and intensity plots vs potential. v_{O-O} (purple dashed lines and points) and v_{O-Surf} (orange dashed lines and points) bands both visibly blue and red Stark shift in TESTFSI and Aze₁₄TFSI, respectively. Both (b) and (d): starting points when bands appear shown in black, coloured arrows are visual aids indicating reduction (dark red) and oxidation (dark blue) directions of potential scanning.....202
- Figure 4. 5.** O₂^x-surface bond structures, left to right: flat, kinked and bent. Visible bond vibrations based on the surface selection rule are shown above each structure.^{7,509,511} The tick and cross indicate which band will be observable by Raman.....207
- Figure 4. 6.** Extended spectra acquired with surface potential control at specified held ORR potentials in O₂ saturated TESTFSI. Standard (black line) refers to TESTFSI at OCP.....211
- Figure 4. 7.** (a) Stacked spectra of rAu surface at OCP and ORR potentials in cation-varied ILs. Dashed lines demarcate weak and strong v_{O-O} and v_{O-Surf} bands (light grey and grey). (b) CV comparison of OR/ERs in O₂ saturated cation-varied ILs cycled at 100 mV s⁻¹. (c) Average v_{O-O} values for ILs plotted on Figure 3. 3b. Calculated trend-line shown (black dotted line). Error bars indicate range over which v_{O-O} shifted with potential. (d) Close-up of IL section. Subs-trends (green dashed lines) for asymmetrical and partially-symmetrical cation containing ILs are denoted by A and B, respectively. All spectral bands are summarised in Table 4.8.214
- Figure 4. 8.** Cation structures generated in Spartan 15: (a) TES⁺ (b) N₁₄₄₄₄⁺ (c) Pyr₁₄⁺ (d) Aze₁₄⁺. Partial-symmetry axis shown by red-dashed line.....215
- Figure 4. 9.** OR/ER CVs at 20, 50 and 100 mV s⁻¹ at an rAu electrode in O₂ saturated ILs: (a) TESTFSI, (b) Pyr₁₄TFSI, (c) Pip₁₄TFSI, (d) Aze₁₄FSI, (e) N₁₄₄₄TFSI, (f) N₁₈₈₈TFSI. Ar-saturated E_{window} also shown (dark grey dashed lines).....218
- Figure 4. 10.** (a) Stacked spectra of rAu surface at OCP and ORR potentials (2.1 and 1.8 V vs. Li/Li⁺) in various ILs with different anions. (b) CV comparison of OR/ERs in O₂ saturated anion-varied ILs at 100 mV s⁻¹. (c) Average v_{O-O} values for ILs plotted on v_{O-O} graph outlined in Figure 3. 3b with the calculated trend line shown (black dotted line). Error bars indicate range over which v_{O-O} shifted with potential in each IL. (d) Close-up of the section pertaining to the ILs. Anion based ILs highlighted in grey222
- Figure 4. 11.** OR/ER CVs at 20, 50 and 100 mV s⁻¹ at an rAu working electrode in O₂ saturated ILs: (a) Pyr₁₄OTf and (b) Pyr₁₄DCA with different anions. Ar-saturated E_{window} also shown (dark grey dashed lines).....223
- Figure 4. 12.** (a) CV of OR/ER at 100 mV s⁻¹ scan rate on Au coated Si-prism, in O₂ saturated Pyr₁₄TFSI. Surface potentials were held at ORR (2.2 V vs Li/Li⁺, red line) and OER (3.2 V vs. Li/Li⁺, black line) potentials. (b) SEIRA spectra recorded for Au thin film at two representative electrode potentials. The reference spectra were taken at the OCP (3.1 V) before the potential sweep started. Work done in collaboration with V. Padmanabhan.227
- Figure 5. 1.** (a) Stacked spectra of rAu surface at OCP and ORR potentials (2.3 and 2.0 V vs. Li⁺/Li) in O₂-saturated Pyr₁₄TFSI based IL:sol blend electrolytes (60:40 vol.% IL:sol ratio).

Dashed lines demarcate weak and strong ν_{O-O} and ν_{O-Surf} bands	(b) CVs of OR/ERs in O_2 -saturated IL:sol blends at 100 mV s^{-1}	237
Figure 5. 2. Li^+ -OR/ERs CVs of; 0, 5, 100 mM LiTFSI in O_2 -saturated Pyr ₁₄ TFSI:DMSO IL:sol blend electrolytes (60:40 vol % ratio) at 100 mV s^{-1} . Ar electrochemical window shown (grey dashed line). Reaction mechanism for current peaks A-C are outlined below (eq. 5. 1-5. 3) and their parameters in Table 5. 2.	240	
Figure 5. 3. Selected Li^+ -ORR CVs in a O_2 -saturated, 5 mM LiTFSI in Pyr ₁₄ TFSI:DMSO (60:40 vol% IL:sol ratio) blend (3) electrolyte during (a) ORR and (b) OER cycling. SERS spectra were collected whilst potentials were held. Stacked SERS spectra of rAu surface at (c) reduction and (d) oxidation potentials (labelled). Where present ν_{O-Surf} , ν_{O-O} (O_2^{2-}) and ν_{O-O} (O_2^{*-}) spectral band regions are highlighted in grey.	244	
Figure 5. 4. Solvent screening versus Li-metal showing visible electrolyte changes after >72 hours exposure. * denote blends that formed an SEI with Li-metal.	246	
Figure 5. 5. Formulate multi-component IL: Red crosses and green ticks indicate unstable and stable electrolytes after 72 hours exposure to Li-metal, respectively.	252	
Figure 5. 6. Dynamic surface potential <i>in situ</i> SERS multi-dimensional: plots, (a) Top: potential (black line)/current (green line) vs. time plots of OR/ER in O_2 -saturated AB2 electrolyte (analogous with CVs in Fig. 5. 7 b). Regions of very low, low and high ν_{O-O} and ν_{O-Surf} band intensities are highlighted in blue, green and red, respectively (top). Bottom: contour plots of SERS data in ν_{O-O} and ν_{O-Surf} regions, respectively, at corresponding times with the electrochemistry (analogous with SERS spectra in Fig. 5. 7 a). (b) 3D visual plot of spectral changes with time.	254	
Figure 5. 7 (a) Selection of stacked SERS spectra of the rAu working electrode surface collected in rapid succession in O_2 -saturated AB2 electrolyte. Left and right are scans of ν_{O-O} and ν_{O-Surf} wavenumber regions, respectively. (b) Top, CV of OR/ER in O_2 -saturated AB2 at 20 mV s^{-1} (green line). Bottom, ν_{O-O} and ν_{O-Surf} wavenumber position/intensity vs. potential plots. Start data points where O_2^{*-} appears shown in black and where possible coloured arrows are included as visual aids indicating reduction (dark red) and oxidation (dark blue) directions of potential scanning. There is a strong visible blue-Stark shift and intensities rise then decrease after the ORR maximum as potential is lowered.	255	
Figure 5. 8. Extended spectra acquired with surface potential control at specified held potentials during ORR in oxygen saturated TESTFSI. ν_{O-Surf} and ν_{O-O} spectral band regions are highlighted in light grey and grey.	256	
Figure 5. 9. (a) Stacked SERS spectra of rAu surface at OCP and ORR potentials in O_2 -saturated multi-component IL:sol blends. ν_{O-Surf} and ν_{O-O} spectral band regions are highlighted in grey. (b) OR/ER CVs of blended electrolytes at 100 mV s^{-1}	257	

List of Tables

Table 1. 1. Specifications of some common commercial secondary batteries. ^{20–27}	7
Table 1. 2. Comparison of Li-graphite ²⁹ and pure alkali/alkali earth metal anodes. See experimental chapter 2 for theoretical specific capacity and energy density calculations.	9
Table 1. 3. Comparison of Li-ion and key non-aqueous M-O ₂ discharge products. See experimental chapter 2 for theoretical specific capacity and energy density calculations.	11
Table 1. 4. Comparison of energy storage methods and devices.	13
Table 1. 5. Overview of Li ⁺ ...O ₂ ^{·-} intermediary and list of electrolyte components that manipulate the ion-ion coupling strength and Li ⁺ and O ₂ ^{·-} solvation. The ion-ion coupling is dependent on the immediate environment and it is likely that a continuum of exists between a more coordinated Li ⁺ ...O ₂ ^{·-} intermediate and fully solvated Li ⁺ and O ₂ ^{·-} ions.....	35
Table 1. 6. Collection of various non-aqueous Li-O ₂ cathode catalysts. As reported catalyst abbreviations used, units included where necessary.....	74
Table 1. 7. Collection of various non-aqueous Li-O ₂ cell redox mediators and a selection of their performances from various reports.....	79
Table 1. 8. Table of some key non-aqueous Li-O ₂ properties that have been reported to-date compared with targets for going beyond Li-ion. Once all targets can be met in a non-aqueous Li-O ₂ battery then it can be considered practical and not just theoretical.	85
Table 1. 9. Terminology for describing and potentially quantifying different ions with examples of hard (H ⁺ /F ⁻) and soft (TBA ⁺ /TFSI ⁻) Lewis acid/bases ions.....	92
Table 1. 10. General trends in physicochemical properties as molecular mass (Mr) and fluorine content (FC) of anion increase.	94
Table 2. 1. Comparison of Fc redox potential shifts between different references electrodes in Pyr ₁₄ TFSI.	129
Table 3. 1. v _{O-O} Raman spectral bands for C ⁺ ...O ₂ ^{·-} complexes with monovalent cation reported in the literature. Mr values, system information and calculated i _v and \mathcal{K}_{iv}^c values of the cation are shown.	152
Table 3. 2. Table of calculated i _v , i _{sa} and \mathcal{K}_{iv}^c , \mathcal{K}_{isa}^c values for common cations and IL cations. Cations with smaller \mathcal{K} values are expected to be stronger Lewis acids.....	157
Table 3. 3. Table of calculated i _v , i _{sa} , \mathcal{K}_{iv}^a , \mathcal{K}_{isa}^a values for common anions and IL anions. Anions with smaller charge dispersions are expected to be stronger Lewis bases.	158
Table 3. 4. KO ₂ doped alkali metal-halogen salt values.	172
Table 3. 5. v _{O-O} Raman Table of alkali-metal O ₂ ^{·-} complexes in Ar matrices ^{458,459,480}	175
Table 3. 6. Bond parameters, v _{O-O} and outer π px, y * valence orbital structures of various O ₂ ^x species listed. v _{O-Ox} = O ₂ ^x (O ₂ ²⁻ , O ₂ ^{·-} , O ₂ , O ₂ ⁺) Raman spectral band. v _{O-Ox} /v _{O-O} – Operoxidere ratios show good approximations with B _o indicating that energy changes in the bond vibration are directly proportional to the addition or removal of a valence electron. Correlating these values allows v _{O-O} to be used to approximate the other bond parameters. 177	
Table 3. 7. Cubic fits from Figure 3. 11 in accordance with equation 3. 4. In theory, all O ₂ ^x parameters can be estimated by measuring v _{O-O} . k values can be calculated more directly using Hooke's law.	179
Table 3. 8. Some reports of various simple (single atom) and complex (multi-valent, molecular) O ₂ ^x species, using their reported names, where both the v _{O-O} and bond lengths have been reported together. Experimentally observed bond length values using XRC are contrasted with those calculated from their respective v _{O-O} using Table 3. 7 and a percentage difference between the observed and calculated bond lengths generated.	185

Table 4. 2. Summary of key IL bands. C ⁺ refers to cation, either TES ⁺ or Aze ₁₄ ⁺ (Note Peak 1 is the designation of the flat conformer of adsorbed O ₂ ^{•-} at ca. 430 cm ⁻¹).....	200
Table 4. 3. Summary of v _{O-Surf} and v _{O-O} bond vibrations (v _x) with dynamic and controlled surface potentials (<i>E</i>) at the rAu interface in O ₂ saturated TESTFSI and Aze ₁₄ TFSI. Δ denotes difference between highest and lowest spectral values shifting with potential.	205
Table 4. 4. OR/ER electrochemical parameters from IL CVs in Figures 4. 9. Scan rates: 20/100 mV s ⁻¹ . Potentials corrected versus ferrocene redox couple.	219
Table 4. 5. Overview evaluating reversibility of CVs and which diagnostic criteria were met in each ILs in Figure 4. 9.	219
Table 4. 6. OR/ER electrochemical parameters from anion varied IL CVs. Scan rate: 20/100 mV s ⁻¹ . Potentials corrected versus fc ^{+/fc} redox couple.....	224
Table 4. 7. Table outlining five diagnostic criteria for evaluating reversibility of IL CVs of three anion varied ILs.	224
Table 4. 8. Summary of O ₂ ^{•-} spectral bands in different ILs; wavenumber ranges (Δν) between lowest and highest peak fitted values due to potential shifts, full width half-maximum (FWHM) ranges and stability of IL when exposed to alkali metals.	226
Table 5. 1. OR/ER electrochemical parameters from IL:sol blend CVs in Figure 5. 1. Scan rate: 100 mV s ⁻¹ . Potentials corrected versus fc ^{+/fc} redox couple.	237
Table 5. 2. OR/ER electrochemical parameters from IL:sol blend CVs in Figure 5. 1. Scan rate: 100 mV s ⁻¹ . Potentials corrected versus fc ^{+/fc} redox couple.	241
Table 5. 3. Important electrolyte properties for an ideal non-aqueous Li-O ₂ battery electrolyte and solvents, ILs and electrolyte additives that fit the criteria, etc.....	250

List of Abbreviations

EV	- Electric Vehicles	O₂	- Dioxygen
CEV	- Combustion engine vehicle	O₂·	- Superoxide
M-O₂	- Metal-oxygen battery	O₂²⁻	- Peroxide
Li-air	- Lithium-air battery	O²⁻	- Oxide
Redox	- Reduction-oxidation reaction	CoO₂	- Cobalt oxide
Li-O₂	- Lithium-oxygen battery	H⁺	- Proton
SEI	- Solid electrolyte interphase	EC	- Ethyl carbonate
Ni-Cd	- Nickel cadmium battery	DMC	- Dimethyl carbonate
Ni-MH	- Nickel metal hydroxide battery	PC	- Propylene carbonate
O₂-cathode	- semi-porous O ₂ cathode	Li⁺	- Lithium cation
Mr	- Relative molecular mass	Na⁺	- Sodium cation
Li-ion	- Lithium ion battery	K⁺	- Potassium cation
C₆Li	- Lithium intercalated graphite	H₂O₂	- Hydrogen peroxide
Li-metal	- Lithium metal	M₂O₂	- Metal peroxide
LiFePO₄	- Lithium iron phosphate	M₂O	- Metal oxide
SERS	- Surface-enhanced Raman spectroscopy	LiO₂	- Lithium superoxide
EPRS	- Electron paramagnetic resonance spectroscopy	Li₂O₂	- Lithium peroxide
Li_xO_y	- Lithium oxides (mix of)	Li₂O	- Lithium oxide
H_xO_y	- Hydrogen oxides (mix of)	LiOH	- Lithium hydroxide
ORR	- O ₂ reduction reaction	NaO₂	- Sodium superoxide
OER	- O ₂ evolution reaction	Na₂O₂	- Sodium peroxide
OR/ERs	- Oxygen reduction/evolution reactions	Cs₂O₂	- Caesium peroxide
Li⁺-ORR	- Lithiated O ₂ reduction reaction	KO₂	- Potassium superoxide
Li⁺-OER	- Lithiated O ₂ evolution reaction	MgO₂	- Magnesium peroxide
Li⁺-OR/ER	- Lithiated O ₂ reduction/evolution reactions	Li-S	- Lithium sulphur battery
AN	- Gutmann acceptor number	NO₃⁻	- Nitrate
DN	- Gutmann donor number	LiNO₃	- Lithium nitrate
RRDE	- Rotating ring disc electrode	LiO₂H	- Lithium hydroperoxide
Li⁺...O₂·	- Lithium superoxide coordination complex	TiO₂	- Titanium oxide
C⁺...O₂·	- Monovalent cation superoxide complex	C⁺	- Cation
M⁺...O₂·	- Metal-superoxide complex	OTF⁻	- triflate anion
TEA⁺	- Tetraethylammonium	LiOTf	- Lithium triflate
TBA⁺	- Tetrabutyl ammonium cation	ClO₄⁻	- Perchlorate anion
TBA⁺...O₂·	- TBA ⁺ superoxide coordination complex	IR	- Infrared
TBA⁺-ORR	- O ₂ reduction reaction with solvated TBA ⁺	DMPU	- Dimethylpropyleneurea
TBAClO₄	- Tetrabutyl ammonium perchlorate	CO₂	- Carbon dioxide
TFSI⁻	- Bis (trifluoromethylsulfonium)imide anion	CO	- Carbon monoxide
LiTFSI	- Lithium bis (trifluoromethylsulfonium)imide	PVDF	- Polyvinylidene fluoride
TBATFSI	- TBA bis (trifluoromethylsulfonium)imide	PTFE	- Polytetrafluoroethylene
LiTFSI	- Lithium bis (trifluoromethylsulfonium)imide	Al₂O₃	- Aluminium oxide
SSIP	- Solvent separated ion-pair	CNFs	- Carbon nanofibers
SS-CIP	- Solvent separated contact ion-pair	GO	- Graphene oxide
CIP	- Contact ion-pair	CPL	- Composite protective layer
¹O₂ or ¹Δ_g	- Singlet oxygen	MnO₂	- Manganese dioxide
³Σ_g⁻	- Triplet oxygen	Co₃O₄	- Cobalt oxide
TEGDME	- Tetraethylene glycol dimethyl ether	TAAs⁺	- Tetraalkyl ammonium
DEMS	- Differential electrochemical mass spectroscopy	GNs	- Graphene nanosheets

PEDOT	- Poly(3, 4-ethylendioxothiophene)	MP	- Melting point
LATP	- Lithium aluminium titanium phosphate	OCP	- Open circuit potential
LUMO	- Lowest unoccupied molecular orbital	IHP	- Inner Helmholtz potential
HOMO	- Highest occupied molecular orbital	OHP	- Outer Helmholtz potential
LiSiCON	- Lithium super ionic conductor	Ar	- Argon
DABCO	- 1,4-Diazabicyclo[2.2.2]octane	DFT	- Density functional theory
E_w	- Electrochemical potential window	WE	- Working electrode
EIS	- Electrochemical impedance spectroscopy	GC	- Glassy carbon electrode
EC	- Electrochemical	CE	- Counter electrode
SEC	- Spectroelectrochemical	RE	- Reference electrode
MWNTs	- Multi-walled nanotubes	G-In	- Gas-in
ATR	- Attenuated total reflection	G-Out	- Gas-out
SEIRAS	- Surface enhanced IR adsorption spectroscopy	SEC	- Spectroelectrochemical
FWHM	- Full width at half maximum	rAu	- Roughened gold
TESTFSI	- Tetraethyl sulphonium TFSI	PEEK	- Polyether ether ketone
Pyr₁₄TFSI	- n-Butyl-n-methyl pyrrolidinium TFSI	ZnSE	- Zinc selenide
Pyr₁₄OTf	- n-Butyl-n-methyl pyrrolidinium triflate	CsI	- Caesium iodide
Pyrr₁₄DCA	- n-Butyl-n-methyl pyrrolidinium dicyanamide	IRE	- Infrared reflection element
Pip₁₄TFSI	- n-Butyl-n-methyl piperidinium TFSI	AFM	- Atomic force microscopy
Pip₁₄OTf	- n-Butyl-n-methyl piperidinium triflate	Fc	- Ferrocene
Aze₁₄TFSI	- n-Butyl-n-methyl azepenium TFSI	Fc⁺	- Ferrocinium
N₁₄₄₄TFSI	- Methyl tributyl ammonium TFSI	m-Pip	- Methyl piperidine
N₁₈₈₈TFSI	- Methyl trioctyl ammonium TFSI	HDPE	- High-density polyethylene
Pyr₁₄HSO₄	- n-Butyl-n-methyl pyrrolidinium hydrogen sulphate	z	- Number of electrons
N₂₂₂₂TFSI ,	- Tetraethyl ammonium TFSI	O-M	- O-to-metal bond
N₃₃₃₃TFSI	- Tetrapropyl ammonium TFSI	DCA⁻	- Dicyanamide anion
N₄₄₄₄TFSI	- Tetrabutyl ammonium TFSI	SO₄²⁻	- Sulphate
SHINERS	- Shell isolated nanoparticle enhanced Raman spectroscopy	OCP	- Open circuit potential
O₂^x	- Dioxygen species (where x = -2, -1, 0, +1)	DMSO	- Dimethyl sulfoxide
EtANO₃	- Ethylammonium nitrate	Me-Im	- Methyl imidazole
Zn-O₂ (aq)	- Aqueous zinc oxygen battery	MeCN	- Acetonitrile
LiPF₆	- Lithium hexafluorophosphate	DME	- Dimethoxy ether
M_xO_y	- Metal oxide (mix/unspecified)	DEGME	- Diglyme
EDL	- Electrochemical double layer	Cs⁺-salt	- Caesium salt
HSAB	- Hard-soft acid-base theory	Li⁺-salt	- Lithium salt
HetBlend	- Heterogeneous IL:solvent based blend	XRD	- X-ray diffraction
LP30	- 1.0 M LiPF ₆ in EC/DMC=50/50 (vol. %/vol. %)	Ge	- Germanium
Di-Im²⁺	- Dimethyl imidazolium dication	R&D	- Research and development
XRC	- X-ray crystallography	IL:sol	- Ionic liquid: solvent blend
XPS	- X-ray photo spectroscopy		

List of Variables

\bar{v}	- Scan rate (mV s^{-1})	Z	- EC equivalent (C g^{-1})
i	- Current (μA)	Q	- Charge (C)
j	- Current density ($\mu\text{A cm}^{-2}$)	U	- Specific energy (W h kg^{-1})
E	- Potential (V)	k	- Bond force constant (N m^{-1})
t	- Time (s)	c	- Speed of light ($2.998 \times 10^{10} \text{ cm s}^{-1}$)
F	- Faraday constant ($96,485 \text{ s A mol}^{-1}$)	v	- Spectral wavenumber (cm^{-1})
n	- Mole (mol)	B_o	- Bond order
i_v	- Ionic volume (\AA^3)	H	- Bond enthalpy (kJ mol ⁻¹)
i_{sa}	- Ionic surface area (\AA^2)	l	- Bond length (\AA)
K_{isa}	- Charge dispersion ($\text{g mol}^{-1} \text{\AA}^2 \text{ C}^{-1}$)	Mr	- Molecular mass (g mol ⁻¹)
K_{iv}	- Charge dispersion ($\text{g mol}^{-1} \text{\AA}^3 \text{ C}^{-1}$)	T	- Temperature (K)
R	- Gas constant ($8.314 \text{ J mol}^{-1} \text{ K}^{-1}$)	z	- N° of electrons
Mr^R	- Reduced mass		

List of Publications

1. Radjenovic P. M., Hardwick L. J., Time-Resolved SERS Study of the Oxygen Reduction Reaction in Ionic Liquid Electrolytes for Non-Aqueous Lithium-Oxygen Cells, *Faraday Discussions*, 2017, **206**, 379-392.
2. Radjenovic P. M., Hardwick L. J., The Vibrational Spectroscopy of Dioxygen (*in preparation*).
3. Radjenovic P. M., Hardwick L. J., Non-Aqueous Lithium-Oxygen Batteries; An Overview (*in preparation*).
4. Radjenovic P. M., Hardwick L. J., Heterogenous Blended Electrolytes for Next Generation Batteries (*in preparation*).

1. Introduction and Review

1.1 Why is Energy Storage Important?

Society's dependence on the consumption of finite hydrocarbon fuel sources is unsustainable. Ideally, the current production-consumption energy model needs replacing with a renewable, non-polluting, one if we are to balance environmental pressures and sustain economic output, whilst continuing to improve standards of living worldwide. Evidently, for this to occur change is needed in many key industries, bordering on a technological revolution.⁹ Such a revolution could occur in the automotive industry¹⁰ with a transition from combustion engine to electrically powered vehicles (EVs). Most countries today possess the infrastructure to generate electricity *en masse* at power stations for distribution through a national grid system to households. Thus, a network of recharging terminals for EVs in public and private is within current capabilities. Energy storage devices, required to store energy and power vehicular transits, would be vital for this transition to occur.

This model of centralised electricity generation for EV use would reduce the public reliance on hydrocarbons and offer key environmental gains through the more efficient use of existing hydrocarbon fuels. Large power station turbines operate at efficiencies up to 65 %,¹¹ much higher than local combustion engines which only have ~30 % maximum efficiencies¹² (practical ‘fuel-to-wheel’ efficiencies are more like 10-15 %).¹³ Also, electricity can be transmitted across long distances with negligible losses through powerlines compared with the current model of; extracting, processing, and transporting finite crude oil derived fuels to vast numbers of regional refuelling stations. Therefore, a substantial reduction in CO₂ emissions would be achieved through increased fuel utility and reduced transportation costs, whilst the consumption of conventional fossil fuels by power stations can be subsidised and gradually replaced by renewable energy sources (as is currently taking place). Thus, helping to transition humanity’s energy system from a resource consumption to a sustainability-based model.

In addition to environmental benefits, the battery industry is forecast to be worth \$120 billion by 2019¹⁴ and many other important industries would seek to benefit from the development of advanced, affordable, energy storage devices:

- **Grid energy storage** – Power station turbines operate most efficiently under a constant load, as stopping and starting greatly increases the likelihood of damage or seizure adding to operating costs for energy suppliers. However, national power demands fluctuate and at times of low demand power surges can damage grid infrastructure. Energy storage techniques provide a mechanism for smoothing these transients in demand and increasing operational efficiencies. Currently, the most common form of grid storage is pumped hydroelectric; however, this requires huge initial capital costs and is geographically dependant. Large battery banks could potentially provide a more practical way of increasing grid storage capacity for energy suppliers.
- **Renewable energy** – Sources such as wind and solar are intermittent due to their dependence on environmental conditions, subsequently, power output often does not match demand. Also, electricity generated in times of low demand can put strain on the electric grid. With efficient grid energy storage, surplus energy can be stored in times of high output for use later (i.e, when the wind/sun is not blowing/shining, respectively), vastly improving the operational efficiency and practicality of renewables.
- **Aerospace** – Many solar panel powered satellites use energy storage devices in periods with no direct exposure to sunlight. These would benefit from more advanced energy storage systems, reducing their weight and improving operational efficiencies.
- **Portable appliances** – The largest market for energy storage devices is in portable appliances which range from laptops to power tools. Higher energy storage capacities would greatly improve their functionality.

1.2 Energy Storage

1.2.1 Past

Volta reported the first battery able to provide a continuous current by connecting alternating Zn and either Cu or Ag plates separated by a brine-soaked cloth. Connected in series, the potential difference between the metals provided a means for electrons to spontaneously flow from the more electropositive Zn metal anode (eq. 1. 1) to the less electropositive Cu/Ag cathode, driving a reduction reaction producing H₂ gas (eq. 1. 2). Charge transfer between electrodes is facilitated by the brine salt bridge; allowing ion diffusion and providing a proton (H⁺) source for the cathode reaction. This discovery subsequently lead to the development of the field of electrochemistry.

Zn anode

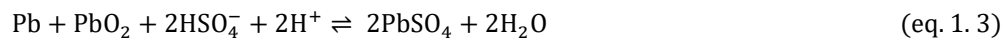


Ag cathode



The first rechargeable, or secondary, battery mechanism was invented by Gaston Planté, in 1859. This consisted of a lead anode and lead dioxide cathode in a sulphuric acid electrolyte. Both the cathode and anode are oxidized and reduced, respectively, during discharge producing Pb²⁺ cations and water. The electrodes are regenerated by applying a reverse potential (eq. 1. 3) allowing batteries to be cycled for the first time. Due to low production costs, lead-acid batteries with modified electrolytes are still in widespread use today for applications where mass and volume are not a constraint.

Overall mechanism



1.2.2 Present

Modern batteries operate on the same principles witnessed by Volta, whereby, electrons are stored in, and released from, electrodes and/or electrolytes via redox mechanisms. Lithium ion (Li-ion) batteries are the current state-of-the-art energy storage technology. The exceptionally low molecular mass and charge density of lithium cations (Li^+) compared with other metal cations making them ideal charge carriers within a battery. Commercial Li-ion batteries exploiting Li^+ were first developed by Sony in the 90's using graphitic anodes to store intercalated lithium (C_6Li) instead of using pure lithium metal (Li-metal) anodes.¹⁵ Graphitic anodes provided a technological breakthrough at the time due to improved safety, efficiency and charge-discharge reversibility. However, with greatly reduced anodic capacitance, compared with using Li-metal anodes. Pure Li-metal anode battery systems date back to the 60's, but were never fully commercialised due to safety concerns associated with dendrite formation on cycling which caused cells to hazardously short circuits.

Figure 1.1 shows a schematic of a practical Li-ion battery. Graphitic carbon anodes store Li which can intercalate into and out of the lattice. Fully charged anodes have a C_6Li composition (six C atoms account for every Li atom stored). Metal oxides, (usually cobalt oxide (CoO_2) compounds with Ni, Mn and Al dopants) are used as cathodes though other oxide cathodes such as iron phosphate (FePO_4) are also used commercially. Common Li-ion battery electrolytes use a mix of linear and cyclic carbonates (i.e. EC/DMC and EC/PC) with a dissolved lithium salt (Li^+ -salt), such as lithium hexafluorophosphate (LiPF_6). The surface of C_6Li anode reacts spontaneously in contact with the carbonate electrolyte forming a chemically stable, electrically insulating and ionically conductive passivation layer, known as the solid electrolyte interphase (SEI). The SEI serves to protect the anode against bulk Li^+ dissolution into the electrolyte whilst allowing Li^+ diffusion into/out of the anode during cell cycling.

Solid-state polymer or ceramic electrolytes are also commercially available¹⁶ and are generally more resilient to temperature fluctuations. However, with the downside of having greater internal resistance which impacts on the overall power of the cell.

During discharge, Li stored in the anode deintercalates from the Li-graphite lattice (eq. 1. 4), diffuses through the SEI and is dissolved into the electrolyte as Li^+ , liberating electrons to the external circuit which are used for work. Dissolved Li^+ diffuses to the metal oxide cathode where it is reduced and forms a variant of the corresponding Li-metal oxide (e.g. $\text{Li}_{1-x}[\text{CoO}_2]$, where $x = 1 \rightarrow 0$). When the cathode reaches Li-saturation (LiCoO_2), the reaction is complete and cell discharge ceases (eq. 1. 5). During charge an external overpotential is applied to the cell, liberating Li^+ from the original cathode back into the electrolyte where it diffuses and subsequently intercalates back into the original graphitic anode. Even with the weight of carbon in the anode and heavy metal oxide cathodes, the Li-ion battery is an effective means of storing energy over consecutive cycles. Key features differentiating Li-ion batteries from other secondary batteries is their use of Li^+ which gives comparatively high specific energy densities (Table 1. 1). However, Li-ion batteries are not the most affordable battery system per kWh (\$ $\text{kW}^{-1} \text{ h}^{-1}$) of energy and in applications where volume and mass are not constraints, or where cooling and/or safety is a concern, other battery technologies are often preferred commercially.

Li-graphite anode



Metal oxide cathode



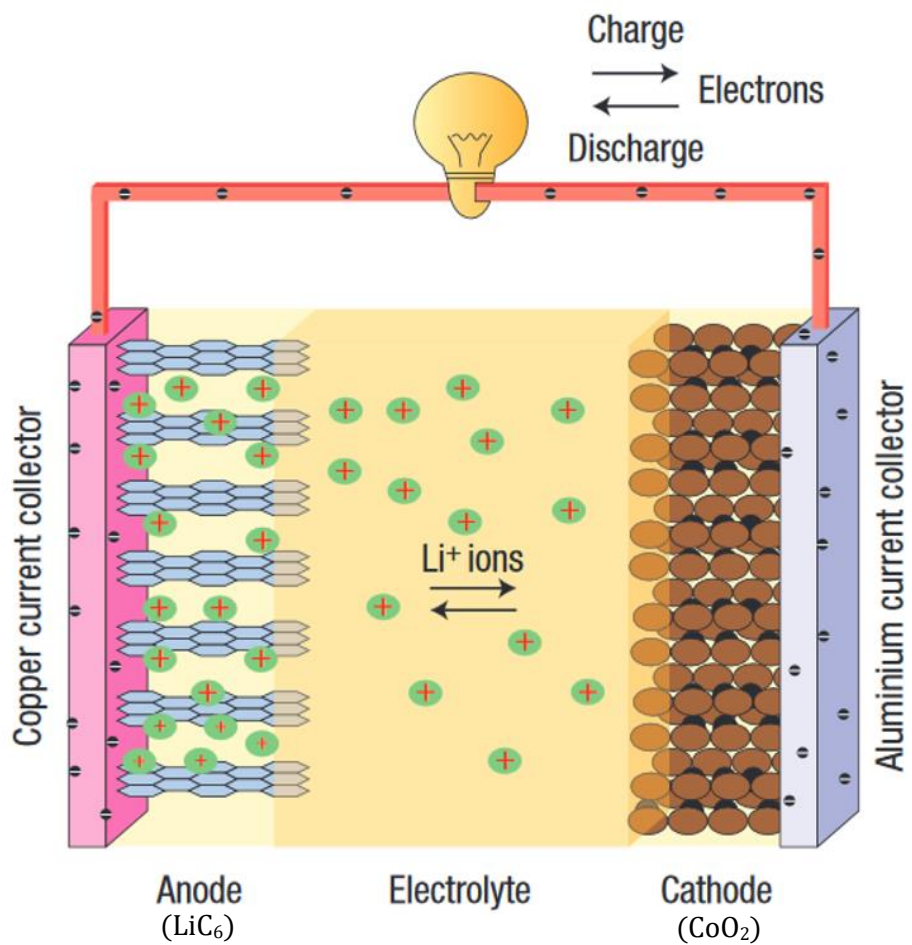


Figure 1. 1. Li-ion battery schematic in fully charged state. Figure reproduced from ref. ¹⁷.

Currently, the cost of Li-ion on the cell up to pack level ranges from > 145 - $800 \text{ \$ kW}^{-1} \text{ h}^{-1}$.¹⁸ Economies of scale can help to significantly reduce battery prices in future which is a necessity if EVs are to become commercially competitive with the combustion engine vehicles (CEVs). This has led to huge investment by many battery companies in battery production, most notably by Tesla into its flagship ‘Gigafactory’. Which has the stated goal of; producing 35 GWh of battery capacity per annum, and reducing the price of commercial Li-ion batteries to $100 \text{ \$ kW}^{-1} \text{ h}^{-1}$ by 2020,^{10,19} in line with the goal set by the US department of energy of $125 \text{ \$ kW}^{-1} \text{ h}^{-1}$ by 2020.^{10,19} These low prices would greatly increase the financial competitiveness of EVs. However, if there are no real improvements in battery technology, then the mileage of EVs will continue to be limited by the theoretical energy densities of Li-ion. If EV mileages are ever to improve to gasoline competitive levels (increasing their practicality and energy efficiency) then novel battery systems are needed to go beyond Li-ion. This will require looking back to pure metal anodes and novel, lighter, cathode materials.

Table 1. 1. Specifications of some common commercial secondary batteries.²⁰⁻²⁷

Battery	Cell voltage (V)	Specific energy (Wh kg ⁻¹)	Cost (\$ kW h ⁻¹)
Deep cycle (lead acid)	2.1	25-45	55-140
Ni-Cd	1.2	50-70	> 400
Ni-MH	1.2	50-550	360
Li-ion (practical)	3.8	180-240	> 145
Li-ion (theoretical)	3.8	387	100

1.2.3 Future

Numerous alternative battery mechanisms, combining various theoretically high capacity anodes and cathodes, have been proposed as future alternatives to Li-ion. Of these non-aqueous alkali-metal air/oxygen ($M-O_2$) batteries have shown significant promise. These batteries are formed by combining a semi-porous cathode with a metal anode and a stable electrolyte.

For the anode, group one metals (Li, Na, K) are conductive and readily oxidised with the possibility of storing substantial amounts of energy, making them theoretically ideal for use in batteries. A comparison of some high capacity Li-graphite alternative anodes is outlined in Table 1. 2. Down group one and two as the metals atoms get heavier and larger; their anode theoretical energy densities decrease ($11,738 \rightarrow 2,009 \text{ Wh kg}^{-1}$), but remain high compared with Li-graphitic anodes (963 Wh kg^{-1}). Li-metal anodes offer the highest gains with an order of magnitude improvement on Li-graphite anodes and offer a potential step-change improvement for energy storage technologies. Whilst Na, K, Ca and Mg are abundant elements that could be effectively exploited commercially.^{2,3,28} However, with higher associated safety risks and lower energy densities than Li-metal.

Table 1. 2. Comparison of Li-graphite²⁹ and pure alkali/alkali earth metal anodes. See experimental chapter 2 for theoretical specific capacity and energy density calculations.

Anode	Anode reaction	No e- stored per molecule (z)	Mr z ⁻¹ (mol g ⁻¹)	Potential (V vs NHE)	Theoretical specific capacity (A h kg ⁻¹)	Theoretical energy density (Wh kg ⁻¹)
C ₆ Li	C ₆ Li ↔ Li ⁺ + C ₆ + e ⁻	1	97.9	-2.84	339	963
Li	Li ↔ Li ⁺ + e ⁻	1	6.9	-3.04	3,861	11,738
Na	Na ↔ Na ⁺ + e ⁻	1	22.9	-2.71	1,166	3,159
K	K ↔ K ⁺ + e ⁻	1	39.1	-2.93	685	2,009
Mg	Mg ↔ Mg ²⁺ + 2e ⁻	2	12.2	-2.37	2,197	5,207
Ca	Ca ↔ Ca ²⁺ + 2e ⁻	2	20.0	-2.87	1,340	3,846

For a complete high capacity and energy density battery the metal-anode needs to be combined with a similar high capacity cathode. For non-aqueous M-O₂ batteries, a semi-permeable cathode (hereon called the O₂-cathode) is used. Ideally, O₂-cathodes are inert, conductive, structures that enable environmental dioxygen (O₂) to diffuse into the M-O₂ cell, facilitate charge transfer and act as scaffold supports for discharge reactions to occur at and for reaction products to deposit onto. However, the O₂-cathode necessarily adds some excess “dead” weight to the overall cell. Graphitic carbons are the most commonly used O₂-cathodes due to their abundance, relatively high surface area structures and low costs, though alternative materials such as; TiO₂,³⁰ Au-foam³¹ and ionic gels,³² have also been used. The energy density and specific capacity of the M-O₂ battery are determined by the metal oxide species (M_xO_y) formed at the O₂-cathode during discharge. M_xO_y species are desirable discharge products due to their: low Mr (compared with Li-metal oxides in Li-ion), use of environmentally abundant O₂ which is stored externally from the cell before discharge (reducing the batteries starting weight). As well as, the ability to form charge dense oxide species; superoxide (O₂[•]), peroxide (O₂²⁻) and oxide (O²⁻),³³ which can store one, two and/or four cations and electrons per O₂ molecule, respectively. An overview of various M-O₂ cathode discharge products and properties is given in Tables 1. 3.

Table 1. 3. Comparison of Li-ion and key non-aqueous M-O₂ discharge products. See experimental chapter 2 for theoretical specific capacity and energy density calculations.

Cathode Product	Cathode reaction	No e- stored per cation (z)	Mr z ⁻¹ (mol g ⁻¹)	Potential (V vs. anode)	Theoretical specific capacity (A h kg ⁻¹)	Theoretical energy density (Wh kg ⁻¹)
LiCoO ₂	Li ⁺ + CoO ₂ + e ⁻ ↔ LiCoO ₂	1	97.9	3.80	274	1,040
LiO ₂	Li ⁺ + O ₂ + e ⁻ ↔ LiO ₂	1	38.9	2.75	688	1,893
Li ₂ O ₂	Li ⁺ + O ₂ + e ⁻ ↔ Li ₂ O ₂	2	22.9	2.96	1,170	3,511
Li ₂ O	Li ⁺ + O ₂ + e ⁻ ↔ Li ₂ O	4	14.9	2.94	1,794	5,274
NaO ₂	Na ⁺ + O ₂ + e ⁻ ↔ NaO ₂	1	55.0	2.27	487	1,106
Na ₂ O ₂	2Na ⁺ + O ₂ + e ⁻ ↔ Na ₂ O ₂	2	39.0	2.33	687	1,602
KO ₂	K ⁺ + O ₂ + e ⁻ ↔ KO ₂	1	71.1	2.48	377	935
MgO ₂	Mg ²⁺ + O ₂ + 2e ⁻ ↔ MgO ₂	2	28.0	2.93	957	2,803

Full cell theoretical properties are calculated by combining a metal anode and its respective O₂-cathode discharge reaction product (e.g. K-metal and KO₂). Table 1. 4 gives an overview of various future M-O₂ and Li-ion alternative batteries. Combining Li with O₂ gives the non-aqueous Li-O₂ battery theoretical gasoline competitive mileages for EVs that would be a hugely important and lucrative advancement in energy storage capabilities.¹³ However, the non-aqueous Li-O₂ battery is currently far from reaching these energy densities in a practical device and is still under R&D, with numerous technical and material constraints that need to be addressed (outlined later). In terms of practical exploitation; the lithium sulphur (Li-S) battery is the closest of the ‘next generation’ battery technologies, with the first generation of batteries now available commercially,³⁴ though estimates for high energy density versions of the battery range from 5-10 years³⁵ and up to 20 years for the non-aqueous Li-O₂ battery.³⁶

Interestingly, some of the reaction mechanisms and problems are similar in different M-O₂ batteries. Therefore, understanding gained in one battery has the potential to illuminate understanding of others. Also, in each system the fundamental reaction pathway driving the discharge and charge reactions at the O₂-cathode are similar but ambiguity remains around the ideal reaction mechanisms as they appear to be malleable depending on the electrolyte, additives and the electrode structure of the cell.^{4,37-41} Thus, by slightly changing key parameters different reaction pathways can be favoured or inhibited, changing the structure and composition of discharge products (discussed in detail below). Therefore, due to similarities in their reaction mechanisms and their low-overpotential and relatively high efficiencies; Na-O₂ and K-O₂, are potential “stepping stone” technologies from the Li-ion towards the practical non-aqueous Li-O₂ battery. Similarly, some light alkali-earth and boron group metals (Mg, Ca, Al) also have the potential to make good M-O₂ battery systems with even higher theoretical energy densities than the non-aqueous Li-O₂ battery⁴² due to their ability to form multivalent

cations storing two or three electrons per cation. However, these systems have not received much attention, with only a handful of publications in each, as there is little evidence yet for the reversible cyclability of their oxide discharge products within practical potential ranges. Therefore, the non-aqueous Li-O₂ battery in turn could potentially be a “stepping stone” to these advanced M-O₂ battery systems.

Table 1. 4. Comparison of energy storage methods and devices.

Energy storage method	Reaction	Cell voltage (V)	Theoretical specific energy (Wh kg ⁻¹)	Theoretical energy density (Wh L ⁻¹)	refs.
Li-ion (theoretical)	C ₆ + Li ⁺ + e ⁻ ↔ C ₆ Li	3.8	387	1,015	29,36
Gasoline (theoretical)	-	--	13,000	10,010	13,43
Gasoline (Practical)	-	--	1,700	1,310	13
Li-S (non-aq.)	2Li + S ↔ Li ₂ S	2.2	2,567	2,199	36,44
Zn-O ₂ (aq.)	2Zn + O ₂ ↔ 2ZnO	1.7	1,350	--	45-48*
Al-O ₂ (aq.)	4Al + 3O ₂ + 6H ₂ O ↔ 4Al(OH) ₃	2.7	2,800	--	46,49-51
Mg-O ₂ (aq.)	Mg + ½O ₂ + H ₂ O ↔ Mg(OH) ₂	2.9	1,200-3,900	--	42,46,51,52*
Ca-O ₂ (non-aq.)	Ca + ½O ₂ ↔ CaO	3.1-3.4	840-2,990	--	53*
K-O ₂ (non-aq.)	K + O ₂ ↔ NaO ₂	2.2	935	2,001	3,46*
Na-O ₂ (non-aq.)	Na + O ₂ ↔ NaO ₂	2.3	1,108	2,434	46,53,54
Na-O ₂ (non-aq.)	2Na + O ₂ ↔ Na ₂ O ₂	2.3	1,605	--	2,53,55
Li-O ₂ (hybrid, alkaline)	2Li ⁺ + O ₂ + H ₂ O ↔ LiOH	3.2	3,582	2,242	36,56
Li-O ₂ (hybrid, acid)	4Li + O ₂ + 4H ⁺ ↔ 4Li ⁺ + H ₂ O	4.3	1,119	3,804	56
Li-O ₂ (non-aq.)	2Li + O ₂ ↔ Li ₂ O ₂	3.0	3,510	3,436	36*

*Calculated based on mass of discharge product

1.3 Metal-O₂ Batteries

The first Li-metal batteries date from the 60's, however, a combination of material problems and technological limitations prevented the development of Li-O₂ systems until much later.⁵⁷ In 1996 using *ex situ* Raman spectroscopy, Abraham *et al.* demonstrated the first non-aqueous Li-O₂ cell which had lithium peroxide (Li₂O₂) as a discharge product. The cell consisted of a polymer electrolyte with an Li-metal anode and a semi-porous carbon O₂-cathode.⁵⁸ A decade later Ogasawara *et al.*⁵⁹ showed that Li₂O₂ could be electrochemically decomposed back to O₂ and Li metal, evidencing for the first time the possibility of a rechargeable (secondary) non-aqueous Li-O₂ battery with theoretical specific energies above 3,500 Wh kg⁻¹. This sparked a new wave of interest in the field resulting in increased levels of R&D in recent years.^{32,60,61}

The high theoretical specific energy and energy densities of Li-O₂ batteries and the sustainability of using environmentally abundant Na, K, Mg and Ca metals in their respective M-O₂ batteries has fuelled recent attention on M-O₂ battery technologies.^{3,53,55} As investigations into Li-O₂ cell designs have progressed three main classifications have emerged differentiated by cell chemistry. These cells can be classified as non-aqueous, aqueous and hybrid systems.³⁰ Solid-state cells are also widely considered as a unique system that utilises a solid-state (usually polymer or ceramic) Li-ion conducting electrolyte, though the charge-discharge mechanisms mirror the other systems.

The focus of this project is investigating the fundamental reaction mechanisms of the non-aqueous Li-O₂ battery; however, due to its similarity with other alkali-metal, a general account of non-aqueous alkali metal-O₂ batteries is given in this section whilst a more detailed account focussing on the non-aqueous Li-O₂ battery is given in section 1.4.

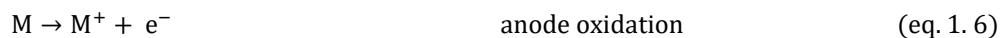
1.3.1 Non-Aqueous Alkali-Metal-O₂ Overview

On discharge of non-aqueous M-O₂ batteries the anode is oxidised to metal cations (M⁺) which dissolve and migrate through the electrolyte to the cathode liberating electrons (eq. 1. 6). O₂ diffuses into the cell through the semi-porous O₂-cathode and undergoes a one electron reduction reaction to form radical O₂^{•-}, a Lewis base (eq. 1. 7). O₂^{•-} reacts readily with M⁺ (Lewis acidity: Li⁺ > Na⁺ > K⁺) dissolved in the electrolyte to form the respective metal-superoxide (MO₂) species (eq. 1. 8). If the MO₂ species is unstable or solvated then an intermediary coordinate complex (M⁺…O₂^{•-}) is formed. Unstable M⁺…O₂^{•-} species eventually disproportionate or are electrochemically reduced to insoluble metal peroxides (M₂O₂) and O₂ (eq. 1. 7-1. 9) via a similar mechanism to the well-studied O₂ reduction reaction (ORR) mechanism in protic media that produces hydrogen peroxide (H₂O₂).⁶²⁻⁶⁵. At high overpotentials a direct two-electron reduction to M₂O₂ or four-electron reduction to metal oxide, M₂O may also occur (eq. 1. 10-1. 12).^{4,66-68}

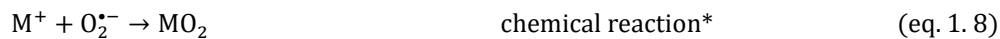
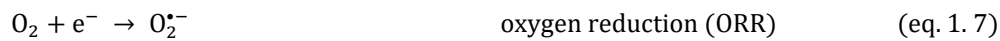
The final discharge product (MO₂, M₂O₂ or M₂O) depends on the reactivity of the dissolved metal cations as they have been shown to control the ORR.⁶⁹ Relatively large/heavy cations (K⁺, Rb⁺) form thermodynamically stable O₂^{•-}-complexes, where O₂^{•-} is more basic, due to weak M⁺ coordination.^{70,71} Whereas, small/light (charge dense) cations (Li⁺, Na⁺) form thermodynamically unstable O₂^{•-} complexes that can catalyse a further disproportionation reaction to O₂²⁻.^{69,72} The cations small size potentially allows adjacent O₂^{•-} anions in the complex to ‘touch’⁷³ and can distort the even charge distribution on the O₂^{•-} dumbbell shaped anion facilitating charge transfer between anions and inducing chemical disproportionation to more stable oxides e.g. O₂ and O₂²⁻.

Discharge

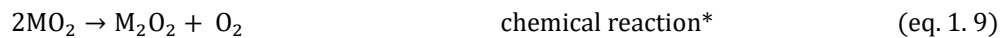
Anode



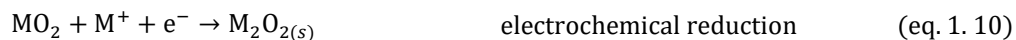
O₂-Cathode



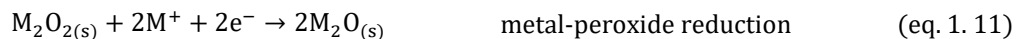
if MO₂ thermodynamically/kinetically unstable then



and/or



Other



Where: M = Li⁺, Na⁺, K⁺, or substitute M⁺ for alkali earth metals: ½Mg²⁺, ½Ca²⁺

*Indicates reaction can occur at electrode surface or in solution

There is some debate over the MO₂/M⁺...O₂^{·-} discharge product/intermediate and this is where the alkali metal-O₂ battery mechanisms begin to differ between Li, Na and K based cells. Fundamental *in situ* surface-enhanced Raman spectroscopy (SERS) studies by Peng *et al.*⁷⁴ provided the first evidence of the presence of what was claimed to be a pure lithium superoxide (LiO₂) intermediary species during the discharge reaction at a roughened polycrystalline gold (rAu) model cathode surface. However, the LiO₂ spectral band was quickly replaced by a Li₂O₂ band, suggesting chemical disproportionation (eq. 1. 9). LiO₂ has long been believed to be both thermodynamically and kinetically unstable at temperatures above 25 K^{54,74-80} and it is still unclear whether this observed intermediary species is a pure LiO₂ phase or a partially electrolyte/electrode stabilised Li⁺...O₂^{·-} complex.^{67,81} Other studies on carbon O₂-cathodes suggest that the LiO₂ species is more stable than previously thought and could potentially be a cyclable discharge product^{82,83} though this is disputed^{39,84,85} and will be discussed in the

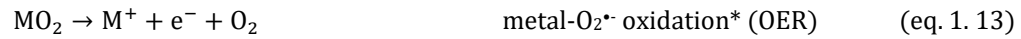
following chapters. Sodium superoxide (NaO_2), though also thermodynamically unstable, can be kinetically stable and the extent to which the disproportionation reaction takes place (if at all) depends on the ability of the electrolyte to accept or donate electron density from/to reaction intermediaries ($\text{O}_2^{\bullet-}$ and Na^+), respectively.^{37,86} On the other hand, potassium superoxide (KO_2) is both thermodynamically and kinetically stable and is the main discharge product in the non-aqueous K-O₂ battery.

For some time, the solvation properties of the electrolyte have been suggested to play an important role in the cathode O₂^{•-} intermediary reaction mechanism.⁸⁷ More recently, solvents used in the non-aqueous Li-O₂ and Na-O₂ electrolytes were indeed shown to directly effect ORRs, inducing either a (1) surface or (2) solution reaction mechanism.^{4,37,88,89} The surface mechanism produces thin, relatively uniform and electrically insulating metal oxide (M_xO_y) films via a ‘surface-up’ deposition mechanism. During discharge, these films of discharge products deposit, eventually passivating the cathode surface, preventing further electron transfer and causing premature cell death. Whereas, a solution discharge reaction mechanism is favoured as it bypasses the formation of passivation films by solvating reaction intermediaries away from the O₂-cathode surface and into the bulk where they react, aggregate and precipitate out of solution. Charge-rich regions on the cathode surface, such as; defect sites^{90,91} and plane edges,⁸⁰ act as nucleation sites that concentrate the precipitation and growth of discharge products allowing for large agglomerates (~5μm)⁹² to grow in a ‘solution-down’ deposition mechanism. Compared with thin films, an agglomerate growth mechanism extends the cathode surface area exposed to the electrolyte much later into discharge, enabling increased charge transfer and producing higher discharge capacities⁴. M_xO_y morphology can also be switched from film to agglomerate by decreasing the discharge current to low rates which gives kinetic information about the reaction.^{93–95}

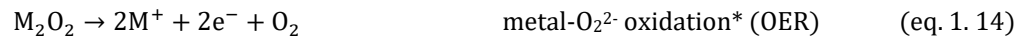
On charge, an overpotential is applied to the cell electrochemically decomposing M_xO_y discharge products at the cathode back to their substituents: M^+ and O_2 (eq. 1. 13 and 1. 14). M^+ migrate back through the electrolyte to the anode, where they are reduced and plated back onto the anode (eq. 1. 15). O_2 is evolved, hence the name O_2 evolution reaction (OER), and diffuses out of the cell into the environment (Fig. 1. 2).

Charge

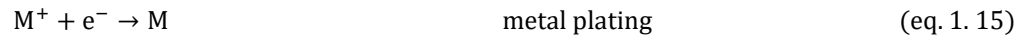
O_2 -cathode



and/or



Anode



Where: $M = Li^+, Na^+, K^+$, or substitute M^+ for alkali earth metals: $\frac{1}{2}Mg^{2+}, \frac{1}{2}Ca^{2+}$

*Indicates reaction can occur at electrode surface or in solution

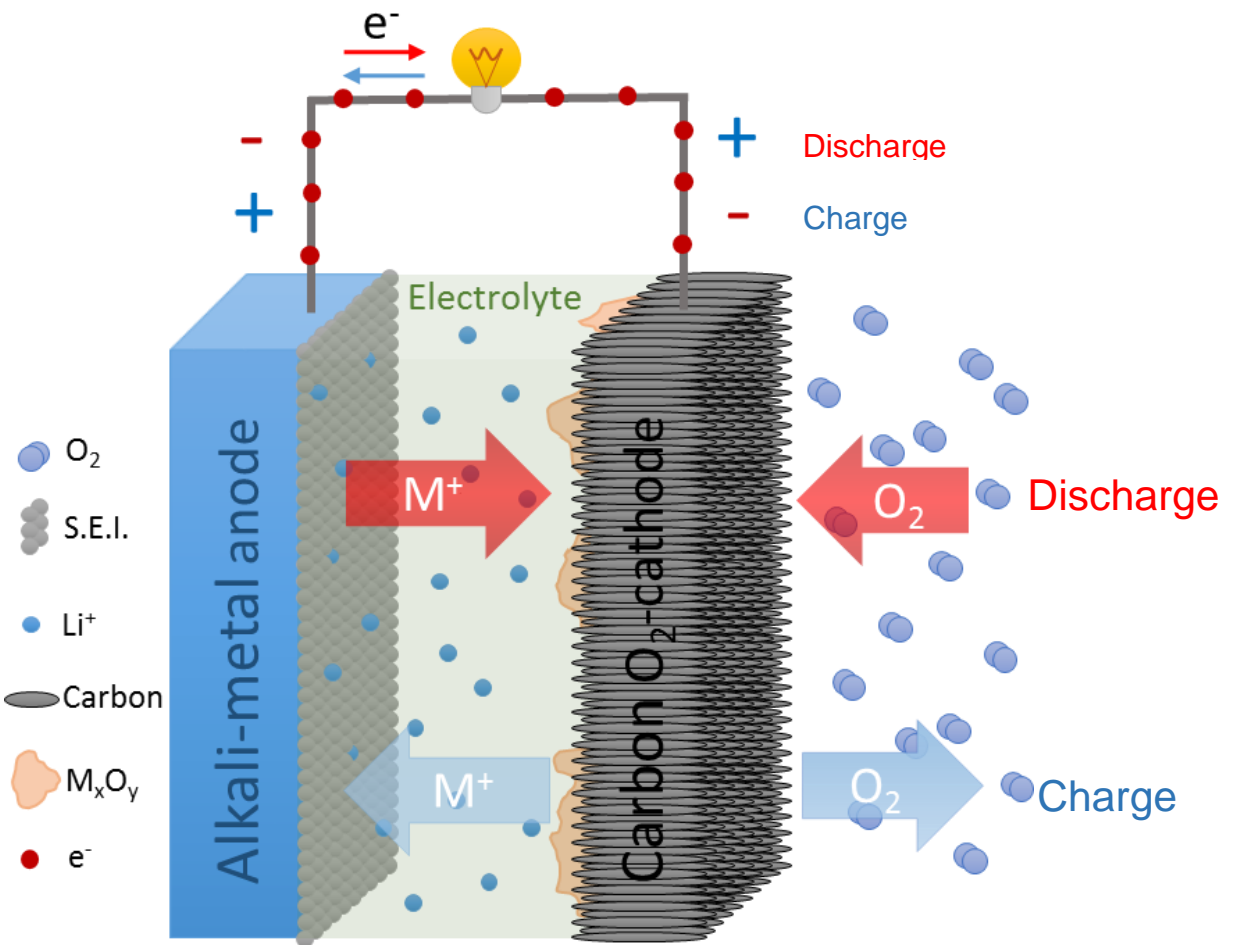


Figure 1. 2. Non-aqueous $M-O_2$ battery schematic, arrows indicate general direction of M^+ , O_2 and electron movement during discharge (red) and charge (light blue).

1.3.2 Aqueous Li-O₂

Aqueous Li-O₂ cells (Fig. 1. 3a) differ from non-aqueous cells due to the presence of water in electrolyte and operate via different pH dependent reaction mechanisms. The basic electrolyte mechanism produces LiOH, as the primary discharge product (eq. 1. 16) on the cathode whilst acidic electrolytes produce solvated Li⁺ and water (eq. 1. 17). The main challenge for aqueous Li-O₂ batteries is that water reacts vigorously with pure Li metal. A similar problem is faced by non-aqueous systems that can absorb atmospheric water from air feed-streams, even though the water content in the electrolyte is much lower and may be overcome by using hydrophobic electrolytes⁹⁶ or efficient air stream scrubbers. One method for overcoming Li dissolution in aqueous electrolyte is to use solid-state protective barriers such as lithium super ionic conductive (LiSICON) membranes that are water stable and allow Li⁺ ion diffusion without exposing the bulk Li anode to the aqueous electrolyte. These barriers are usually polymer, silicone or ceramic based, however, they generally have low conductivity leading to power issues associated with their use.^{36,97–100} That said, if these problems can be overcome, then the aqueous system has the potential to be an interesting battery as it removes the engineering problem of dehumidifying feed air.

Alkaline electrolyte – discharge/charge⁹⁸



Acidic electrolyte – discharge/charge³⁶



1.3.3 Hybrid Li-O₂

Hybrid Li-O₂ cells combine components of both the aqueous and non-aqueous cells (Fig. 1. 3b). Aprotic electrolytes are used in contact with the Li metal anode, inhibiting anode dissolution and degradation whilst facilitating fast Li⁺ ion diffusion during discharge and charge. An aqueous electrolyte is used in contact with the semi-porous cathode and both electrodes and electrolytes are separated by a solid Li⁺ ionic conductor¹⁰¹ which acts as a salt bridge, facilitating Li⁺ ion diffusion from the non-aqueous to the aqueous electrolytes whilst preventing mixing. During cell cycling, Li⁺ diffuses from/to the anode by migrating through the electrolyte to/from the cathode during discharge and charge, respectively. Where, depending on the pH of the aqueous electrolyte, it follows the reaction mechanisms outlined previously (eq. 1. 16 and 1. 17),^{13,101–105}

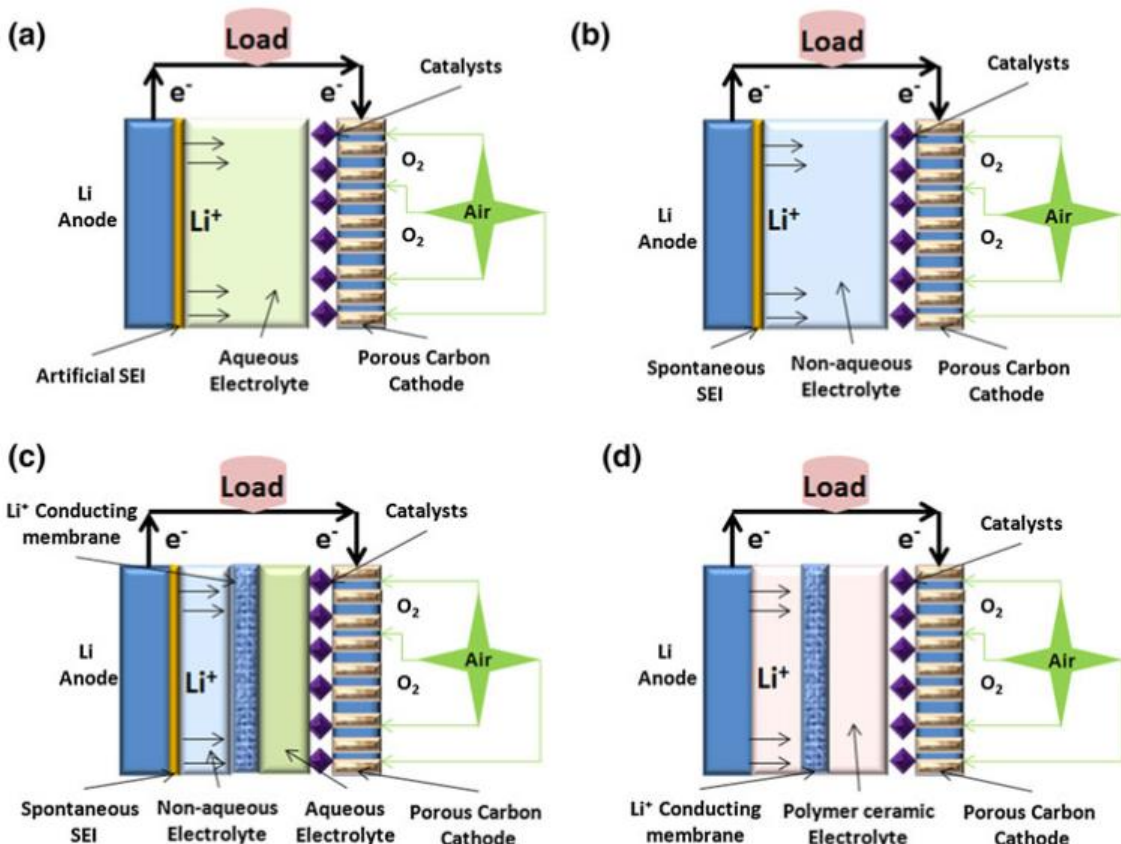


Figure 1. 3. Types of Li–O₂ batteries: (a) Aqueous electrolyte, (b) aprotic/non-aqueous electrolyte, (c) mixed (aprotic-aqueous), and (d) solid-state. Figure reproduce from ref. ¹⁰⁶

1.4 Non-Aqueous Li-O₂ batteries

The non-aqueous Li-O₂ battery, comprises; a pure Li-metal anode acting as a reservoir for storing electrochemical potential energy, an O₂-cathode structure allowing O₂ to diffuse in/out of the cell and a Li⁺ salt containing electrolyte that facilitates ion diffusion and charge transfer between electrodes. Due to numerous material and technical challenges limiting the overall battery performance, individual areas will be addressed in the following sections:

1. discharge reaction mechanism,
2. charge reaction mechanism,
3. O₂-cathode composition and structure,
4. Li-metal anode & SEI,
5. electrolyte; solvent and salt additives,
6. catalysis.

1.4.1 Discharge

ORR mechanism overview

One electron oxidation of Li-metal to Li^+ at the anode (eq. 1. 18) and reduction of O_2 to radical $\text{O}_2\cdot^-$ at the O_2 cathode in a Li^+ containing electrolyte (Li^+ -ORR, eq. 1. 19) are the main reaction mechanisms driving the non-aqueous $\text{Li}-\text{O}_2$ battery. As a moderate Lewis base and hard Lewis acid, respectively, $\text{O}_2\cdot^-$ and Li^+ react (eq. 1. 20) to form a $\text{Li}^+\cdots\text{O}_2\cdot^-$ intermediary at the O_2 -cathode surface or in solution (if the electrolyte is sufficiently solvating). As mentioned previously, a pure LiO_2 phase is unlikely above 25 K, rather an intermediary $\text{Li}^+\cdots\text{O}_2\cdot^-$ ion complex temporarily stabilised either by the electrolyte⁶⁷ or defect/binding sites on the electrode surface¹⁰⁷ is more probable. The $\text{Li}^+\cdots\text{O}_2\cdot^-$ intermediary reactions (eq. 1. 20-1. 21b) are limiting reactions responsible for capping the capacity of the battery, directly affecting its efficiency and cyclability.⁴ The Li^+ -to- $\text{O}_2\cdot^-$ ion coupling strength is dependent on the electrolyte environments ability to solvate and accept/donate electron density from/to the ions, respectively.⁶⁷ $\text{Li}^+\cdots\text{O}_2\cdot^-$, whether at the surface (eq. 1. 21a) or in solution (eq. 1. 21b), is chemically unstable and disproportionates to O_2 and insoluble Li_2O_2 ($E_p^r = 2.96\text{V}$ vs Li/Li^+) which deposits on the O_2 -cathode.^{108,109} At high overpotentials in electron donating electrolytes $\text{Li}^+\cdots\text{O}_2\cdot^-$ may undergo an additional one electron reduction at the cathode surface to Li_2O_2 directly (eq. 1. 22).^{4,66-68}

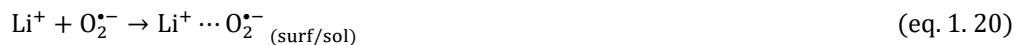
Four e^- reduction of O_2 (eq. 1. 23) to lithium oxide (Li_2O), where $\text{Li}^+\cdots\text{O}_2\cdot^-$ and Li_2O_2 are intermediary steps, has also been shown.^{108,110} As a final discharge product, Li_2O has the highest theoretical energy density (Table 1. 3) for the non-aqueous $\text{Li}-\text{O}_2$ battery as more Li^+ is stored per unit mass of O_2 than any other lithium oxide species (Li_xO_y). However, Li_2O_2 is the preferred battery discharge product as oxidation of Li_2O requires a large thermodynamic driving force to reform the O-O bond and it is unclear if it can be reversibly oxidised within

practical potential ranges. Until its oxidation/decomposition mechanism can be shown, Li₂O is considered a parasitic discharge product to be avoided as it electronically insulates the O₂-cathode when formed, reducing the available surface area for charge transfer and, thus, the depth of charge and cell discharge capacity of the cell.

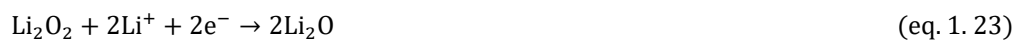
Anode



Cathode/electrolyte



Other



Where: *surf* denotes surface species and *sol* denotes solution solvated species.

After fundamental studies first provided evidence for the formation of Li⁺...O₂^{•-} during the discharge reaction at a rAu cathode surface.⁷⁴ It was subsequently suggested that equation 1. 19 does not occur, rather that O₂ is directly reduced in the presence of Li⁺ to LiO₂ without the existence of a radical O₂^{•-} species at the cathode.³⁹ However, this was later shown using SERS and electron paramagnetic resonance spectroscopy (EPRS) to be heavily dependent on the electrolyte solvent and that free O₂^{•-} is the intermediary in electrolytes with high Gutmann donor numbers (Lewis bases).^{4,111} The Gutmann donor and acceptor numbers (DN and AN) are empirically derived values for estimating a solvents affinity for donating or accepting electron density, respectively, from solvated species and, thus, the approximate strength of solvent-solute interactions^{95,112}.

The quantity of Li_xO_y generated and stored in the O_2 -cathode is proportional to surface area available for charge transfer, pore volume and the depth of discharge.^{100,113,114} Whilst, the thickness and morphology^{93,95,115,116} of the Li_xO_y deposits, i.e. whether they form thin films or a series of large agglomerates on the surface, depends on the electrolyte,^{4,88} discharge rates^{94,117,118} and the cathode structure.¹¹⁹ Li_xO_y deposits have wide band gaps and are electrically insulating.¹²⁰ During discharge, as surface deposits thicken, the available surface area for charge transfer on the O_2 -cathode decreases and electrons must tunnel through surface deposits to the electrolyte phase boundary for the discharge reaction to continue. This causes the cell internal resistance to increase until charge transfer is completely inhibited and discharge ceases. Surface deposits also block pores within the cathode structure preventing O_2 from entering the cell and reacting further limiting the depth of discharge.

Premature cell death caused by O_2 -cathode surface passivation and the blocking of pores by discharge products are major problems limiting cell discharge capacities. A combination of three main methods have been proposed for overcoming these problems, using:

1. Electrolyte solvents¹²¹ and Li^+ salt additives¹²² like methyl-imidazolium (Me-Im) and lithium nitrate (LiNO_3), respectively, capable of dissolving some or all discharge intermediaries into the electrolyte away from the cathode surface, switching the Li^+ -ORR to a solution mediated mechanism. Li_xO_y species formed in solution precipitate onto the O_2 -cathode surface, circumventing surface passivation films, producing large agglomerated surface deposits (~0.5-5 μm diameter) dispersed across the cathode surface. In turn, the cathode surface remains exposed to the electrolyte for longer, enabling Li^+ -ORR to continue further into discharge, producing high discharge capacities^{92,123} compared to thin passivating films produced in weakly solvating electrolytes.
2. Phase-transfer catalysts, redox shuttles/mediators^{4,41,68,87,88,122,124-126} and/or complexing

agents³⁸ dissolved in the electrolyte that bind reaction intermediaries at the surface and shuttle them into the bulk promoting a solution mechanism reducing surface passivation,¹²⁷ whilst also storing some discharge products in the electrolyte.

3. O₂-cathode morphologies with high surface areas and pore volumes capable of accommodating larger quantities of discharge products,^{119,128–130}

The propensity of the electrolyte to donate or accept electron density from intermediary species was shown to directly affect Li⁺-ORR, inducing either a surface (eq. 1. 20a) or solution (eq. 1. 20b) mechanism.^{4,88} For the surface (surface-up deposition) mechanism, electrolyte solvation of intermediaries is weak, and reactions are concentrated at the surface, O₂^{·-} is consumed as it is produced forming Li₂O₂, which deposits uniformly in a surface-up mechanism forming thin passivating films of generally uniform thickness across the surface. Li₂O₂ film deposition insulates the O₂-cathode and charge transfer is completely inhibited at ~ 10 nm film thicknesses.⁹² For the solution (solution-down deposition) mechanism, reaction intermediaries dissolve in the electrolyte, diffuse away from the surface and react in solution. Insoluble Li₂O₂ is eventually formed and precipitates out onto the O₂-cathode surface.¹³¹ Two distinct paths for inducing the solution mechanism have since emerged; (1) high DN^{4,67,132} and (2) high AN^{41,88,89} mechanisms.

High DN solution mechanism

High DN solvents (Lewis bases) coordinate Li⁺ well through strong ion-dipole Coulombic attraction and form strong solvation shells around the cation^{67,132,133} which weaken its Lewis acidity and shield it from O₂^{·-} generated at the O₂-cathode. Essentially, O₂^{·-} competes with the solvent to coordinate Li⁺ and must penetrate the solvation shell for the disproportionation reactions to occur. Generally, the higher the DN of the electrolyte solvent the; stronger the

solvation shell, weaker the Li^+ Lewis acidity and weaker the influence of $\text{O}_2\cdot^-$ on Li^+ .^{4,70,74,134} Therefore, high DN solvents slow/inhibit the intermediary reaction by stabilising Li^+ in solution, enabling $\text{O}_2\cdot^-$ to dissolve and diffuse away from the cathode surface. Solvated Li^+ -ORR intermediaries react in solution when $\text{O}_2\cdot^-$ penetrates the Li^+ solvation shell. These charge-rich intermediaries agglomerate and chemically disproportionate to insoluble Li_2O_2 which precipitates out of solution. Charge rich regions on the cathode surface act as nucleation sites, concentrating precipitants into large structures whilst the rest of the surface remains exposed to electrolyte. Therefore, it has been concluded that High DN solvents are more ideal electrolytes.¹³¹

The high DN solution mechanism was shown with rotating ring disk electrode studies (RRDE) in high DN solvents: DMSO, and Me-Im (DN: 30 and 47, respectively).⁴ High electrode rotation rates continuously circulated fresh electrolyte and reactants to the ring disk electrode surface, preventing diffusion gradients in the electrochemical double layer (EDL) from forming. Thus, soluble reduction products generated on the inner disk electrode were removed from the surface and detected on the outer ring electrode. In the high DN electrolytes Li^+ -ORR and Li^+ -oxygen evolution reaction (Li^+ -OER) currents were similar on inner and outer-ring electrodes, respectively. Indicating the bulk of Li^+ -ORR discharge intermediaries ($\text{Li}^+\cdots\text{O}_2\cdot^-$, $\text{O}_2\cdot^-$) generated at the inner electrode were stable (at least short term), solvated into the electrolyte and oxidised on the outer ring electrode, see Figure 1. 5a (right-hand pathway). At high overpotentials, a second electrochemical reduction reaction of solvated/surface $\text{O}_2\cdot^-$ directly to $\text{O}_2^{2-}/\text{Li}_2\text{O}_2$ (eq. 1. 22) is also possible. Conversely, low DN solvents such as acetonitrile (MeCN, DN: 14) were shown to stabilise Li^+ poorly in the solvent, producing a stronger ‘charge starved’ Lewis acid Li^+ species that reacted readily with $\text{O}_2\cdot^-$ at the surface evidenced by minute Li^+ -OER outer-ring electrode currents. MeCN has a relatively high AN

(19) that normally has good MeCN \cdots O₂ $^{\bullet-}$ solvation, however, this is easily overcome by Li $^+$, forming visible Li $^+\cdots$ O₂ $^{\bullet-}$ at the surface, which disproportionates accordingly to form a uniform insulating layer of Li₂O₂, resulting in low discharge capacities.

On the down-side, solvents with good O₂ $^{\bullet-}$ solvation are often susceptible to nucleophilic attack and are prone to degradation¹³⁵ as free O₂ $^{\bullet-}$ has been shown to be a cause of electrolyte and cathode degradation in many non-aqueous Li-O₂ cells, limiting their capacities and cyclability.^{136,137} Therefore, selection of stable electrolytes that facilitate desired reaction mechanisms, stabilises and solvates the radical intermediaries and form Li $^+$ permeable protective SEIs on Li metal surface is paramount for a practical non-aqueous Li-O₂ battery to be realised.

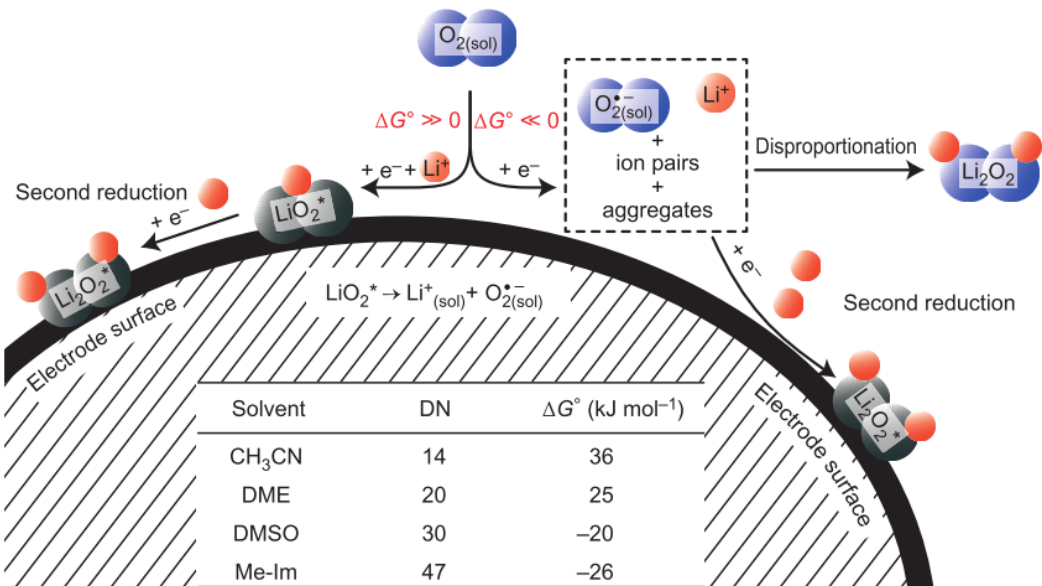
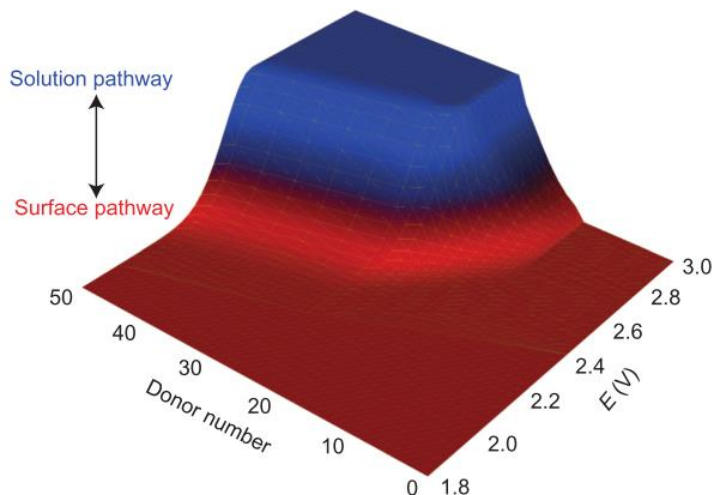
a**b**

Figure 1. 4. (a) ‘Schematic of the Li⁺-ORR mechanism in an aprotic solvent containing Li⁺, showing the; surface pathway in low DN electrolytes (left), solution pathway (top-right) and second electrochemical reduction reaction (bottom-right) in high DN solvents, respectively. (b) 3D plot showing the dominant pathway as a function of DN and potential. O₂ reduction in high-DN solvents and at high potentials (low overpotentials) follows the solution pathway (blue) and at low potentials (high overpotentials) the surface pathway (red). O₂ reduction in low-DN solvents at all potentials follows the surface pathway (red) forming uniform films.’ Figures reproduced from ref. ⁴.

High AN solution mechanism

Similar to the ability of high DN solvents to stabilise solvated Li^+ , high AN solvents stabilise and solvate $\text{O}_2^\cdot-$ well.⁶⁷ It has been shown in both non-aqueous Li and Na-O₂ systems^{41,88,138–140} that a solution mechanism can be induced using small amounts of a high AN (Lewis acid) solvent additives in the electrolyte, primarily water (H_2O , AN: 55).^{112,141} A proton source (H^+ being a stronger acceptor than Li^+) produces protonated intermediaries (H_xO_y : HO_2 , H_2O_2) which are highly soluble in polar solvents and readily diffuse into the bulk electrolyte, where they react with excess Li^+ to form Li_2O_2 , displacing H^+ , which is reused in Li^+ -ORR. Thus, water behaves as a phase-transfer catalyst. Lithium-hydroperoxide (LiO_2H) has been shown to be the intermediary species formed during the transition from H_xO_y to Li_2O_2 .¹⁴² Like the high DN mechanism, for the high AN mechanism; Li_2O_2 deposits onto the O₂-cathode surface in a solution-down mechanism, producing large toroid shaped Li_2O_2 agglomerates^{88,139} (Fig. 1. 5a). As little as 10 ppm H_2O can induce the solution mechanism.⁴¹ However, too much water may lead to the formation of LiOH , a parasitic four electron side reaction product¹⁴³ that may also be cyclable.⁴⁰ Figure 1. 5b is a DN vs AN plot of some common solvents, the dark-red area (circled in black) denotes the properties of an ideal electrolyte. Electrolytes with both high DN and ANs could theoretically stabilise and solvate both Li^+ and $\text{O}_2^\cdot-$, reducing their propensity to react or coordinate each other, though electrolytes with these properties appear to be highly uncommon.

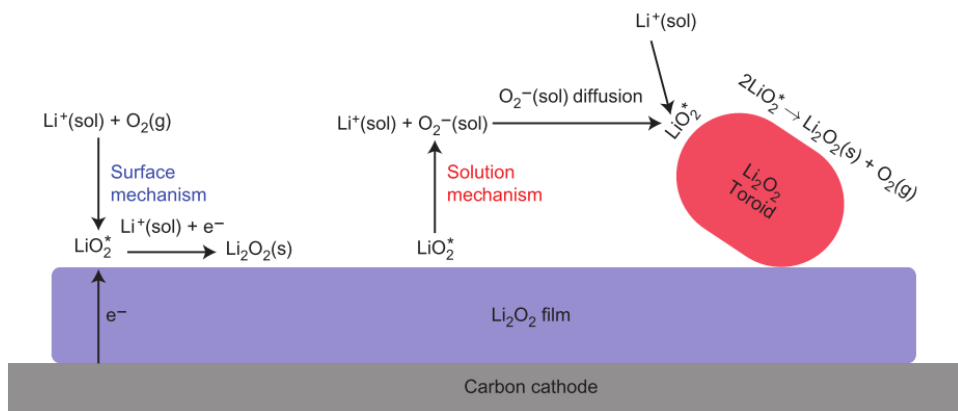
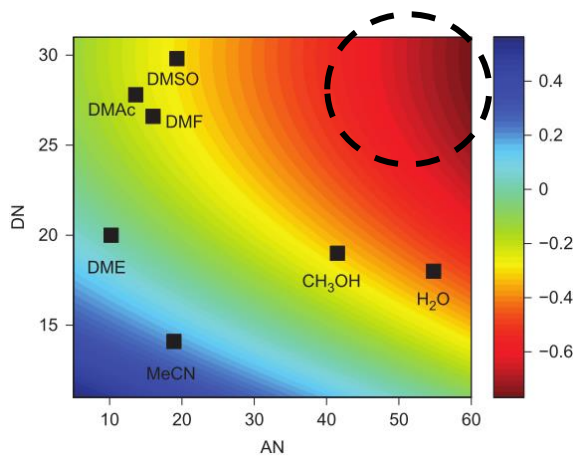
a**b**

Figure 1. 5. (a) ‘Schematic of Li^+ -ORR for the growth of Li_2O_2 toroids in H_2O containing electrolyte. Solvation of intermediaries circumvents the conductivity limitations produced with surface-up film growth. **(b)** Quantitative chart for solvent selection for high-capacity $\text{Li}-\text{O}_2$ batteries. The free energy of dissolution scale (red/high, blue/low) for $\text{Li}^+ \cdots \text{O}_2^\cdot$ into $\text{Li}^+(\text{sol})$ and $\text{O}_2^\cdot(\text{sol})$ in different solvents is a function of the Gutmann AN & DN and is normalized relative to pure Dimethoxyethane (DME). High DN solvents like DMSO are capable of stabilizing Li^+ , on the other hand, high ANs like H_2O stabilize O_2^\cdot . Solvents that fall in the top-right quadrant (black dotted-line) of this plot are predicted to favour solution-mediated deposition of Li_2O_2 , which will be essential for high-capacity $\text{Li}-\text{O}_2$ batteries.’ Figure reproduced from ref. ⁸⁸.

If both intermediary ions (Li^+ and $\text{O}_2\cdot^-$) can be fully stabilised by the electrolyte, then theoretically the disproportionation reaction would not take place until much later into discharge. Instead, Li^+ and $\text{O}_2\cdot^-$ generated at the anode and cathode, respectively, would be solvated in the electrolyte, as stable solvent separated ion-pairs (SSIPs) or free ions, until the solvent reaches saturation. Only then will precipitates form on the O_2 -cathode. A lack of precipitates on the O_2 -cathode structure would leave the surface free for charge transfer throughout Li^+ -ORR, drastically improving the capacity of the cell (provided the metal anode is adequately protected against degradation/dissolution reactions driven by dissolved $\text{O}_2\cdot^-$ crossover), the $\text{Li}^+\cdots\text{O}_2\cdot^-$ intermediary is discussed in detail below. Therefore, an ideal electrolyte should have an ‘amphoteric like’ nature, with both highly accepting and donating components capable of effectively stabilising and solvating both charged species. However, many high AN solvents also tend to be poor donors that weakly solvate Li^+ , which, due to its greater charge density, may overcome the solvent’s affinity for $\text{O}_2\cdot^-$. Only accepting solvents and additives that are similar or more accepting than Li^+ will have the solubility required to draw intermediaries away from the surface and drive the solution mechanism.

Li^+ -ORR cyclic voltammetry

Electrochemical techniques are instrumental for determining fundamental reaction mechanisms at the electrode surface. For the one electron ORR, using solvent electrolytes with high ANs,⁶⁷ or replacing large organic cations like tetrabutylammonium (TBA⁺-ORR) with smaller more electrophilic ones (Li^+ -ORR), produces a large positive shift in ORR onset potentials (Fig. 1. 6b) that approaches the thermodynamic potential for Li^+ -ORR of 2.96 V vs Li⁺/Li.¹⁴⁴ A positive shift in ORR onset potential indicates a more thermodynamically favourable mechanism and demonstrates that $\text{Li}^+\cdots\text{O}_2\cdot^-$ species are formed more readily than TBA⁺ $\cdots\text{O}_2\cdot^-$ due to Li^+ being more electrophilic.¹²⁰ Therefore, the cation has a large influence

on the ORR mechanism. Whereas, in high DN solvents, like Me-Im, no such shift in onset potential for the first one electron ORR occurs and the current densities remain the same when changing from TBA^+ -ORR to Li^+ -ORR (Fig. 1. 6a) signifying that the cations influence on ORR is effectively suppressed by the solvent, preventing the formation of $\text{Li}^+ \cdots \text{O}_2^\bullet$ in favour of freely solvated O_2^\bullet that likely exists as SSIPs in solution before disproportionating to Li_2O_2 as discussed previously.

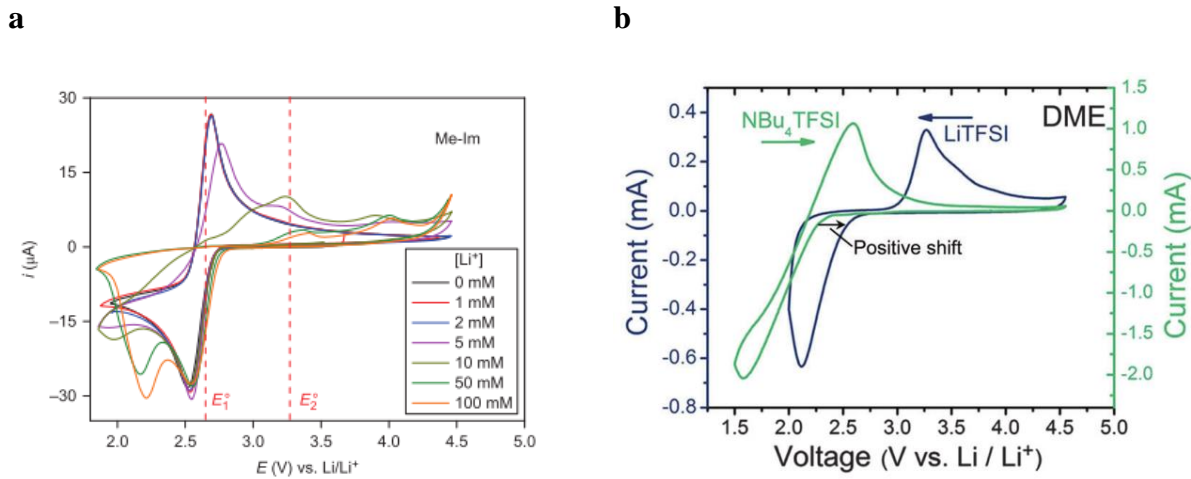


Figure 1.6. Cyclic voltammograms (CVs) of OR/ERs showing thermodynamic potential shifts in various electrolytes saturated with O_2 . (a) Varying ratios of $\text{TBAClO}_4:\text{LiClO}_4$ (ClO_4^- maintained at 100 mM) in Me-Im (high DN: 47) at a Au working electrode. No noticeable shift in onset reduction potentials with and without Li^+ present implying the same solvated O_2^\bullet species is generated regardless of the cation present. (b) 1 M TBATFSI (green line) or 1 M LiTFSI (blue line) dissolved in DME (low DN: 20) at a glassy carbon (GC) electrode. Large positive shift (~250 mV) in ORR onset implies $\text{Li}^+ \cdots \text{O}_2^\bullet$ is more thermodynamically favourable than solvated $\text{TBA}^+ \cdots \text{O}_2^\bullet$. Figure (a) and (b) reproduced from ref. ⁴ and ¹²⁰, respectively.

Li⁺...O₂^{•-} intermediaries

Some ambiguity remains around the nature and stability of the Li⁺...O₂^{•-} intermediary produced during Li⁺-ORR which needs to be addressed as these species are instrumental in the performance of non-aqueous Li-O₂ batteries. When not adequately stabilised the Li⁺...O₂^{•-} intermediary increases the likelihood of parasitic side reactions occurring with the electrolyte and O₂-cathode, limiting the capacity and cyclability of the battery. The strength of Li⁺...O₂^{•-} ion-ion coupling influences Li⁺ and O₂^{•-} solvation which in turn dictates the discharge mechanism (see above). In general, strong ion-ion coupling favours rapid Li⁺...O₂^{•-} disproportionation to Li₂O₂ and the surface mechanism,¹²⁵ whereas, weak coupling favours Li⁺ and O₂^{•-} solvation and the solution mechanism. Li⁺...O₂^{•-} ion-ion coupling strength is dependent on the Lewis acidity and basicity of Li⁺ and O₂^{•-} respectively which have been shown to vary depending on electrolyte solvent and additives.^{122,145–147} Surface catalysts and active/defect sites may also influence Li⁺...O₂^{•-} coupling at the surface. Thus, several methods have been explored for manipulating Li⁺...O₂^{•-} ion-ion coupling, summarized in Table 1. 5. It is unlikely that the Li⁺...O₂^{•-} ion coupling is black and white, instead a continuum of varying degrees of coupling based on the ability of the electrolyte environment to interact with each ion is proposed, see Figure 1. 7.

Table 1. 5. Overview of $\text{Li}^+ \cdots \text{O}_2^{\bullet-}$ intermediary and list of electrolyte components that manipulate the ion-ion coupling strength and Li^+ and $\text{O}_2^{\bullet-}$ solvation. The ion-ion coupling is dependent on the immediate environment and it is likely that a continuum of exists between a more coordinated $\text{Li}^+ \cdots \text{O}_2^{\bullet-}$ intermediate and fully solvated Li^+ and $\text{O}_2^{\bullet-}$ ions.

Strong	$\leftarrow \text{Li}^+ \cdots \text{O}_2^{\bullet-} \text{coupling} \rightarrow$	Weak
$\text{Li} \cdots \text{O}_2$ coordinate complex		$\text{Li}^+ + \text{O}_2^{\bullet-}$ free solvated ions
surface mechanism (surface-up Li_2O_2 deposition)		solution mechanism (solution-down Li_2O_2 deposition)
<ul style="list-style-type: none"> • low DN/AN solvent^{4,74,132} • poor solvation/diffusivity of intermediaries¹⁴⁸ • soft (charge dissociated) cation and anion salt additives 		<ul style="list-style-type: none"> • high DN solvent^{4,72,121,132,149} • high AN additive^{41,88,89} • hard (charge dense) anion^{122,124} • Li^+ solvating redox mediator^{122,127} • $\text{O}_2^{\bullet-}$ solvating redox mediator^{38,146,147}

Li₂O₂ morphology

Three main categories of Li₂O₂ surface precipitate morphologies have been reported to form during discharge, namely (1) homogenous films, (2) heterogeneous agglomerates or (3) a mixture of both.⁹⁵ Li₂O₂ film growth is determined by the rate of electron tunnelling through the passivating film.¹⁵⁰ The critical thickness where growth stops, was calculated to be 5-10 nm based on a layer-by-layer deposition mechanism,¹⁵¹ though films up to 70 nm have been grown on GC via a suggested discrete spiral growth mechanism.¹⁵² Charge-conduction mechanisms have also been proposed for explaining thick film growth, whereby electrons tunnel through or along conductive regions in the Li₂O₂ precipitate.⁹³ Li₂O₂ agglomerates are generally formed by a solvent mediated inner-sphere reaction mechanism,¹⁴⁹ producing a crystalline core with an amorphous outer surface. The morphology of surface agglomerate deposits vary greatly, from small particles (< 20 nm),⁹⁵ platelets/flakes/dics/toroids (40-200 nm),^{88,95,153,154} hexagonal-shaped (500 nm)¹⁵⁵ to cylindrical and large heterogeneous surface structures (> 1,000 nm).^{121,156}

As discussed above, the size of Li₂O₂ surface agglomerates is dependent on the electrolyte environment and correlates well with discharge capacities.⁹³ Depending on potential limits, Li₂O₂ agglomerate growth is generally a mass-transport-limited deposition process driven by the diffusion of Li₂O₂ precipitates from solution to the surface. Thus, discharge current densities and rates also heavily influence Li₂O₂ morphologies.^{93,94,157} Low discharge current densities and slow discharge rates produce large Li₂O₂ agglomerates and relatively high capacities. In addition, Viswanathan *et al.* showed large *iR* drops at fast discharge rates and concluded that reducing cell impedance was a central issue for increasing discharge capacities.¹⁵⁸ Both Li₂O₂ films and agglomerates have also been shown simultaneously on the O₂-cathode surface, with agglomerates forming at active sites via solution deposition, whilst

the remaining surface is passivated with a thin film via the surface mechanism. Ideally, the electrolyte should fully solvate both Li^+ and $\text{O}_2\cdot^-$ and only after full saturation should precipitates be expected to form on the O_2 -cathode. This would prevent pore blocking, keep the cathode surface exposed throughout discharge, increases discharge capacities and reduce charge overpotentials improving cycling efficiencies.¹⁵⁵ An overview of the different Li_2O_2 morphologies is shown schematically in Figure 1. 7 and contrasted with the possible $\text{Li}^+\cdots\text{O}_2\cdot^-$ intermediaries responsible for their formation.

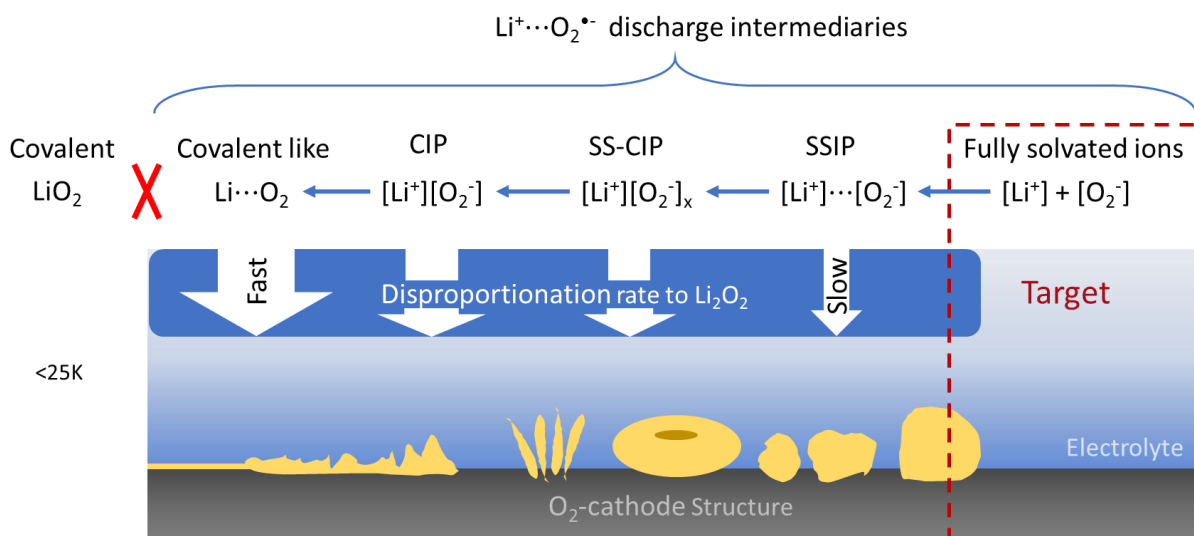


Figure 1. 7. Schematic overview of different possible $\text{Li}^+\cdots\text{O}_2^-$ intermediary species generated during discharge of a non-aqueous Li-O_2 cell on a generalised continuum of increasing ionicity going from left to right. A pure LiO_2 phase at $< 25\text{ K}$ is used as the lowest, most covalent, species in the continuum, however, this species will not be generated during discharge of a cell as it is not thermodynamically or kinetically feasible.^{76,80} From left to right as the electrolyte's ability to solvate Li^+ and/or O_2^- increases, the $\text{Li}^+\cdots\text{O}_2^-$ intermediary likely goes from covalent like or partially stabilised surface complexes,^{83,159} to contact ion-pairs (CIPs),^{4,67,74} solvent separated contact ion-pairs (SS-CIPs), SSIPs,^{4,67,147} to free and fully solvated ions.¹⁵⁵ The relationship between O_2^- solvation, its disproportionation rate and Li_2O_2 surface morphology has also been well established. Therefore, assuming the electrolyte and O_2 -cathode are stable, then the disproportionation rate will slow and the lifetime of the $\text{Li}^+\cdots\text{O}_2^-$ intermediary will increase from left to right. The resulting Li_2O_2 morphology (yellow structures) on the O_2 -cathode surface for $\text{Li}^+\cdots\text{O}_2^-$ can similarly be approximated on a matching continuum: transitioning from uniform ~10 nm films⁹² to heterogenous amorphous films,¹²¹ followed by large platelet,¹⁴⁸ toroidal⁸⁸ and surface aggregates⁴ and finally to low or no O_2 -cathode surface passivation¹⁵⁵ when the bulk of discharge products are solvated in solution. Any generated $\text{Li}^+\cdots\text{O}_2^-$ intermediary will likely disproportionate by transitioning

down this continuum. For example, Coulombic attraction between fully solvated ions may lead to the formation of SSIP aggregates in solution which, in turn, continue to attract, eventually penetrating each other's solvation shells and forming a solvent separated contact ion pair (SS-CIPs). These too will aggregate with other CIPs and penetrate each other's solvation shells enabling disproportionation to Li_2O_2 . However, further work is required to support this mechanism.

1.4.2 Charge

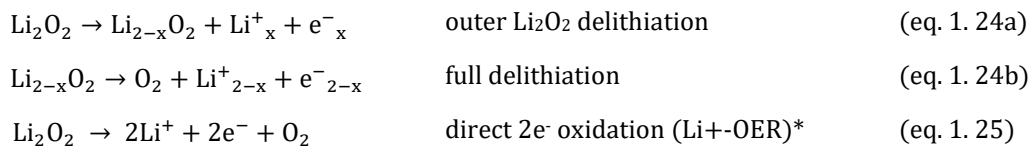
OER mechanism overview

On charge, an external potential is applied to the cell oxidising Li_2O_2 and any parasitic side-products on the O_2 -cathode back to Li^+ and O_2 (eq. 1. 24-1. 26). O_2 is evolved back to the atmosphere, exiting the cell through the semi-porous membrane. Whilst, Li^+ dissolves back into the electrolyte and migrates through the bulk electrolyte to the original anode where it is reduced and plated, regenerating the Li metal anode. Uncertainty remains around the exact Li_2O_2 oxidation mechanism (Li^+ -OER) as it is dependent on the cathode composition/structure and the electrolyte of the cell. However, in general, it is thought that at low charge potentials (< 3.5 V vs Li^+/Li) Li_2O_2 undergoes delithiation, liberating Li^+ into the electrolyte and forming a Li deficient $\text{Li}_{2-x}\text{O}_2$ outer surface (eq. 1. 24a). $\text{Li}_{2-x}\text{O}_2$ then either undergoes a direct reduction (eq. 1. 24b) or chemically disproportionates back to Li_2O_2 (eq. 1. 21) via a solution mechanism releasing O_2 . This gradually occurs on the surface of Li_2O_2 deposits until their size is reduced completely. Any amorphous Li_2O_2 present on the O_2 -cathode surface is depleted first as it is more easily polarised¹⁵⁶ than crystalline Li_2O_2 . As amorphous Li_2O_2 is depleted, higher surface polarisations are required to oxidise bulk crystalline Li_2O_2 causing the oxidation potential to gradually rise.

Above 3.5 V vs Li^+/Li , direct two electron oxidation occurs (eq. 1. 25).^{160,161} However, at these higher overpotentials Li_2O_2 can react with the electrolyte and carbon cathode surface.^{136,154} Causing a thin interfacial layer to form between Li_2O_2 and the surface composed of Li_2CO_3 and LiRCO_3 species (where R = H/alkyl group).^{162,163} Cell impedance increases as the interfacial layer grows during charge, further pushing up the overpotential. Above 4.0 V vs Li^+/Li , both Li_2CO_3 and LiOH degradation products are also oxidised.⁸⁰ LiRCO_3 species cannot be oxidised within stable potential ranges and, if not mitigated against, accumulate on the

surface eventually, leading to full cathode passivation and cell death after consecutive cycles.¹⁶⁰ Due to the thermodynamic stability of Li₂O₂, an external driving force and high surface polarisations are required to dissociate it to its substituents during charge, which is visible by high overpotentials and sluggish Li⁺-OER kinetics compared with Li⁺-ORR.¹⁶⁰ Therefore, it has been concluded that both discharge and charge reactions occur via different stages in a quasi-reversible mechanism and further fundamental cathode investigations are required to improve charging efficiencies.^{74,164–167} High overpotentials impact the overall cycling efficiency and practicality of the battery and, ideally, need to be reduced to below 600 mV. To that end, many strategies have been presented in the literature to date with some success, namely (1) novel O₂-cathode morphologies, (2) electrolytes, (3) solid-state catalysts, and (4) redox shuttles capable of oxidising Li₂O₂ at lower potentials.

Original O₂-cathode



Original anode



*singlet O₂ (1O₂) produced above 3.5 V vs. Li/Li⁺¹⁶⁸

Li⁺-OER cyclic voltammetry

OER oxidation potentials are heavily dependent on the coordinating cation, the stronger the cation (C^+) interaction with electrochemically generated $O_2^{·-}$ and O_2^{2-} anions, the larger the surface polarisation potential (overpotential) required to dissociate the product to its constituents, reflected by higher OER potentials (Fig. 1. 8). OR/ERs in electrolytes containing large ‘bulky’ organic cations where the positive charge is relatively dispersed, like TBA⁺ or EMI⁺, are essentially reversible due to weak $C^+...O_2^{·-}$ coupling. However, transitioning down the alkali-metal group from K⁺ to Li⁺, as the cations gets smaller a clear shift to higher overpotentials is visible, which also corresponds with $O_2^{·-}$ disproportionating to O_2^{2-} switching from a one to a two electron OER mechanism. A concomitant drop in OR/ER peak currents also indicates that surface passivation films are formed blocking further O₂ reduction. In the opposite direction, when dissolving differently sized tetraalkylammonium (TAA⁺) cations in MeCN, a similar weaker effect occurs going from the small tetraethylammonium (TEA⁺) to large TBA⁺ cation (Fig. 1. 8b), whereby OER shifts positive due to slower kinetics and surface blocking by the larger cations.⁷⁰ Therefore, small cations and large cations both have the effect of shifting OER oxidation potentials positive through strong $C^+...O_2^{·-}$ bond and sluggish kinetics, respectively.

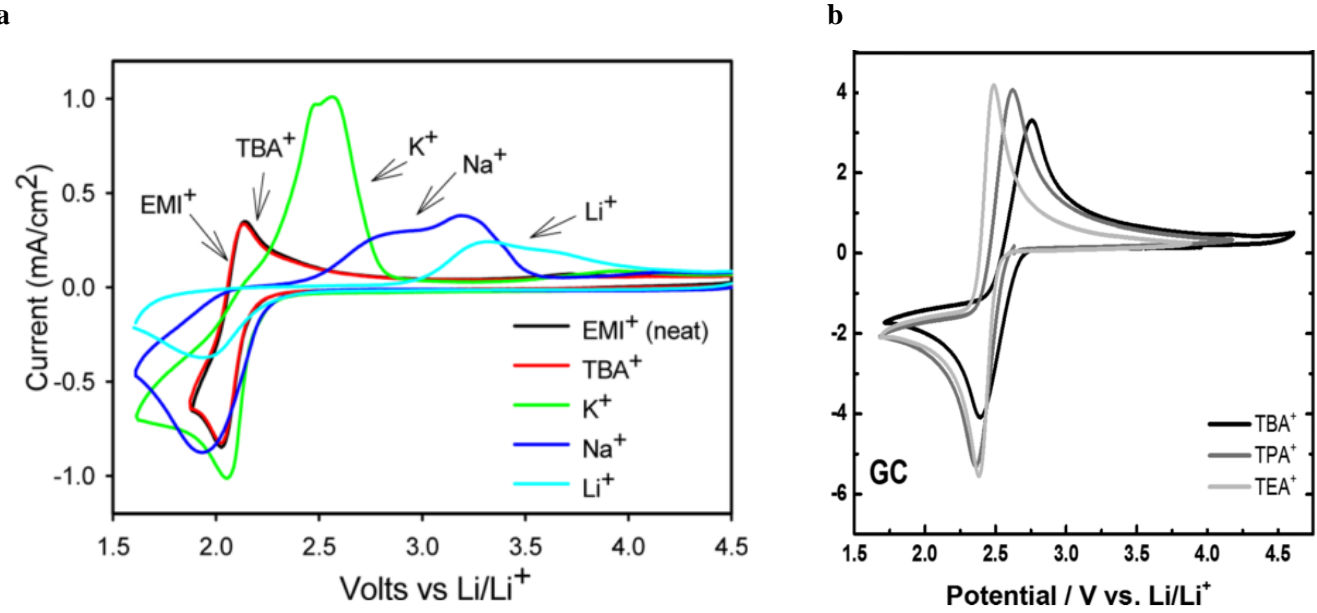


Figure 1.8. CVs of O_2 saturated electrolytes on GC electrodes at 100 mV s^{-1} showing the impact of cation size on OER potentials. **(a)** 0.25 M of various TFSI^- based salts in EMITFSI. More charge dense cations ($\text{TBA}^+ > \text{EMI}^+ > \text{K}^+ > \text{Na}^+ > \text{Li}^+$, i.e. as cation size approaches that of $\text{O}_2^{*^-}$) require larger electrode polarisations to degrade the complex formed during ORR thus overpotentials increase and OER potentials shift positive. **(b)** 0.1 M of TAAOTf in MeCN. When the size of the cations is increased after a point, the same shift in OER is visible and coordination strength decreases due to slower surface charge-transfer kinetics. Figure (a) and (b) reproduced from ref. ¹⁶⁹ and ⁷⁰, respectively.

As discussed previously, there is a positive shift in ORR onset potentials in low DN electrolytes when Li⁺ is added (Fig. 1. 9a), producing Li⁺...O₂^{•-} instead of ‘free’ O₂^{•-}. No such shift is present in high DN electrolytes (Fig. 1. 9b) as Li⁺ is kept solvated in solution. For OER, large (~1,000–1,500 mV) shifts occur in both types of electrolyte with the addition of Li⁺ and the peak associated with free O₂^{•-} oxidation disappears. However, when DMSO is cycled to no lower than the ORR peak maximum (2.39 V vs Li⁺/Li), both a reversible oxidation peak (a₁) corresponding to free O₂^{•-} oxidation and a higher potential peak (a₂) for Li₂O₂ oxidation are present. Therefore, much of the generated O₂^{•-} remains free in solution without disproportionating fully to Li₂O₂ due to the low rate of Li⁺ and O₂^{•-} interaction in high DN solvents. However, when the potential is cycled below the ORR current maxima, both the disproportionation reaction and a second direct reduction at the surface can occur⁴ and free O₂^{•-} disappears. When cycled to even lower potentials Li₂CO₃ (a₄) is produced, likely from electrolyte degradation. For an IL (Pyrr₁₄TFSI) with 25 mM Li⁺ salt added, there is a matching OR/ER profile to low DN electrolytes (Fig. 1. 9c inset). However, cycled to lower potentials a quasi-reversible redox couple corresponding to O₂/O₂^{•-} is also present and indicates that the formal charge on the IL cation can help stabilise free O₂^{•-} in solution, regardless of the presence of solvated Li⁺.

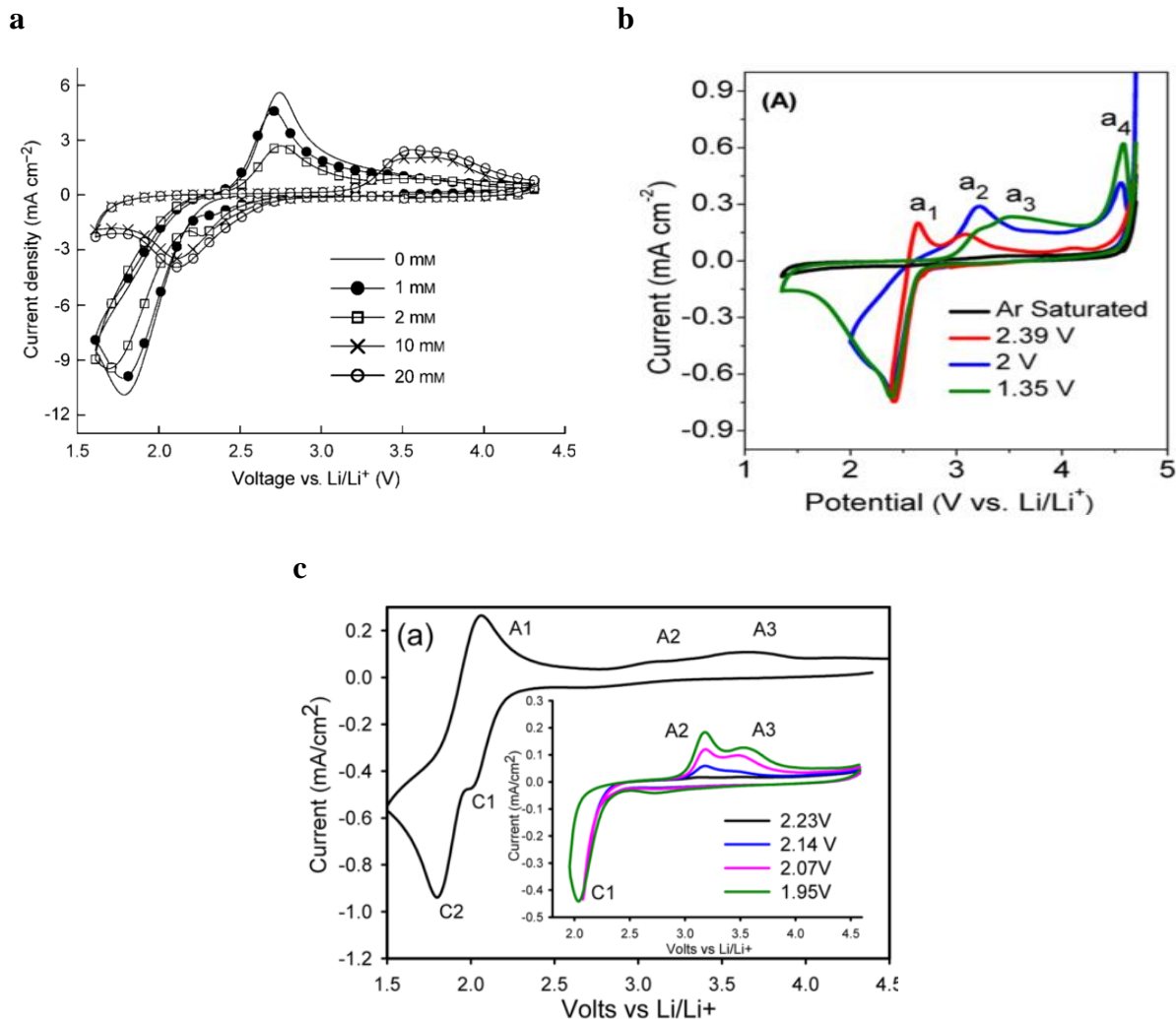


Figure 1.9. CVs of Li^+ -OR/ER in various electrolytes saturated with O_2 **(a)** Varying concentrations of LiClO_4 in a 100 mM $\text{TBAClO}_4/\text{MeCN}$ (low DN solvent) electrolyte at a Au WE, cycled at 1,000 mV s⁻¹. ORR onset and OER shift to higher potentials in Li^+ saturated electrolytes. **(b)** 100 mM LiClO_4 in DMSO (relatively high DN: 27) at a GC cathode cycled to three different reduction potentials at 100 mV s⁻¹. OER currents are heavily dependent on the reduction potential indicating different reduction products. **(c)** 25 mM LiTFSI in $\text{Pyr}_{14}\text{TFSI}$ on a Au electrode. Inset CVs at various cathodic limits of 1.95 V and higher. OER similarly dependent on the reduction potential. Figure (a), (b) and (c) reproduced from ref. ⁷⁴, ¹¹⁰ and ⁶⁹, respectively.

Singlet O₂

Singlet oxygen (¹O₂ or ¹Δ_g) is an electrophile and strong oxidising agent known to attack negative species in the electrolyte solvent^{168,170} that was hypothesised to play a part in non-aqueous Li-O₂ cell death.¹⁰⁸ *In operando* electron paramagnetic resonance (EPR) spectroscopy with sterically hindered secondary amine spin traps 2,2,6,6 tetramethyl-4-piperidone (4-Oxo-TEMP) were first used to detect ¹O₂ as a product of Li₂O₂ oxidation.¹⁶⁸ Approximately 0.5% of O₂ produced (eq. 1. 24b and 1. 25) was in the form of ¹O₂ (¹Δ_g) and was formed at > 3.5 V vs Li⁺/Li during Li₂O₂ oxidation. Carbon O₂-cathodes are normally stable up to 4 V vs Li⁺/Li, however, C¹³ labelling showed that electrode degradation/corrosion starts > 3.5 V vs Li⁺/Li in non-aqueous Li-O₂ cells which matches the potential of ¹O₂ formation during charging.¹⁶⁰ Recently, ¹O₂ was shown to be the main radical, catalysing parasitic side reactions with the electrolyte and O₂-cathode not O₂^{·-}. Therefore, ¹O₂ is responsible for divergence away from 100% O₂ ↔ Li₂O₂ conversion in Li⁺-OR/ERs.^{171,172} ¹O₂ is produced in small quantities during discharge (eq. 1. 21), however, the bulk was produced during charge.¹⁷² 1,4-diazabicyclo[2.2.2]octane (DABCO), a known ¹O₂ quench,¹⁷³ was shown to inhibit ¹O₂ formation and provides a strategy for mitigating parasitic reactions limiting non-aqueous Li-O₂.¹⁷²

1.4.3 Electrolyte

Selecting and designing an electrolyte that can support the ideal Li^+ -OR/ERs that is also stable in contact with a pure Li-metal anode is key for the success of the non-aqueous $\text{Li}-\text{O}_2$ battery and requires considerable attention. Conventional electrolytes contain ions dissolved in a solvent which facilitates charge transfer between electrodes. Ideally, the electrolyte provides a chemically inert medium for any redox reactions and charge transfer processes to occur whilst possessing physicochemical properties that support fast reaction kinetics and solvation of products. Non-aqueous $\text{Li}-\text{O}_2$ electrolytes ideally satisfy the following criteria:

- high conductivity (preferably $> 10^{-3} \text{ S.cm}^{-1}$)¹⁵¹
- low vapour pressure,
- low flammability,
- autoxidation stability in presence of radical oxides,
- wider electrochemical stability window than operating potentials (e.g. -0.5 to 4.5 V vs Li^+/Li)¹⁷⁴
- high Li^+ , O_2 , $\text{O}_2^\bullet-$, $\text{Li}^+\cdots\text{O}_2^\bullet-$, Li_2O_2 solubility,^{175,176}
- high Li^+ , O_2 , $\text{O}_2^\bullet-$, $\text{Li}^+\cdots\text{O}_2^\bullet-$, Li_2O_2 diffusivity,¹⁷⁷⁻¹⁷⁹
- stability vs. Li metal anode i.e. form stable Li^+ permeable SEI^{38,98}
- stable reversible Li^+ -OR/ER chemistries
- stable in the presence of $\text{O}_2^\bullet-$ and Li^+ species^{32,177,180,181}.

By facilitating ion diffusion through the solvent, the electrolyte dictates the conductivity and power of the cell.⁴ As discussed previously, the electrolyte also plays a crucial role in non-aqueous $\text{Li}-\text{O}_2$ cell chemistry related to its ability to stabilise and solvate Li^+ , $\text{O}_2^\bullet-$ and $\text{Li}^+\cdots\text{O}_2^\bullet-$ intermediate species.^{95,112} In addition to the solvent, a solvated Li^+ -salt is used in the electrolyte to provide the initial Li^+ required at the O_2 -cathode for cell redox chemistry. As the cation is

Li^+ , only the anion needs to be selected. The main physical properties of the Li-salt anion are good solubility, oxidative and thermal stability and stable electrode interactions.^{182–184} It is common practice to maintain homogeneity within the electrolyte by selecting Li^+ -salts with matching anion groups to any other salt species that may be present in the electrolyte as this improves Li^+ salt solubility.¹⁷⁵ Solvent and salt additives may also be added to the electrolyte to aid in Li^+ or $\text{O}_2^{\cdot-}$ solvation and transport through the electrolyte.^{70,185,186}

Electrolyte solvent

Initial research into non-aqueous Li-O_2 batteries was focussed around using conventional aprotic carbonate solvent systems. Their low viscosity, high conductivity, salt solubility and diffusivity coefficients serve to promote ion kinetics within the solvent which has been found to have a direct impact on the discharge and rate capacity of the cell, making them attractive solvents for batteries.¹⁸⁷ However, many of these solvents have been shown to decompose in the presence of Li^+ -OR/ER intermediaries, causing the passivation of electrodes and the pollution of the solvent, inhibiting desired cell activity. Also, many organic solvents have undesired physical properties such as high volatility, toxicity and flammability which raises questions about both immediate, and environmental safety when used with a semi-porous O_2^- cathode.^{188,189} Several studies screening electrolytes for application in non-aqueous Li-O_2 have been performed and some of the more commonly used organic solvent group are outlined below.^{180,190–192}

Carbonates – Carbonates are currently the most widely used solvents in the battery industry, specifically Li-ion. However, they are unsuitable for application within non-aqueous Li-O₂ systems as they undergo Li⁺ catalysed nucleophilic degradation in the presence of radical oxides after as little as one discharge-charge cycle (Fig. 1. 10).¹³⁷ Carbonate degradation has also been shown by the absence of Li₂O₂ after discharge and the detection of undesired side products such as evolved CO₂ and Li₂CO₃ and alkyl carbonates at the O₂-cathode.^{13,162,193–202}

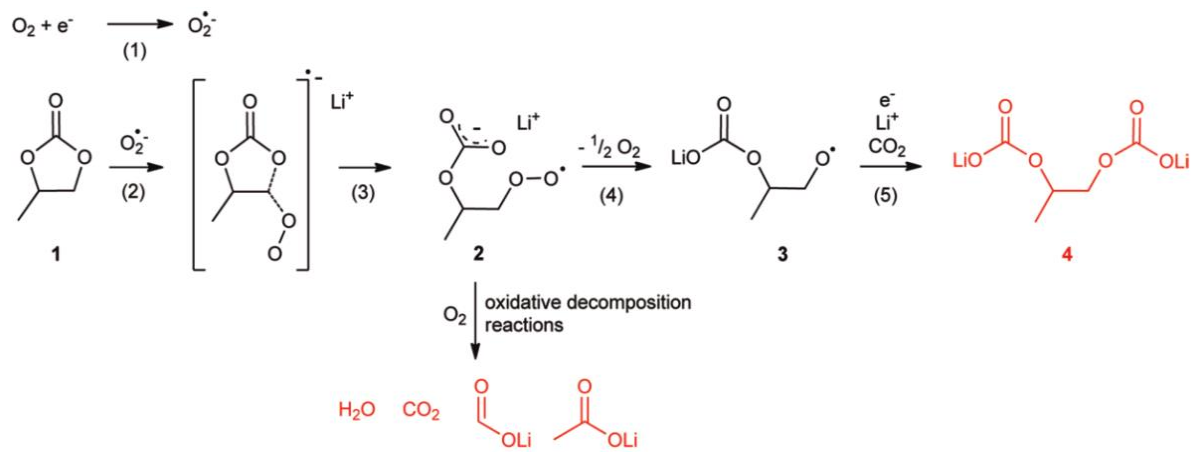


Figure 1. 10. Reaction scheme depicting methyl carbonate degradation mechanism during Li⁺-ORR forming numerous degradation products. Figure reproduced from ref: ¹⁹⁵.

Ethers – Due to the poor performance of carbonates, ethers gained attention as possible solvents for non-aqueous Li-O₂ as they were deemed unlikely to degrade via proton abstraction when exposed O₂^{•-} during discharge.^{200,203} There have been mixed reports so far with these systems; some glyme complexes, namely Tetraethylene glycol dimethyl ether (TEGDME) initially showed positive results with Li₂O₂ being detected at the O₂-cathode during discharge.^{204–206} Furthermore, 100 charge-discharge cycles have been shown using a TEGDME-LiOTf electrolyte.⁶⁰ However, the high potentials for charge (> 3.8 V vs Li⁺/Li) suggest the presence of L₂CO₃. Also, though having good initial levels of Li₂O₂ detected on discharge, TEGDME was shown to be unstable and decompose to carbonate on discharge-charge cycling which contrasts with previous findings.^{200,203} This can also be compared with studies in other phase change batteries such as lithium sulphur and Na-O₂ systems which show similar degradation results with ethers.^{205,207–209} In spite of this, DME and TEGDME have emerged as a semi-standard electrolytes for non-aqueous Li-O₂ batteries to compare against as they possess good Li-metal stability and reasonable Li⁺-OR/ER chemistries, though they lack the solubility required to drive the solution mechanism without using solvation additives¹²⁷ and they, too, have shown poor radical oxide stability (Fig. 1. 11).²¹⁰ Therefore, novel electrolyte strategies are required.

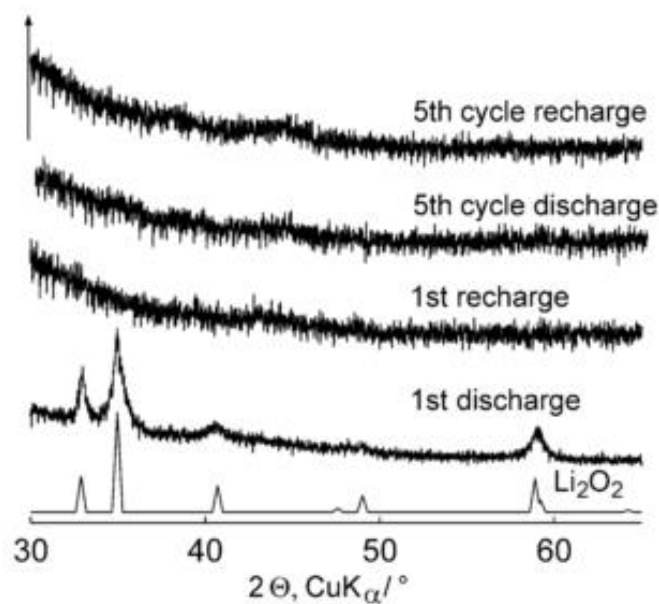


Figure 1. 11. Powder X-ray diffraction patterns of Super P/Kynar composite O₂-cathodes cycled in TEGDME with 1M LiPF₆ under 1 atm. Absence of Li₂O₂ on fifth scan demonstrates cyclability issues with electrolyte when fully discharged. Figure reproduced from ref: ²⁰⁰.

Other – Some nitrogen and sulphur based solvents, namely MeCN and DMSO are well documented electrolyte solvents with known Li⁺-OR/ER chemistries.^{196,211–216} DMSO in particular cycles via the desirable solution mechanism, however, both electrolytes decompose Li-metal and have shown O₂^{•-} instability, though the reaction with radical oxides is generally slow.^{182,216–218} Adding DMSO to TEGDME has recently been shown to improve the discharge capacity of the resulting blend, indicating it could be a good solvation additive to improve the performance. Similarly, blending unstable PC solvents with ILs was shown to synergistically improve PC Li⁺-OR/ER redox stability and the ILs physical properties compared to neat solvents.¹⁹⁸ Dimethylpropyleneurea (DMPU) was recently shown to have extremely low initial discharge-charge overpotentials of ~0.6 V due to efficient solvation of Li⁺-ORR intermediaries though, this increased after the first cycle signalling the presence of parasitic processes.²¹⁹ Sulfolane electrolytes have shown good charge-discharge cyclability (> 100) and had initial discharge potentials of ~2.9 V vs. Li/Li⁺ very close to theoretical Li₂O₂ formation potential of 2.96 V vs. Li/Li⁺.²²⁰ Bryantsev *et al.* have performed several computational studies screening solvent stabilities and their interactions with Li⁺ and O₂^{•-}.^{67,180,190,203,215} Autoxidation via proton abstraction from electron starved regions on solvent structures, particularly in ringed species, was one of the main causes of solvent degradation during charge.

ILs or eutectic electrolyte systems are good alternatives to organic solvents as these have excellent stability vs. Li-metal and promising Li⁺-OR/ER redox chemistries.²²¹ Consequently, these are also being looked at as possible alternative electrolyte solvent systems due to a number of innate physical and electrochemical properties, also they possess an amphoteric-like nature due to having formal charges on both the cation and anion which could have a positive influence on solvating Li⁺-OR/ER intermediaries.²²² ILs are a field of study in their own right and are discussed in detail below. On a side note, molecules containing multiple bonds (>1)

and atoms with variable valences (i.e. below 2nd group atoms in the periodic table, excluding halogens) can be readily polarised making them susceptible to nucleophilic and electrophilic attack. Therefore, solvent structures should generally be limited to those containing single bonds of the following atoms: C-, N-, O-, F-, Cl- and H- should be limited to stable alkyl chains (reducing the likelihood of abstraction reactions occurring with radical oxides).

Li salt

Several studies have probed the effect of the Li⁺-salt on Li⁺-OR/ERs and it is clear that they influence the stability of the whole electrolyte.^{145,223–225} Li⁺-salt anions vary in Lewis basicity from relatively strong triflate (OTf⁻) to the weaker PF₆⁻ and TFSI⁻ anions. The anion was shown to have no significant effect on O₂ solubility and diffusivity within the electrolyte, however, it does effect O₂²⁻ and Li⁺ solvation and transport.¹⁴⁵ Solvated Li⁺ existed as SSIPs in LiOTf and as CIPs in LiPF₆ containing electrolytes which was attributed to the DN difference in the two anions. O₂²⁻ is also more readily solvated in the LiOTf containing electrolytes, attributed to the better Li⁺ stabilisation in the electrolyte. Therefore, the Li⁺-salt anion can be used to improve an electrolytes overall DN and help induce the solution mechanism.^{145,226} Studies screening multiple different Li⁺-salt showed it also has a significant impact on cell discharge capacities (Fig. 1. 12).²²⁴ Though TFSI⁻ and OTf⁻ were shown to be electrolytes with some of the best capacities these faded in all electrolytes after the first cycle and multiple decomposition products were observed on the cathode in addition to Li₂O₂. Of all the salts screened, LiClO₄ was deemed the most stable and discharge capacity fade resulted from the electrolyte, as opposed to the anion, degrading.²²⁴ In addition to this, electrolytes containing LiTFSI degraded aluminium (Al) current collectors which effects the weight of a cell as heavier stainless steel current collectors are required. However, this may be mitigated by adding IL additives to stabilise the electrolyte.²²⁷

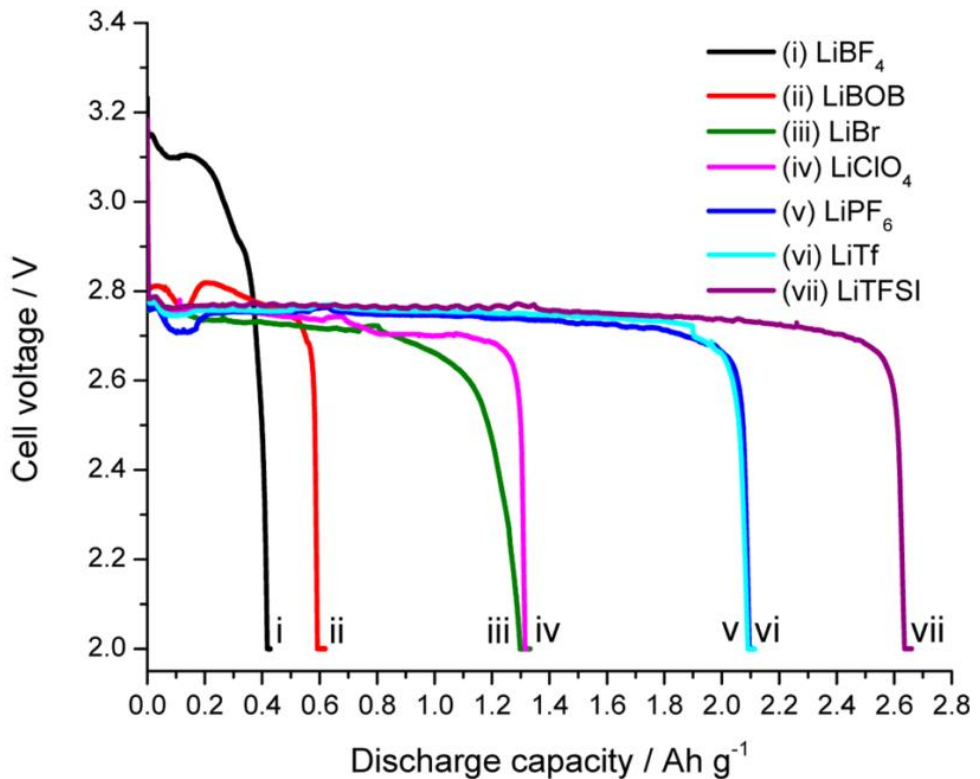


Figure 1. 12. Discharge voltage profiles of non-aqueous $\text{Li}-\text{O}_2$ batteries with different Li^+ -salts

discharged at a current density of 0.05 mA cm^{-2} . Figure reproduced from ref. ²²⁴.

Ultra-high Li⁺-salt concentrated electrolytes have emerged as another extremely interesting type of electrolyte. MeCN and other solvents that normally react with Li-metal can be stabilised by adding an abundance of Li⁺ into the electrolyte, enabling efficient Li-stripping and plating and providing a viable strategy for using otherwise unstable electrolytes in Li-batteries.^{228,229}

Other reported²³⁰ positive properties of ultra-high Li⁺-salt electrolytes are:

- high reductive stability
- high oxidative stability
- Al current collector stability
- high thermal stability
- low volatility
- high carrier density
- fast electrode reactions

On the downside, Li⁺-salts are typically expensive and are the most expensive aspect of the battery which make ultra-high concentrated electrolyte prohibitively expensive for practical use. Also, diffusion and reaction kinetics are low in non-aqueous Li-O₂ cells which favours the surface, low capacity, discharge mechanism.

1.4.4 O₂-Cathode

Due to O₂ being a gas, a porous semi-permeable membrane is required to allow O₂ to diffuse into and out of the electrolyte, however, this adds some excess weight to the cell. This membrane acts as a current collector and provides a localised area for the cell reactions to take place and possibly be catalysed.²³¹

There have been two schools of thought concerning OER at the O₂-cathode, the first suggests it is insensitive to the cathode surface structure and surface catalysis, and that noble metal catalysts may even catalyse degradation of some electrolytes,²³² suggesting that a merely conductive and chemically inert interface is what is important.³⁰ The second suggests that surface structural morphology and catalysts are important and can reduce OER overpotentials to below 4.0V.^{160,233} Considering the recent understanding gained about the electrolyte environment, both these mechanisms can be considered true. For a surface driven Li⁺-ORR mechanism (a low AN and DN electrolyte), discharge reactions occur uniformly across the surface and intermediaries disproportionate too rapidly to be kinetically aided by catalysts on the O₂-cathode surface. However, for a solution driven Li⁺-ORR mechanism (High AN or DN electrolyte), disproportionation occurs more slowly allowing intermediaries to adsorb onto active sites on the surface and for a second two electron reduction mechanism to be catalysed.²³⁴ Surface catalysts, active/defect sites and O₂-cathode morphology and crystallinity²³⁵ will then also affect charge transfer, act as nucleation-sites for precipitating discharge products and influence diffusion of solvated intermediaries away from the surface, respectively.^{80,91,95,236} Desirable features that are agreed upon are that the O₂-cathode must have a large surface area so as not to limit charge transfer during discharge and charge and it must have a good mix of macro, meso, micropore and nanopore volumes that can store discharge deposits and allow effective O₂ diffusion throughout the cathode.¹²⁸

Carbon O₂-cathodes

Activated and conducting carbons are the most commonly used O₂-cathodes in non-aqueous Li-O₂ cells. However, carbon cathodes have been shown to decompose to Li₂CO₃ and CO₂ at potentials above 3.5 V vs Li⁺/Li during non-aqueous Li-O₂ charge-discharge cycling. One suggested method for improving the carbon cathode stability is to dope nitrogen²³⁷ or Al₂O₃²³¹ onto surface defect/active sites that are susceptible to attack from radical oxides. However, these active sites have also been shown to play a significant role in OR/ER charge-transfer, potentially catalysing the reactions.^{91,236} Using lithium nitrate (LiNO₃) additives has been shown to completely suppress CO₂ formation in gaseous outlet streams with differential electrochemical mass spectroscopy (DEMS).²³⁷ However, capacity fade on cycling still occurred, indicating that the degradation of the bulk electrode/electrolyte still may occur but that soluble or solid side-products are formed as opposed to gaseous ones. Alternative prototype carbons derived from biomass have been synthesised from materials such as coconut shell²³⁸ and wood.²³⁹ Biomass derived carbons have intrinsically high surface areas and are abundant cheap resources with significant exploitation potential making them attractive O₂-cathode materials though they currently lack the performance profiles required for practical batteries.^{240,241}

Binders

Commercial carbons are often supplied in particulate form and require mixing with polymer binders for structural support and to connect particles into a conductive matrix.²³⁹ PVDF, a common binder in Li-ion batteries, has been strongly suggested to degrade in the presence of O₂^{•-}.^{84,85} PTFE is a common alternative to PVDF known to have excellent chemical stability though it is more insulating, which impacts on cell impedance. Therefore, care must be taken when selecting binders. Some studies probing polymer stabilities have been performed.²⁴² However, considering the binder's ubiquitous presence in O₂-cathodes, more systemic studies to optimise the O₂-cathode binder's structure are required.

Free-standing cathodes

Polymer binders are inactive; increasing the weight, volume and complexity of the O₂-cathode. An alternative to polymer binders is to synthesise conductive macro structures that can be used as free-standing O₂-cathodes.²⁴³ Benefits include reduction of binder weight, easy incorporation of catalysts into cathode structure during synthesis, increased capacity and good conductivities as the entire structure can support charge transfer. Thus, many interesting free-standing structures have emerged in recent years, such as:

- carbon nanofibers (CNFs) on a porous ceramic substrate²⁴³
- Pd decorated honeycomb-like hollow spherical carbons,²⁴⁴
- multi-walled nanotubes (MWNTs),²³⁶
- RuO₂ carbon nanotubes (RuO₂/CNTs),²⁴⁵
- vertically aligned few-walled CNT,²⁴⁶
- Pd-CNT sponge,⁶¹
- graphene oxide stabilised graphene nanoplatelet paper (GNP/GO),^{113,247}
- graphene paper,²⁴⁸

- 3D graphene films,¹⁵⁶
- microstructured conducting poly(3, 4-ethylendioxythiophene) (PEDOT) polymer,²⁴⁹
- CeO₂/CNT,²⁵⁰
- free-standing Co₃O₄ nanoarrays,²⁵¹
- GO gel derive hierarchically porous carbon (FHPC) in nickel foam,²⁵²
- hierarchically porous carbon nanotubes (FHP-CNT),²⁵³
- activated carbon nanofibers.²⁵⁴
- free-standing TiO₂,²⁵⁵
- free-standing Flexible TiO₂ nanowire array textiles (NAs/CT)²⁵⁶

Conductive aerogels are another family of versatile, low-weight, free-standing cathode structures that possess large pore volumes^{257–260} and can be made to be superhydrophobic, helping to deter polar species (e.g. CO₂, CO, H₂O etc.) in the feed-stream from entering the cell.^{261,262}

Other O₂-cathodes

To bypass the carbon degradation reactions altogether, some other non-carbon cathode interfaces have also been investigated to varying degrees:

- Au,³⁰
- Ti_xO_y,²⁰²
- gel cathodes,³².
- RuO_x /titanium nitride nanotube arrays (RuO_x/TiN NTA)²⁶³
- gel cathode (IL + SWNTs),²⁶⁴
- Lithium aluminium titanium phosphate (LATP) cathode (O₂ selective membrane),²⁶⁵
- RuO₂ spheres²⁶⁶
- Cobalt-based cathodes²⁶⁷

1.4.5 Lithium Anode

Li-metal is an exceptionally light anode with a high specific capacity ($3,842 \text{ mA h g}^{-1}$) and negative electrode potentials, which gives it a large energy density ($11,738 \text{ Wh kg}^{-1}$).^{268,269} Li-metal anodes store far more energy, in terms of charge per unit mass, than conventional Li-ion anodes.²⁷⁰ However, there are significant safety concerns associated with pure Li-metal anodes as the continued stripping and plating of Li-metal on the anode during cell charge-discharge cycling leads to fissures in the anode SEI structure causing the growth of dendrites on the surface. Dendrites expand into the electrolyte eventually short-circuiting the cell when they contact the cathode resulting in hazardous cell failure (Fig. 1. 13). Therefore, anode safety concerns need to be addressed fully if a working Li-metal anode is to be realised. Using protective solid/polymer ion conducting separators or Li^+ ion conducting coatings on the anode surface are some strategies proposed for overcoming Li-metal limitations.^{13,164,271}

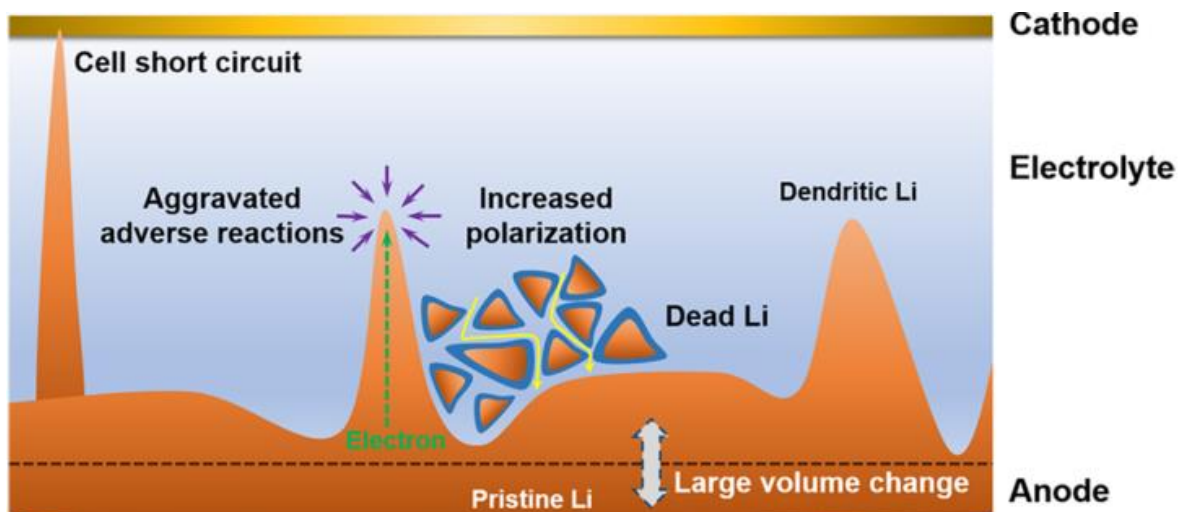


Figure 1. 13. Scheme of some key Li-metal anode problem areas, from left to right: dendrite formation, highly polarised region that can induce parasitic reactions, anode structural fracturing leading to isolated (dead) regions insulated by SEI build-up and large volume changes during charge discharge. Figure reproduced from ref:²⁷².

Li-metal is a strong reducing agent that can readily donate valence electrons to its environment. For this reason, many electrolyte components (solvents, Li-salts, additives) react with the surface of the Li-metal anode. However, provided the species formed at the surface are stable and insoluble in the electrolyte then a thin passivating film is formed, known as the SEI layer.^{177,270,273} The SEI layer is an integral part of the Li-metal anode protecting bulk Li metal from dissolution into the electrolyte, whilst Li⁺ cations are generally small enough to diffuse through it and along grain boundies.^{274,275} Crossover of radical oxide species from the cathode to the anode during non-aqueous Li-O₂ cell discharge can compromise the SEI layer, inducing bulk dissociation, decomposition and dissolution of the Li-metal anode. Therefore, the structure and stability of the SEI is a crucial area and numerous strategies for improving it have been developed.^{191,227} Cheng *et al.* recently published a thorough review of Li-metal anodes to date and a brief overview of key areas is given below.²⁷²

Solid Electrolyte Interphase

A relationship exists between the lowest unoccupied orbital (LUMO) and highest occupied orbital (HOMO) of the electrolyte and the electrochemical potentials (Fermi energies) of the anode and cathode.^{276,277} Electrons flow from high (anode) to low (cathode) electrochemical potentials. However, if the voltage associated with the LUMO of the electrolyte is below the anode potential, then electrons will also flow into the electrolyte fuelling reduction reactions at the anode surface. Due to its high electropositivity (-3.04 V vs NHE), Li-metal anode surfaces react with many organic solvents and Li⁺-salts. If the SEI products are soluble in the electrolyte then it is unstable as the reduction reactions continues until all the Li-metal is dissociated. However, if the reduction products are insoluble then grow on the surface until an equilibrium thickness is reached, i.e. the SEI. The SEI layer acts as a barrier preventing further electron transfer between the anode and electrolyte and ideally should possess low electrical

conductivity ($< 10^{-10}$ S cm $^{-1}$) and high ionic conductivity ($> 10^{-4}$ S cm $^{-1}$).²⁷⁶ Similarly, an SEI layer can form on the cathode if the electrolyte HOMO is above the cathode potential, in which case electrons flow from the electrolyte into the cathode, fuelling surface oxidation reactions.

SEI growth on the Li-metal anode is regulated by (1) electron tunnelling²⁷⁸ and (2) solvent diffusion²⁷⁹ mechanisms. SEI layer growth beyond the electron tunnelling depth of the layer is fuelled by diffusion of radical species (such as F $^-$) through the SEI until increasing diffusion resistance prevents this, too. The chemical composition of the SEI depends on the electrolyte and the structure is generally an inhomogeneous mosaic type (Fig. 1. 14).²⁸⁰ The chemical composition varies across the SEI with low diffusivity and high oxidation state compounds like Li₂CO₃, ROCO₂Li, ROLi, and RCOO₂Li forming the outer layer and high diffusivity, low oxidation state compounds like Li₂O, LiF, Li₃N, and LiOH forming the inner part.²⁷² Inhomogeneity in SEI composition is responsible for high ionic diffusivity through grain boundaries in the structure, however, it is also the cause of varying charge distributions across the surface allowing plating to be concentrated at kinetically favourable nucleation sites on the anode which then grow into dendrites.

Comparing high and low oxidation state interfaces: Li₂CO₃/Li and LiF/Li, respectively; Li₂CO₃/Li is more mechanically stable, less likely to delaminate and has lower energy barriers to Li $^+$ migration (0.227-0.491 eV) than LiF/Li (0.729 eV). Then again, LiF/Li interfaces are less likely to result in Li-dendrite nucleation growth and are more stable against displacement by radical oxides produced during Li $^+$ -OR/ER.^{272,281,282} Overall, an ideal SEI film must have: (1) good thickness to prevent electron transfer to the electrolyte but support fast Li $^+$ ion transfer between the electrode and the electrolyte, (2) high ionic conductivity, (3) mechanical stability to withstand volume changes, (4) stable morphology and structure during excessive cycling.

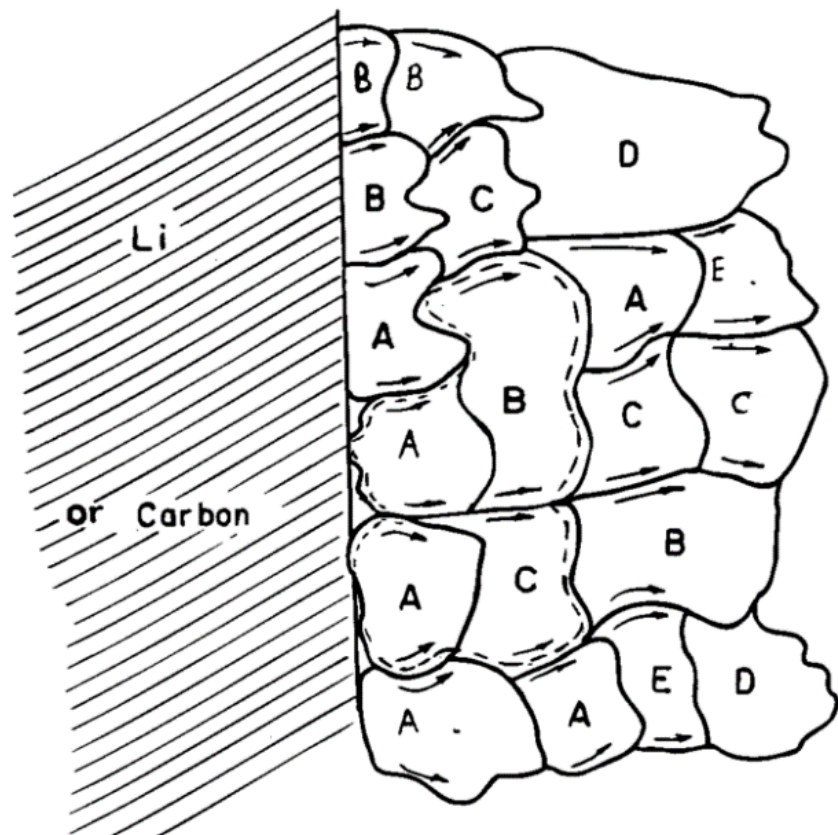


Figure 1. 14. Schematic of mosaic SEI layer structure proposed by Peled *et al.* Arrows denote Li⁺ diffusion pathways during discharge. A = Li₂O, B = LiF, C = Li₂CO₃, D = polyolefins, E = semi-carbonates. Figure reproduced from ref:²⁸⁰

Dendrite suppression

Some studies suggest solvents play a critical role in dendrite formation and require careful selection, whilst Li⁺-salts do not.²⁸³ However, others have shown LiNO₃ additives can significantly suppress detrimental cycling effects in non-aqueous Li-O₂.^{274,275} Nitrate (NO₃⁻) is borderline basic and bonds strongly at the Li-metal surface forming a stable SEI component compared with weaker electrolyte anions, making displacement by radical oxides species less likely.²⁷⁴ Small amounts of caesium salt (Cs⁺-salts) electrolyte additives have been also been shown to shield Li-dendrites via a self-healing mechanism. Whereby, Cs⁺ deposits on sharp dendrite peaks deterring further Li⁺ deposition via electrostatic repulsion, in favour of a more uniform Li⁺ deposition.^{284,285}

Protective layers

Due to SEI fragility, extra Li⁺-conductive protective layers have been employed in many studies as a means of improving Li-metal anode performance. Li⁺-conducting membranes are usually either ceramic, glass, polymer or inorganic structures. Crystalline-glass lithium super ionic conductors (LiSICONs) are probably the most well-known and commonly used family of Li⁺-conducting membranes, with ionic conductivities ranging from 10⁻³ to 10⁻⁶ S cm⁻¹. These improve considerably at higher temperatures although they can be extremely expensive.^{4,88,286} Li-metal anodes coated with interconnected carbon nano-spheres were shown to allow Li⁺ to uniformly diffuse through them producing uniform deposits that expand and contract with charge and discharge respectively, inhibiting dendrite nucleation and growth (Fig. 1. 15).²⁶⁹ Good cyclability (> 100) with high Coulombic efficiencies (~100 %) was achieved with a non-complex and cheap silly putty surface coating that easing strain in the SEI and prevented cracking which often leads to dendrite formation.²⁸⁷ A composite protective layer (CPL) using inorganic nanoparticles and plasticised polymer electrolytes showed good performance for

non-aqueous Li-O₂ batteries with > 50 cycles at 1,000 mA h g⁻¹ and a ~1.0 V charge-discharge voltage gap.²⁸⁸ Another promising anode coating for non-aqueous Li-O₂ is SnO₂ asymmetric membrane with > 400 cycles at 500 mA h g⁻¹ and ~100% coulombic efficiency at discharge rates of 280 mA g⁻¹.²⁸⁹

The number of novel Li-metal protective layers and films being investigated is increasing bringing closer the prospect of a practically viable Li-metal anode. However, commercially LiSICON and other membranes are prohibitively expensive, and Li-metal protective layers generally increase the columbic resistance, weight and complexity of to a cell. Therefore, an ideal anode would have (1) a thin highly conductive (or no) SEI and would be (2) cyclable without forming dendrites. Both these characteristics are to some degree dependent on the electrolyte and further support the importance of selecting a suitable electrolyte. Until such an electrolyte can be formulated protective layers are vital for prolonged safe Li-metal cycling.

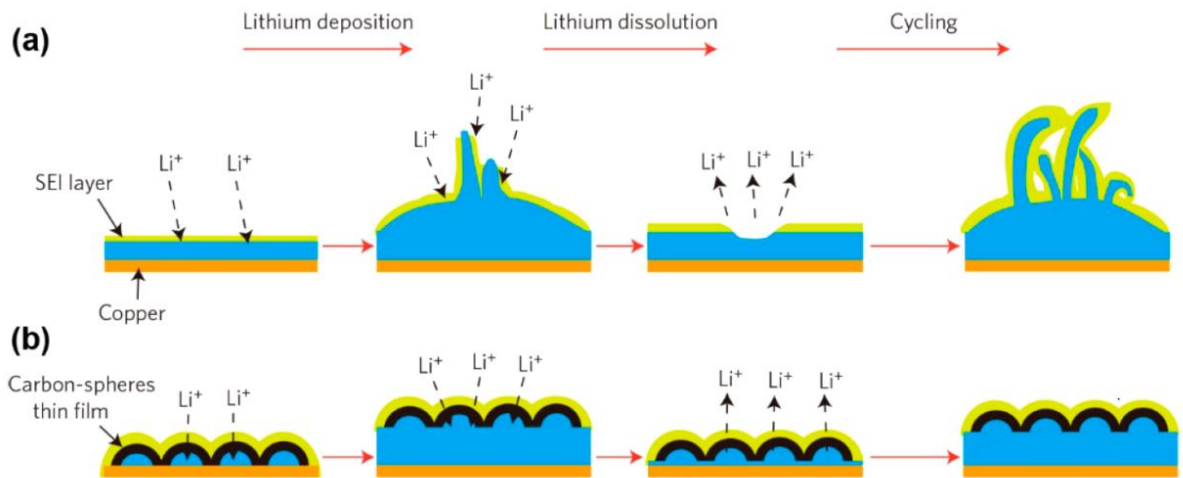


Figure 1. 15. Schematic of Li stripping/plating (dissolution/deposition) with **(a)** conventional SEI and **(b)** carbon nano-spheres protective layer. For (a) after the first cycle surface inhomogeneity increases and dendrites nucleate, dissolve and grow on cycling leading to cell failure. For (b) carbon nano-spheres protect and allow uniform Li-deposition and volume expansion on the metal anode. Figure reproduced from ref:²⁶⁹

Other anodes

Several alternative high capacity Li-based anodes in preliminary stages of development may also show promise for non-aqueous Li-O₂. Li-Silicon anodes (Li_{4.4}Si) have theoretical capacities and energy densities much higher than conventional Li-ion anodes (4,199 mA h g⁻¹ and 1,608-1,927 Wh kg⁻¹, respectively)^{290,291} and have promise combined with the O₂-cathode to mitigate the dendrite concerns associated with Li-metal. Though, there is an associated 300-400 % volume change between charge and discharge, which adds significant mechanical strain on the cell. Carbon coatings can help to mitigate this, however, more work is required to overcome the volume change constraint.²⁹² Li-Ge anodes have shown good performance in Li-ion systems with practical capacities and energy densities of 1,184 mA h g⁻¹ and 475 Wh kg⁻¹, respectively, at high current densities of 5,000 mA g⁻¹ for 150 cycles with ~95% Coulombic efficiencies, however, these too suffer from large volume changes.²⁹³ Li-antimony (Li₃Sb) anodes are another interesting anode with good reversibility and relatively high theoretical capacities (660 mA h g⁻¹),²⁹⁴ though there are currently no publications using these anode in non-aqueous Li-O₂ systems to the best of my knowledge. Recently, graphene nanoribbon asphalt-Li anodes with ultrahigh surface areas (> 3000 m² g⁻¹) have shown great promise with high reversible practical energy densities (943 Wh kg⁻¹) and exceptionally high discharge rates 5-40 A g⁻¹_{carbon} for 500 cycles, and would also make interesting potential anodes for non-aqueous Li-O₂ batteries.²⁹⁵

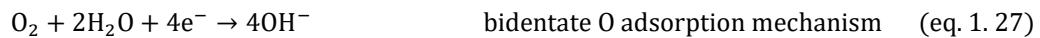
1.4.6 Catalysis

High charge-discharge cell overpotentials result in low Faradaic efficiencies (produce waste heat). Electrocatalysts help to reduce these inefficiencies to within workable ranges. OR/ER catalysis began in earnest in the 60's with research into fuel cells and aqueous air batteries, as a result, a wealth of information now exists on various chemical compounds, substrates, morphologies, dopants and their reaction kinetics.⁹¹ OR/ER catalysis in aqueous media is focussed around improving the sluggish kinetics associated with O₂ bond cleavage and reformation. Classical catalysts favour either a two or four electron reduction mechanism depending on O₂ adsorption at metal-centres (eq. 1. 27-1. 29) and follows the pattern below:

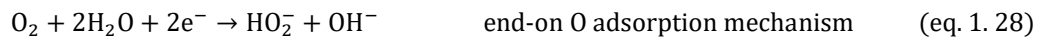
1. O₂ diffusion into O₂-cathode (gas to liquid phase)
2. O₂ adsorption (on catalyst embedded on cathode surface)
3. electron transfer
4. O₂ bond weakening/cleavage (addition of H⁺/Li⁺)
5. 2OH⁻ diffusion away from surface.

OER follows the reverse mechanism to ORR and is generally much slower due to high overpotentials required to reform the O₂ double bond after cleavage. Non-aqueous Li-O₂ batteries have the advantage that the O-O bond remains intact throughout charge and discharge, therefore, improving surface diffusion, adsorption and reduction activation energy barriers for charge transfer are the primary catalyst roles.

Four electron mechanism



Two electron mechanisms



Or



*occurs in extremely basic electrolytes, H_2O_2 can disproportionate further to H_2O , OH and O_2^\cdot .²⁹⁶

The number of catalysis reports in the non-aqueous Li-O₂ literature in recent years is substantial as decades of OR/ER catalysis has been leveraged against it. However, it could be argued that first a stable well defined and cyclable system is needed before looking to improve its capabilities with catalysts. That said, catalysts provide a method of circumventing energetically unfavourable mechanisms that currently limit the battery. Thus, potentially enabling cell cyclability and improving cell efficiencies (though often at excessive costs and complexities) so their current practicality remains an open question. Ultimately, catalysis for non-aqueous Li-O₂ batteries comprises two strategies: (1) surface, solid-state and (2) solution, solvated additive based, with the later method showing the most promise for non-aquesous Li-O₂ batteries to date.

Surface and solid-state

As outlined by Wang *et al.*,⁹¹ there are seven main OR/ER catalyst groups:

- (i) transition metal-oxides, single/mixed metal,
- (ii) functionalised carbons, nanostructured/doped,
- (iii) metal-oxide/nano-carbon hybrids,
- (iv) metal-N complexes, pyrolyzed/non-pyrolyzed,
- (v) transition metal-nitrides,
- (vi) conductive polymers,
- (vii) precious metal/alloys.

A brief overview of each group and their application to non-aqueous Li-O₂ is given below.

(i) Transition metal oxides: single-metal oxides – OR/ERs in single-metal oxides (A_xO_y , where A = transition metal) have been well studied in aqueous electrolytes due to their high abundance, relatively low cost, easy preparation, environmentally benign character, multiple variable valence states and defined structures. Two common catalysts with bifunctional character are manganese dioxide (MnO_2) and cobalt oxide (Co_3O_4), where the metal centres vary between the 4⁺-to-3⁺ and 3⁺-to-2⁺ valences respectively, facilitating oxidation/reduction of adsorbed species at the surface. For MnO_2 , the crystallographic structure is also important as catalytic activity follows $\alpha- > \beta- > \gamma-MnO_2$ trend. Single-metal oxide OR/ER catalysis in aqueous media has recently translated into the non-aqueous Li-O₂ literature with numerous combinations of various structures and heterogeneous cathode morphologies to increase cyclability, discharge capacities and reduce charge-discharge overpotentials.

Mixed-metal oxides – Spinel oxides (AB_2O_4 , where: A = divalent metal, B = trivalent metal) are one of the three most common families of mixed metal oxide catalysts. Electron transfer to

adsorbates occurs via a hopping mechanism between A²⁺ tetrahedral and B³⁺ octahedral sites, reducing charge transfer activation energies. Perovskite-type oxides (ABO₃ or A_{1-x}A'_xB_{1-x}B'_xO₃, where A = rare-earth, A' = alkaline earth, B/B' = transition metal) are another common family of mixed metal oxide catalysts. A site substitution is known to affect oxygen (O) surface adsorption and B site substitution effects O activity, therefore, the catalyst's activity can be tuned. Pyrochlore-type oxides (A₂B₂O₆O'_{1-δ}, where A = Pb or Bi and B = Ru or Ir) are another type of catalyst that have explored. However, the literature is extensive and beyond the scope of this discussion.

(ii) Functionalised carbon materials, nanostructured carbon – carbon cathodes generally have poor catalytic performance, however, varying the cathode's microstructure (i.e. pore volume, pore size surface area) has been used to optimise the morphology of Li₂O₂ discharge deposits and improve discharge capacities.²⁵² Mesoporous structures with large pore volumes (2-50 nm) produce higher specific capacities, whilst small nano-pores (< 2 nm) play little or no role.²⁹⁷ There are three main types of nanostructured carbon architectures; 1D (nanotubes or nanofibers), 2D (graphite/graphene nanosheets (GNs)), 3D (nonporous structures). Graphene based 2D structures have shown superior electrical conductivity, excellent mechanical flexibility, thermal conductivity and surface areas which increases with the number of edge/defect sites. Defect sites on GNs act as nucleation and growth sites during the solution Li⁺-ORR mechanism and favour isolated Li₂O₂ deposits.²⁹⁸ Tight aggregation of porous carbons by binders showed low O₂ diffusivities with less space for Li₂O₂ deposits to be stored resulting in low capacities.⁹¹ Whereas loose carbon packing in the cathode leads to higher void volume for storing Li₂O₂ deposits for a more efficient utilisation of carbon mass.²⁴³

Doped carbon – Heteroatom (N, B, P, S, O, F) doping into the carbon structure can improve

the ORR catalytic performance of carbon O₂-cathodes. Doping increases the number of defect/edge sites in the structure and surface electronic heterogeneity, improving the number of active sites available for charge transfer. Adding hydrophobic long chain fluorinated compounds to the cathode surface has also been shown to influence Li₂O₂ accumulation and charge transfer and on the surface.^{299,300}

(iii) Metal oxide-nanocarbon hybrid materials – Catalyst particles tend to aggregate on the O₂-cathode surface and have conductivity issues associated with pore surface contact. A common strategy to mitigate this is to disperse the catalysts on a conductive carbon substrate which increases the conductivity and distribution of active sites across the O₂-cathode.

(iv) Metal-nitrogen complexes – Carbon-supported transition metal/ nitrogen (M–N_x/C where: M = Co, Fe, Ni, Mn, etc., and normally x = 2 or 4) materials are a promising low-cost alternative to common precious metal catalysts and come in two forms (a) pyrolyzed with inorganic states and (b) non-pyrolyzed with organic states.

(v) Transition metal nitrides – Charge transfer occurs between nitrogen and transition metal atoms due to a high disparity in electronegativity which can produce high conductivity ORR active compounds such as molybdenum³⁰¹ and titanium nitrides³⁰².

(vi) Conductive polymers – These materials have shown catalytic ORR activity particularly when high S or N contents are present and are interesting cathodes. However, they generally lack the conductivity and efficiency of conventional carbon cathodes in real-air gas feedstreams.^{249,303}

(vii) Noble metal, alloy, and oxides – Pt is the most effective ORR catalyst with excellent stability and catalytic activity, though its prohibitively high-cost makes it impractical. Other cathodes, such as porous Au, have shown good cyclability and efficiency, but they are generally too expensive for practical uses.

It is also common for various catalyst types (i → vii) to be combined to boost non-aqueous Li-O₂ cycling performance. Table 1. 6 is an overview of many different surface catalysts strategies used to date for non-aqueous Li-O₂ batteries with key cycling information. Some things to note from Table 1. 6, the bulk of surface catalysis cell cycling occurs with a 1 V voltage gap between charge and discharge which suggests the formation of carbonates, which reduces the cell efficiencies and will need to be reduced substantially for a practical cell. The near ubiquitous use of TEGDME as a standard electrolyte may be contributing to this problem with cells cycling primarily via the surface as opposed to the solution discharge mechanism.

Table 1. 6. Collection of various non-aqueous Li-O₂ cathode catalysts. As reported catalyst abbreviations used, units included where necessary.

Surface catalyst	Electrolyte/ Other information	Capacity (mA h g ⁻¹)	Rate (mA g ⁻¹)	Voltage gap (ΔV)	Cycle number	Ref.
α , β , γ -MnO ₂	1 M LiPF ₆ -PC/	400/	70/	~1.5/	15/	304
	1 M LiTFSi-TEGDME	11,000	70	~1.5	1	
MnO _x @CeO ₂	1 M LiTFSi-TEGDME	1,000/	200/	0.8-1.8/	30/	305
		>2,500	100	0.8-1.8	1	
Co-salen/	1 M LiTFSi-TEGDME	2,000	500	~1.2	+50	306
MCNTs@MnO ₂						
np-RuO ₂ /nr-MnO ₂	1 M LiOTf-TEGDME	500/	50/	~0.8/	>70/	307
		4,000	200	~1.3	20	
MnO ₂ /PILCNT	0.1 M LiClO ₄ -DMSO	400/	100/	~0.8/	40/	308
		1,800	100	~1.3	1	
Co ₃ O ₄ NW arrays	1 M LiOTf TEGDME/ Optimised	300	100	~1.5	55	251
	Co ₃ O ₄ rectangular NSs, 0.5263 cm ³ g ⁻¹ pore vol.					
Co ₃ O ₄ @Ni	DMSO-based	1,000/	100/	~1.3	160/	267
		11,000	100	~1.3	1	
Co ₃ O ₄ @Ni	1 M LiPF ₆ PC	~1,500/	0.1 mA cm ⁻² /	~0.9/	5/	309
		4,000	0.02 mA cm ⁻²	0.5	1	
mp-Co ₃ O ₄	LiTFSI-DME/	~2,200	0.1 mA cm ⁻²	~0.6	6	310
	Optimised 10.5 nm pores dia., 0.35 cm ³ g ⁻¹ pore vol.					
BCFN perovskite	1 M LiPF ₆ -EC:DEC/	1,200-580	50	~1.8	3	311
	Bifunctional					
Pd/Co ₃ O ₄ NWA	1 M LiClO ₄ -TEGDME	500	100	~1.5	258	312
Co ₃ O ₄ NSs	1 M LiTFSI-TEGDME/	500/	400/	1-1.5/	150/	313
	NSs better than bulk Co ₃ O ₄	~24,000	100	-	1	
Ni-NPs@bio Co ₃ O ₄ NWs	0.1 M LiClO ₄ -DME	200/ 8,000	100 _{carbon} /	~0.8-1.5 V	~50	314
			400 _{carbon}			
Cu ₂ O	1 M LiTFSI-TEGDME/	1,000	500	~0.6	100	315
	15 s optimal deposition rate					
MoO ₂ /Mo ₂ C@3D NCF	1 M LiOTf TEGDME/	500/	100/	~0.33/	~130/	316
	89.1 % round-trip efficiency	5,000	1,000	~0.7	~40	
Pt@MCN	LATP _{solid} (10 ⁻⁴ S cm ⁻¹)	~1,600	0.02 mA cm ⁻²	~0.5	1	317

Surface catalyst	Electrolyte/ Other information	Capacity (mA h g ⁻¹)	Rate (mA g ⁻¹)	Voltage gap (ΔV)	Cycle number	Ref.
Mn, Co, Ru-O _x	1 M LiTFSI-DME/ RuO ₂ best cycling	1 mA h	400	~1.2	~20	318
2D-NP-NiO/CNT	0.5 M LiTFSI-TEGDME	1,000	250	~1.6	~70	319
Cr-NPs	1 M LiClO ₄ -DME	750	100	~1.1	1	320
3DOM-ZnCo ₂ O ₄	1 M LiOTf-TEGDME	500	100	1.15-1.37	~30	321
3DOM-FePO ₄	1 M LiTFSI-TEGDME	1,000/ ~5,000	250/ 500	~1.8/ 2	300/ 5	322
pNCO/CB	1 M LiTFSI-TEGDME	1,000/ ~5,800	200/ 100	~1.4	110/ 1	323
mp-NiFe ₂ O ₄ -NPs	1 M LiTFSI-TEGDME	1,000/ ~5,800	0.2 mA cm ⁻² / 0.2 mA cm ⁻²	~1.5	25	324
CoFe ₂ O ₄ /rGO	1 M LiTFSI-TEGDME	1,000/ ~12,200	50/ 50	~1.3/ 1.3	30/ 1	325
om-TiN	1 M LiClO ₄ -TEGDME	430	70	~0.7	30	302
MoN/N-C	1 M LiTFSI-TEGDME	400	0.1 mA cm ⁻²	~1.1	30	301
Ir/B ₄ C	1 M LiOTf-TEGDME	200	10	~1.2	23	326
NS-GC	1 M LiTFSI-TEGDME	1,000/ ~11,000/ 500	100/ 100/ 50	~1.2V/ ~1.2V/ ~1.2V	38/ 1/ 100	327
B-rGO	1 M LiTFSI-TEGDME	1,000/ ~9,000/ ~17,000	1,000/ 2,000/ 100	~1.5/ ~1.5/ ~1.5	34/ 1/ 1	328
N-, S-doped G	1 M LiTFSI-TEGDME/ S doping better cyclability, N doping higher capacity	1,000/ 10,400	300/ 200	~1.9/ 1.9	300/ 1	329
O-, PFC-MWCNTs	0.5 M LiTFSI-TEGDME	~500	70	~1.5	5	300
hp-CoN	1 M LiTFSI-TEGDME/ CoN better than Co ₃ O ₄	~1,300	100	~1.32	50	234
Co(phen) ₂ /C	1 M LiPF ₆ -PC:DEC	~1,500	0.1 mA cm ⁻²	~1.3	10	330
RuO ₂ @pLSCM	1 M LiTFSI-TEGDME	500	50	~1.3	100	331
PEI-AQ	1 M LiOTf-TEGDME	500	100	~1.6	20	303

Surface catalyst	Electrolyte/ Other information	Capacity (mA h g ⁻¹)	Rate (mA g ⁻¹)	Voltage gap (ΔV)	Cycle number	Ref.
AuNPs-VACNTs	LiTFSI-DME/ LiTFSI-TEGDME	1,100/ ~6,200	0.1 mA cm ⁻² / 0.1 mA cm ⁻²	~1.3/ ~1.5	8/ 1	332
TiC	0.5 M LiPF ₆ -TEGDME / 0.5 M LiClO ₄ -DMSO	~350/ ~525	1 mA cm ⁻² / 0.5 mA cm ⁻²	~0.8/ ~1	25/ 100	30
pAu	0.1 M LiClO ₄ -DMSO	~325	500	~0.5-1	100	31
Pt@N-SWCNTs	1 M LiOTf-TEGDME	3,000/ ~7,800	100/ 500	~1/ ~1	50/ 1	333
Pt ₃ Co/CNT	1 M LiTFSI-TEGDME	1,000	200	~0.5	70	334
Pd-rGO	1.0 M LiTFSI-TEGDME	500/ 500/ 500/ ~17,000/ ~6,000/	200/ 500/ 1,000/ 100/ 2,000/	~0.35/ ~0.5 ~0.7 -/	40/ 100/ 100/ -	335
Ru-OrGO	LiOTf:TEGDME (1:4)	2,000/ 5,000	200/ 500	~0.8/ ~1.1	30/ 30	336
hRu-Nspheres	1 M LiNO ₃ -DMSO	~4,000/ 1,000	200/ 500	0.76/ 0.53-0.9	20/ 80	337
Ru@MWCNTPs	LiOTf:TEGDME (1:5)	5,000/ ~27,000	500/ *	0.8-1.5/ ~1.04	50	338
Ru@MWCNT/ sponge	0.1 M LiTFSI-DMSO	300	200	0.5-1	300	339
Ru/MWCNT-Pd/PAN	1 M LiClO ₄ -TEGDME	1,000	500	~1	60	340
Ru, Pd CNTs	0.1 M LiOTf-TEGDME / <i>E_{discharge} fades Ru > Pd</i>	1,000	500	~1.3	100	341
CNT@RuO ₂	LiOTf:TEGDME (1:5)	500/ 300	500/ 500	~1/ ~1	20/ 100	342
Ir@DHG	-	1,000	2,000	0.4-1.2	150	343
3D M-MoSSe	1 M LiClO ₄ -DMSO	~750	50	~1	30	344
TiC	1 M LiTFSI-TEGDME	~5,800	0.05 mA cm ⁻²	~1.4	20	345
CNS@Co(OH) ₂	0.5 M LiTFSI-TEGDME	715	75	~1.5	40	346
NCO@N-rGO	1 M LiTFSI-TEGDME/ N-doping reduces <i>E_{charge}</i>	1,000	200	~1.2	>115	347
Ru-FeCoN/rGO	1 M LiTFSI-TEGDME	1,000	500	~1.5	120	348

Surface catalyst	Electrolyte/ Other information	Capacity (mA h g ⁻¹)	Rate (mA g ⁻¹)	Voltage gap (ΔV)	Cycle number	Ref.
Fe-N-GS	0.1 M LiTFSI-DMSO	500/ 6,000	0.1 mA cm ⁻² / 0.1 mA cm ⁻²	~1.2/ ~1.5	50/ 1	349
LCFMO/GNS	LiPF ₆ :EC-DMC (1:1)	~1,000	100	~1.0	100	350
α-MnO ₂ @GN	DMSO-based	1,000	50	~0.8	45	351
MP pyrochlore	LiPF ₆ -TEGDME	~1,500/ 10,000	200/ 70	~1.3/ ~1.3	27/ 3	352
RuO ₂ -HNSs	0.5 LiClO ₄ -DMSO	~1,000/ ~650	500/ 1,000	~0.76/ ~1	100/ 5	266
Li _{0.5} MnO ₂	1 M LiTFSI-TEGDME	1,000	200	~1.3	200	353
Ru-CB	0.1 M LiClO ₄ -DMSO	4,000/ 1,000/ ~10,000	200/ 1,000/ 200	~0.9/ ~1.3/ ~0.6	40/ 100/ 15	354
MGNACs	1 M LiTFSI-TEGDME	500	0.2 mA cm ⁻²	~1.6	601	241
TMCs	LiTFSI-TEGDME	1,000	0.1 mA cm ⁻²	~1.3	10	355
MoS ₂ -NFs	0.1 M LiTFSI-EMIMBF ₄	~500	0.1 mA cm ⁻²	~0.7	50	356
NCONWAs	1 M LiTFSI-TEGDME	1,000	1,000	~1.2	200	357
SNO ₂ @C	1 M LiTFSI-TEGDME	1,000/ 1,000	75/ 200	~1.4/ ~1.6	26/ 32	358
CoCNF	1M LiClO ₄ -TEGDME:DMSO (1:1)	500	100	~1.5	60	359
GPC-Co ₃ O ₄	1 M LiTFSI-TEGDME	500	250	~1.4	50	360
ALD-Al ₂ O ₃ -Pd	1M LiOTf-TEGDME	500	500	~0.6	10	231
β-FeOOH/ MWNTs	1 M LiTFSI-TEGDME	600	200	~1.5	20	361

Solution

Many strategies for improving non-aqueous Li-O₂ cell performance and offsetting detrimental cell activity using electrolyte solvated additives have been employed such as redox mediators, phase-transfer catalysts, complexing agents and solvating additives (Table 1. 9). Solvated additives diffuse to active sites when required and are heavily dependant on physical and kinetic properties of the electrolyte to function effectively. One method to promote their activity is to Reduce catalyst diffusion distances by decreasing the O₂-cathode pore size.³⁶² The chemical mechanisms vary greatly depending on the solvated catalysts but their functions are generally one of the following:

- To stabilise and solvate radical oxide Li⁺-ORR intermediaries into solution.^{38,172}
- To effectively stabilise Li⁺ and O₂^{•-} in solution, lowering their Lewis acidity and basicity.
- To act as redox mediators that facilitate charge transfer to O₂ and Li⁺ in solution below normal cycling overpotentials.
- To suppress degradation reactions at the O₂-cathode or Li-metal anode.

Table 1. 7. Collection of various non-aqueous Li-O₂ cell redox mediators and a selection of their performances from various reports.

Surface catalyst	Electrolyte	Capacity (mA h g ⁻¹)	Rate (mA g ⁻¹)	Voltage gap (ΔV)	Cycle number	Ref.
TDPA	0.1 M LiTFSI-TEGDME + 0.5mM TDPA/	500/ 8,000	mA cm ⁻² / 0.1 mA cm ⁻²	~0.6/ ~0.8	100/ 1	363
TTF	1.0 M LiClO ₄ -DMSO + 0.05 M TTF/	500 2,000 28,000 ^a	1,000 2,000 200 ^a	~0.75 ~0.85 -	100 100 1	364-370
TTF/LiCl	0.5 M LiTFSI-DEGDME + 50 mM TTF + 0.1 M LiCl/	1,000	200	~0.7	50	371
TTM	1 M LiOTf-TEGDME/ ORR mediator	2.5/ 7.5	0.5 mA cm ⁻² / 0.1 mA cm ⁻²	>1.3/ >1.3	1/ 1	365
TEMPO	1.0 M LiClO ₄ -TEGDME + 0.05 M TEMPO/ ²⁸⁸	1,000/	250/	~1-1.3/	60/	288,372- 374
	0.1 M LiClO ₄ -DEGDME + 10 mM TEMPO ³⁷²					
DTBBQ/TMPPA	1 M LiTFSI in TEGDME + 20 mM TMPPA+ + 20 mM DTBBQ/	6 mA h	0.5 mA cm ⁻²	~1.3	3	375
	Redox flow battery					
TMAO	1 M LiTFSI-DEGDME + 10 mM TMAO	1,000	0.1 mA cm ⁻²	~0.8	1	374
1-Me-AZADO	1 M LiTFSI-DEGME + 10 mM 1-Me-AZADO	1,000	0.1 mA cm ⁻²	~0.9	1	374
LiI ₃ /BuOH	1M LiTFSI-TEGDME:BuOH (1:1) + 0.05M LiI	1,168.5	0.1 C	~0.7	-	376
InI ₃	0.5 M LiClO ₄ -DMSO + 16.7mM InI ₃	2,000/ 1,000	2,000/ 1,000	~0.75/ ~0.65	20/ 20	377
LiI	0.25 M LiTFSI-DME + 0.05M LiI/ ⁴⁰	1,000/ ⁴⁰	1,000/ ⁴⁰	~0.6/ ⁴⁰	2,000/ ⁴⁰	40,143,377 -381
	1M LiTFSI TEGDME + 0.05 M LiI ³⁷⁸	5,000/ ⁴⁰ 1,000/ ³⁷⁸	5,000/ ⁴⁰ 2,000 ³⁷⁸	~0.6/ ⁴⁰ ~1 ³⁷⁸	300/ ⁴⁰ 900 ³⁷⁸	
LiBr	1 M LiBr DEGDME/ ³⁸²	~0.5 mA h cm ⁻² /	0.05 mA cm ⁻² /	~0.7/ ³⁸²	30/ ³⁸²	382-384
	0.2 M LiTFSI DEGDME + 50 mM LiBr / ³⁸²	~0.5 mA h cm ⁻² /	0.05 mA cm ⁻² /	~0.8/ ³⁸²	40/ ³⁸²	
	1 M LiTFSI-DEGDME	500/ ³⁸³	2,000/ ³⁸³	~1.0/ ³⁸³	15/ ³⁸³	

Surface catalyst	Electrolyte	Capacity (mA h g ⁻¹)	Rate (mA g ⁻¹)	Voltage gap (ΔV)	Cycle number	Ref.
	+ 10 mM LiBr ³⁸³					
RuBr ₃	0.1 M RuBr ₃ + 1 M LiTFSI-DMSO	~0.5 mA h cm ⁻²	0.208	~0.9	50	384
CsI	0.05 M CsI, 0.5 M LiTFSI-TEGDME	1,500	500	~0.84-1.8	129	285
Br ⁻ /NO ₃ ⁻	1 M LiNO ₃ -TEGDME + 0.05 M LiBr	1 mA h	0.1 mA cm ⁻²	~0.8	38	385
FePc	0.1 LiTFSI-DMSO + 0.002 M FePc	1,000	0.5 mA cm ⁻²	~1.3	~130	362
DMPU (solvent)	1 M LiTFSI DMPU	500	50 μA cm ⁻²	~0.8	5	219
BHT	1 M LiTFSI DMPU + 4mM BHT	500	50 μA cm ⁻²	~0.7	20	219
Pyr ₁₄ TFSI	0.1 M LiClO ₄ DME:Pyr ₁₄ TFSI (1:1)	500	100	~0.55	5	221
DBBQ	1 M LiTFSI TEGDME + 10 mM DBBQ	430 mA h m ⁻²	0.1 mA cm ⁻²	-	1	127
DMPZ	1 M LiTFSI DEGDME + 0.2 M DMPZ ³⁸⁶	~0.5 mA h cm ⁻²	0.05 mA cm ⁻²	~0.5	5	386,387
EtV(OTf) ₂	0.3 MLiTFSI- Pyr ₁₄ TFSI + 1 mM EtV(OTf) ₂	-	-	-	-	388,389
pD (Melanin)	1 M LiTFSI TEGDME + 0.009M pD	600	200	~0.7	100	390
Phenol	1m LiTFSI TEGDME + 30mm phenol	9 mA h cm ⁻²	0.05 mA cm ⁻²	-	1	391
H ₂ O	0.5 M LiTFSI-DEGDME + 1,000 ppm H ₂ O	5-6 mA h m ⁻²	30 μA	~1.3	11	41,88,139, 140
Co(Terp) ₂	1M LiTFSI-Pyr14TFSI:DEGDME (1:1) + 50 mM Co(Terp) ₂	1,000	200	~1.3	4	368
MPT	1.0 M LiOTf-TEGDME + 0.1 M MPT	1,000	150	~0.9	50	392
comp. agents	MonoTFSI, C ₈ TFSI, 1,3-Di-ImTFSI, Di-ImTFSI and Tri-ImTFSI	-	-	-	-	38
Cation additives	K ⁺ , Ca ²⁺ , Ba ²⁺ , Na ⁺	6,800	100	~1.2	1	147
Quinone derivatives	AQ, BQ, Methyl NQ, Methoxy NQ, Methyl BQ, Methoxy BQ	-	-	-	-	393
TMCs with MC-ligands	Co TPP, Co Me-TPP, Co tert-butyl Pc, Co butoxy Pc	-	-	-	-	394
FEC-Sep.-DMPZ	1M LiTFSI-TEGDME + RE/ SE/ FEC	2,000	400	~0.5	60	387

Surface catalyst	Electrolyte	Capacity (mA h g ⁻¹)	Rate (mA g ⁻¹)	Voltage gap (ΔV)	Cycle number	Ref.
HEME	1M LiClO ₄ -TEGDME + Heme	2,750	100	~1	1	395
DMDMP (solvent)	0.2 M LiTFSI DMDMP	6.7	0.64 mA cm ⁻²	~0.62	~40	396
DABCO or DMA		-	-	-	-	172
LiF		-	-	-	-	281
LiNO ₃	1 M LiNO ₃ DEGDME/ ¹²²	0.15/ ¹²²	0.1 mA cm ⁻² / ¹²²	~1/ ¹²²	30/ ¹²²	122,155,23
	LiNO ₃ -KNO ₃ / ¹⁵⁵	~680/ ¹⁵⁵	160/ ¹⁵⁵	~0.15/ ¹⁵⁵	~40/ ¹⁵⁵	7,274,397,
	{1 M LiNO ₃ -DME}:{ 0.5MLiNO ₃ - TEGDME} (1:1) ²³⁷	1 mA h ²³⁷		~0.9	10	398

1.4.7 Non-Aqueous Li-O₂ Overview

Benefits

- Theoretical specific energies and energy densities an order of magnitude higher than modern state-of-the-art batteries (3505Wh kg^{-1} compared to 387Wh kg^{-1} for Li-ion).³⁹⁹
- O₂ taken directly from air, unlimited supply.
- Potential for drastic improvements in energy storage. Applications could revolutionise multiple industries; particularly the automotive industry by extending the range of EVs.
- Realistically, reaching the theoretical specific energies is unlikely in the short term and would not need to be shown in a practical Li-O₂ cell, merely the demonstration of a safe battery with Li-ion comparable capabilities would be a major advancement in energy storage technology as the system could be further optimised in the future.

Summary

- A solution mechanism driven by solvation of O₂^{•-} and Li⁺... O₂^{•-} intermediaries is ideal for high charge-discharge capacities and can be induced using high DN or AN solvent/additives or solvation catalysts.
- Li₂O₂ degradation is still ambiguous but by and large follows a delithiation followed by disproportionation mechanism releasing O₂.
- Above 3.5 V vs. Li⁺/Li on charge ¹O₂ is produced which, if mitigated against, drastically improves cell cycling.
- Many conventional organic electrolytes show long term instability to radical oxides and Li-metal anodes, ruling them out as practical electrolyte's. However, Li-salts and additives can mitigate against these effects and improve cell performance. High Li-salt concentrations can also dramatically improve electrolyte and Li-metal stability.
- Carbon O₂-cathode structures are susceptible to degradation on charge. However,

passivating films can reduce this on cycling and large pore volumes, surface areas and defect sites favour higher discharge capacities.

- Li-dendrites and SEI instability reduce the safety and cyclability of the cell but can be mitigated against using SEI stabilising additives and thin passivating films.
- Surface electrocatalysts can aid Li^+ -OR/ERs i.e. discharge and charge performance by promoting fast O_2 reduction mechanisms with low activation energies producing amorphous (easily polarised) deposits.
- Solution catalysts, redox mediators, charge transfer catalysts, complexing agents, solvating additives and SEI stabilising additives can improve solvate and stabilise reaction intermediaries, promote lower overpotential Li^+ -OR/ERs and protect Li-metal anodes.

Obstacles remaining

- High overpotentials between charge and discharge effect cell efficiencies. Cell engineering and catalysis can play a role in offsetting this with some promising results so far.^{316,335,364}
- Safety concerns due to dendrite formation on cycling still not resolved.⁴⁰⁰
- H_2O and CO_2 removal systems required for purifying air feed-streams will reduce the batteries energy density. However, they are necessary to prevent side reactions from occurring, lowering the capacity and cycle life of the cell, polluting the electrolyte and causing the electrodes.¹³¹
- Li_2O_2 is insoluble in most electrolytes resulting in passivation of cathode surface and blocking of cathode pores during discharge which ultimately prevents further reactions from taking place, limiting the capacity of the battery.
- $\text{O}_2^\cdot-$ and ${}^1\text{O}_2$ ORR/ER products are unstable in many conventional aprotic battery

solvents and can attack carbon O₂-cathodes.

- $2\text{Li}^+ + \text{O}_2 + 2\text{e}^- \leftrightarrow \text{Li}_2\text{O}_2$ forwards and backwards reaction mechanisms are quasi-reversible which produces high voltage gaps between charge and discharge that effect cycling efficiencies.
- Many good performing cells use expensive components and complex techniques. A practical battery will need to be made from inexpensive components via scalable processes with minimal environmental impact and that can be recycled at the end of its working life.

List of key variables to consider for non-aqueous Li-O₂ cells:

1. Cell temperature
2. Electrolyte solvent(s)
3. Li⁺-salt
4. Li⁺-salt concentration
5. Solvated additive
6. Solvated additive concentration
7. Cathode composition (chemical nature, free-standing or binder {binder chemical nature, binder concentration})
8. Cathode morphology (pore size, pore shape, pore volume)
9. Cathode surface catalyst (chemical nature, structure)
10. Current collector
11. Li-anode coating or SEI stabilising agent
12. Separator

Table 1. 8. Table of some key non-aqueous Li-O₂ properties that have been reported to-date compared with targets for going beyond Li-ion. Once all targets can be met in a non-aqueous Li-O₂ battery then it can be considered practical and not just theoretical.

Property	Units	Target	Reported	Refs.
Cycle life	cycles	1000	1000 _{Li-metal} / 601 _{cathode}	241,401
Specific capacity	mA h g ⁻¹	>200	15,000-27,000 _{cathode} *	306,338
Specific energy, gravimetric	Wh kg ⁻¹	>500	325	402
Charging efficiencies	%	>85	~100 _{Li-metal}	218
Discharge potential	V vs. Li+/Li	2.96	~2.9	403
Charge-discharge overpotential	V	<0.6	0.54-0.8	402
Charge-discharge current density	mA cm ⁻²	~10	5-40 _{Li-metal}	137,404

*open systems

There is considerable ambiguity in literature reports of actual cell capacities, with many papers using the weight of carbon O₂-cathodes to standardise discharge performance which gives much higher values than are theoretically possible for a practical non-aqueous Li-O₂ battery discharging with Li₂O₂ as the main discharge product (1,170 mA h g⁻¹).^{111,168,246} This makes it difficult to evaluate the actual cell performance with respect to the weight of active components (and therefore the current state of the field). A change in reporting methods is required if we are to better gauge how far the current non-aqueous Li-O₂ capabilities are from bearing fruit. This would help with exposing key problem areas so as to double down efforts on solving them.

1.5 Ionic Liquid Electrolytes

1.5.1 Overview

Ethylammonium nitrate (EtANNO_3) was the first ionic liquid (IL) synthesised by neutralising nitric acid with ethylamine and was reported by Paul Walden in 1914.⁴⁰⁵ The definition given by Walden himself a century ago, describing ILs as “*materials composed of cations and anions which melt at or below 100°C*” is still widely used today. However, this temperature is arbitrary and as the field expands, it is becoming more common to class salts that are molten at ambient temperatures (~20°C) as ILs, sometimes referred to as room temperature ILs (RTILs). After being generally overlooked for the past century, the number of papers published about, and patents filed using, ILs has recently begun to grow exponentially year-on-year as investigators find novel ways to exploit their unique physicochemical properties (Fig. 1. 16).⁴⁰⁶

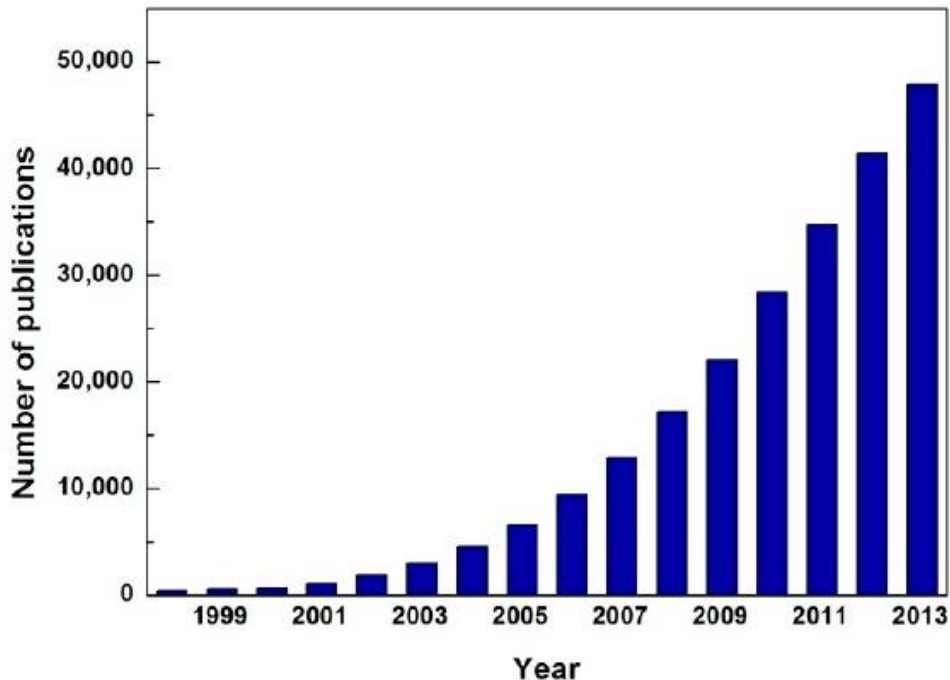


Figure 1. 16. Annual growth of IL publications 1998 – 2013, Figure reproduced from ref. ⁴⁰⁷

From nuclear fission reactors to energy storage, the field of ILs has a great deal of potential applications, with broad implications on science and engineering as a whole.⁴⁰⁸ However, as a field, ILs are still considered to be underdeveloped as production methods have not yet been scaled-up to large plant-volume production capacities. As a result, most ILs are generally synthesised in small batches making them expensive, impacting upon their accessibility, though at the current pace of change this will inevitably change soon. One of the most significant things of interest about ILs is the ability to tailor their properties as required for individual systems. This has resulted in ILs being labelled as ‘designer solvents’, as constituent ions can be selected depending on their physicochemical properties to optimise a system’s performance.¹³² However, not all oppositely charged ions can be combined to form ILs, therefore, an understanding of the properties that produce the liquid phase is needed for their design. It is important to first consider salts in terms of their melting points (MPs) and what factors influence it, as this ultimately dictates whether a certain compound will be an IL or not.

There are four main factors affecting the MP of a salt:

1. ion size, measured by ionic radii (i_r), ionic surface area (i_{sa}) or ionic volume (i_v), units: Å, Å², Å³, respectively.
2. anion and cation ionic mass-to-charge or Mr/z ratios (mol g⁻¹)
3. molecular symmetry
4. conformation

Considering a common salt, such as table salt (NaCl), NaCl contains small, charge dense ions that form a strong highly ordered crystal lattice structure with high melting points due to each Na⁺ cation being strongly attracted to adjacent Cl⁻ anions in an octahedral structure. As a result, these small ion salts are well-ordered thermally stable compounds that are soluble in polar solvents capable of effectively coordinating the different ions. However, larger multi-

molecular ions have lower MPs due the charge being dispersed over a greater ionic mass and volume, which impacts the ability of oppositely charged ions to attract and stabilise the motion of partner ions. Therefore, as a rule of thumb, the MP of a salt is usually inversely proportional to the size and ionic mass-to-charge ratio of its constituent ions (large i_v and Mr/z values → low MP salt). However, it is important to note that the ion size can also affect its diffusion kinetics which can also influence the MP via an opposite trend, i.e. increasing the size of an ion by adding large nonpolar appendages (e.g. alkyl groups) increases intermolecular forces present between the larger ions, increasing the IL viscosity and resistance to ion motion, producing solid-ionic polymer/plastic-like compounds.

Symmetry in large multi-molecular ions has also been shown to have a significant effect on salt MPs; ILs with asymmetrical (commonly referred to as ‘ugly’) ions,⁴⁰⁵ have lower MPs and those with symmetrical (‘beautiful’) ions have higher MPs.⁴⁰⁵ This is due to the more symmetrical ions being able to coordinate with neighbouring ions more easily, making crystallisation more thermodynamically favourable, resulting in glass or polymorphous solid crystalline structures. Whereas the lack of symmetry in asymmetric ions disrupts crystallisation and prevents ordered patterned arrangements from forming between ions, lowering the MP.^{409–411} Finally, any conformational differences (i.e. steric hindrance) in ions can impact upon the MP in a similar fashion to asymmetric ions. Crystallisation is disrupted through poor coordination and a lack of structurally ordered arrangements between counter-ions. Another important thing to note, unlike conventional liquids, which are in the liquid phase because of relatively weak intermolecular forces, ILs are in the liquid phase because of structural and intermolecular heterogeneity and, therefore, preserve their strong ionic nature. This makes evaporation from the bulk liquid as single ions or ion pairs highly unfavourable energetically, resulting in exceptionally low vapour pressures.

1.5.2 Batteries

Most aprotic ILs possess beneficial physical properties that make them advantageous for electrochemical applications^{189,412} compared with many conventional organic solvent-based electrolytes which are unstable in the presence of Li-metal and/or radical oxides. Even those organic electrolytes with relatively good Li⁺-OR/ER chemistries, such as DMSO, have shown instability after prolonged exposure to O₂^{•-},¹⁶⁶ as well as in the presence of Li-metal, ruling them out as practical battery electrolytes. One method of overcoming this may be to use ILs as additives or neat electrolytes. ILs have many innate properties that are favourable for use as electrolytes in non-aqueous Li-O₂ batteries, such as:

- large electrochemical stability windows (4 - 6.2 V),^{413,414}
- high chemical and thermal stability,
- innate conductivity,
- hydrophobicity,
- amphoteric-like nature (opposite ions with formal charges)
- can act as both a solvent and electrolyte,
- low flammability and vapour pressures,⁴¹⁵
- ‘designer-solvents’ with tuneable natures⁴¹⁶

ILs also fit the ideal amphoteric solvent model for the solution mechanism as they contain ions with both positive and negative formal charges that could be used to better solvate Li⁺-ORR intermediaries. Even more encouraging, many common ILs have excellent stability in the presence of alkali metals forming thin and stable SEIs. Also, their properties can be tailored to application requirements (depending on constituent ions selected) making them extremely versatile solvent-electrolyte candidates. However, there is little information available on how to tailor an ‘ideal electrolyte’. Also, IL ionic conductivities are typically lower than organic

solvent based electrolytes, ranging from 10^{-4} - 10^{-3} S cm⁻¹ however, this is still sufficient for applications as electrolytes in battery systems.^{166,417,418} Low conductivities influence the internal resistance and power output of a battery, though this could be improved by selecting an appropriate IL and with the addition of small amounts of stable aprotic solvents as electrolyte additives, see chapter 5.⁴¹⁹⁻⁴²¹

1.5.3 Selecting ILs

Based on known data about certain chemical families of ions and due to the various trends in the physical properties of these groups, ions can be selected specifically to promote non-aqueous Li-O₂ battery mechanisms. Schmeisser *et al.* correlated the relationship between the cation and anion of an IL with its acceptor (AN) and donor numbers(DN).⁴²² In general, the AN and DN of the IL correlates with the size and Mr of the cation and anion, respectively. Expanding on this, bulky ions (term '*bulky ion*' refers to ions that are spatially large with high Mr values and low charge states) generally have high steric hindrance, slow kinetics, high charge delocalisation and are less able to interact with the electrostatic charge of neighbouring ions. Whereas, slender ions (the term '*slender ion*' refers to ions that are spatially small, have high charge states and have a low molecular/atomic masses) generally have strong interactions with neighbouring ions due to charge on the ion being more localised.

This can be further explained in terms of hard-soft acid-base (HSAB) theory. Hard acids interact better with hard acids and soft acids with soft bases. Bulky ions can be considered soft Lewis acids/bases and interact less with harder slender ions.⁴²³ Table 1. 9 outlines some of the terminology for describing and quantifying ion properties that will be used in the following chapters. For Li⁺-OR/ERs, O₂^{•-} is a hard base and slender-anion therefore, large bulky-IL cations will be expected to interact less with it than smaller slender-cations. Evaluating the chemical nature of O₂^{•-} intermediaries at the electrode interface, thus, provides valuable information for the ion selection process of an IL-electrolyte.

Table 1. 9. Terminology for describing and potentially quantifying different ions with examples of hard (H^+/F^-) and soft ($TBA^+/TFSI^-$) Lewis acid/bases ions.

Properties	H^+/F^-	$TBA^+/TFSI^-$	Units
Ion size	small	large	\AA^3
Ion mass	light	heavy	mol g^{-1}
ion size and mass	slender	bulky	$\text{\AA}^3 \text{ mol g}^{-1}$
charge on ion*	localised	delocalised	-
ionic charge density	high	low	$\text{\AA}^{-3} \text{ mol g}^{-1} \text{ z}^{-1}$
ionic charge dissociation	low	high	$\text{\AA}^3 \text{ mol g}^{-1} \text{ z}^{-1}$
Lewis acidity/basicity	hard	soft	-

*depends on electronic structure of ion i.e. delocalized orbitals and electronegativity of substituent atoms.

Cation

Early electrochemical studies of OR/ER chemistries in aprotic ILs were focused around imidazole ring based cations.⁴²⁴ Imidazolium cations have relatively high conductivities and ionic diffusivities which made them ideal initial candidate electrolytes.¹²² However, stability studies in the presence of $O_2^\cdot-$ found the imidazole ring to be susceptible to nucleophilic attack, forming detectable ring opening species.^{166,410} Theoretical calculations by Katayam *et al.* confirmed that due to poor charge delocalisation within the imidazole ring, the central carbon has a slight δ^+ charge, making it susceptible to attack by $O_2^\cdot-$ (Fig. 1. 17c and d), thus, ruling out imidazolium based electrolytes for use in Li-O₂ systems.¹⁷⁵ The same study found ammonium and pyrrolidinium cations to be stable in the presence of $O_2^\cdot-$ which was corroborated experimentally.^{425–427} However, pyrrolidinium cations are also subject to degradation by $O_2^\cdot-$, inducing β -C deprotonation, though at much lower rates.³² $O_2^\cdot-$ stability is key to the non-aqueous Li-O₂ system as these cations will likely interact with the generated radical oxide throughout cycling due to their opposing charges. Ideally the cation should be

able to stabilise and help solvate the radical oxides when generated at the O₂-cathode surface allowing for desired cell chemistry to occur without kinetically restricting diffusion.^{274,275} The Pyrr₁₄⁺ cation and TFSI⁻ anion have been well studied to-date making them good ILs for initial reference studies. OR/ERs have also been investigated in some phosphorus cation systems such as with the weakly acidic P_{14.666}⁺ cation.²³⁷ These cations, like imidazoles, have been shown to react with O₂^{•-} species by α -proton abstraction mechanism, ruling them out for further study. Sulphur-centred cations are other possible systems that are available though there is currently very little literature on OR/ERs in these electrolytes.¹²²

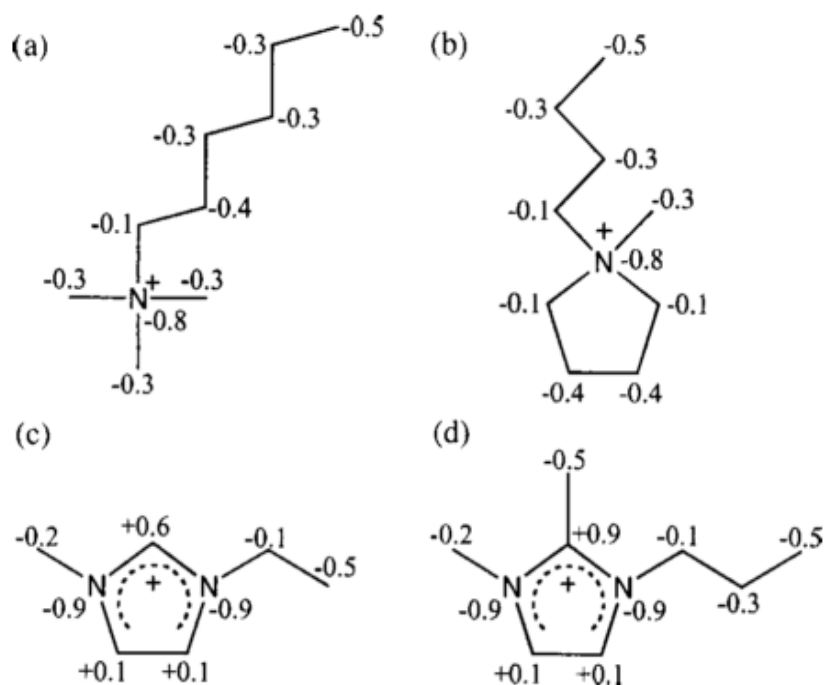


Figure 1. 17. Mulliken charge of carbon and nitrogen atoms in (a) TMHA⁺ (b) Pyrr₁₄^{+[BMP⁺] (c) EMI⁺ (d) DMPI⁺. Figure reproduced from ref. ¹⁵⁵}

Anion

Due to Coulombic repulsion, IL anions are generally far less susceptible to nucleophilic attack from O₂^{•-} species, though they have been shown to degrade and stabilise the Li metal SEI layer.⁴²⁴ Their stability allows anions to be more widely selected based on desirable secondary

system requirements than the cation (e.g. hydrophobicity, conductivity, O₂ solubility, SEI stability and Li⁺ coordination strength). Kuboki *et al.* showed that smaller, well documented ions such as triflate (OTf⁻), though having higher conductivities, were more hydrophilic compared with larger anions such as TFSI⁻, BETI⁻ or IM₁₄⁻.³⁶³ Other studies have also shown that higher fluorine content aids O₂ solubility.³⁶⁷ Generally, a trade-off is required as the properties that lead anions to having some positive physical properties, such as hydrophobicity, can negatively affect other desired system properties, such as viscosity and ion diffusivities.³⁷² General trends in the physicochemical properties of the anion are outlined in Table 1. 8, although the extent of the trend will naturally vary between anions and ILs. Anions also coordinate Li⁺ dissolved in the electrolyte, the strength of coordination determines its acidic nature which impacts upon Li⁺-ORR mechanism and the coordination and transference numbers which determine resistance to ion motion and diffusion.³⁹⁴

Chemical Appendages

It is possible to further refine both the IL cation and anion by adding molecular appendages such as long methyl or ether chains.³⁷⁵ These can have beneficial effects on physicochemical properties such as increasing O₂ solubility, lowering viscosity or increasing ion stability in the presence of radical oxides.³⁶²

Table 1. 10. General trends in physicochemical properties as molecular mass (Mr) and fluorine content (FC) of anion increase.

As anion Mr and FC increase	
Increase	Decrease
Viscosity, Hydrophobicity, O ₂ solubility, Li ⁺ ...O ₂ ^{•-} solubility, Thermal stability, Electrochemical stability	Li ⁺ diffusivity, O ₂ diffusivity, Conductivity, Discharge capacity

1.5.4 IL Electrolyte Screening

Due to the practically infinite combinations of ions and the high IL cost, both anion and cation chemistries need to be considered carefully before an electrolyte can be selected for synthesis or purchase. An IL electrolyte for application in the non-aqueous Li-O₂ battery must have the properties:

1. cation – stable against nucleophilic attack from radical oxides and Li metal,
2. anion – effectively solvate and transport Li⁺.

These criteria can be tested for in prospective IL-based electrolytes using; (1) preliminary diagnostic tests for screening numerous different electrolytes, (2) followed by more advanced tests focussed on electrolytes that show promise. These tests do not necessarily need to be limited to only IL-electrolytes.

Diagnostic tests:

1. Adding Li metal to the IL and leaving for > 72 hours to test if the IL forms stable SEI.
2. CVs of OR/ER with and without the presence of Li⁺-salts to test redox cyclability

If the IL electrolyte can be maintained for multiple Li⁺-OR/ER electrochemical redox cycles and it is stable vs. Li-metal, then it has the potential for application within a non-aqueous Li-O₂ system. These first two diagnostic tests can be used to screen out inadequate electrolytes. Electrolytes with suitable properties can be further investigated in more detail using advanced tests.

Advanced tests:

3. Physicochemical evaluation of key electrolyte parameters such as ionic conductivity, diffusivity etc.
4. *In situ* techniques capable of visualising desirable redox species at the cathode interface during discharge and charge providing qualitative information on (un)desired electrolyte behaviour
5. Quantitative techniques can be used to correlate electron transfer rates with reactant consumption and product formation and affirm whether the desired redox processes are occurring
6. ILs electrolytes can then be assembled into prototype non-aqueous Li-O₂ cells and cycled to evaluate capacity and other major battery properties

Ideally a standard would first need to be evaluated fully to help compare other electrolytes against. Ion structures within the IL can then be varied in favour of ones with more desirable physicochemical properties that improve the electrolyte and battery performance. Comparing the properties and performance of the standard IL with ideal electrolyte performance, allows the short-fall in current electrolyte capabilities to be gauged. The IL-electrolyte can then be optimised by observing which changes in the electrolyte produce desirable cycling performance and the procedure iterated in the direction of targets. This methodology allows for a multiplicity of IL-electrolytes to be screened whilst also allowing resources to be focussed on those electrolytes that show promising properties. Most literature reports often use a combination of these tests, however, for a clear view of a battery electrolytes performance all six need to be used in combination.

2. Experimental

2.1 Techniques

2.1.1 Electrochemistry

Electrochemistry investigates electrical and chemical reactions that result from the flow of current and is usually concerned with the study of electrically conductive solid-electrode interfaces. Electrode potentials are related to the sum of all the electronic processes occurring at the electrode-electrolyte interface, known as the electrical double layer (EDL). Thus, they are dependent on the surfaces, electronic structure, morphology and the composition/orientation of electrolyte molecules (molecular and ionic) at the EDL. When no bias potential is applied to the electrode and diffusion of electrolyte species to and from the bulk is balanced, the surface and electrolyte are in (Nernst) equilibrium, known as the resting or open circuit potential (OCP). Due to the law of charge conservation, the overall electrode-electrolyte interface is neutral, therefore, when an externally-defined (bias) potential is applied to the electrode surface, the EDL reorganises to balance the surface charge. This reorganisation results in molecules at the surface reorienting, coming to or being expelled from the EDL which produces a measurable current response.⁴²⁸ Based on the Grahame model of the EDL, three main layers exist (Fig. 2. 1), the:

1. Inner Helmholtz potential (IHP) layer; specifically adsorbed counter-ions and solvent molecules oriented with oppositely charged ions and dipoles toward the surface, counteracting surface charge.
2. Outer Helmholtz potential (OHP) layer; comprised of solvated ions attracted to the surface but separated from it via a solvation shell leaving them free to move via electrostatic and thermal forces. (Helmholtz layers have capacitor-like behaviour, storing much of the charge balancing the surface polarization. Inner sphere and outer sphere electron transfer mechanisms occur between the surface and the IHP and OHP,

respectively.)

3. Diffuse layer; a partially charged layer whose composition differs from that of the bulk electrolyte and accounts for the remaining charge not stored in the Helmholtz layers. Due to increasing Brownian motion, electrostatic forces attracting electrolyte molecules to the surface become increasingly dispersed away from the surface resulting in an exponential decrease in potential with distance (Fig. 2. 1). Combined charge in the Helmholtz layers and diffuse layers must equal the surface charge.

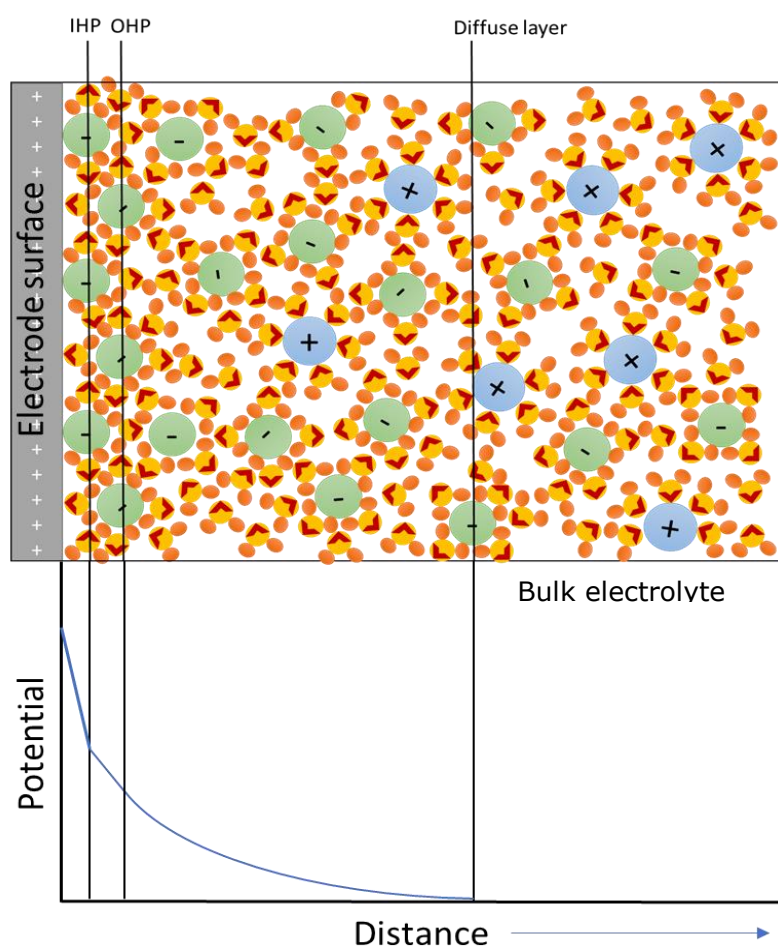
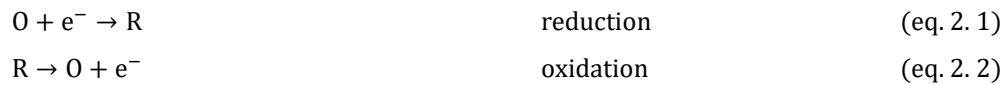


Figure 2. 1. Schematic representation of EDL (top) with a positive bias potential applied to the electrode surface. Anions shown in green, cations in blue and solvent molecules in orange/pink (red pointers indicate direction of negative dipole on solvent molecule). IHP, OHP and the diffuse layer are depicted and their relationship to changes in potential with distance into the bulk electrolyte (bottom).

Applying a bias potential to the electrode surface alters its Fermi level. Increasing the surface potential above the LUMO of the electrolyte causes the electrolyte to be reduced due to charge transfer from the surface. Whilst, decreasing the surface potential below the HOMO of the electrolyte causes the surface to be oxidised via charge transfer from the electrolyte. Both redox processes produce a current response (positive for oxidation and negative for reduction) and the potential range between the LUMO and HOMO of the electrolyte is known as its electrochemical potential window (E_w), which dictates the range of potentials over which the electrolyte is stable. The electrolyte can act as a reaction medium by dissolving redox active species that can be reduced/oxidised (eq. 2. 1, 2. 2) at potentials within the electrolyte's E_w . Thus, the electrolyte facilitates diffusion of redox active species to and from the electrode surface and charge transfer between the electrode and reactant species without directly taking part in the reaction.



Cyclic voltammetry

Cyclic voltammetry (CV) measures the current change in a system as the potential is cycled using a potentiostat over a specified range. Addition of a bias potential at an electrode surface changes the chemical equilibrium in the EDL and induces any thermodynamically viable redox reactions to occur. Peaks in CVs correspond to the onset of diffusion control when reactants are consumed faster than they can be replenished by diffusion of additional reactants from the bulk electrolyte into the EDL. After the peak maximum, redox reactions become limited by the diffusion of reactants to, and products away from, the surface causing the current response to decrease. The combination of thermodynamic and kinetic information that can be acquired over relatively short time periods makes CV a highly versatile technique for characterising solution/electrode interfaces with unknown properties.

Potential cycling can give a survey of the redox processes occurring in an electrolyte within a specified potential range, with cathodic reduction reactions producing a negative current response and anodic oxidation processes a positive one, as shown by the O_2/O_2^\cdot redox couple in Figure 2. 2. CVs were obtained by scanning from the open circuit potential (OCP) to the ORR potential region (red arrow) then back towards positive OER potentials (blue arrow). No Faradaic current response is visible in the Ar saturated IL due to the absence of redox species and the stability of the electrolyte within the potential range. For the O_2 saturated IL a strong current response is visible due to O_2 reduction to O_2^\cdot and the subsequent oxidation back to O_2 . CVs are recorded using a potentiostat to consecutively step-change surface potentials allowing the current response to be recorded. The rate at which the potential step is changed is known as the scan rate (\bar{v}) calculated using eq. 2. 3. Slow \bar{v} 's allow the electrode surface to approximate equilibrium conditions between diffusion of reactants and products to/from the surface, respectively. Whereas, fast scan rates approximate pure EDL capacitance behaviour.

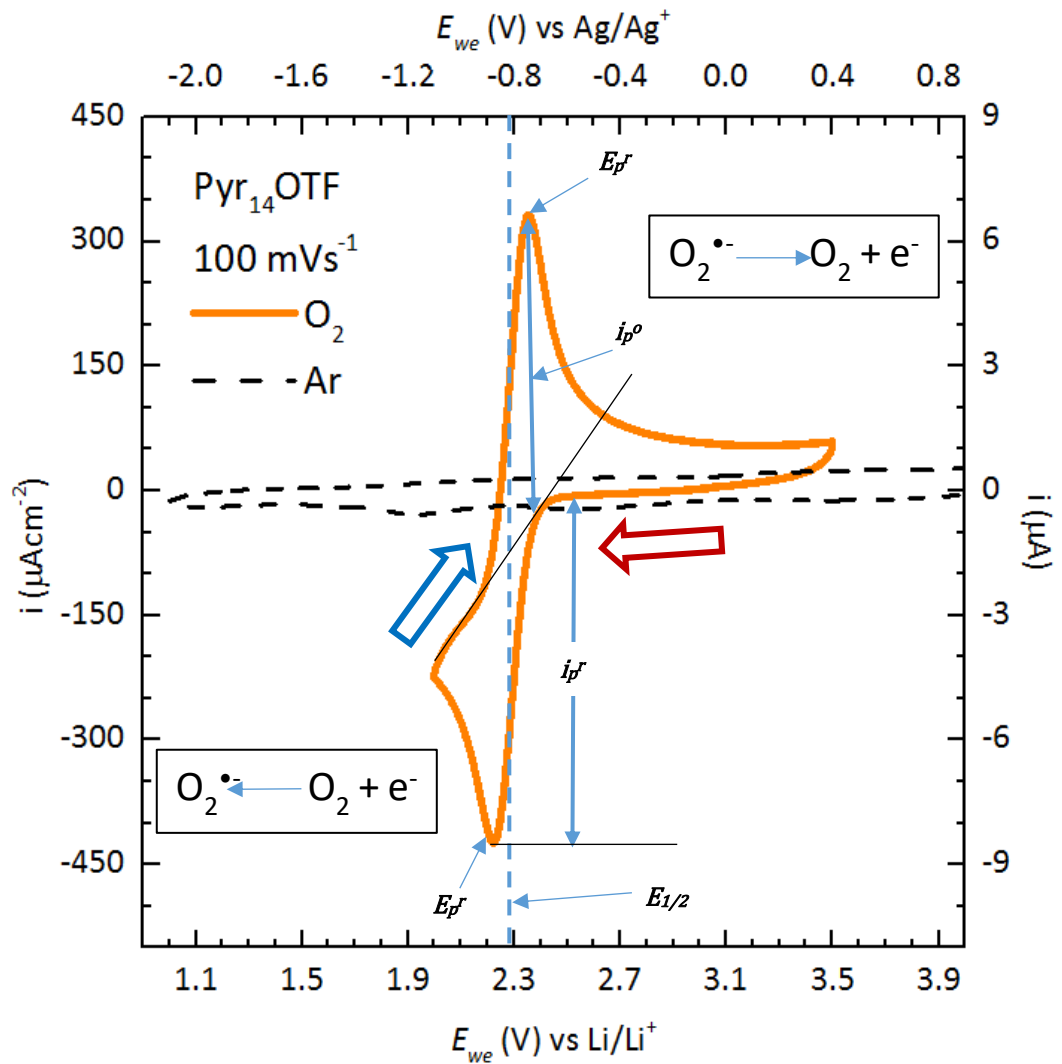


Figure 2. 2. Example CV of argon (Ar) (black dashed line) and O_2 (orange line) saturated IL-electrolyte ($Pyr_{14}OTf$). Working electrode (WE): 1.6 mm diameter glassy carbon (GC); reference electrode (RE): Ag; counter electrode (CE): Pt; scan rate: 100 mV s^{-1} . Where, E = standardized potential (V vs Li/Li^+), i = current response measured with current density ($\mu\text{A cm}^{-2}$), subscript ‘p’ = peak, superscripts ‘r’ and ‘o’ = reduction and oxidation, respectively, $E_{1/2}$ = redox half-potential. i_p^r is measured by extrapolating a baseline as the potential for the oxidation scan is typically positive of the equilibrium potential.

$$\bar{v} = \Delta E / t \quad (\text{eq. 2. 3})$$

Where: \bar{v} = scan rate (mV s^{-1}), ΔE = change in potential (V), t = time (s).

Generally, a reversible electrochemical (EC) reaction is one where electron transfer kinetics are rapid, compared with diffusion rates, and Nernst equilibrium is maintained at the surface at all potentials (i.e. reactant/product concentrations at the surface are independent of potential and electron transfer occurs instantaneously when the system is thermodynamically viable).

Five key criteria exist for assessing the reversibility of a CV (eq. 2. 4-2. 8), are:

1. potential differences (ΔE) between reduction and oxidation peaks should be $\sim 59 \text{ mV}$
¹. Where z = number of electrons transferred, resulting from $2.3RT/nF$ (Nernst equation at 25°C),
2. ratio of reduction and oxidation peak currents (i_p) should equal 1 (i.e. the charge passed should be equal),
3. i_p changes proportionally with the square-root of \bar{v} ,
4. position of peak potentials (E_p) are independent of \bar{v} ,
5. current passed beyond the E_p is proportional to the square-root of time.

CVs that do not fit these five criteria are not considered reversible and electron transfer rates are insufficient to maintain surface equilibrium, requiring overpotentials to drive the redox reactions and acquire the same level of current as a reversible system. CVs that fit some but not all the criteria can be considered quasi-reversible. Those that fit none of the criteria are irreversible.

1. $\Delta E = E_p^a - E_p^c = 59/z \text{ mV}$ (eq. 2. 4)
 2. $|I_p^a / I_p^c| = 1$ (eq. 2. 5)
 3. $I_p \propto \bar{v}^{1/2}$ (eq. 2. 6)
 4. E_p independant of \bar{v} (eq. 2. 7)
 5. at potentials beyond E_p , $I \propto t^{-1/2}$ (eq. 2. 8)
-

Galvanostatic cycling

Mimicking real battery charge-discharge cycling, during galvanostatic cycling, a constant current is imposed on the EC cell and the potential recorded for a set length of time measured in C-rate (rate of battery discharge relative to its maximum capacity), or until specified potential limits are reached. Key cell properties can be elucidated such as, the thermodynamic discharging and charging potentials which provides information on the discharge reaction pathway, precipitation and disintegration of non-aq. Li-O₂ redox products.^{4,121} Summing the amount of current passed quantifies the amount the redox precipitates formed and how effective the system is at supporting redox processes whilst changing the current rate provides information on cell kinetics and chemical diffusion coefficients of mobile species in the electrode. A common technique used in the non-aqueous Li-O₂ literature, galvanostatic cycling combined with quantitative techniques like differential electrochemical mass spectroscopy (DEMS) which observes the consumption and production of species from the gas feed-streams gives powerful evidence to supporting the cell efficiency and whether the ideal two electron charge transfer mechanism is occurring.¹⁴⁴

2.1.2 Surface Enhanced Raman Spectroscopy

Raman spectroscopy is an important analytical tool for characterising and exploring fundamental molecular structures and bonding due to its generally non-destructive, non-invasive ultra-sensitive nature.⁴²⁹ Raman spectroscopy is the measurement of inelastically scattered light after a sample has been exposed to an intense light source of a set wavelength (energy). Most incident light is either absorbed or elastically (Rayleigh) scattered by the sample and maintains its starting frequency and energy.⁴²⁹ However, polarisation of vibrating bonds causes a small amount of incident light (1 in 10^7 photons)⁴³⁰ to be inelastically scattered (Fig. 2. 3a) and results in photons exciting electrons within vibrating molecules to a virtual energy level, on relaxation to ground states some photons are reemitted with less (Stokes) or more (anti-Stokes) energy than incidence (Fig. 2. 3c). Raman spectra are derived by subtracting the energies of incident and scattered light; Stokes and anti-Stokes scattering produce symmetrical patterns about the origin. Different vibrational modes specific to individual bonds within a molecule have different energies which are excited or damped by photon incidence providing important vibrational information about a system on a molecular level.⁴³¹

Surface enhanced Raman spectroscopy (SERS) is the process whereby a normal Raman scattering signal of an analyte is enhanced up to $\sim 10^{11}$ times using an enhancement active (e.g. Cu, Ag, Au, Pt) nanostructured ($\sim 50\text{-}200\text{ nm}$) rough surface (Fig. 2. 3b).⁴²⁹ Common consensus has concluded the enhancement is a result of two main mechanisms:

1. Electromagnetic (EM) enhancement – exciting light radiation causes the delocalised ‘electron gas cloud’ near the surface of conductive coinage metals to oscillate, known as a surface plasmon. Collective excitation of the surface plasmon by incident light induces strong near fields which resonate with (amplifying the signal of) any EM fields close to the smooth surface in the normal plane. Troughs in roughened surfaces

concentrate photons and give surface plasmons a perpendicular component,⁴³² allowing EM signals produced by polarisation of oscillating bonds vibrating adjacent to surface to appear visibly amplified which is detectable.⁴³³

2. Chemical enhancement – incident light induces charge transfer via back donation from the surface orbitals into those of analyte molecules adsorbed on the surface, increasing the polarisability of chemical bonds and the Raman scattering signal. Chemical enhancement is weaker than EM enhancement.⁴³²

Raman, is ideal for detecting changes in bond polarisability (covalent character) of bond vibrations, whereas, IR detects changes in dipole moments (ionic character) in bonds. Combining the high surface sensitivity of SERS with EC studies by using roughened metal surfaces as Wes allows for electrode interfaces and chemical reaction mechanisms to be probed *in situ*. Providing real time vibrational information about the reactants being consumed, products being formed, molecules adsorbed, leaving and reorienting on the surface. Thus, *in situ* SERS is a powerful analytical tool, ideal for investigating the fundamental mechanisms of EC energy storage systems. As discussed in the introduction, *in situ* SERS has been used to great effect in non-aq. Li-O₂ cells, helping to elucidate complex discharge mechanisms.^{4,74}

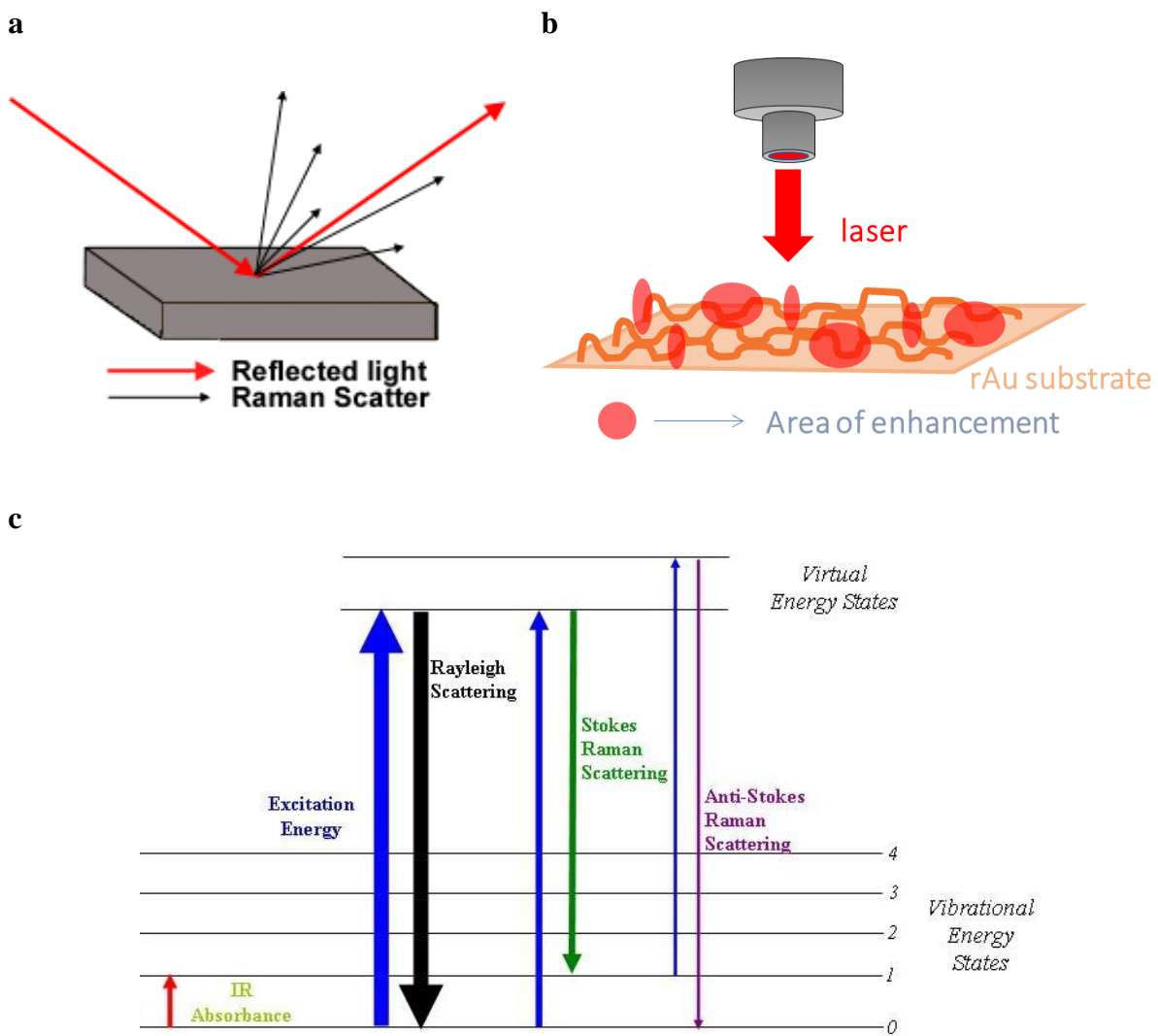


Figure 2.3. (a) Schematic depicting Rayleigh and inelastic scattering of light by a sample, (b) depiction of roughened coinage metal surface with regions of surface enhancement, (c) energy diagram depicting the effect of incident light on vibrating molecules. From left to right; incident photons that are absorbed by the vibrating molecules causing a noticeable shift in the vibrational energy state of the sample (IR absorption). Incident photons, which excite vibrating molecules to a virtual energy state and are reemitted on relaxation of the molecules back to their starting vibrational state, are Rayleigh scattered. Incident photons that excite molecules to a virtual energy state and are reemitted with less/more than initial energy due to molecules relaxing to a higher/lower energy vibrational state are, Stokes/anti-Stokes scattered respectively. Figure (c) reproduced from ref. ⁴³⁴.

2.1.3 Surface Enhanced Infra-Red Adsorption Spectroscopy

Like Raman; Infra-red (IR) spectroscopy is a vibrational spectroscopy, which detects molecular bond vibrations sensitive to changes in dipole moments (ionic character). *In situ* attenuated total reflection (ATR) surface enhanced infrared adsorption spectroscopy (SEIRAS), can provide detailed analysis of the electrode interface and has been employed to gain mechanistic insight into degradation pathways in the non-aqueous Li-O₂ battery.¹³⁷ First pioneered by Osawa *et al.*,¹³⁷ by exploiting internal reflection through an IR prism with coinage metal films deposited on the surface (Fig. 2. 4), ATR-SEIRAS has the advantage over other IR techniques of being highly surface sensitive and of minimising bulk electrolyte signals. Combined, *in situ* surface sensitive SEIRAS and SERS techniques provide exceptional understanding of surface processes enabling most vibrational bonds and molecules to be probed throughout EC cycling.

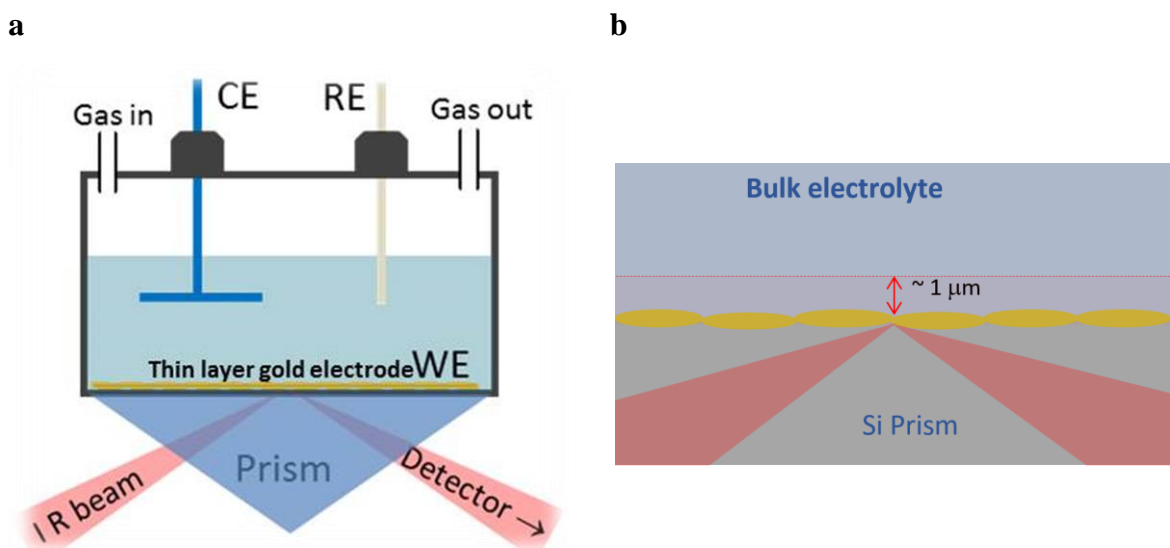


Figure 2. 4. (a) *In situ* SEIRAS cell schematic. EC cell built on top of Au-coated IR prism. The Au film acts as a WE whilst the IR prism facilitates reflection of the IR beam off the Au surface. **(b)** Close-up of reflection shows an approximate 1 μm penetration depth of the IR laser, whilst surface enhancement factors are much smaller $\sim 10 \text{ nm}$. Subtracting spectra from spectra at onset potentials removes signal from the bulk predominantly showing changes in molecular composition of the surface, see below.⁴³⁵ Schematics by V. Padmanabhan.

Deposition of a coinage metal film (typically Au) on IR crystal has the dual purpose of acting as an electrode and producing a localised surface plasmon enhancement with which to probe interfacial speciation when excited by incident light. Compared with SERS, the SEIRAS enhancement factor is relatively weak ($\sim 10^{-4}$ times), however, still large enough to give beneficial information on the interface.⁴³⁶ In ATR-IR spectroscopy, the evanescent IR field extends for up to several hundreds of nanometres into the bulk electrolyte (Fig. 2. 5a). The depth of penetration of the IR wave is determined by the wavelength of light, angle of incidence and all refractive indices. However, in ATR-SEIRAS spectroscopy, the nanostructured metal film enhances IR fields by the excitation of surface plasmons (Fig. 2. 5b), photons are concentrated at the surface and the evanescent wave decays exponentially with distance from the surface. The strength of the enhancement depends on the morphology of the surface and decays sharply above 10 nm from the surface. Thus, it is highly sensitive to species adsorbed or adjacent to the surface, allowing for the interfacial region to be discriminated from the bulk electrolyte.

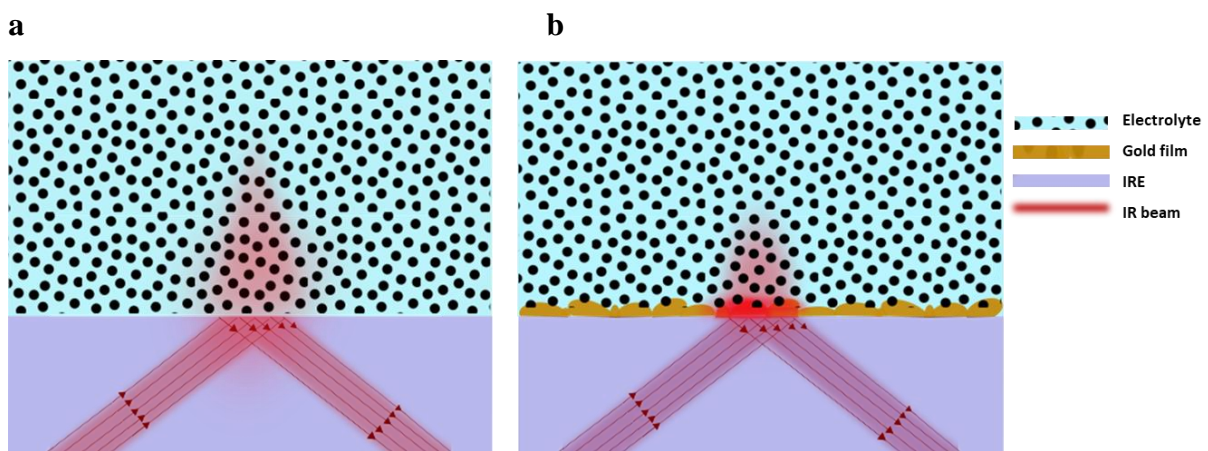


Figure 2. 5. Schematic comparison of (a) clear ATR-IR spectroscopy and (b) ~ 20 nm Au-film coated IR prism surface for SEIRAS. Penetration of IR evanescent into bulk electrolyte and photon concentration in enhancement active surface. Schematics by V. Padmanabhan.

2.1.4 Karl Fischer Coulometric Titration

Karl Fisher titration is a conventional technique for determining the moisture content of samples to an accuracy within a few parts per million (ppm) and is an essential analytical tool for verifying the H₂O content of non-aqueous electrolytes. Automated equipment is commercially available and widely used for detecting water content of moisture sensitive systems. In principle the titration mechanism is driven by the oxidation of sulphur dioxide (SO₂) by iodine (I₂) in a methanolic hydroxide solution and consuming H₂O in the process (eq. 2. 9). Volumetric and coulometric techniques work on the same principles but differ based on whether I₂ is added to, or generated electrochemically in, the cell. Only the coulometric system is considered here.

Titration



For coulometric titrations, I₂ is generated via the pulsed EC oxidation of dissolved iodide (I⁻) in an excess of SO₂ dissolved in methanol. A basic buffering agent (RN) is present to neutralise any acids (HI and H₂SO₄) that could form and allows an equilibrium shift to the right of equation 2.9. Any H₂O present in an added sample is immediately consumed by the generated I₂ which is continuously produced until a trace amount of excess I₂ are detected indicating all H₂O has been consumed and reaction has stopped. The amount of I₂ consumed corresponds to the quantity of H₂O added to the system which in turn, can be quantified by the amount of electricity required to oxidise I⁻ for the reaction to reach completion. Thus, the water content can be easily calculated using Faraday's law.

2.1.5 Modelling Ion Properties

Several ion properties (ionic volume (i_v), ionic surface area (i_{sa}), Raman and IR spectra in a vacuum, charge distributions, electrostatic potential surface distributions and HOMO/LUMO energy levels) for a number of IL ions were modelled using density functional theory (DFT, B3LYP functional, 6-31G* basis set) in Spartan 16. Ionic volumes and surface areas for single molecule cations were calculated using a simple CPK model.

2.1.6 Theoretical Calculations

Theoretical specific energy

Calculations used to determine theoretical specific energy values in tables 1. 1-1. 4 are explained here. In accordance with Faraday's 1st law, integrating the total i passed at an electrode over time gives the total amount of charge (Q) passed (eq. 2. 10)⁴³⁷ and is directly proportional to the quantity of products formed and reactants consumed. Thus, the EC equivalent (Z) can be calculated using the molecular mass of the product (eq. 2. 11) and readily converted to the theoretical capacity ($Q_{t,cell}$) of the cell (eq. 2. 12). This allows the theoretical specific energies ($U_{t,cell}$) of battery to be calculated (eq. 2. 14) by multiplying $Q_{t,cell}$ with the calculated theoretical cell voltage ($E_{t,cell}$, eq. 2. 13).

$$Q = \int i \, dt \quad (\text{eq. 2. 10})$$

$$Z = (zF) / Mr \quad (\text{eq. 2. 11})$$

$$Q_{t,\text{cell}} = Z / 3.6 \quad (\text{eq. 2. 12})$$

$$E_{t,\text{cell}} = \Delta G_f / -nF \quad (\text{eq. 2. 13})$$

$$U_{t,\text{cell}} = Q_{t,\text{cell}} \times E_{t,\text{cell}} \quad (\text{eq. 2. 14})$$

Where: Q = charge passed (C), i = current passed (A), dt = change in time (s^{-1}), Z = EC equivalent ($C g^{-1}$), z = N^o of e^- passed (dimensionless), F = Faraday constant ($96,485 C mol^{-1}$), Mr = relative molecular mass of product ($g mol^{-1}$), $Q_{t,\text{cell}}$ = theoretical cell capacity ($A h kg^{-1}$), $3.6 = (3,600 A s to A h) / (1,000 g^{-1} to kg^{-1})$ conversion factor, $E_{t,\text{cell}}$ = theoretical cell voltage ($kg m^2 s^{-3} A^{-1} \rightarrow V$), ΔG_f = Gibbs free energy of formation ($J mol^{-1}$), $U_{t,\text{cell}}$ = theoretical specific energy of cell ($W h kg^{-1}$).

Example, calculating U of non-aqueous Li-O₂ cell producing Li₂O₂ as a discharge product:

- Mr of Li₂O₂ = 45.88 g mol⁻¹
- for reaction: Li⁺ + 2e⁻ + O₂⁻ → Li₂O₂, z = 2
- ΔG_f of Li₂O₂⁴³⁸ = -570,800 J mol⁻¹

$$Z = (2 \times 96,485) / 45.88 = 4,205.9 C g^{-1} \quad \text{step 1}$$

$$Q_{t,\text{cell}} = 4,205.9 / 3.6 = 1,170.4 A h kg^{-1} \quad \text{step 2}$$

$$E_{t,\text{cell}} = -570,800 / (-2 \times 96,485) = 2.958 V \quad \text{step 3}$$

$$U_{t,\text{cell}} = 1,170.4 \times 2.96 = 3,464.3 W h kg^{-1} \quad \text{step 4}$$

ν_{O-O} bond force constant

Ignoring any environmental influences and anharmonic oscillations; dioxygen (O_2^x , where $x = -2, -1, 0, +1$, i.e.; O_2^- , O_2^{2-} , O_2 , O_2^+) O-O bonds can be considered as simple diatomics and their force constant calculated with a rearranged version of Hooke's law by first calculating the reduced mass (M_r^R , eq. 2. 13) and using the wavenumber of the spectroscopically observed O_2^x bond vibration (ν_{O-O} , eq. 2. 14). Force constant values were calculated for the ν_{O-O} of a variety of different reported O_2^x spectra (~183 species) in an excel spreadsheet (see chapter 3 for discussion and data plots).

$$\frac{1}{M_r^R} = \frac{1}{M_r^A} + \frac{1}{M_r^B} \quad (\text{eq. 2. 13})$$

$$k = 4\pi^2 c^2 \nu^2 M_r^R \quad (\text{eq. 2. 14})$$

Where: M_r^R = reduced mass, M_r^A = molecular mass of 1st atom in bond, M_r^B = molecular mass of 2nd atom bond, k = bond force constant ($N m^{-1}$), c = speed of light ($2.998 \times 10^{10} cm s^{-1}$), ν = spectral wavenumber of bond vibration (cm^{-1})

Example, O_2SbF_6 :

- ν_{O-O} of O_2^+ = $1,861 \text{ cm}^{-1}$ ⁶
- M_r^A and M_r^B are both O, therefore = 15.99 g mol^{-1}
- g mol^{-1} (Da) to kg conversion factor = 1.66×10^{-27}

$$\frac{1}{M_r^R} = \frac{1}{(15.999 \times 1.66 \times 10^{-27})} + \frac{1}{15.999 \times 1.6605 \times 10^{-27}} \quad \text{Step 1}$$

$$M_r^R = 1.327 \times 10^{-26} \text{ kg} \quad \text{Step 2}$$

$$k_{O-O} = 4\pi^2 (2.998 \times 10^{-10})^2 (1,861)^2 (1.327 \times 10^{-26}) \quad \text{Step 3}$$

$$k_{O-O} = 1,629 \text{ N m}^{-1} \quad \text{Step 4}$$

Ionic charge dispersion

It was found that for ions coordinating O_2^x species, the size, mass and charge influences the strength of coordination and in turn the O-O bond force constant which causes detectable changes in ν_{O-O} (see chapter 3 for further discussions). Thus, the physical parameters of one ion can indirectly influence the bond force constant and wavenumber of bonds present in the counter-ion. These values for ions can be simply quantified in terms of the Mr, ionic volume (i_v) and the charge on the ion (z). In O_2^x complexes; changes in the Mr and i_v of the coordinating counter-ions were found to be inversely proportional to changes in ν_{O-O} whilst changes in the charge of the counter-ion were proportional, see chapter 3 for more detailed discussion. The ‘ionic charge dispersion’ (\mathbb{K}) has been derived as a simple value to describe these ionic properties and is a measure of how ‘bulky’ the counter-ion is (eq. 2. 15). The Cyrillic symbol for \check{Z} (\mathbb{K}) is used for ionic charge dispersion, subscripts $_{iv}$ and $_{isa}$ denote the use of ionic volume or ionic surface area, respectively, and superscripts a and c denote anion and cation, respectively. \mathbb{K}^c denotes the cationic charge dispersion and \mathbb{K}^a the anionic charge dispersion. For O_2^{+} complexes, the higher the \mathbb{K}^c value of the coordinating cation the bulkier (more charge dispersed) it is and the less strongly it interacts with O_2^{+} , therefore, the weaker the influence on its bond force constants and in turn the lower the ν_{O-O} value. This trend in the \mathbb{K}^c can be used to indirectly determine the chemical nature of O_2^x using its measured ν_{O-O} .

$$\mathbb{K}_{iv}^c = \frac{(i_{iv}^c \text{ Mr})}{z} \quad (\text{eq. 2. 15})$$

$$\nu_{O-O} \propto \frac{1}{\mathbb{K}_{iv}^c} \quad (\text{eq. 2. 16})$$

Example 1, TBA⁺:

- Mr = 242.5 g mol⁻¹
- $i_v = 324 \text{ \AA}^3$
- Å³ to m³ conversion factor = 1×10^{-30}
- z = +1 (can be dimensionless or have units C)
- z to Coulomb conversion = 1.602×10^{-19} C

$$\mathbb{K}_{iv}^{TBA} = \frac{(242.5 \times 324)}{1} \quad \text{Step 1a}$$

$$\mathbb{K}_{iv}^{TBA} = 76,566 \text{ \AA}^3 \text{ mol g}^{-1} \quad \text{Step 2a}$$

or

$$\mathbb{K}_{iv}^{TBA} = \frac{(242.5)(324 \times 10^{-30})}{(1 \times 1.602 \times 10^{-19})} \quad \text{Step 1b}$$

$$\mathbb{K}_{iv}^{TBA} = 4.90 \times 10^{-7} \text{ g mol}^{-1} \text{ m}^3 \text{ C}^{-1} \quad \text{Step 2b}$$

Example 2, K⁺:

- Mr = 39.1 g mol⁻¹
- $i_v = 21.1 \text{ \AA}^3$
- z = +1

$$\mathbb{K}_{iv}^K = \frac{(39.1 \times 21.1)}{1}$$

$$\mathbb{K}_{iv}^K = 826.5 \text{ \AA}^3 \text{ mol g}^{-1}$$

or

$$\mathbb{K}_{iv}^K = \frac{(39.1) \times (21.1 \times 10^{-30})}{(1 \times 1.602 \times 10^{-19})}$$

$$\mathbb{K}_{iv}^K = 5.15 \times 10^{-9} \text{ g mol}^{-1} \text{ m}^3 \text{ C}^{-1}$$

Comparing \mathbb{K} of the two cations TBA⁺ and K⁺ with the reported ν_{O-O} of their respective O₂^{•-} salts: the bulkier TBA⁺ has a weaker influence on the force constant of O₂^{•-} than K⁺ as observed by the lower ν_{O-O} wavenumber, below.

TBA ⁺	$\mathbb{K}_{iv}^{TBA} = 4.90 \times 10^{-7} \text{ g mol}^{-1} \text{ m}^3 \text{ C}^{-1}$	$\nu_{O-O} = 1,123 \text{ cm}^{-1}$
K ⁺	$\mathbb{K}_{iv}^K = 5.15 \times 10^{-9} \text{ g mol}^{-1} \text{ m}^3 \text{ C}^{-1}$	$\nu_{O-O} = 1,145 \text{ cm}^{-1}$

2.2 Equipment and Procedure

2.2.1 Electrochemistry

EC experiments were performed using Biologic (VSP100, VMP) potentiostats with EC-Lab software to run CV and galvanostatic charge-discharge cycle experiments. Some additional EC charge-discharge cell measurements were carried out on a battery cycler (Maccor Series 4000) in a controlled atmosphere at 30°C. The cycling procedures where generally varied depending on the electrolyte and materials being tested and are described below. BT-Lab software was used for processing data files

Most EC measurements were carried out within a glass, multi necked vacuum-tight cell within an inert Ar atmosphere glovebox (< 30 ppm O₂, < 0.5 ppm H₂O) at ambient temperature ~23°C. Polycrystalline Au, Pt and GC disc electrodes (0.16 cm dia.) were used as WEs. The electrode surfaces were polished mechanically with decreasing grain sized alumina slurries (1.0, 0.3 and 0.05 µm), washed in Milli-Q water (18.2 MΩ) and sonicated before being dried at 100°C in a vacuum oven for a minimum of 12 hours before use. A flame annealed Pt coiled wire was used as a counter electrode and a Ag wire as a quasi-reference electrode, both electrodes were sonicated in ethanol and Milli-Q water and similarly dried at 100°C in a vacuum oven for a minimum of 12 hours before use. Galvanostatic cycling was carried using assembled coin cells.

2.2.2 Low-Volume Spectro/Electrochemical Cells

Conventional in-house made EC cells required relatively large volumes (≥ 5 ml) of electrolyte for each experiment. Due to the high-cost and limited supply of many IL electrolyte sample, multiple low-volume (0.4-0.8 ml sample per experiment) EC cells were designed. Unless specified otherwise, cell parts for all cells were washed thoroughly with acetone and sonicated in ethanol then Milli-Q water before drying overnight in a vacuum oven at 100°C before use. All EC measurements were performed at room temperature and CVs were obtained by scanning from OCP to the ORR potentials (~2.0-2.8 V vs. Li⁺/Li) then back toward positive potentials ORR potentials (~2.4-3.4 V vs. Li⁺/Li), then back to OCP.

Electrochemical cell

Multiple generic glass EC cells (Fig. 2. 6) were fabricated in-house with five cell inlets for:

1. WE – 3 or 1.6 mm diameter disc: GC, Au or Pt.
2. Counter electrode (CE) – Pt coil.
3. Reference electrode (RE) – Ag wire, Ag⁺/Ag or Li⁺/Li fritted electrodes (see below).⁴³⁹
4. Gas-inlet (G-In) – an inlet fixture that allows Ar and O₂ gas saturation of the electrolyte.
5. Gas outlet (G-Out) – connected to atmospheric outlet.

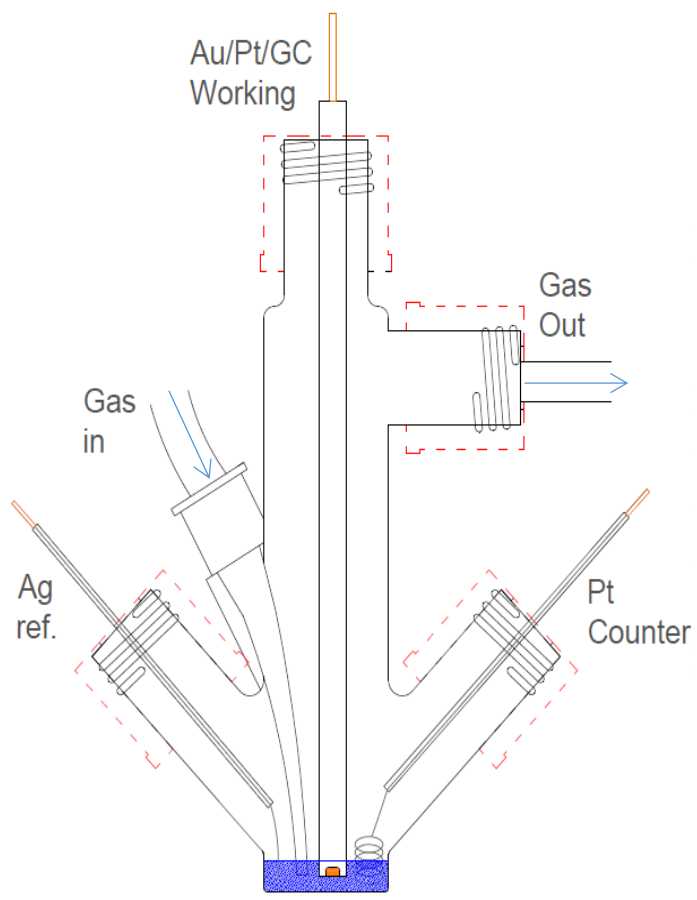
a**b**

Figure 2. 6. (a) Schematic of low volume IL cell design and **(b)** picture of assembled cell with electrodes in 0.5 ml liquid sample (inset bottom right).

EC-SERS cell

A modified low-volume spectroelectrochemical (SEC) cell was designed for SERS experiments. This was similar to the EC cell except with a 16 mm diameter open base, built in-house. A 2 mm thick spectroscopy grade sapphire window was sealed to the open base with ultra-high vacuum (UHV) rated chemically resistant adhesives by TMS Vacuum. Electrolyte samples (0.4-0.8 ml) were injected into the cell using a 1,000 μ l adjustable accurate pipette (Thermo Fischer). Electrodes were submerged in the electrolyte and arranged with the roughened Au (rAu) WE (roughening procedure below) positioned behind the sapphire window (Fig. 2. 8b). Cells were assembled inside of an Ar glovebox (< 0.1 ppm H₂O, < 20 ppm O₂) and after saturating the electrolyte with gas feed-streams (Ar or O₂) the cell was sealed off with caps to maintain the integrity of the cell's internal atmosphere. The SEC cell was then removed from the glovebox and clamped over the spectrometer and the laser focal point focused via a microscope on the rAu surface visually with a x50 objective.

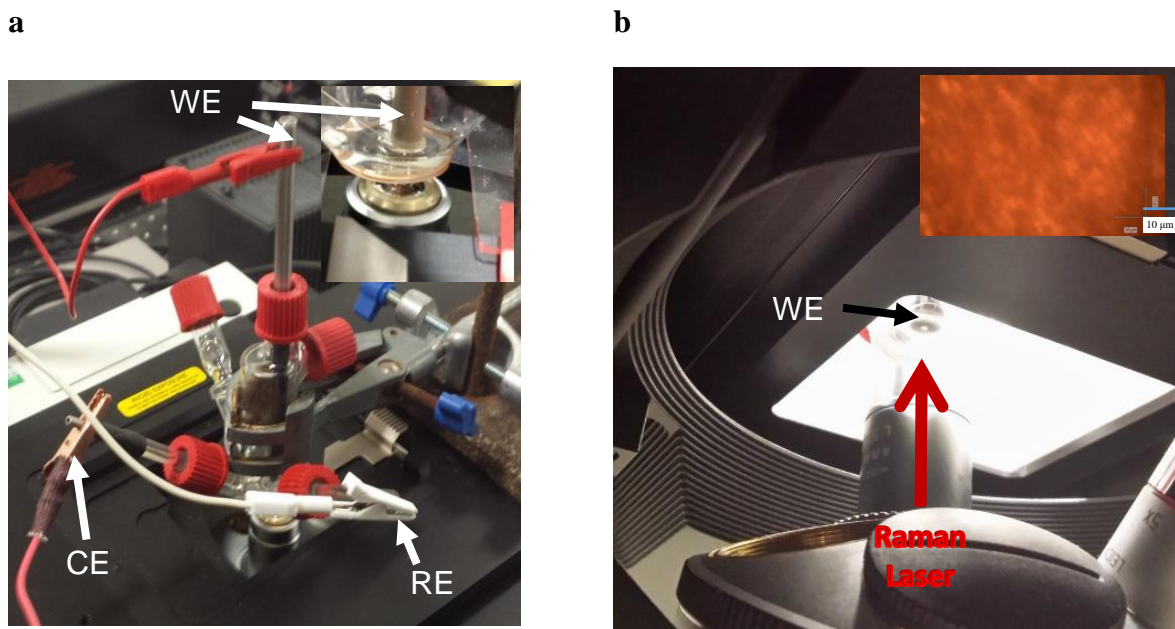


Figure 2. 7. (a) Low-volume SERS cell fully setup and clamped over spectrometer with rAu WE focused over Raman laser. (inset: close-up of WE) **(b)** Raman laser positioned directly underneath rAu WE with image of rAu surface taken from x50 microscope (10 μ m scale bar).

EC-SERS cell with temperature control

For temperature control experiments, an additional inlet in the cell was required for a thermocouple/thermometer. To accommodate this, a modified cone-shape cell was fabricated. A glass KF-16 glass flange (Allectra) was fused to the base of the cone cell and used in conjunction with a KF-16 sapphire window, o-ring and clamp (Allectra, UHV rated) to aid in removal and cleaning of the spectroscopic window and remove the need for chemical adhesives. High vacuum rated GL-14 fittings for electrodes with PTFE inners were also purchased from BOLA, which allowed cells to be hermetically sealed. Vacuum rated gas inlet/outlets were made using in-house modified Youngs taps. For gas bubbling, a PTFE tube extension was used to prevent the use of glass inlets prone to snapping.

For temperature control, heating tape (Omega, temperature range: < 760°C) and a thermocouple (TCDirect) were wrapped around the electrolyte reservoir, ensuring the WE remained visible through the spectral window. A mineral coated chemically resistant thermocouple (TCDirect) was placed inside of the cell. The heating tape and thermocouple were connected to a PID temperature controller (Stafford Instruments) and followed custom programmed settings. The cell's cone shape had the added benefit of removing the proximity of the plastic electrode fittings to the heating tape.

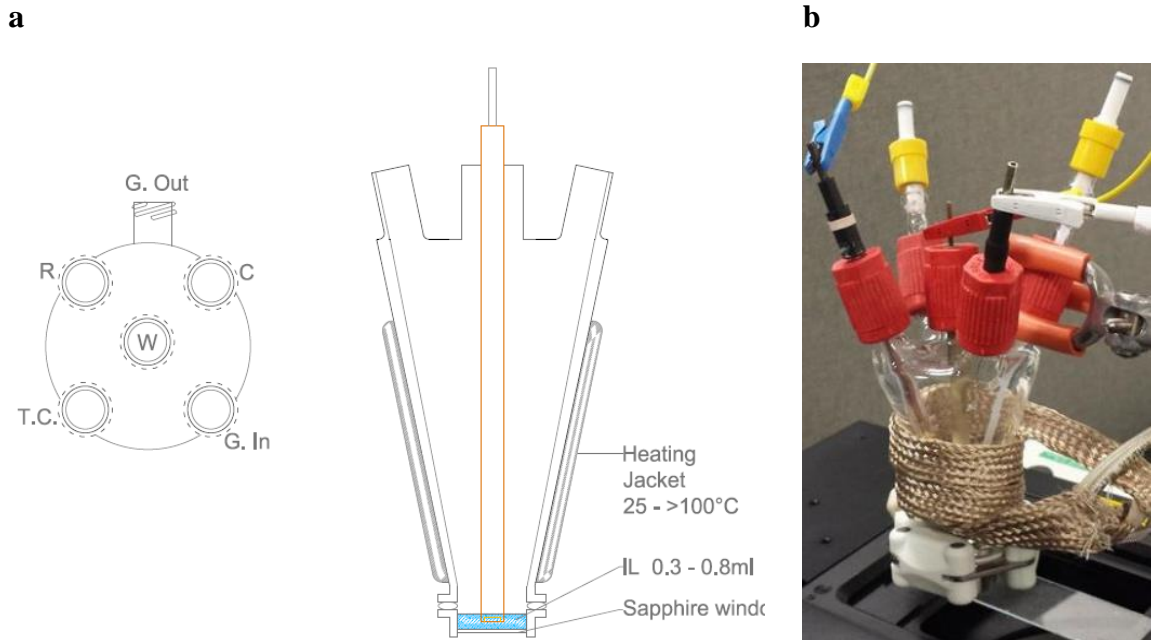


Figure 2.8. SERS cell design for temperature-control measurements accommodating 0.4-0.8 ml electrolyte volumes. **(a)** (left) Top view of cone with marked inlets going clockwise: G-Out, CE, G-In, thermocouple, RE and WE in the middle. (right) Profile view of cell with WE, electrolyte reservoir and heating jacket. **(b)** Photo of full temperature-controlled SEC cell setup on Raman spectrometer.

EC-SEIRAS cell

All in-house EC-SEIRAS cells were made from Teflon® or PEEK^{137,404} and purchased from AFT Fluorotec. These cells consisted of a hollow PEEK cup screwed to a PEEK base-plate on top of cylindrical 2 mm diameter 1.5 mm tall, ATR internal reflection elements (IRE) with two 60° cleaved faces (Fig. 2. 4a) in a Kretschmann configuration. Veemax® silicone (Si), zinc selenide (ZnSE), germanium (Ge) ATR-IRE crystal prisms were purchased from Kromatek and CsI ATR-IRE crystal prisms from Crystran. The IRE prism particularly its FT-IR transparency was investigated in more detail as described in chapter 6. Each IRE prism was polished thoroughly and cleaned with Milli-Q water before being carefully sonicated in ethanol and dried overnight in a vacuum oven before use.

The Au film WE were formed by depositing an initial 60±1 nm thick Au outer ring on the polished IRE surface via vapour deposition of Au (99.999 %) using a Leybold Univex 300 thermal evaporation system with the centre of the crystal shielded from deposition. A second 20±1 nm thick Au film was then deposited on the total surface to form the percolated interconnected Au island structure necessary for generating SEIRAS enhancements⁴³⁶ as described previously.⁴⁰⁴ The Au-coated IRE prism was then placed on a supporting plate which was screwed into the underside of the base-plate when the cell was fully assembling (Fig. 2. 10a). A Kalrez® chemically resistant o-ring was used to seal the cell and separate the crystal from the PEEK cell cup (Fig. 2. 10c). The thick outer Au ring was used to make a good electrical contact by pressing Au foil (placed underneath the o-ring) onto it, whilst spectra were collected from the thinner more transparent inner Au film region. The Au vapour deposition time and rates were calibrated by depositing Au on Si wafers and using AFM to measure the thickness at a step edges (Fig. 2. 11c) as described by Vivek *et al.*⁴⁰⁴ A PEEK top plate with 3 mm holes was used for hosting Ag RE and Pt-coil CE and 1/16" PEEK tubing (Sigma) which

had tapped G-In and G-Out valves tightened onto them and were sealed onto the plate using epoxy resin (Loctite 3431 A and B). An o-ring on the cell cup enabled a hermetic seal to be made by screwing the top plate onto it. The Pt-coil RE was flame annealed and any oxide layer on the Ag quasi-reference removed by scraping with a scalpel blade before use.

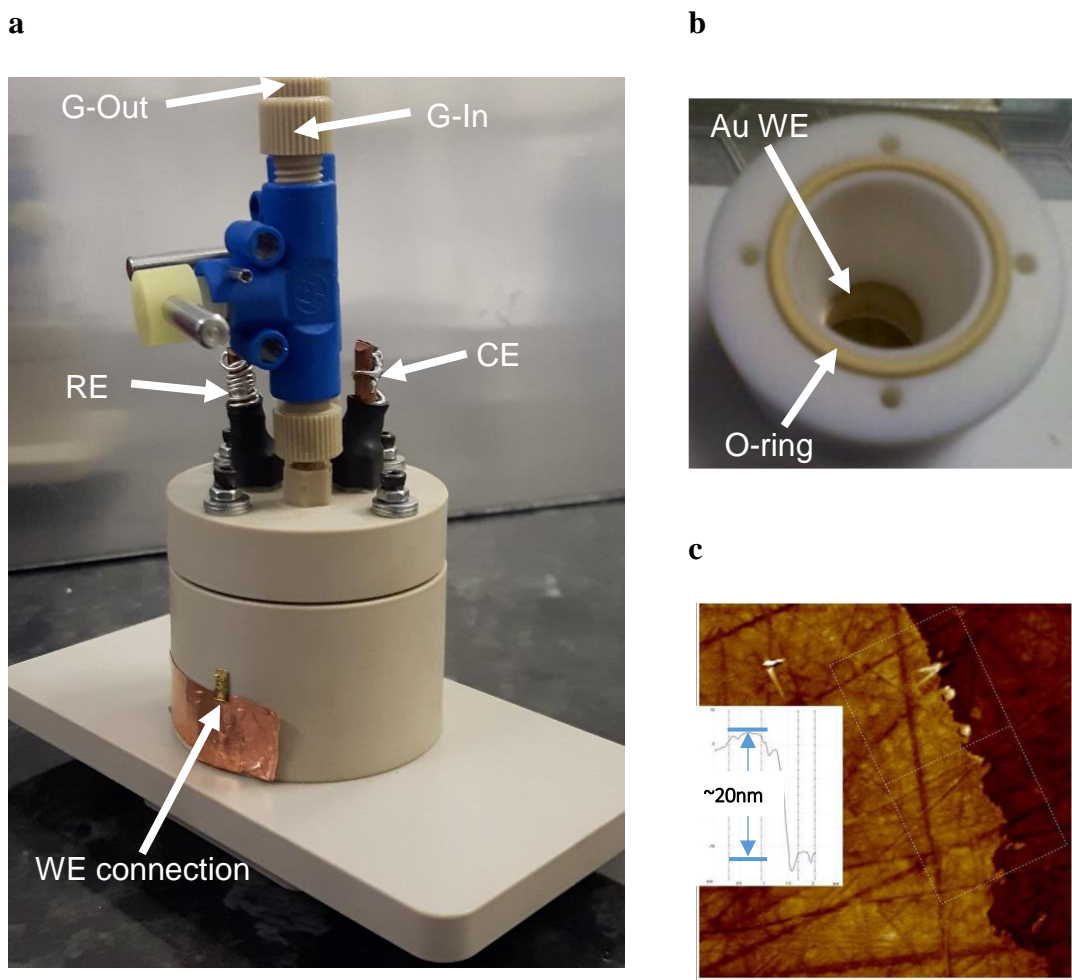


Figure 2.9. (a) Assembled low-volume (0.5-1 ml) SEIRAS cell with tapped G-In and G-Out and custom Ag RE, Pt-coil CE and Au foil WE connection attached to cell with copper tape. (b) Inside of cell showing Au film coated IRE, electrolyte reservoir space and O-ring. (c) AFM image of Au film surface structure on Si showing that the layer thickness at step edge is approximately 20 nm (inset).⁴⁰⁴ All Au films were deposited by G. Papageorgiou and AFM was provided by V. Padmanabhan.

EC flow-field cell

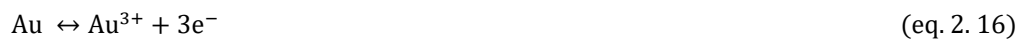
Custom flow-field cells designed and built by collaboration partners (Johnson Matthey) were used for non-aqueous Li-O₂ cells composed of a Li-metal anode, an electrolyte soaked (~75 µl) polypropylene membrane separator (Cellguard 2500 Microporous Monolayer Membrane) and carbon O₂-cathode, assembled inside an Ar atmosphere (< 0.1 ppm H₂O, < 0.1 ppm O₂) glovebox. A continuous controlled flow of ultra-pure (> 99.999%) O₂ gas was exposed to the O₂ cathode only and the cell allowed to rest for an hour before performing galvanostatic cycling (Maccor) measurements in a temperature controlled atmosphere (30°C). EIS measurements of the cell were taken before and after every cell charge and discharge cycle.

2.2.3 Coin-Cell Assembly

2025 type coin-cells were assembled in an Ar filled glove box (O_2 , $H_2O < 1\text{ppm}$) for Li-Li symmetrical cell cycling experiments. Two Li-metal electrodes (0.75 mm thickness x 16 mm diameter, Sigma) were used; one pressed to the stainless-steel casing and another to a stainless-steel spacer (0.5 mm thick). An electrolyte soaked (~85 μl) polypropylene membrane separator (Cellguard 2500 Microporous Monolayer Membrane) was used to separate the two Li-metal electrodes. A polypropylene o-ring gasket ensures a hermetic sealing. At least two coin-cells were tested for each different electrolyte formulation. Galvanostatic charge-discharge cycling (x100) measurements (MACCOR) were performed in a temperature-controlled environment (30°C) with low charge discharge rates: $\sim 0.012 \text{ mA cm}^{-2}$ to offset dendrite formation. Each charge-discharge cycle took two hours. EIS measurements were taken before, and after every 10 charge-discharge cycles for the first 50 cycles and then once at the end after cycling was complete to track any changes in cell impedance.

2.2.4 Electrochemical Au Electrode Roughening

Au WEs for *in situ* SERS experiments were roughened using an oxidation/reduction cycling procedure described previously by Tian *et al.*⁴⁴⁰ Consecutive CVs were performed in a 0.1 M aqueous KOH electrolyte to roughen the Au WE (Fig. 2. 10). Essentially, the Au surface is oxidised to Au³⁺ by sweeping the potential and briefly holding at positive values. The potential is then swept negative and held for a prolonged time until Au³⁺ is reduced back to Au (eq. 2. 16) and plated back on the surface (this has been completed when the current response returns to 0). Repeat cycling at different scan rates greatly increases the heterogeneity of the surface plating allowing topographically rough nanostructured (~50-200 nm) colloidal-like, SERS active, Au films to deposit and grow on the surface.⁴⁴¹



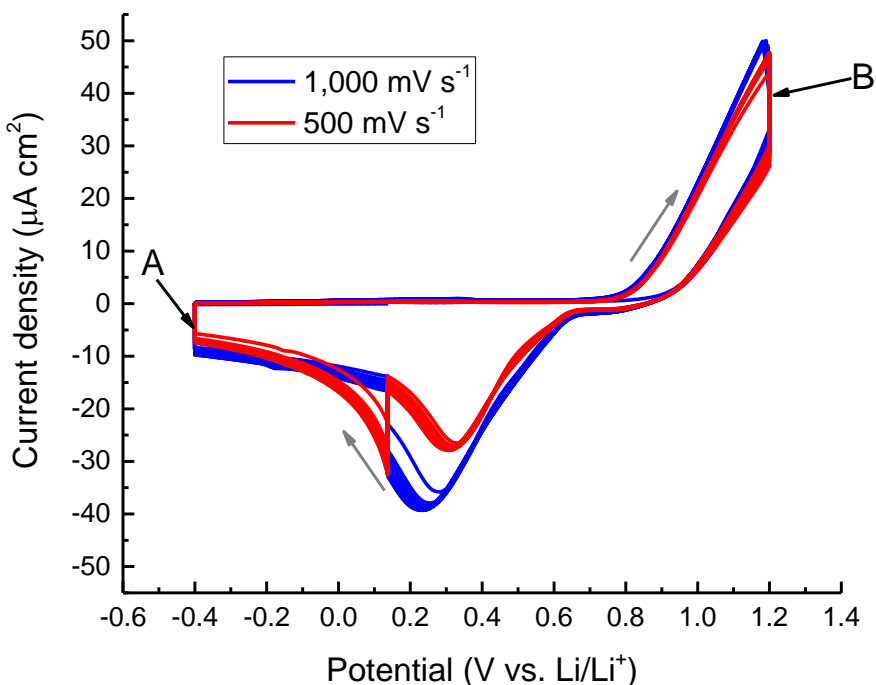
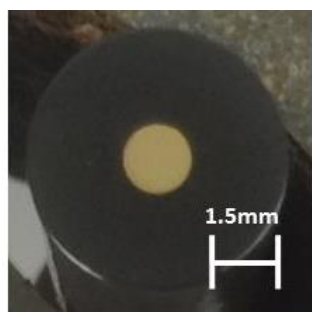
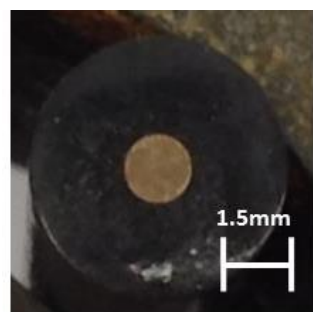
a**b****c**

Figure 2. 10. (a) Au WE roughening CVs in 0.1 M KOH with Pt-coil CE and AgCl/Ag aqueous RE. Potentials were first cycled in the negative direction from OCP and held at -0.4 V for 40 s (region A). Potentials were then cycled positive and briefly held at 1.2 V for 1.2 s (region B). No current response was observed on the first cycle until after the surface had been oxidised. The first scan at $1,000 \text{ mV s}^{-1}$ (blue line) was followed by a scan at 500 mV s^{-1} (red line). In this order, CVs were repeated 20 times at consecutively different scan rates. **(b)** Smooth Au WE before cycling **(c)** rAu WE after cycling, noticeably darker surface roughened film.

2.2.5 Reference Electrodes

Multiple different in-house-made reference electrodes were electrochemically standardised vs. a ferrocinium/ferrocene (Fc^+/Fc) redox couple in each electrolyte used.^{442,443} This was done by dissolving a small amount of Fc in the electrolyte solutions and then sweeping the potential until the Fc^+/Fc redox couple was found. Comparing the measured $E_{1/2}$ of the Fc redox peaks in the electrolyte being probed, with the known $E_{1/2}$ of Fc vs NHE (0.40 V) it was possible to find the associated shift for each reference electrode in each electrolyte.^{443,444} This enabled CV potentials to be referenced directly against Li^+/Li potentials. Due to ease of use, a Ag wire quasi-reference electrode was used primarily for CVs, however, Ag^+/Ag and novel Li^+/Li stable reference electrodes were also made and used.

Table 2. 1. Comparison of Fc redox potential shifts between different references electrodes in $\text{Pyr}_{14}\text{TFSI}$.

	Ag wire	Ag/Ag^+	Li/Li^+	Units
E_p^a	0.442	-0.385	3.416	V
E_p^c	0.344	-0.308	3.513	V
ΔE	98	78	97	mV
$E_{1/2}$	0.393	-0.346	3.464	V

2.2.6 Raman

A Renishaw inVia Raman spectrometer with 532, 633 and 785nm wavelength lasers and 1200 or 1800 1 mm^{-1} gratings calibrated against a silicon wafer reference was used. Spectra were recorded by WiRE 4.3 software. *In situ* SERS spectra were collected using a x50 objective with the 785 nm laser, unless specified otherwise. Two methods of collecting *in situ* SERS spectra were used, in brief:

1. Multiple quick spectra were collected in rapid succession during normal potential cycling with a dynamic WE surface potential.
2. Detailed full extended wavenumber spectra were collected whilst the WE surface was held under potential control.

The EDL can be assumed to be in flux during cycling and in equilibrium when under potential control. Comparing these two methods gave some insight into surface ordering and how surface speciation variation with potential and time can be obtained (see chapter 4).

Dynamic surface potential

The WE potential was cycled normally whilst spectra of the surface were collected in quick succession (every ~ 1.37 s). The inherently short laser exposure times can lead to high background noise; however, multiple spectra can be amassed in much smaller time frames than with normal scanning, allowing for detailed multi-dimensional contour plots (see chapter 4) to be generated when the data was imported into Origin 15. During rapid scanning, wavenumber ranges are automatically limited ($\sim 380\text{ cm}^{-1}$) by the machine to protect gratings from damage and misalignment. Therefore, probing multiple bands of interest that lie outside of the machine limits required independent scans to be taken over each respective spectral range. This technique was quick and useful for probing immediate changes in surface speciation, however, slight potential differentials at the surface during spectra acquisition means that the EDL will

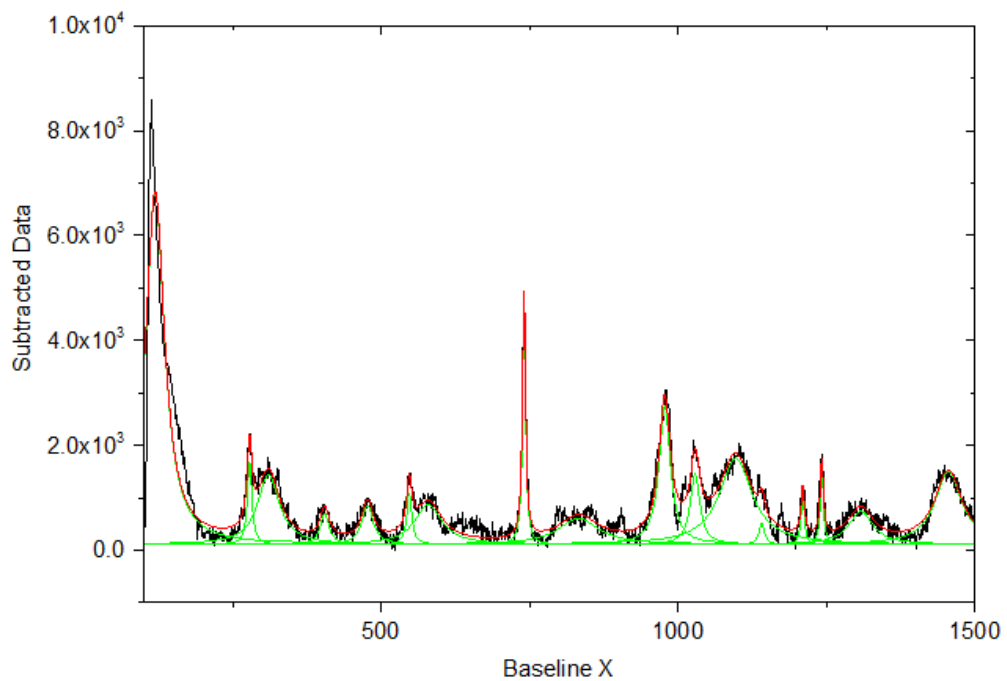
not be in equilibrium. Giving some qualitative insight into the kinetics of the surface chemical/redox processes. These effects could be minimised by slowing the scan rate.

Controlled surface potential

The potential was held during the collection of the surface spectrum (~5 minutes per spectrum). Holding the potential for a prolonged time allows for scanning over large wavenumber ranges, multiple acquisitions and for extended laser exposure times that significantly improve the signal-to-noise ratio (helpful in cases of weak enhancement). Once spectra were collected, the potential was cycled back to OCP and the process repeated at lower potentials on reduction and vice versa on oxidation.

2.2.7 Spectral Peak Fitting

To derive accurate SERS spectral data such as the peak height (intensity), the full width at half maximum (FWHM) and band position, it was necessary to accurately peak fit data. Necessary baselines were subtracted from the spectra and a Lorentzian fitting function was used in Origin Pro 15 to fit the spectral bands (Fig. 2. 11). This was done for all SERS spectra discussed herein.



Fitting Results

Peak Index	Peak Type	Area Intg	FWHM	Max Height	Center Grvty	Area Intg P
1.	Lorentz	297508.66922	38.16751	6700.27942	-	26.07435
2.	Lorentz	22527.73352	9.22566	1569.25626	-	1.97438
3.	Lorentz	89310.07428	44.59361	1327.1376	-	7.82734
4.	Lorentz	26735.87426	23.24351	742.01452	-	2.34319
5.	Lorentz	15480.09168	10.30099	961.72659	-	1.35671
6.	Lorentz	64616.80334	55.72744	758.80583	-	5.66317
7.	Lorentz	45608.94742	6.19152	4702.2013	-	3.99727
8.	Lorentz	62248.99072	82.1858	499.60718	-	5.45565
9.	Lorentz	94915.34593	23.05417	2647.6598	-	8.3186
10.	Lorentz	40932.3805	19.50233	1347.98482	-	3.58741
11.	Lorentz	166750.90453	66.50629	1648.26724	-	14.61444
12.	Lorentz	7052.9067	10.81317	417.48823	-	0.61813
13.	Lorentz	9978.62032	6.90303	923.77074	-	0.87455
14.	Lorentz	13951.45353	6.18376	1441.50229	-	1.22274
15.	Lorentz	47522.93251	49.72204	629.53232	-	4.16502
16.	Lorentz	110936.5836	54.5045	1385.99043	-	9.72274
17.	Lorentz	8696.7188	7.53351	790.19077	-	0.7622
18.	Lorentz	16226.17731	17.78473	587.69095	-	1.4221

Figure 2. 11. Example of Lorentzian peak fitted spectra from Origin 15. Example spectra taken of a rAu-WE surface in Pyr₁₄TFSI:TEGDME (60:40 vol. %) electrolyte held at -1.5 V vs Ag/Ag⁺.

2.2.8 Fourier Transform Infrared spectrometer (FT-IR)

For electrolyte characterisation, spectra were taken with a Nicolett is50 ATR FTIR spectrometer (Thermo Scientific) in an inert nitrogen glovebox. A droplet of the analyte was placed on a diamond window and recorded using OMNIC software (between 30s and 5 mins per spectrum).

For *in situ* SEIRAS measurements a Bruker IFS66v spectrometer equipped with MCT (mercury cadmium telluride; low frequency cut off ca. 550 cm⁻¹) was used. A detailed account of the machine setup has been reported previously.¹³⁷ P-polarized IR radiation was used and the angle of incidence was set at 65° in conjunction with 60° IRE planes. IR spectra were collected approximately every 30 s either when the electrode potential was being held (surface under potential control) or while the electrode potential was being varied (dynamic surface potential) at a relatively slow scan rate (10 mV s⁻¹). To distinguish subtle changes at the interface, *in situ* SEIRA spectra acquired at different potentials were compared with the spectrum at OCP using eq. 2. 17. Processing of multiple spectra was performed in Origin 15.

$$\Delta S/S = (S_{variable} - S_{OCP}) / S_{OCP} \quad (\text{eq. 2. 17})$$

Where: S_{OCP} = IR signal obtained at OCP, $S_{variable}$ = IR signal obtained at various potentials during potential cycling. Negative ΔS/S bands indicate an increase in absorbance compared to OCP and vice versa for positive bands.

2.2.9 Karl Fischer Coulometric Titration Procedure

To determine the H₂O content of an IL electrolyte (~0.5–1 ml) after drying, a sample was extracted from its container with a syringe and accurately weighed in grams to 4 significant figures (s.f.). The sample was then added to the EC cell in the automatic coulometric Karl Fischer titrator (Mettler-Toledo). After inputting the sample weight, the Hydralan reagent solution was stirred vigorously with a magnetic stirrer bar for ~15 seconds before outputting a value for the water content of the sample. The Titrator was routinely calibrated with a Hydralan standard of known water content of 100 ppm water and the reagent solution replaced approximately every 2 months.

2.3 Electrolytes

2.3.1 Ionic Liquids

ILs ($\text{Pyr}_{14}\text{TFSI}$, $\text{Pip}_{14}\text{TFSI}$, $\text{Aze}_{14}\text{TFSI}$, $\text{N}_{1444}\text{TFSI}$, $\text{Pyr}_{14}\text{HSO}_4$) where synthesised via reported methods¹⁸⁶ and kindly provided by Queens University Belfast or purchased from Sigma-Aldrich (TESTFSI), Solvionic (Pyrr₁₄DCA) or Iolitec (Pip₁₄OTf, N₁₈₈₈TFSI). Once received they were dried at either 100-130°C in a silicone oil or sand bath on a heater stirrer (Asynt) for 24 hours under UHV (10^{-6} pa) or for 72 hours under normal vacuum (10^{-3} pa) before being stored in an Ar ($\geq 99.998\%$) atmosphere glovebox. Water content was reduced to 1-6 ppm, measured using coulometric Karl Fischer titration, described previously.

ILs have an affinity for solvating contaminant ions and polar molecules via strong ion-ion and ion-dipole coulombic interactions, respectively. Common IL ionic impurities are alkali metal cations (Li^+ , Na^+ , K^+) and halogen anions (Cl^- , Br^-) left over from synthesis and often account for any visible IL discolouration. All ILs were purchased or received from collaborators and had the bulk of the ionic contaminates removed before arrival, however, washing multiple times (> 10) with an insoluble solvent (H_2O or Acetonitrile) was occasionally performed to further improve the ILs clarity, as even low (ppm) levels of Br^- can cause persistent brown discoloration. Polar impurities such as H_2O and CO_2 poison the electrode surface⁴⁴⁵ and are undesirable contaminates in non-aqueous $\text{Li}-\text{O}_2$ experimental systems. Therefore, as they readily absorb in ILs from the atmosphere, even in relatively hydrophobic ILs, it was important that the IL purity was optimised and maintained before and during experimentation. Most ILs have negligible vapour pressures due to strong interionic forces. As a result, ILs have extremely high vapour pressures allowing dissolved species and polar impurities to degas when exposing to high vacuums, whilst, stirring and heating speed-up this process.

IL drying apparatus

Due to persistent problems with low-level H₂O contaminants in ILs being detected electrochemically, a vacuum drying station was setup and apparatus designed to allow electrolyte samples to be stirred and heated whilst exposed to moderately high vacuum (10⁻³ Pa, Fig. 2. 12). Further UHV (10⁻⁶ Pa) drying apparatus were designed to refine the drying process by replacing the PTFE vacuum tap (denoted by 2 in Fig. 2. 12) with a glass KF-16 glass flange (Allectra) attached to an Edwards SP16K speed valve using quick release clamps and a KF-16 PTFE glass-to-metal O-ring. The Edwards SP16K speed valve was connected in series to an acetone/dry-ice cooled solvent trap and UHV pump system. All samples were stored in an Ar (\geq 99.998%) atmosphere glovebox before and after drying without being exposed to ambient atmosphere.

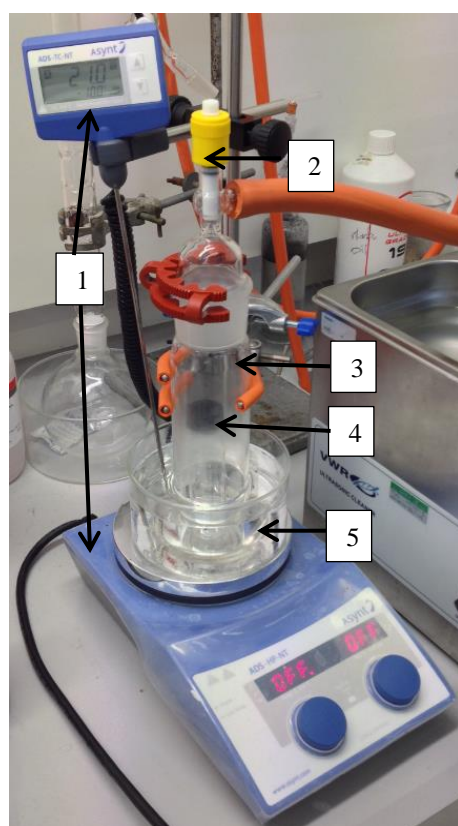


Figure 2. 12. Drying station setup. (1) Asynt temperature controller and hotplate-stirrer. (2) PTFE vacuum tap-vacuum pump connection. (3) Inhouse made glass vacuum dryer. (4) IL sample with untightened screw cap (5) Silicone-oil bath.

2.3.2 Solvent and Salts

High purity dimethyl sulfoxide (DMSO, \geq 99.8%), acetonitrile (MeCN, 99.5%), N-Methylpiperidine (m-Pip, 99%) were purchased from Sigma-Aldrich and dried over 4 \AA freshly activated molecular sieves for two weeks, H₂O contents were determined to be < 15 ppm via Karl Fischer titration. Alternatively, DMSO, MeCN and additional solvents DME and DEGDME were also bought in ultrapure form from ROMIL (4-30 ppm H₂O) and were transported over molecular sieves with septum caps. Solvents were extracted with disposable syringes inside an Ar glovebox to minimise contamination. H₂O concentrations from shipped documentation were verified with Karl Fischer titration. To further verify purity; FT-IR and Raman standards were taken of all solvents and compared with an in-house spectra database.

Salts N₂₂₂₂TFSI, N₃₃₃₃TFSI and N₄₄₄₄TFSI were kindly synthesised and provided by Queens University Belfast. Salts Pyr₁₄I, Pyr₁₄Cl, and Pip₁₄I were purchased from Iolitec at ~99% purity. All other salts: lithium bis(trifluoromethane) sulphonyl imide (LiTFSI, 99.5%), lithium nitrate (LiNO₃, 99.99%), Lithium trifluoromethanesulfonate (LiOTf), lithium perchlorate (LiClO₄, 99%), potassium nitrate (KNO₃, 99%), sodium nitrate (NaNO₃) were purchased from either Sigma Aldrich or Alfa Aesar depending on availability. Salts were dried at elevated temperatures (80-110°C) under vacuum (10^{-3} Pa) for three days and the water content in the salt determined by forming a 1 M solution in a solvent with a known water content and measuring the difference in the recorded coulometric Karl Fischer titration, generally < 10 ppm H₂O. For lithium iodide (LiI), lower drying temperatures (60°C) were necessary to prevent I₃ formation. Molecular sieves used for drying solvents required washing to minimise dust contamination of solvents by consecutively washing and heating the sieves with Milli-Q water and acetone until no more dust was visible. The molecular sieves were then reactivated by drying for 24 hours at 300°C in a sand bath and then transferred to the glovebox for use.

2.3.3 Drying of Gas Feed Streams

High purity O₂ (\geq 99.999%) and Ar (\geq 99.998%) purchased from BOC were dried by passing through multiple phosphorus pentoxide (P₄O₁₀) filled desiccant drying tubes before entering the Ar atmosphere glovebox through Swagelok gas-tight fittings. Gas streams were then connected to flow controllers (max. 0.5 ml min⁻¹) purchased from the M J Wilson Group. Semi-flexible HDPE tubing fitted with quick release valves compatible with (S)EC cells were connected to the cells from the flow controllers. A similar quick release valve fitted HDPE tube was connected to vent out to atmosphere which was used as a gas outlet. This allowed (S)EC cells to be connected to controlled flowrates of either O₂ or Ar gas feed streams inside a controlled Ar glovebox without compromising the glovebox atmosphere enabling optimal rigorously clean experimentation and storage of cell components. All S(EC) cells had a measured volume below 100 ml, thus, electrolytes were bubbled in excess for 10 mins. They were then allowed to rest for ~30 minutes before running EC experiments to ensure electrolytes were fully saturated with the bubbled gas.

3. Dioxygen

3.1 Introduction

Oxygen is a highly reactive and abundant element of immense chemical, biological, astrophysical and environmental importance, arguably warranting classification as a field of study in its own right similar to organic and inorganic chemistries.^{446,447} Gaseous O₂, composed of two covalently bonded homonuclear atoms, constitutes 20.95% of Earth's atmosphere providing an oxidising environment and thermodynamic driving force for many biological processes. However, living organisms must possess kinetic barriers to slow equilibration with O₂ in the environment to survive. On the one hand, it is the controlled use of O₂ to oxidise glucose during aerobic respiration (or the yet more oxidising CO₂ to oxidise H₂O during photosynthesis) that allows life on Earth to thrive. On the other hand, it is the gradual decay of these kinetic barriers to oxidation reactions in the body that is responsible for aging. In humans, reactive oxide species (O₂^{•-}, O₂²⁻, O²⁻, HO₂, H₂O₂, OH[•]) are produced as by-products of normal cell processes and are used in the immune response of white blood cells. However, their excessive production adds oxidative stress to cells causing DNA damage (specifically mitochondrial DNA) and mutation which are heavily linked to cancer.^{448,449}

Controlled oxidation of metals with environmental O₂ is the driving force in M-O₂ batteries and a successful system must deal with many of the same problems faced by biological systems such as slowing the reaction rate (corrosion) and production of radical oxides. Therefore, the chemistry of O₂^x (where x = -2, -1, 0, +1) species has warranted much detailed scientific study.^{446,447,450}

O₂^x species possess simple covalent O-O bonds with characteristic spectroscopically detectable stretching vibrations ($\nu_{\text{O-O}}$) that can be probed to determine their chemical natures. The chemical nature, oxidation state and reactivity of O₂^x depends on the number of electrons

occupying the $\pi^*(2p_{xy})$ valence antibonding orbitals (Fig. 3. 1), and their spin state(s). Dioxygenyl cations (O_2^+), have a bond order (B_o , defined as the number of covalent bonds, eq. 3. 1) of 2.5 and possess one electron in the $\pi^*(2p_x)$ antibonding orbital. Due to the positive charge on the O_2^+ cation, O-O bonding electrons experience a high effective nuclear charge, resulting in relatively short O-O bond lengths. The B_o in O_2^x decreases by 0.5 every time an electron is added into the $\pi^*(2p_{xy})$ orbital due to increased antibonding and mutual repulsion between bonding electrons, causing the O-O bond length to increase and visible red-shifts in the ν_{O-O} . Neutral O_2 contains two electrons in the $\pi^*(2p_{xy})$ orbital(s) that can occupy three different spin states (Fig. 3. 1); high energy singlet (${}^1\Sigma_g^+$), singlet (${}^1\Delta_g$) and triplet (${}^3\Sigma_g^-$). Unlike many common diatoms and organic molecules, which favour the ${}^1\Delta_g$ state, the ${}^3\Sigma_g^-$ state is the lowest energy ground state of O_2 with two electrons in degenerate orbitals with the same spin. The ${}^3\Sigma_g^-$ O_2 orbital structure complicates coupling with other molecules in the ${}^1\Delta_g$ state which adds to the chemical stability of ${}^3\Sigma_g^-$ O_2 .⁴⁴⁷

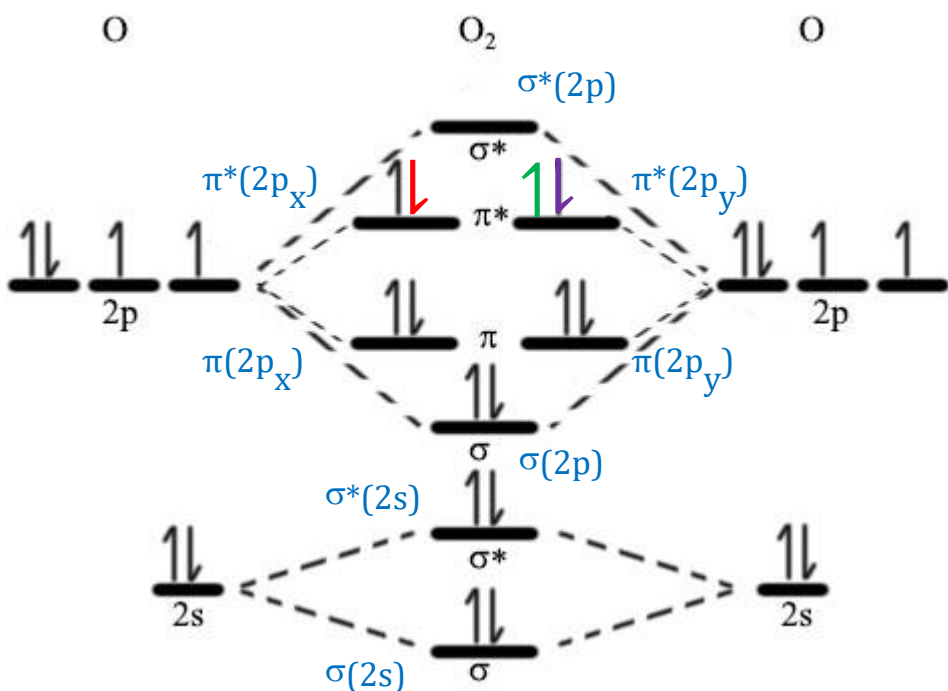


Figure 3. 1. Molecular orbital diagram of dioxygen species (O_2^x) based on filled $\pi^*(2p_{xy})$ valence orbitals: O_2^+ (black arrow only), high energy singlet (${}^1\Sigma_g^+$) O_2 (black and purple arrows only), singlet (${}^1\Delta_g$) O_2 (black and red arrows only), triplet (${}^3\Sigma_g^-$) O_2 (black, green arrows only), O_2^- (black, green, red arrows only) and O_2^{2-} (black, green, red, purple arrows). Figure partly reproduced from ref. ⁴⁵¹

It is the charge transfer induced transition from the $^3\Sigma_g^-$ O₂ to free radical superoxide (O₂^{•-}) and peroxide (O₂²⁻) and back again, that underpins the OR/ER mechanisms of non-aqueous M-O₂ batteries. In addition to bond lengthening, each electron transferred to O₂ causes a decrease in bond force constant, B_o, and a drop in the bond dissociation enthalpy (H) of the O-O bond producing characteristic red shifts in vo-o spectra. A brief description of some key bond parameters:

- Bond length (*l*) is the average distance between the nuclei of two bonded atoms in a molecule. Units: Å.
- Bond enthalpy (H) or bond-dissociation enthalpy, is a measure of the strength of a chemical bond. Defined as the energy required to cleave the bond under standard conditions (298 K). Units: kJ mol⁻¹.
- Bond force constant (k) proportionality constant in a harmonic oscillator, proportional to the square of the wavenumber of the bond vibration. Units: N m⁻¹ or mdyn Å⁻¹.
- Bond order (B_o) – the number of chemical bonds (electrons shared) between two atoms (eq. 3. 1). Units: dimensionless

$$B_o = \frac{(z - z^*)}{2} \quad (\text{eq. 3. 1})$$

Where B_o = bond order, z = number of bonding electrons, z^* = number of antibonding electrons.

In situ SERS studies of vo-o are extremely important for non-aqueous Li-O₂ batteries and have been used to prove the intermediary reaction mechanism and justify the existence of Li₂O₂ as the primary discharge product.^{4,74} Thus a detailed look at the vo-o spectra of species produced during OR/ER is required to probe the battery fundamentals.

3.2 Superoxide Raman Spectroscopy

3.2.1 Superoxide Meta-Analysis

Creighton *et al.* first reported the O₂^{•-} stretch, ν_{O-O}, with Raman spectroscopy for pure KO₂ and contaminated Na₂O₂ in 1964.⁴⁵² This was corroborated and expanded upon with the rest of the group 1 alkali-metal cations in MO₂ compounds (where M = Li, Na, K, Rb or Cs) in the following decade at a variety of different temperatures.^{453–460} The first stable organic cation-superoxide salt was synthesised and characterised spectroscopically by Sawyer in 1983 by substituting K⁺ with tetramethylammonium (TMA⁺). TMAO₂ had a spectrum analogous to previous MO₂ species, though slightly red shifted.⁷¹ Since then, the ν_{O-O} of many different O₂^{•-} complexes (C⁺...O₂^{•-}) have been detected in a variety of phases and systems, primarily as a solid salt,^{71,452} doped into other salts,⁴⁶¹ dissolved in organic solvents¹⁹⁰ or generated electrochemically at a SERS active electrode-electrolyte interface.^{4,70,74,462} See Table 3. 1 for a catalogue of some C⁺...O₂^{•-} complexes.

Raman band positions reflect molecular vibrational energy levels and are influenced by (1) the mass of the atoms in a bond, (2) the bond force constant and (3) lattice/symmetry effects. For O₂^{•-}, counter ions (or strongly coordinating solvents) attract bond electron density at different rates from the O-O bond, influencing the force constant of the vibration resulting in ν_{O-O} band shifts.⁴⁶³ When the O₂^{•-} interaction with counter-cations is weak, the electron cloud is concentrated on the anion and the effective nuclear charge experienced by valence electrons in the O-O bond is lower and the bond is longer than when it is strongly coordinated. This effect is visible by a lower ν_{O-O} bond vibration compared with a strongly coordinated O₂^{•-} complex. Plotting many of the reported ν_{O-O} values for C⁺...O₂^{•-} complexes with monovalent coordinating cations (independently of their phase) against the Mr of their respective

coordinating cation (Fig. 3. 1) shows a clear inverse correlation. Therefore, the immediate coordinating environments ability to interact with $\text{O}_2^{\cdot-}$ can dictate the spectral band position of a $\text{C}^+ \cdots \text{O}_2^{\cdot-}$ complex which provides interesting information about the reactivity and basicity of $\text{O}_2^{\cdot-}$ in the complex. From Figure 3. 2, $\text{C}^+ \cdots \text{O}_2^{\cdot-}$ complexes with heavy cations (e.g. TBA^+) have weak electrostatic interactions with $\text{O}_2^{\cdot-}$ and do not influence the O-O bond force constant much, due to their high charge-to-mass ratios (Mr z^{-1} values). Thus, they have low $\nu_{\text{O-O}}$ values indicative of a more ionic $\text{O}_2^{\cdot-}$ species. In these complexes, $\text{O}_2^{\cdot-}$ more readily donates electron density to its environment and is relatively more Lewis basic. Vice versa, well-coordinated $\text{O}_2^{\cdot-}$ complexes containing cations with low Mr z^{-1} values (e.g. H^+) can be expected to have more covalent-like C^+ -to- $\text{O}_2^{\cdot-}$ interactions, resulting in higher $\nu_{\text{O-O}}$ bands indicative of a weaker Lewis base $\text{O}_2^{\cdot-}$ complex. Two further sub-trends are apparent in Figure 3. 2 for; (1) single atom cations and (2) molecular cations. Single atom cations such as Rb^+ and Cs^+ have similar Mr z^{-1} values as TMA^+ and TEA^+ , respectively, but have higher frequency $\nu_{\text{O-O}}$ spectral bands ($> 15\text{cm}^{-1}$). This can be accounted for by considering the size difference in these cations. Single atom alkali-metal cations are smaller spatially (less bulky) allowing them to get closer and interact more with the $\text{O}_2^{\cdot-}$ electron cloud with more covalent-like interactions than the molecular organic cations which effects the O-O bond length.

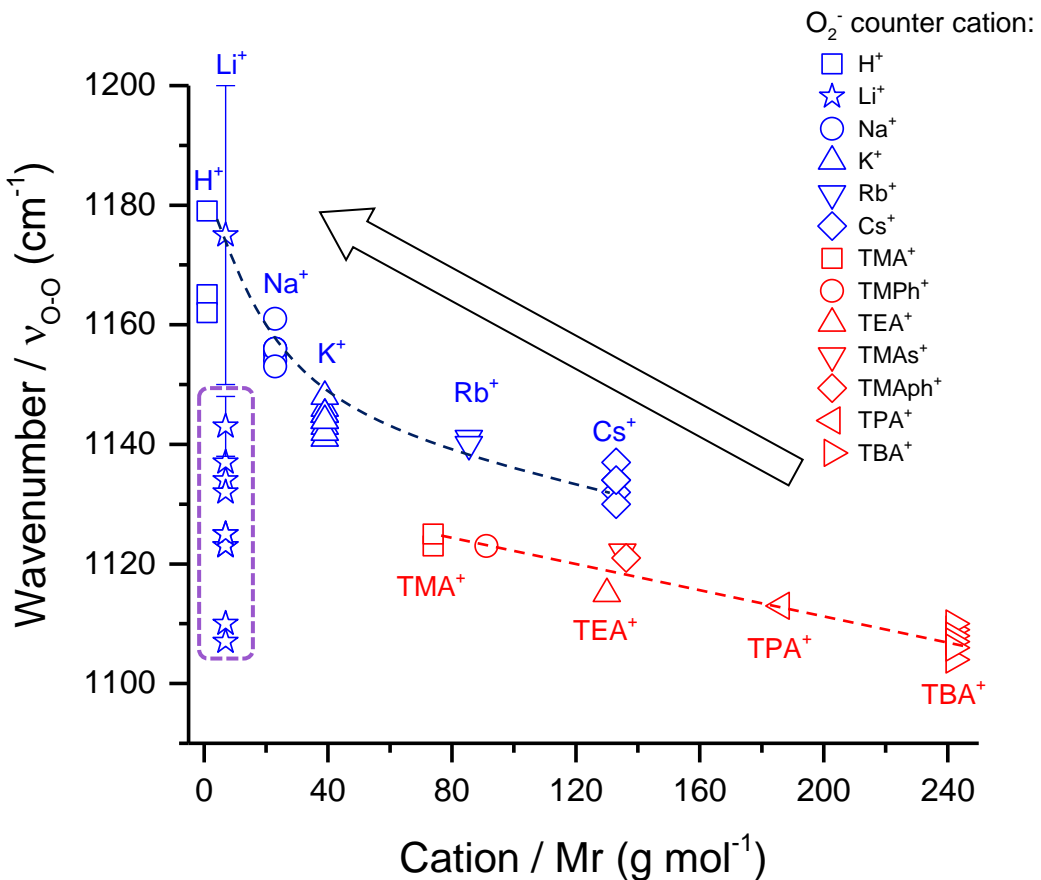


Figure 3. 2. $\nu_{\text{O}-\text{O}}$ Raman spectral peak positions for $\text{O}_2^{\cdot-}$ complexes from numerous reports plotted against the Mr of the coordinating cation, references listed in Table 3. 1. A general inverse relationship is visible with heavier coordinating-cations producing complexes with lower $\nu_{\text{O}-\text{O}}$ bands indicating a less energetic $\text{O}_2^{\cdot-}$ bond vibration and a ‘freer’ more Lewis basic species. A general fit produced an R^2 values of 0.757 for the overall trend. Two sub-trends are apparent; (1) single atom (blue) and (2) molecular (red) coordinating-cations. Lines of best fit for both trends (dashed lines) had R^2 values of 0.850 and 0.867 for single atom and molecular coordinating cations, respectively. Circled outlines (purple dashed line) are all reports of LiO_2 related species from the non-aqueous Li-O₂ battery literature. These do not match the expected trend for Li^+ and will be discussed in section 3.2.3. Error bar refers to broad band between 1,150-1,200 cm⁻¹ observed by Xia et al.¹⁵⁹

Considering the inverse relationship observed between v_{O-O} and the coordinating cation's size in a $C^+ \cdots O_2^-$ complex. The cation's size can be quantified by either the ionic volume (i_v) or the available ionic surface area (i_{sa}) measured in \AA^3 and \AA^2 , respectively. These values are well known for most simple ions, like the alkali metal cations, whilst more complex molecular cations can be calculated computationally using CPK or DFT models. Factoring for both the $Mr z^{-1}$ and a spatial component (i.e. i_v) of the coordinating cation gives a much stronger correlation when compared to the reported v_{O-O} values (Fig. 3. 2). Therefore, the cations influence on the v_{O-O} of a $C^+ \cdots O_2^-$ complex is proportional to its charge and inversely proportional to its mass and ionic size (eq. 3. 2). Assuming a uniform charge distribution over the ion; multiplying the mass, charge and spatial components of the cation accordingly ($i_v Mr z^{-1}$) gives a variable, hereon named the 'ionic charge dispersion' (\mathbb{K}), with which it is possible to roughly quantify the cation's influence over the O_2^- anion's bond force constant and v_{O-O} . \mathbb{K} is an analogue of the charge density of an ion ($Mr z^{-1} i_v^{-1}$) however, charge density does not account for the proportional relationship between the ion's Mr and i_v values and their effect on the ions overall columbic attractive strength.

Excluding outliers, plotting the reported v_{O-O} values against the calculated \mathbb{K}_{iv}^c or \mathbb{K}_{isa}^c of each coordinating cation shows an inverse exponential relationship (Fig. 3. 3a and c, respectively) which produces a much better correlation than using the coordinating cation's Mr or i_v alone. The spatial components i_{sa} and i_v are used to calculate \mathbb{K} but it appears to be unimportant which, as they both generally change proportionally with one another between different cations. However, i_v gives a slightly better fit with a higher R^2 value of 0.952 (surprisingly good given the larger number of independent reports using different phases, systems and detection equipment spanning over > 50 years) compared with 0.942 using i_{sa} . Plotting on a logarithmic scale (Fig. 3. 3b and d) shows this correlation more clearly. Hydrogen superoxide (HO_2) has

the highest reported ν_{O-O} and $O_2^{\cdot-}$ can be considered more covalent-like in character, whereas, tetrabutylammonium superoxide ($TBAO_2$) has the lowest and can be considered to contain ionic dissociated ions. Thus, when detecting the ν_{O-O} of $O_2^{\cdot-}$, the derived equation for the line of best-fit (eq. 3. 3) can be used to help estimate its ionic character and the coordination strength of the environment in terms of \mathbb{K}_{iv}^c . With this knowledge, $O_2^{\cdot-}$ has the potential to be used as a diagnostic molecule to probe electrolyte interactions spectroscopically. This relationship between ν_{O-O} and \mathbb{K}_{iv}^c (Fig. 3. 4) was found to hold in most cases. However, it can be manipulated by changing the symmetry, steric hinderance and charge of the cation as well as the solvent AN/DN and the potential at an electrode surface, where $O_2^{\cdot-}$ is generated electrochemically (discussed in the following chapters).

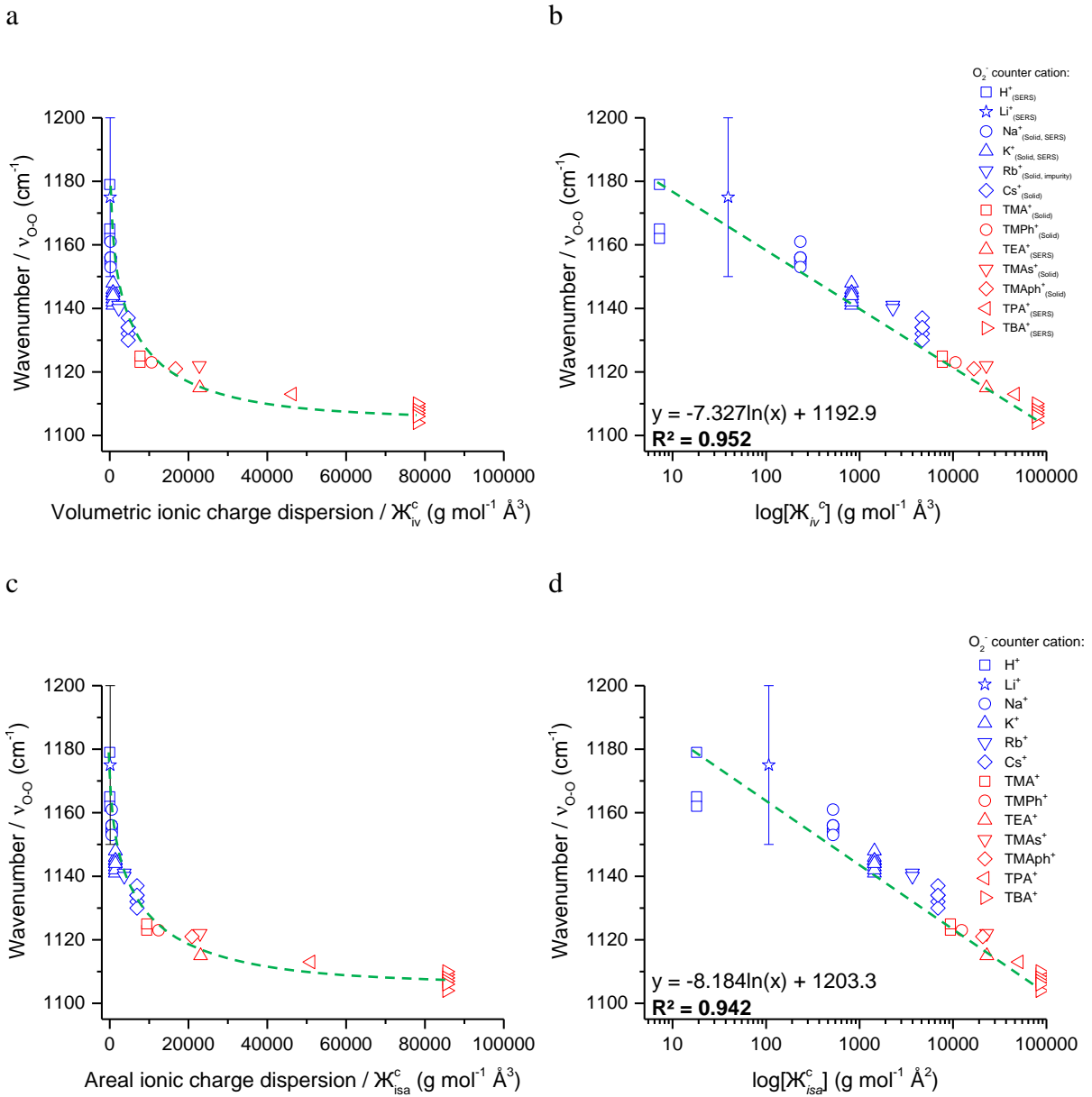


Figure 3.3. **(a)** Reported $\nu_{\text{O-O}}$ spectral bands (listed in Table 3. 1) plotted against \mathbb{K}_{iv}^c of the coordinating cation. **(b)** Log₁₀ plot of \mathbb{K}_{iv}^c with line of best fit (green dashed line) and empirically derived equation in bottom left-hand corner ($R^2 = 0.952$) derived in Origin Pro 15. **(c)** Reported $\nu_{\text{O-O}}$ spectral bands plotted against \mathbb{K}_{isa}^c of the coordinating cation. **(d)** Log₁₀ plot of \mathbb{K}_{isa}^c , with line of best fit ($R^2 = 0.942$) and derived equation. \mathbb{K}^c calculated using i_v gives a slightly better approximation than i_{sa} . Cation i_v and i_{sa} values were generated in Spartan 15 using a CPK model for single atom cations (blue) and DFT (B3LYP, 6-31G*) for molecular

cations (red). Only one reference reporting LiO₂ has been considered due to the ambiguity in the composition in the rest of reports. It has been long believed that LiO₂ was both thermodynamically and kinetically unstable.^{54,74–79} There have been many recent Raman studies reporting the observation of LiO₂, though they may also be other species.^{39,84,85} Due to the strength of Li⁺ as a coordinator, a pure LiO₂ species generated at room temperature would be expected to have a high ν_{O-O} shift (> 1167 cm⁻¹) similar to the broad band reported by Xia *et al.* centred at 1175 cm⁻¹.¹⁵⁹

$$\nu_{O-O} \propto \frac{Mr}{z}, i_v, i_{sa} \quad (\text{eq. 3.2})$$

$$\nu_{O-O} = -7.327 \log[X^c_{iv}] + 1192.9 \quad (\text{eq. 3.3})$$

where: ν_{O-O} = O₂^{•-} stretch (cm⁻¹), Mr = molecular mass of coordinating cation, z = charge on ion, i_v = ionic volume (Å³).

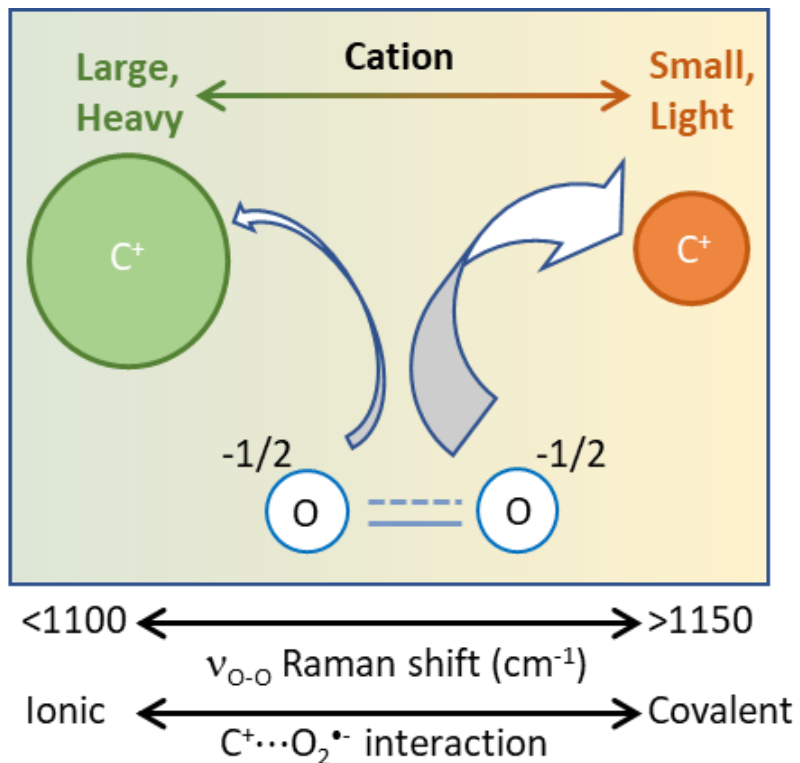


Figure 3. 4. Schematic depicting the relationship between cation interactions with $\text{O}_2^{\bullet-}$ and the effect this has on $\nu_{\text{O-O}}$ Raman peak position in each respective system due to changes in force constant of the O-O bond vibration. Arrow sizes represent the strength and the nature of the interaction with coordinating cations i.e. small, light ions have concentrated charges with stronger electrostatic forces of attraction with $\text{O}_2^{\bullet-}$ and may even be able to abstract electron density producing a covalent-like interaction, whilst the reverse is true for charge dispersed ions.

Table 3. 1. $\nu_{\text{O-O}^-}$ Raman spectral bands for $\text{C}^+ \cdots \text{O}_2^{*-}$ complexes with monovalent cation reported in the literature. Mr values, system information and calculated i_v and \mathbb{K}_{iv}^c values of the cation are shown.

Mr	$\nu_{\text{O-O}^-}$ (cm ⁻¹)	$\nu_{\text{O-O other}}$ (cm ⁻¹)	i_v (Å ³)	\mathbb{K}_{iv}^c	$\text{C}^+ \cdots \text{O}_2^{*-}$ salt/electrolyte	Cathode	Ref.
Cation: H ⁺							
1	1,165*		7.2	7.2	0.1M HClO _{4(aq.-acidic)}	rAu [†]	63
1	1,162*		7.2	7.2	0.1M HClO _{4(aq.-acidic)} + 0.5 mM Bi ³⁺	rAu [†]	63
1		1,147	7.2	7.2	H ₂ O (+ NaOH, pH 10)	PEI [#]	464
1	*	1,150 _(NaO2)	7.2	7.2	0.1M NaOH _(aq.-basic)	rAu [†]	296
1	*	1,135 _(Na2O2.H2O)	7.2	7.2	0.1 M NaOH _(aq.-basic) + 10mM H ₂ O ₂	rAu [†]	296
1	1,179		7.2	7.2	0.1 M TBAClO ₄ /DMSO	GC [‡]	462
1	1,182		7.2	7.2	Pyr ₁₄ TFSI (leaking cell)	rAu [†]	ex.
Cation: Li ⁺							
7	1,137		5.6	39.3	0.1 M LiClO ₄ /MeCN	rAu [†]	74
7	1,125	1,500 _(vC-0)	5.6	39.3	0.5 M LiClO ₄ /DMSO	GC [‡]	462
7	1,128	1,500	5.6	39.3	0.5 M LiClO ₄ /MeCN	GC [‡]	462
7	1,130	1,543 _(vC-0)	5.6	39.3	0.5 M LiClO ₄ /DMSO	SP/PTFE (1.9 V) [‡]	465
7	1,098	1,490 _(vC-0)	5.6	39.3	0.5 M LiClO ₄ /DMSO	SP/PTFE (3.1 V) [‡]	465
7	1,134		5.6	39.3	0.1 M TBAOTf:0.1 M LiOTf/DMSO	rAu [†]	466
7	1,132		5.6	39.3	0.1 M LiClO ₄ /MeCN	rAu [†]	4
7	1,110		5.6	39.3	0.1 M LiClO ₄ /DMSO	rAu [†]	4,38
7		1160	5.6	39.3	0.1 M LiClO ₄ /DMSO/ Complexing-agent	rAu [†]	38
7	~1,143		5.6	39.3	0.1 M LiClO ₄ /DMSO	Au-Ni foam [†]	467
7	1,107		5.6	39.3	0.01 M LiTFSI/Pyr ₁₄ TFSI	NS Au [†]	134
7	1,110		5.6	39.3	0.01 LiTFSI/EmimTFSI	NS Au [†]	134
7	~1,175		5.6	39.3	0.5 M LiOTf/DEGME	KB/ PTFE [#]	159
7	1,123		5.6	39.3	1.0 M LiOTf/TEGDME	AC/ PVDF [#]	468
7	1,123	1,505 _(vC-0)	5.6	39.3	1.0 M LiOTf/TEGDME	AC/ PVDF [#]	469
7	1,123	1,505 _(vC-0)	5.6	39.3	1.0 M LiOTf/TEGDME	AC/ PVDF [#]	470
7	1,123	1,500 _(vC-0)	5.6	39.3	1.0 M LiOTf/TEGDME	AC/ PVDF [#]	204

Mr	ν_{O-O^-}	ν_{O-O} other	i_v	\mathbb{K}_{iv}^c	$C^{+}\cdots O_2\cdots$ salt/electrolyte	Cathode	Ref.
	(cm ⁻¹)	(cm ⁻¹)		(Å ³)			
7	1,125	1,500 _(vC-O)	5.6	39.3	1.0 M LiOTf/TEGDME	Ir-rGO/ PVDF#	83
7	1,125	1,525 _(vC-O)	5.6	39.3	Unspecified	C/ PVDF#	39
7	1,123		5.6	39.3	0.1 M LiClO ₄ /TEGDME	RuCNT/PVDF#	340
7	1,128	1525 _(vC-O)	5.6	39.3	0.7 M LiTFSI/TEGDME	Super P/ PVDF#	ex.
Cation: Na ⁺							
23	1,156		10.1	233	NaO ₂ salt	#	456
23	1,156		10.1	233	NaO ₂ salt (300-200 K)	#	454
23		1,164 _(80 K)	10.1	233	NaO ₂ salt (80 K)	#	454
23	1,156	1,107, 488 _(vAu-O) ,	10.1	233	0.1 M NaOTf/DMSO	rAu [†]	37
23	1,161	1,119	10.1	233	0.1 M NaOTf/DMA	rAu [†]	37
23		1,109	10.1	233	0.1 M NaOTf/DEGDME	rAu [†]	37
23		1,108	10.1	233	0.1 M NaOTf/MeCN	rAu [†]	37
23	1,156		10.1	233	0.5 M NaOTf/DEGDME	GDL#	2
23	1,155		10.1	233	0.5 M NaOTf/DEGDME	CP#	471
23		1,135 _(Na2O2.H2O)	10.1	233	0.5 M NaOTf/DEGDME	CP#	471
23	1,154		10.1	233	NaOTf/PC:Pip ₁₃ TFSI: TEGDME	VACNT#	472
23	1,156		10.1	233	0.1 M NaClO ₄ /DME	CNT#	79
23		1,136 _(Na2O2.H2O)	10.1	233	0.1 M NaClO ₄ /DME +air	CNT#	79
23	1,153		10.1	233	1 M NaClO ₄ /DME	P50 C#	473
23	1,156		10.1	233	0.5 M NaOTf/DEGDME	KB/ PTFE#	474
23		1,136 _(Na2O2.H2O)	10.1	233	0.5 M NaOTf/DEGDME	KB/ PTFE#	474
23		1,142 _(Na2O2.H2O)	10.1	233	N ₂ O ₂ salt impurity	#	452
23		1,141 _(Na2O2.H2O)	10.1	233	N ₂ O ₂ salt impurity	#	453
23		1,136 _(Na2O2.H2O)	10.1	233	N ₂ O ₂ salt impurity	#	457
Cation: K ⁺							
39	1,143		21.1	824	KO ₂ salt	#	475
39		1,163 _(HO2?)	21.1	824	impurity in KO ₂	#	475
39	1,141		21.1	824	KO ₂ salt (300 K)	#	454
39	~1,145		21.1	824	KO ₂ salt (200-80 K)	#	454
39	1,146		21.1	824	KO ₂ salt	#	455
39	1,148		21.1	824	K ₂ O ₂ impurity	#	457
39	1,145		21.1	824	KO ₂ salt	#	71
39	1,145		21.1	824	KO ₂ salt	#	452
39	1,142		21.1	824	0.5 M KPF ₆ /DME	SP-Ni foam#	3

Mr	ν_{O-O^-} (cm ⁻¹)	ν_{O-O} other (cm ⁻¹)	i _v (Å ³)	\mathbb{K}_{iv}^c	C ⁺ ...O ₂ ^{..-} salt/electrolyte	Cathode	Ref.
39	1,144		21.1	824	KO ₂ salt	#	ex.
Cation: TMA ⁺							
74	1,123		104.1	7,700	TMAO ₂ salt	#	71
74	1,125		104.1	7,700	TMAO ₂ salt	#	476
Rb ⁺							
85.5	1,141		26.6	2,273	Rb ₂ O ₂ salt	#	457
85.5		1,124	26.6	2,273	Rb ₂ O ₂ impurity	#	457
85.5	1,140		26.6	2,273	RbO ₂ salt (75-300 K)	#	454
85.5	1,140		26.6	2,273	RbO ₂ salt	#	455
Cation: TMPh ⁺							
91.1	1,123		117.3	10,660	TMPhO ₂ salt	#	476
Cation: TEA ⁺							
130	1,115		175.7	22,846	0.1M TBAOTf/MeCN	rAu [†]	70
Cation: Cs ⁺							
133	1,132		35.2	4,682	CsO ₂ salt	#	475
133	1,134		35.2	4,682	CsO ₂ salt	#	477
133	1,130		35.2	4,682	0.1 M CsClO ₄ /DMSO	rAu [†]	466
133	1,137		35.2	4,682	CsO ₂ salt (80-300 K)	#	454
133	1,134		35.2	4,682	CsO ₂ salt	#	478
Cation: TMAs ⁺							
135.1	1,122		168.5	22,751	TMAsO ₂ salt	#	478
Cation: TMAp ⁺							
136.2	1,121		122.8	16,725	TMAph salt	#	479
Cation: TPA ⁺							
186.4	1,113		248.9	46,329	0.1 M TBAOTf/ MeCN	rAu [†]	70
Cation: TBA ⁺							
242	1,109	491 _(vAu-0)	322.5	78,038	0.1 M TBAClO ₄ / MeCN	rAu [†]	74
242	1,110	486 _(vAu-0)	322.5	78,038	0.1 M TBAClO ₄ / DMSO	rAu [†]	218

Mr	ν_{O-O^-} (cm ⁻¹)	ν_{O-O} other (cm ⁻¹)	i _v (Å ³)	\mathbb{K}_{iv}^c	C ⁺ ...O ₂ ^{..-} salt/electrolyte	Cathode	Ref.
242	1,110		322.5	78,038	0.1 M TBAClO ₄ / DMSO	rAu [†]	4
242	1,110	490 _(vAu-O)	322.5	78,038	0.1 M TBAClO ₄ / DMSO	rAu [‡]	462
242	1,110	490 _(vAu-O)	322.5	78,038	0.1 M TBAClO ₄ / DMSO	Au [‡]	462
242	1,108	456-484 _(vAu-O)	322.5	78,038	0.1 M TBAClO ₄ / DMSO	Pt [‡]	462
242	1,108	486 _(vAu-O)	322.5	78,038	0.1 M TBAClO ₄ / DMSO	Pd [‡]	462
242	~1,115	~1,520 _(vC-O)	322.5	78,038	0.1 M TBAClO ₄ / DMSO	GC [‡]	462
242	1,106		322.5	78,038	0.1 M TBAOTf/ DMSO	rAu [†]	70
242	1,106		322.5	78,038	0.1 M TBAOTf/ DMSO	rAu [†]	ex.
242	1,104		322.5	78,038	0.1 M TBAOTf/ MeCN	rAu [†]	70
242		1,131 _(NH₃ impurity)	322.5	78,038	TBAO ₂ salt	#	479

[†] denotes *in situ* SERS studies at the electrode interface. [‡] denotes *in situ* shell isolated nanoparticle enhanced

Raman spectroscopic (SHINERS) studies at the electrode interface. # denotes *ex situ* Raman measurements. ex.

denotes spectral bands observed experimentally.

Ionic charge dispersion of other ions

The \mathbb{K} value estimates the dispersion of a formal charge across an ion by assuming the charge is delocalised (i.e. dispersed uniformly across its i_v and i_{sa}). \mathbb{K} is a simple value that can be calculated for any ion to give an approximation of its coordination strength and/or propensity to interact with oppositely charged ions. Small \mathbb{K} values indicate ions that are relatively strong coordinators or hard Lewis acid/bases whilst large values represent weak, soft, ones. Tables 3.2 and 3.3 list calculated \mathbb{K} values for some common salt/IL cations and anions, respectively. The \mathbb{K} value is a clear simplification of the ion's charge, excluding many important contributions to inter-ion interactions such as charge distributions, steric hindrance and symmetry. However as discussed previously, \mathbb{K}^c values give a surprisingly good approximation of the cation's influence on the $O_2^{+}\text{-O-O}$ bond vibration and is likely applicable to other systems, too. Furthermore, additional quantifiable values for other ion properties could be added to refine the \mathbb{K} value further (see Future Work and Conclusions chapter). \mathbb{K} values (and possibly $\mathbb{K}^c:\mathbb{K}^a$ ratios) can also be used to quickly screen some of the near infinite number of ion combinations that can be selected for ILs, giving a quick and cheap starting point when designing and tailoring a novel IL electrolyte or salt additive (see chapter 5) compared with more precise computational or experimental techniques which are expensive, time consuming and would necessarily come later after first narrowing the field of search.

Table 3. 2. Table of calculated i_v , i_{sa} and \mathbb{K}_{iv}^c , \mathbb{K}_{isa}^c values for common cations and IL cations.Cations with smaller \mathbb{K} values are expected to be stronger Lewis acids.

Cation	Mr (g mol ⁻¹)	i_v (Å ³)	i_{sa} (Å ²)	n	\mathbb{K}_{iv}^c (g mol ⁻¹ Å ³)	\mathbb{K}_{isa}^c (g mol ⁻¹ Å ²)
H ⁺	1.0	7.2	18.1	1	7.2	18.1
Li ⁺	6.9	5.6	10.2	1	38.9	70.5
Na ⁺	23.0	10.1	19.3	1	233	443
K ⁺	39.1	21.1	37.0	1	827	1,446
Ca ²⁺	40.1	15.0	29.4	2	301	589
Bi ³⁺	209.0	31.85	48.60	3	2,219	3,386
Rb ⁺	85.5	26.6	43.1	1	2,272	3,681
Cs ⁺	132.9	35.2	51.9	1	4,678	6,903
TMA ⁺	74.1	105.2	128.4	1	7,799	9,523
TMP ⁺	91.1	115.2	141.8	1	10,497	12,923
TES ⁺	119.3	148.5	109.8	1	17,704	13,093
TEA ⁺	130.3	195.4	177.5	1	25,451	23,115
TMA _{As} ⁺	135.1	122.8	153.2	1	16,584	20,696
TMAph ⁺	136.2	170.2	186.4	1	23,179	25,390
Pyr ₁₄ ⁺	142.3	183.2	129.4	1	26,060	18,408
Pip ₁₄ ⁺	156.3	203.6	134.2	1	31,826	20,967
Aze ₁₄ ⁺	170.3	216.8	139.6	1	36,929	23,775
TPA ⁺	186.4	250.4	273.8	1	46,662	51,030
Di-Im ²⁺	296.4	358.0	338.4	2	53,062	50,154
N ₁₄₄₄ ⁺	200.4	266.9	175.3	1	53,492	35,118
TBA ⁺	242.5	324.0	355.0	1	78,566	86,065
N ₁₈₈₈ ⁺	368.7	489.0	540.1	1	180,316	199,128

Table 3. 3. Table of calculated i_v , i_{sa} , \mathbb{K}_{iv}^a , \mathbb{K}_{isa}^a values for common anions and IL anions.

Anions with smaller charge dispersions are expected to be stronger Lewis bases.

Anion	Mr (g mol ⁻¹)	i_v (Å ³)	i_{sa} (Å ²)	n	\mathbb{K}_{iv}^c (g mol ⁻¹ Å ³)	\mathbb{K}_{isa}^c (g mol ⁻¹ Å ²)
O ²⁻	16.0	14.7	29.0	2	118	232
F ⁻	19.0	14.5	28.8	1	276	547
OH ⁻	17.0	17.1	32.8	1	291	558
O ₂ ²⁻	32.0	25.1	44.1	2	402	705
O ₂ ^{•-}	32.0	23.1	40.7	1	738	1,302
Cl ⁻	35.5	23.7	39.9	1	840	1,415
Br ⁻	79.9	28.0	44.7	1	2,239	3,569
NO ₃ ⁻	62.0	41.2	61.6	1	2,552	3,817
SO ₄ ²⁻	96.1	55.0	73.7	2	2,642	3,538
I ⁻	126.9	34.8	51.5	1	4,414	6,539
DiCN ⁻	66.0	65.0	88.7	1	4,295	5,859
ClO ₄ ⁻	99.4	54.1	70.2	1	5,384	6,981
OTf ⁻	149.1	83.6	81.4	1	12,455	12,127
TFSI ⁻	280.1	153.5	115.2	1	43,014	32,262

3.2.2 Other Superoxide Spectral Trends

Several reports of vo-o spectral bands for different $C^+ \cdots O_2^\cdot-$ complexes that show interesting trends (1) LiO_2 , (2) HO_2 , (3) multi-valent complexing agents, (4) doped halide lattices and (5) low temperature studies, are discussed individually below.

Lithiated superoxide

Several conflicting reports in recent years mention Raman spectral bands in the $O_2^\cdot-$ region ($1,100\text{-}1,200\text{ cm}^{-1}$) as either being chemically stable LiO_2 (Fig. 3. 5a) or PVDF binder degradation (Fig. 3. 5b) during cycling of non-aqueous Li-O₂ cells.^{83,84,469} Fundamental *in situ* SEC studies also report the presence of LiO_2 as an intermediate (Fig. 3. 5c) in the Li^+ -ORR mechanism.^{4,74,462} This has led to some ambiguity over whether LiO_2 can exist as a stable: discharge product; intermediate; or at all, as it was previously considered thermodynamically unstable and thought to rapidly degrade if generated.⁸⁰ Another possibility that has been suggested is a $Li^+ \cdots O_2^\cdot-$ complex that is partially stabilised by the electrolyte or electrode surface.⁶⁷ In light of the trend in vo-o of $O_2^\cdot-$ observed previously, looking at the vo-o spectra of $O_2^\cdot-$ could help understanding these reports.

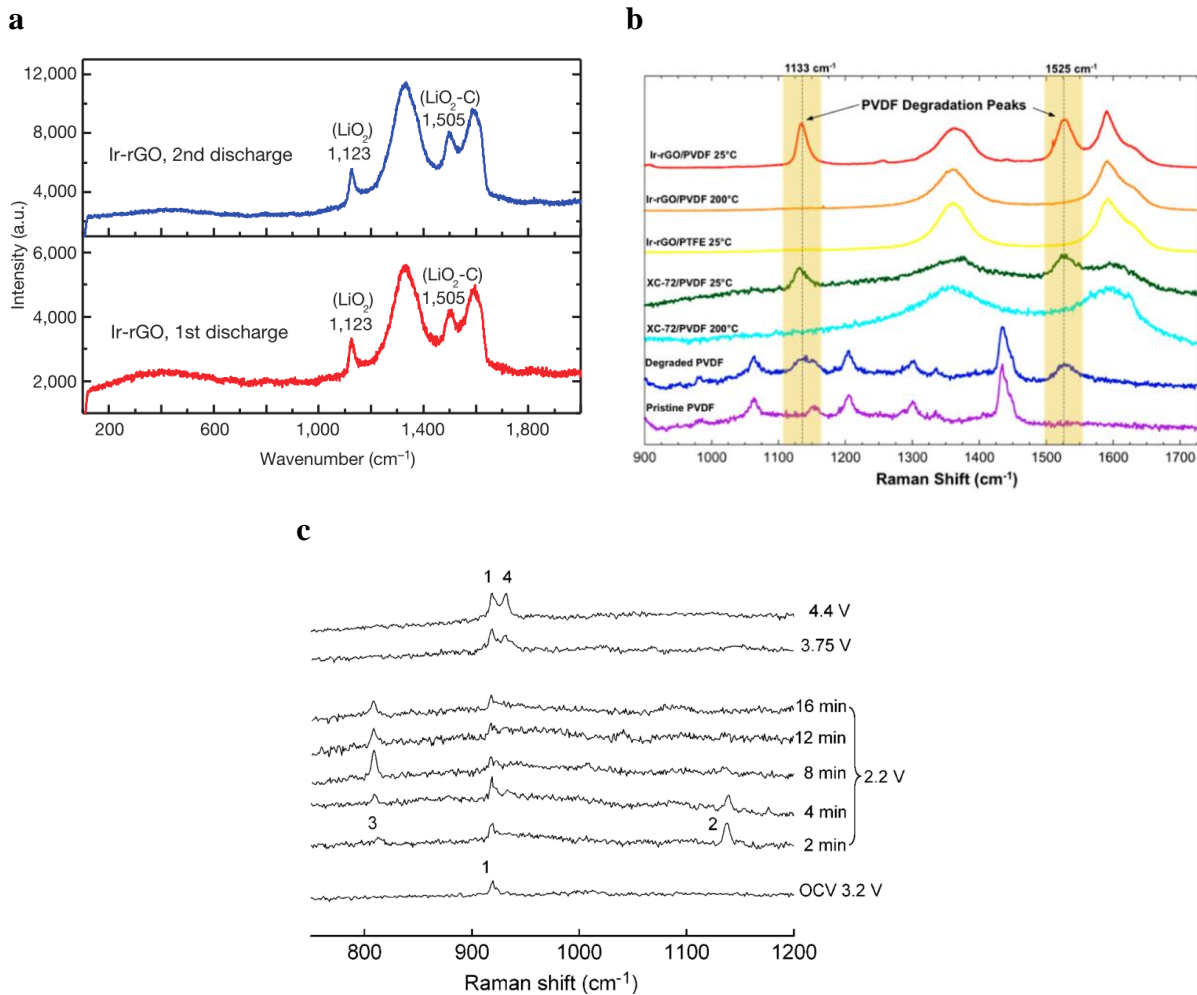


Figure 3.5. (a) Raman Spectra of an Ir-rGO cathode using PVDF binder in non-aqueous Li-O₂ cell after discharging. Spectral bands at 1,123 cm⁻¹ and 1,505 cm⁻¹ reported as the v_{O-O} of LiO₂, and the interaction between LiO₂ and the graphitic surface, respectively.¹ **(b)** Raman spectra of an Ir-rGO cathodes with PVDF binder. Spectral bands at 1,133 cm⁻¹ and 1,525 reported as PVDF degradation products.⁸⁴ **(c)** *In situ* SERS during Li⁺-OR/ER at rAu surface in 0.1 M LiClO₄ MeCN. Spectral bands **2** at 1,137 cm⁻¹ and **3** at 808 cm⁻¹ are reported as the v_{O-O} of an LiO₂ intermediate and Li₂O₂ discharge products during cycling on an rAu WE.⁷⁴

Many reports (Fig. 3. 6) have been published using *ex situ* Raman of various cathodes after discharge (using PVDF as a binder) claiming bands at 1,123-1,125 cm⁻¹ to be LiO₂ and a G-band (C-C graphitic stretch at ~1,583 cm⁻¹) shoulder at 1,505-25 cm⁻¹ to be a LiO₂-C interaction with the surface.^{39,83,159,204,468-470} HE-XRD and computational simulations are presented with the Raman spectra to verify these claims.¹ However, others report extremely similar bands (though at slightly higher wavenumbers) using *ex situ* Raman studies of similar (and in some cases identical)⁸⁴ discharged cathodes using PVDF-binder, reporting their spectral bands in the v_{O-O} region (1,122-1,135 cm⁻¹) along with an accompanying G-band shoulder at 1,525 cm⁻¹. However, these bands have been explained to be degradation product bands associated with proton abstraction and alkylation of the PVDF carbon skeleton using PXRD, XPS and iodometric titrations to support their claims.^{39,84,85} These bands were also shown to disappear when PVDF is replaced with PTFE binder, thus PTFE was said to be a stable binder due to the lack of proton abstraction reactions with O₂^{•-}.^{39,84}

However, Galloway *et al.* observed both the v_{O-O} and graphitic coupling bands (1,125 cm⁻¹ and 1,500 cm⁻¹, respectively) using *in situ* SHINERS on a pristine GC electrode surface.⁴⁶² Following this, it was shown that carbon black cathodes with PTFE binder also produced Raman bands at 1,130 cm⁻¹ and 1,543 cm⁻¹ claimed as v_{O-O} and O-C coupling during discharge (potentially contradicting other previous claims about PTFE binders).⁴⁶⁵ This seems to support the claim that the v_{O-O} band of some sort of O₂^{•-} related species can be generated at the carbon surface during discharge and the ubiquitous presence of the C-O coupling bands suggest that the surface is stabilising O₂^{•-} resulting in a distortion in the G-band vibration. These bands were observed to significantly red-shift on charge and were attributed to LiO₂ degradation to Li₂CO₃.⁴⁶⁵ Another possibility not explored by the authors is that of a carbon cathode stabilised Li⁺...O₂^{•-} species, partially intercalated into the carbon lattice, producing the ubiquitous G-band

shoulder through $\text{Li}^+ \cdots \text{O}_2^\bullet$ interacting with the localised vibrational modes of the extended phonon of graphitic ring, possibly causing some coupling or dampening of the C-C graphitic stretch. The shift from $1,130 \text{ cm}^{-1}$ to $1,098 \text{ cm}^{-1}$ could then be associated with delithiation of the $\text{Li}^+ \cdots \text{O}_2^\bullet$ species on the surface and possible further coupling/intercalation of O_2^\bullet into the lattice at positive potentials. This would account for the stretch at $1,098 \text{ cm}^{-1}$ which seems to be too high to be carbonate (normally $\sim 1,080 \text{ cm}^{-1}$) as claimed and is more in line with a free/poorly coordinated O_2^\bullet species. The increased interaction with the graphitic ring associated with a delithiated O_2^\bullet species at positive potential could also explain the simultaneous large-shift from $1,583$ to $1,490 \text{ cm}^{-1}$ in the G-band shoulder, however, further work is required to substantiate this claim.

Unlike *ex situ* Raman studies of carbon cathodes after discharge, *in situ* SERS investigations during electrochemical potential cycling show the real-time formation of O_2^\bullet species at the electrode interface in conjunction with Li^+ -ORR current responses.^{4,38,74,134,462,466,467} The vo-o band position (and O_2^\bullet solvation) is heavily dependent on solvent coordinating environment with high DN (Me-Im, DMSO)⁴ and highly ionic ($\text{Pyr}_{14}\text{TFSI}$, EmimTFSI)^{134,221} electrolyte solvents stabilising dissolved Li^+ in solution (discussed in Introduction chapter). Thus, free poorly-coordinated O_2^\bullet species with low vo-o ($1,107$ - $1,110 \text{ cm}^{-1}$)^{4,134} bands, that match poorly coordinating tetraalkylammonium superoxide (TAAO_2) species,⁷⁰ are detected at the surface even when Li^+ salts are present in the electrolyte.

Unlike in high DN electrolytes, in low DN electrolytes (e.g. MeCN), solvated Li^+ is poorly coordinating and can interact more freely with O_2^\bullet during ORR with markedly higher vo-o bands ($1,128$ - $1,137 \text{ cm}^{-1}$).^{4,74,462} Thus, these vo-o bands have been widely considered to be a pure LiO_2 species.^{4,74} However, when considering the strength of Li^+ as an acceptor and its

χ_{iv}^c value, a pure LiO₂ phase would be expected to have a vo-o band in the region of 1,167 cm⁻¹ (Fig. 3. 6) or at least a higher value than that of NaO₂ (1,156 cm⁻¹).⁴⁵⁶ Therefore, all the reported LiO₂ values to date, bar the broad band (1,150-1,200 cm⁻¹) reported by Xia *et al.* on a Ketjenblack (KB) and PTFE-binder based cathode surface,¹⁵⁹ are too low to be pure LiO₂ phases (as the thermodynamics suggest). Rather it would be more accurate to suggest they are lithiated-O₂^{•-} (Li⁺...O₂^{•-} or [Li⁺]_{1-x}[O₂^{•-}]_x, where 0 < x < 1) partially electrolyte or electrode stabilised complexes⁶⁷ as the low vo-o value suggests a O₂^{•-} rich species. Therefore, environmental contributions are likely having a large influences on the complex, as indicated by the ubiquitous presence of a C-O coupling band on carbon electrodes.^{462,465} Exceptions to this trend would be high vo-o bands in DMSO (high DN electrolyte) reported by Gittleson *et al.*⁴⁶⁷ who reported potential dependant bands (between 1,137-1,147 cm⁻¹) on Au coated Ni foam electrodes and Galloway *et al.*,⁴⁶² who also report relatively high vo-o bands (1,128 cm⁻¹) on GC electrodes. This could possibly be accounted for a strong substrate/surface-O₂^{•-} interaction or wet electrolytes.

In summary, the suggested possibilities for the low LiO₂ vo-o/ PVDF degradation bands that have been observed, along with some other possibilities are: (1) O₂^{•-} is reacting with PVDF abstracting a proton and forming an alkene bond with a serendipitously similar bond vibration to O₂^{•-} that causes a concomitant shift in the G-band. (2) δ⁺ proton sites in the structure of PVDF ([-CH₂-CF₂-]_n) binder are stabilising O₂^{•-} and Li⁺ interactions allowing stabilised Li⁺...O₂^{•-} species to deposit and grow on the binder. Contributions from repulsion with adjacent, highly electronegative, F-C bonds in the binder would also be expected to contribute to lower wavenumber vo-o bands. This could explain the accompanying distorted carbon G-band (~1,505 cm⁻¹) as Li⁺...O₂^{•-} stabilisation/coupling with the PVDF would add strain to the PVDF -C-C- skeleton. (3) A Li₂O₂.2H₂O phase similar to the Na₂O₂.2H₂O phase observed in

non-aqueous Na-O₂ batteries is being formed when H₂O is present in the electrolyte.⁴⁷¹ (4) A thermodynamically irregular or amorphous LiO₂ phase or a weakly coordinated Li⁺...O₂^{·-} complex is formed. (5) A partially intercalated O₂^{·-} species in the carbon cathode that allows Li⁺ to bind but inhibits disproportionation to Li₂O₂ is formed. The interaction between O₂^{·-} and the graphitic layers could produce the observed G-band (~1,505 cm⁻¹) shift.

Current evidence suggests; that for species generated on cathodes with PVDF binder (1) is the most probable cause of these reported ‘vo-o’ spectral bands. However, (2) and (5) are other possibilities but not pure LiO₂. Also, during *in situ* spectroelectrochemical investigations of the interface partially electrolyte stabilised Li⁺...O₂^{·-} complexes are being detected. Though, the report by Xia *et al.* suggests that it may still be feasible to produce a pure LiO₂ phase during discharge if the conditions are right though the presence of toroid discharge product morphologies (associated with wet electrolytes)^{88,121} may suggest a wet HO₂ like species was detected instead. Further work is required to remove doubt surrounding whether or not a pure thermodynamically stable LiO₂ can be generated under ambient conditions.

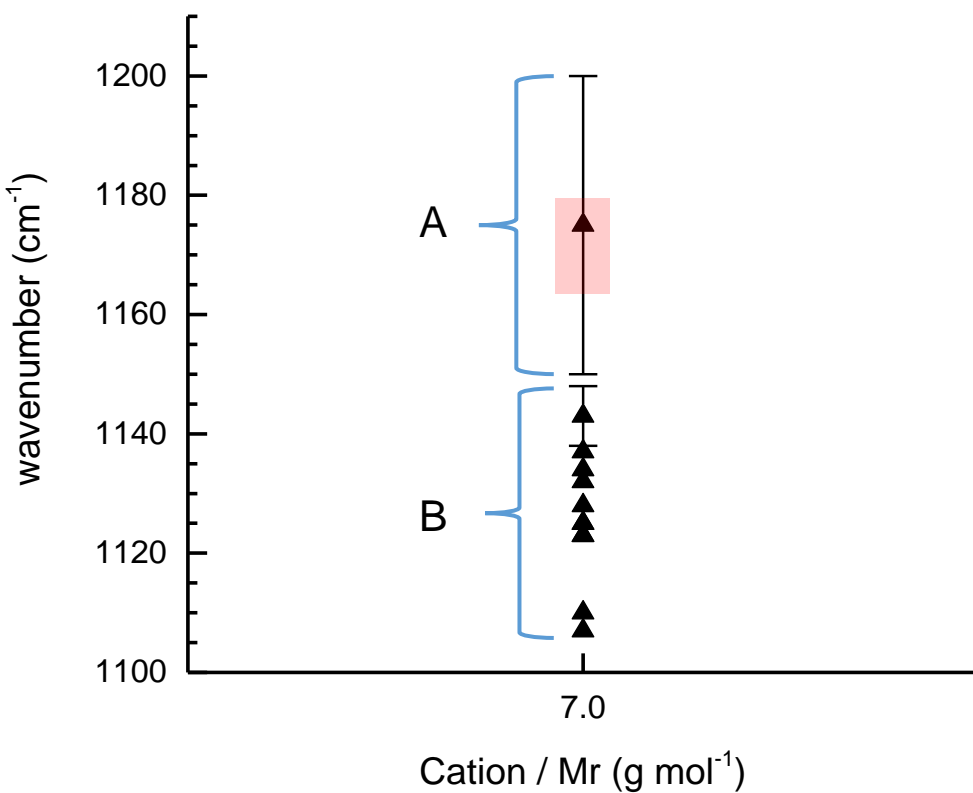


Figure 3.6. Plot of $\nu_{\text{O-O}}$ spectral bands attributed to LiO₂ in the non-aqueous Li-O₂ literature (see, Table 3.1) against the molecular mass of Li⁺. The estimated $\nu_{\text{O-O}}$ for LiO₂ based on the coordinating cation (Li⁺) is $1,167 \pm 10 \text{ cm}^{-1}$, calculated from derived $\mathbb{X}_{\text{iv}}^{\text{c}}$ relationship, shown in red. Region (A) $\nu_{\text{O-O}}$ values would fit with the expected value of a LiO₂ species. Only one value matched this and it was reported by Xia *et al.* who observed a broad $\nu_{\text{O-O}}$ band (1,150–1,200 cm⁻¹) after discharging non-aqueous Li-O₂ batteries.¹⁵⁹ Region (B) $\nu_{\text{O-O}}$ values would be expected to be partially stabilised Li⁺...O₂^{·-} species' or misallocated bands. Other reports of $\nu_{\text{O-O}}$ in a variety of different systems (Table 3.1) are likely solvated surface/solution LiO₂ species or possibly PVDF degradation product in cases where PVDF binder is present.^{39,84,85}

Protonated superoxide

The Gewirth group twice reported the electrochemical generation of $O_2^{\cdot-}$ in aqueous media and the detection of ν_{O-O} protonated superoxide (HO_2) using *in situ* SERS.^{63,296} The first report was of roughened (1) Au and (2) Bi-modified Au electrodes in acidic 0.1 M $HClO_4$ electrolytes.⁶³ In the absence of Bi^{3+} , the ν_{O-O} stretch for HO_2 was relatively high at $1,165\text{ cm}^{-1}$ but was only visible at low reduction potentials, $< 0.2\text{ V vs Ag/Ag}^+$ ($E_p^c = \sim 0.67\text{ V vs NHE}$), that were below the ORR current maximum. This suggests the reaction could be occurring at too high a rate to be detected at the higher reduction potentials and therefore can only be seen at low potentials once detectable concentrations of HO_2 have built up at the surface.

At the Bi-modified electrode, the ν_{O-O} for a Bi^{3+} -stabilised HO_2 intermediary species was visible at all potentials throughout reduction before disproportioning to H_2O_2/OH^- . The presence of Bi^{3+} at the surface provides an electropositive binding site catalysing the O_2 reduction reaction, stabilising $O_2^{\cdot-}$ when produced and possibly slowing the disproportionation charge transfer kinetics allowing the HO_2 species to be visible even at more positive potentials. Bi^{3+} is a large catalytically active species that is partially bound to, or near, EC generated HO_2 and thus able to exert some sway over its bond vibration. This interaction likely accounts for the slightly lower ν_{O-O} value of $1,162\text{ cm}^{-1}$ for Bi- HO_2 (estimated ν_{O-O} of pure $Bi^{3+}[O_2^{\cdot-}]_3$ is $\sim 1,133\text{ cm}^{-1}$ and $H^+[O_2^{\cdot-}]$ is $\sim 1,180\text{ cm}^{-1}$).

The second report by Gewirth *et al.* was again using *in situ* SERS at the rAu electrode, this time in basic 0.1 M $NaOH$ solutions (1) without and (2) with 10 mM H_2O_2 .²⁹⁶ In the first solution (1) ν_{O-O} is reported at $1,150\text{ cm}^{-1}$ during ORR at potentials below 0V vs $AgCl/Ag$ ($E^0 = \sim -0.065\text{ V}$, ORR shifted to more negative potential in base compare with acid). This band is low and unlikely to be HO_2 as it fits more with a weakly associated NaO_2 species ($\sim 1,155\text{ cm}^{-1}$

¹, Table 3. 1). The basicity of the solution would greatly limit the concentration of dissociated H⁺ available to interact with O₂^{•-}, when generated, leaving the weaker Na⁺ cation free. However, this too would have a weak interaction with O₂^{•-} due to the strong competing negative dissociated OH⁻ charge donor in solution, hence the slightly lower NaO₂ (~ 5 cm⁻¹) vo-o band. A band is also detected at 874 cm⁻¹ at low reduction potentials though this is assigned as a AuO-H bending mode. However, this would fit better with the O₂²⁻ stretch of H₂O₂ as shown in Figure 3.7 and would indicate that the generated vo-o is a stable intermediary that undergoes 2e⁻ reduction to H₂O₂ before perhaps being fully reduced to 2OH⁻ as reported.

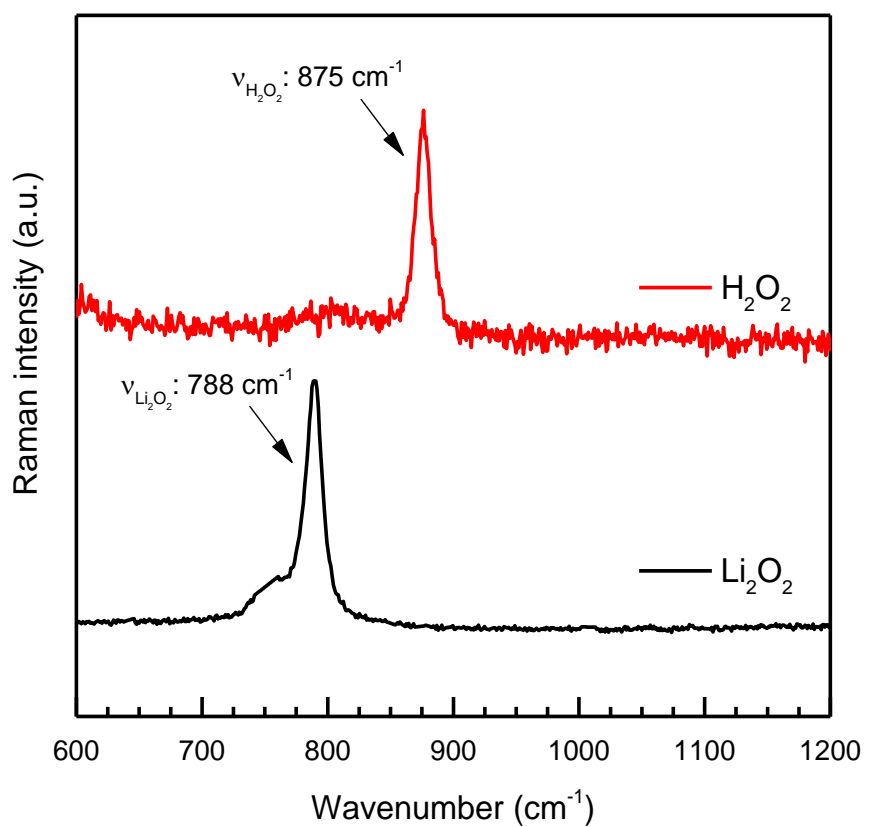


Figure 3. 7. H₂O₂ (30%, aq.) and Li₂O₂ (99 %, Sigma) Raman standards.

Adding 10 mM H₂O₂ to the basic solution interestingly sees ν_{O-O} red-shift further away from that of HO₂ to 1,135 cm⁻¹. It is interesting that this value is almost identical to that reported in the early literature for moisture contaminated Na₂O₂ and more recently in the non-aqueous Na-O₂ battery literature as Na₂O₂.2H₂O.^{79,452,453,457,471,474} It is likely all three of these are one and the same species. The vibration at approximately 1,135 cm⁻¹ is likely a low energy thermodynamic transition state between NaO₂ and Na₂O₂ that arises from the Na⁺ and adjacent H⁺ cation's small size and the inability of Na⁺ to stabilise O₂^{•-}, rendering NaO₂ thermodynamically unstable and leading to the transition towards the more stable peroxide species. The kinetics of this transition are slow (12 hrs),⁴⁷⁴ however, it can be stabilised or accelerated in different electrolyte environments.³⁷ The reducing nature of H₂O₂ (i.e. the presence of O₂²⁻) in the basic solution likely shifts the equilibrium away from H₂O₂ production in favour of Na₂O₂.2H₂O. Janik *et al.*⁴⁶⁴ also reported generating HO₂ by pulsed electron irradiation in an aqueous (pH 10) NaOH solution and detected its ν_{O-O} using time-resolved Raman to be 1,147 cm⁻¹. This value is extremely like the band reported by Gewirth *et al.* using *in situ* electrochemical SERS (Fig. 3. 8) in an extremely similar (basic) solution and would suggest weak proton association in favour of a Na⁺ coordinated O₂^{•-} complex. Therefore, these basic values attributed to HO₂ were treated as NaO₂ outliers and not representative of HO₂. Thus, they were excluded from the χ_{iv}^c fits (Fig. 3. 2, 3. 3). Considering the coordination strength and χ_{iv}^c of H⁺, in an inert environment HO₂ would be estimated to have a band at 1,179cm⁻¹ like that reported by Galloway *et al.*⁴⁶²

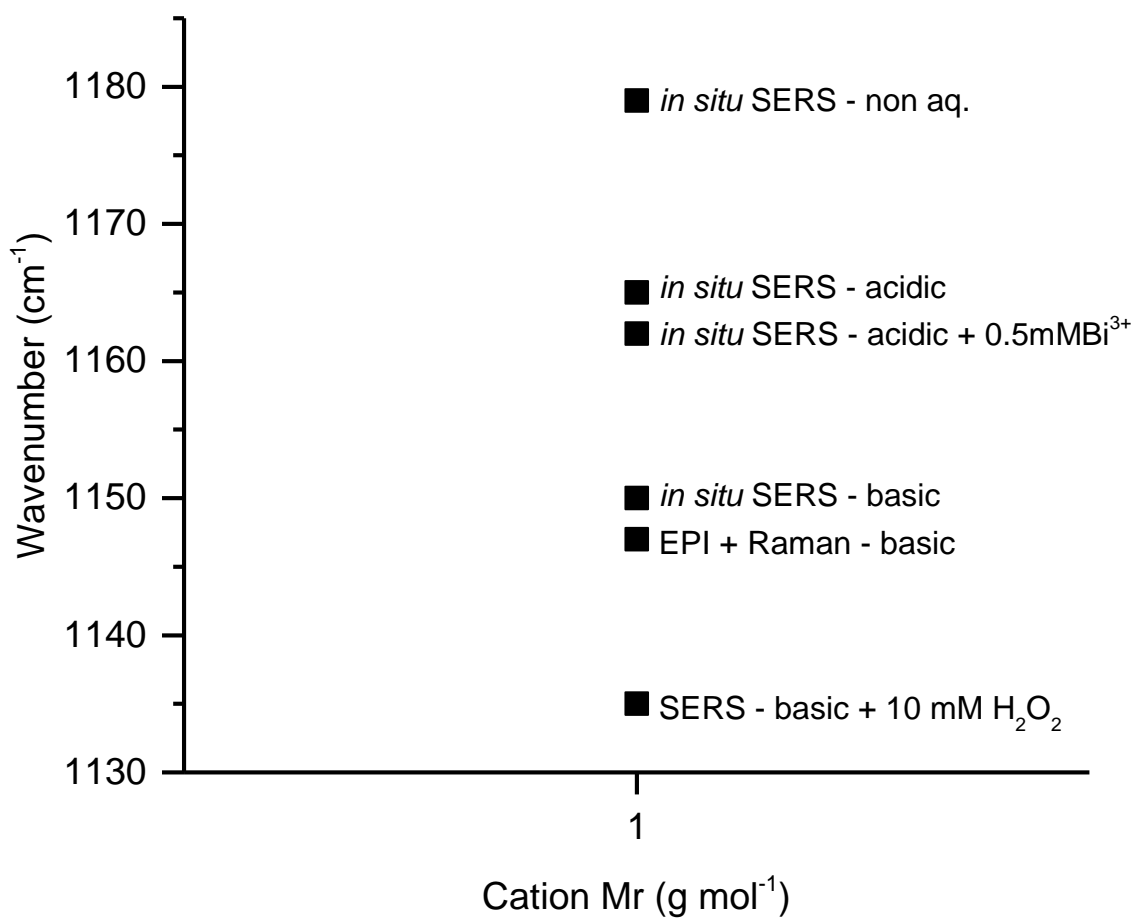


Figure 3. 8. Plot of ν_{O-O} spectral bands attributed to HO₂ in the literature (see, Table 3. 1) against the Mr of H⁺.

Polycationic complexing agents.

At first look, one apparent anomaly to the charge \mathbb{K}_{iv}^c trend are electrolytes with polycationic complexing agents, reported by Li *et al.*³⁸ Electrochemically generated $O_2^{\cdot-}$ in an electrolyte containing a Di-Im²⁺ complexing agent had a high vo-o band at 1,160cm⁻¹ indicative of a strong $C^+ \cdots O_2^{\cdot-}$ interaction due to good steric coordination between $O_2^{\cdot-}$ and the 2⁺ charge on the di-cation. The band is unchanged with and without Li⁺ present in solution indicating Di-Im²⁺ is the primary $O_2^{\cdot-}$ coordinator.³⁸ The strong coordination between $O_2^{\cdot-}$ and the di-cation fits the trend of good coordination = high vo-o, even though Di-Im²⁺ has a large calculated \mathbb{K}_{iv}^c value (53,061 g mol⁻¹ Å³). This suggests that the charge of the cation and the steric structure also play an important part in the strength of inter-ion interactions, something that is well-known and not surprising. In further work, more precise quantified values of these variables for ions could be added and used to further refine the \mathbb{K} concept to further help characterise more complex ion structures and their effect on ion-interactions.

Potassium superoxide doped alkali-metal halogen salts

Holzer *et al.*⁴⁶¹ doped a variety of alkali-metal halogen salt melts with $\sim 3 \times 10^{-3}$ mole fraction of KO₂ and measured the v_{O-O} (Figure 3. 9, values in Table 3. 4), showing the effect of anions in the immediate coordination environment of O₂^{•-} on its bond vibration. As the anion of the salt and lattice parameter increased in size from Cl⁻ to I⁻, the v_{O-O} decreased by $\sim 10 \text{ cm}^{-1}$ each time, indicative of a freer, more ionic O₂^{•-} species that is less coordinated by neighbouring cations in the salt lattice. This was explained due to O₂^{•-} experiencing less repulsion from its neighbours as the interionic distance increases. Some other contributions not mentioned could also be (1) increased O₂^{•-} lattice mismatching in the much larger Br⁻ and I⁻ anion based salts. (2) Negative Coulombic repulsion between larger halogen anions close to or touching O₂^{•-} lowering the bands. (3) As the lattice parameter of the crystal increases with the larger halogen anions, the coordinating cations are further away from O₂^{•-} and shielded by the larger anion further isolating it from coordination centres and charge.

Counterintuitively, salts with the most electronegative halogen anion (Cl⁻) had the highest v_{O-O} bands. This can be explained when considering Cl⁻ has a comparable $\mathcal{K}_{\text{iv}}^{\text{a}}$ value as O₂^{•-} (840.2 and 738.2 g mol⁻¹ Å³, respectively) therefore, there would be good lattice matching and O₂^{•-} will substitute well into the Cl⁻ salt crystal lattices. This is supported by the fact that values for v_{O-O} in doped KCl (1,145 cm⁻¹) and RbCl (1,141 cm⁻¹) salts are identical to reports of v_{O-O} for pure KO₂ (1,145 cm⁻¹)^{71,452,454,455} and RbO₂ (1,141 cm⁻¹),^{454,455,457} respectively. In NaCl (1,144 cm⁻¹) the v_{O-O} is lower than pure NaO₂ (\sim 1,156 cm⁻¹)^{454,455,457} and this is most likely due to the small spherical nature of Cl⁻ facilitating stronger coordination with Na⁺ than O₂^{•-} which is thermodynamically unstable in the presence of Na⁺ (as discussed previously). The combination of these two factors could account for this low v_{O-O}. It is important to note that this trend is apparent in constrained crystal lattices but where the cation/anion coordination is in flux and

ions can form coordination complexes with each other in the liquid phase, the spectra would differ as discussed previously.

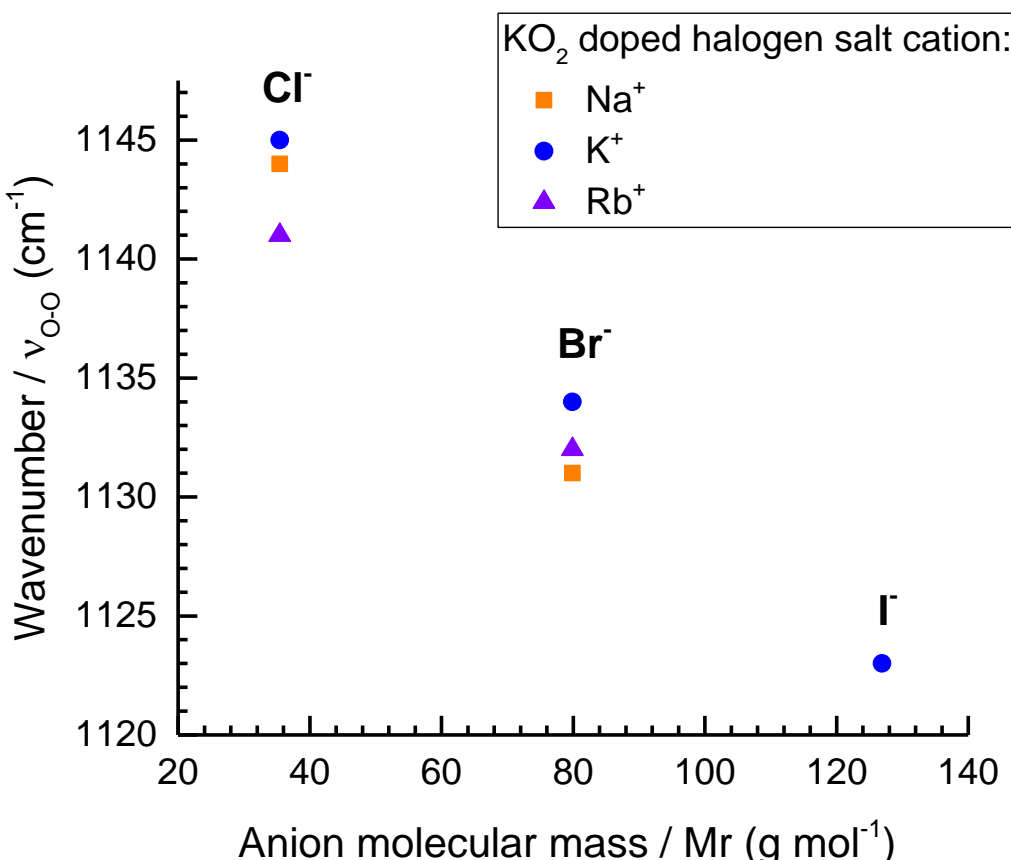


Figure 3. 7. Plot of ν_{O-O} of KO₂ doped alkali-metal halogen salts against the molecular mass of the anion in the salt.⁴⁶¹

Table 3. 4. KO₂ doped alkali metal-halogen salt values.

Anion	Mr ^a (g mol ⁻¹)	λ_{eff}^a (g mol ⁻¹ Å ³)	ν_{O-O} (cm ⁻¹)	Lattice
Cl ⁻	35.5	840.2	1144	KO ₂ doped into NaCl
Br ⁻	79.9	2,238.9	1131	KO ₂ doped into NaBr
Cl ⁻	35.5	840.2	1145	KO ₂ doped into KCl
Br ⁻	79.9	2,238.9	1134	KO ₂ doped into KBr
I ⁻	126.9	4,413.7	1123	KO ₂ doped into KI
Cl ⁻	35.5	840.2	1141	KO ₂ doped into RbCl
Br ⁻	79.9	2,238.9	1132	KO ₂ doped into RbBr

Low temperature

Andrews *et al.*^{459,460,480} reported Raman $\nu_{\text{O-O}}$ bands in the 70's for $\text{O}_2^{\cdot-}$ with alkali-metal cations in Ar lattices at low temperatures (15-16 K). $\nu_{\text{O-O}}$ increases as the mass and size of the coordinating cation increases (Fig. 3. 10), indicating a more coordinated $\text{O}_2^{\cdot-}$ species which is the reverse of the trend at room temperature. Though overall the trend is reversed, the $\nu_{\text{O-O}}$ are still 20-50 cm^{-1} below the spectral bands of their room temperature equivalents, indicative of reduced charge interactions due to slower ion kinetics and more ionic species at lower temperatures. The trend in $\nu_{\text{O-O}}$ at low temperatures can be explained by the larger cations forming more stable lattices with $\text{O}_2^{\cdot-}$ with increased stability and interion coordination. As the cation size increases, the lattice parameter also increases and so too will the distance between anions, reducing any internal repulsion in the lattice through shielding by the larger cation. There is a significant difference between the $\nu_{\text{O-O}}$ of LiO_2 and NaO_2 with the other alkali cations ($\sim 15 \text{ cm}^{-1}$, see Fig. 3. 10). This is logical considering their known thermodynamic instability. Considering Landé and the case of LiI , it was shown that lithium ions, being much smaller than Γ anions, can fit into holes within the crystal lattice, allowing the Γ anions to touch.⁷³ The same could be occurring in the Li and NaO_2 lattices at these low temperatures with the $\text{O}_2^{\cdot-}$ dumbbell shaped anions touching. This mutual repulsion gives rise to a spectral band extremely close to that of free $\nu_{\text{O-O}}$, which has been, suggested to be at $1,090\text{-}1,097 \text{ cm}^{-1}$.^{7,461} If this is the case and $\text{O}_2^{\cdot-}$ can touch in these small cation complexes then this could also facilitate barrier free charge transfer between anions and could explain the thermodynamically favourable $\text{O}_2^{\cdot-}$ disproportionation reaction in H^+ , Li^+ and Na^+ at room temperature. However, though Na^+ (K_{iv}^c : $233 \text{ g mol}^{-1} \text{ \AA}^3$) is smaller than $\text{O}_2^{\cdot-}$ (K_{iv}^c : $738 \text{ g mol}^{-1} \text{ \AA}^3$), NaO_2 is kinetically stable so $\text{O}_2^{\cdot-}$ can be expected to be better stabilised than by Li^+ and H^+ which would explain its observed stability in the non-aqueous Na-O₂ battery literature, with disproportionation reactions of NaO_2 to Na_2O_2 occurring slowly, if at all.^{2,3,37} One simplistic way of visualising this may be to

compare the \mathbb{K}_{iv}^c of K^+ and Na^+ with $\text{O}_2^{\bullet-}$ (826.5, 233.1 and 738.2 g mol⁻¹ Å³, respectively).

Na^+ is much smaller, and K^+ slightly larger, than the $\text{O}_2^{\bullet-}$ anion. Cations larger than $\text{O}_2^{\bullet-}$ are able to interact uniformly with its charge in a side-on fashion,^{7,481} allowing for stable repeating units and lattices to form. Whereas, cations smaller and more charge dense than it will tend to distort the e⁻ density of the O-O^{•-} anion dumbbell out of unity producing partial dipole moment on the anion. If anions can also touch (as would be expected with the presence of small coordinating cations e.g. Li^+ and H^+) this could lead to charge transfer between neighbouring $\text{O}_2^{\bullet-}$ anions forming more charge balanced and thermodynamically stable O_2 and O_2^{2-} , hence the instability of H^+ , Li^+ and $\text{Na}^+ \cdots \text{O}_2^{\bullet-}$ complexes and the ORR disproportionation reaction.

Overall by reviewing and investigating the v_{o-o} of $\text{O}_2^{\bullet-}$ we can see clear spectroscopic links between the vibrational frequency, thermodynamic state of the bond and its physical properties when influenced externally by coordinating cations, neighbouring ions and solvents in electrolyte or lattice structures.

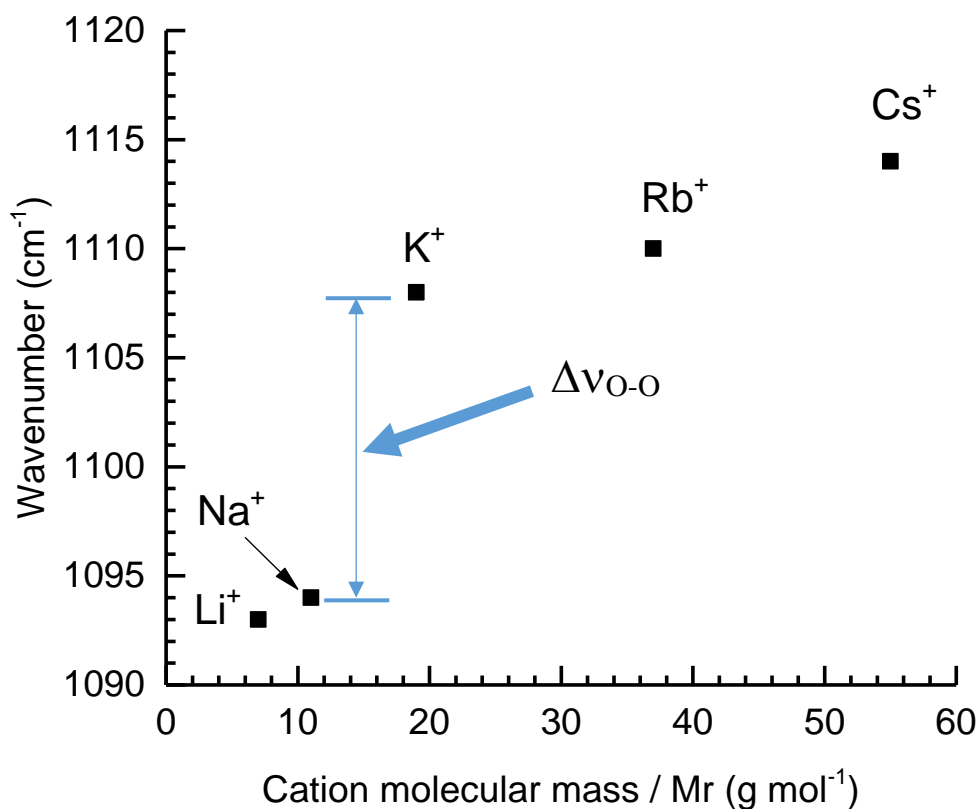


Figure 3. 8. Low temperature (15-16 K) $v_{\text{O-O}}$ spectral positions of alkali-metal O_2^- in Ar matrices vs the cation Mr , see Table 3. 5 for values. $\Delta v_{\text{O-O}}$ gap between thermodynamically; stable (KO_2 , RbO_2 , CsO_2), and unstable (LiO_2 , NaO_2) $\text{M}^+\cdots\text{O}_2^-$ species'.

Table 3. 5. $v_{\text{O-O}}$ Raman Table of alkali-metal O_2^- complexes in Ar matrices^{458,459,480}

Cation	Mr (g mol^{-1})	$v_{\text{O-O}}$ (cm^{-1})	i_v (\AA^3)	\mathcal{K}_c ($\text{g mol}^{-1} \text{\AA}^3$)	Conditions	Ref.
Li^+	6.9	1,093	5.6	38.9	Ar, 15K	458
Na^+	23.0	1,094	10.1	233.1	Ar, 16K	480
K^+	39.1	1,108	21.1	826.5	Ar, 16K	480
Rb^+	85.5	1,110	26.6	2,271.8	Ar, 16K	459
Cs^+	132.9	1,114	35.2	4,678.3	Ar, 16K	459

3.3 Dioxygen Raman Spectra and Bond Parameters

3.3.1 Important Bond Parameters

A list of bond parameters for different O_2^x species are shown in Table 3.6. It is of great practical value to relate physical bond parameters with spectral measurements so that they can be derived with ease. To that end, several efforts have been made, however, the method generally remains empirical.⁴⁸² Key O_2^x bond parameters such as bond length (l), bond enthalpy (H), bond force constants (k) and bond orders (B_o) require various experimental procedures, such as X-ray crystallography (XRC) to derive. That said, reported parameter values for most O_2^x species exist and can be correlated well with empirically measured ν_{O-O} values to estimate variations in each parameter based on the spectroscopically measured O_2^x ν_{O-O} band of unique systems.

Considering the relationship between ν_{O-O} and the coordinating cation discussed above, $C^+ \cdots O_2^{2-}$ complexes with strongly coordinating cations can be considered covalent-like with O_2^{2-} sharing some amount of its outer valence bond electron with the coordinating cation. The amount of electron sharing or charge transfer can be estimated by considering other O_2^x species, and their bond parameters i.e. the roughly linear relationship between the B_o and k (ν_{O-O}) in the O-O bond.^{483,484} Calculating the ratio of ν_{O-O} values between free O_2^x species with free O_2^{2-} ($B_o = 1$), generates values that match well the actual B_o (Table 3. 6), supporting the relationship between ν_{O-O} and the B_o .⁴⁸⁵ Due to their relatively large sizes and masses; TBA^+ and Cs^+ are weak coordinating cations with well characterised ν_{O-O} bands for $TBAO_2$ and Cs_2O_2 complexes,^{70,454,475,477,478,485} therefore, their B_o values can be assumed to be 1.5 and 1, respectively. In reality, both oxides will have some slight covalent nature (non-unity B_o) however, even without considering this and contributions from anharmonicity in the O-O bond vibration (which are relatively small and decrease in magnitude from O_2^+ to O_2^{2-}),⁴⁸⁵ we see

good agreement between the B_o and ν_{O-O} ratios in Table 3. 6. Fitting bond parameters in Figure 3. 11 with respect to known B_o values allows equations to be derived (eq. 3. 4 and Table 3. 7) for estimating O_2^x bond parameters. The trends are approximately linear, however, cubic fits where used as these better approximate the results with all fits having R^2 values equal to 1.

Table 3. 6. Bond parameters, ν_{O-O} and outer $\pi_{p_{x,y}}^*$ valence orbital structures of various O_2^x species listed. $\nu_{O-O}^x = O_2^x (O_2^{2-}, O_2^{\bullet-}, O_2, O_2^+)$ Raman spectral band. $\nu_{O-O}^x/\nu_{O-O}^{peroxide}$ ratios show good approximations with B_o indicating that energy changes in the bond vibration are directly proportional to the addition or removal of a valence electron. Correlating these values allows ν_{O-O} to be used to approximate the other bond parameters.

O-O bond parameters	O_2^{2-}	$O_2^{\bullet-}$	O_2	O_2^+	Ref.
$\pi_{p_{x,y}}^*$ MO valence structure	1\ 1\	1\ 1	1 1	1	-
Bond length / $l(\text{\AA})$	1.49	1.34	1.24	1.12	⁴⁸⁶
Bond enthalpy / H (kJ mol ⁻¹)	149	360	498	644	⁴⁸⁶
Bond force constant / k (mdyn Å ⁻¹)	2.56	6.18	11.4	16.3	^{452,487,488}
ν_{O-O}^x	742 ^a	1,108 ^b	1,556 ^c	1,876 ^c	6,454,475,478,485,489,490
Bond order	1	1.5	2	2.5	-
$\nu_{O-O}^x/\nu_{O-O}^{peroxide}$	1	1.493	2.097	2.528	*

Where: $a = \nu_{O-O}$ of (weakly coordinated) Cs_2O_2 , $b = \nu_{O-O}$ of $TBAO_2$ oxide salts, $c = \nu_{O-O}$ of gaseous oxides.

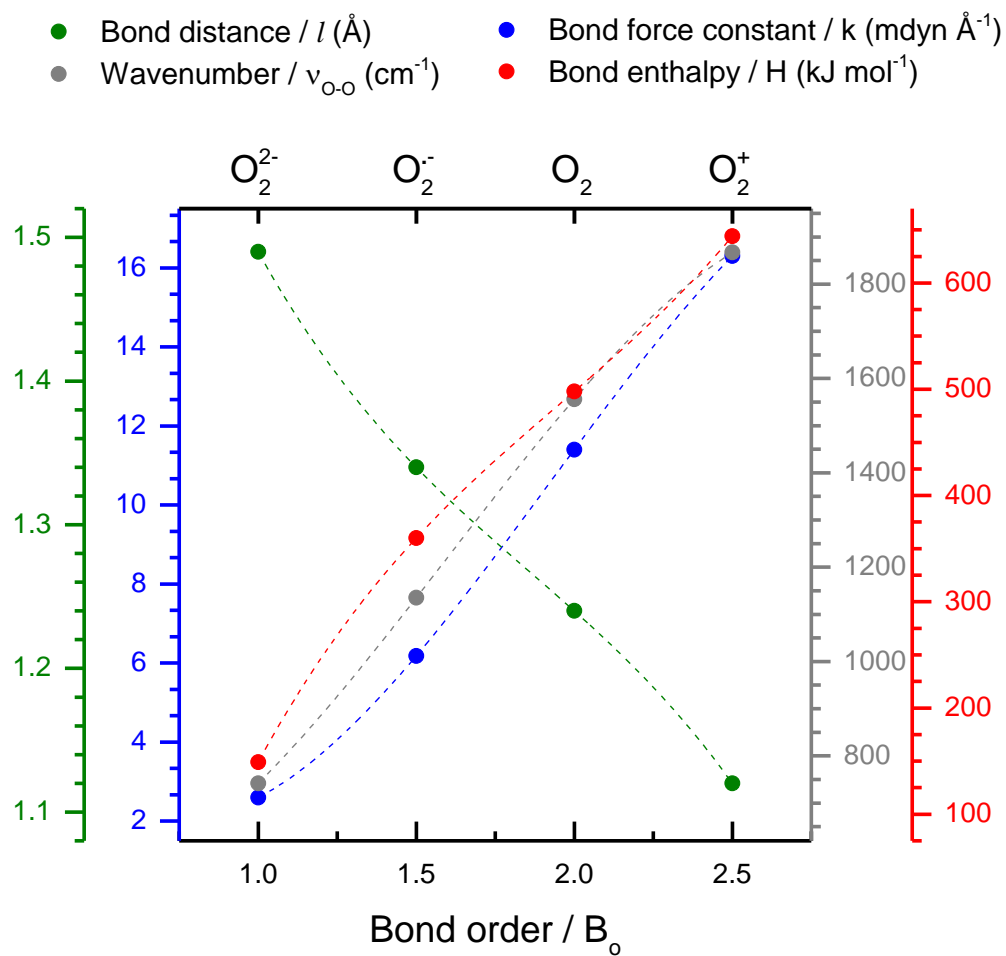


Figure 3.9. Fitted plots of O_2^x bond parameters from Table 3. 6 against the B_o . All colour-coordinated axis labels are shown above the graph. Cubic lines of best fits are shown by dashed lines, all fits generated an R^2 value of 1. Fit values shown in Table 3. 7

$$y = Ax^3 + Bx^2 + Cx + D \quad (\text{eq. 3. 4})$$

Where B_o = bond order, n = number of bonding electrons, n^* = number of antibonding electrons.

Table 3. 7. Cubic fits from Figure 3. 11 in accordance with equation 3. 4. In theory, all O_2^x parameters can be estimated by measuring v_{O-O} . k values can be calculated more directly using Hooke's law.

x	y	A	B	C	D
v_{O-O}	B_o	7.835×10^{-10}	-2.976×10^{-6}	0.00483	-1.268
B_o	l	-0.0933	0.52	-1.157	2.22
B_o	k	-2.607	15	-17.948	8.15
B_o	H	108	-632	1489	-816

To further qualify that the relationship between the $\nu_{\text{O-O}}$ of O_2^x and its bond properties are approximately linear/cubic; it would be expected that a covalent-like O_2^x species (i.e. the outer valence electron is partially shared with its coordinating environment and the B_o of the O-O stretch is between that of two free ionic O_2^x species e.g. a species between O_2^{2-} ($B_o = 1$) and $\text{O}_2^{\cdot-}$ ($B_o = 1.5$) would be expected to have a B_o of ~ 1.25) with a $\pi^*(2p)$ orbital structure between the peroxy-superoxide, $[1\downarrow 1\downarrow] \rightarrow [1\downarrow 1]$, would have a detectable bond vibration and $\nu_{\text{O-O}}$ band somewhere between a strongly coordinated O_2^{2-} (e.g. H_2O_2 : 875 cm^{-1}) and a free $\text{O}_2^{\cdot-}$ ($\sim 1097 \text{ cm}^{-1}$) species.⁴⁸⁴ $\nu_{\text{O-O}}$ values between these can be considered covalent-like with roughly half the valence bond electron being shared by O_2^x with its coordinating environment. Such a O_2^x species' bonds would be expected to have a partial dipole moment, therefore, the $\nu_{\text{O-O}}$ band would be both Raman and IR active.⁴⁹¹ Searching the literature this was indeed found to be the case for the $\nu_{\text{O-O}}$ of organic peroxyls,^{492,493} transition metal superoxo-complexes,^{450,494,495} and metalloenzymes,⁴⁹⁶ which all have values reported in this range in Raman and/or IR. This trend in $\nu_{\text{O-O}}$ would also be expected to be the same for superoxo-oxyl and oxo-dioxygenyl species which is also the case and discussed in detail below. To clarify language the O_2^x valence electron is here assumed to be partially shared with the coordinating species and:

- Peroxy-superoxyl refers to a coordinated O_2^x species with covalent-like character, a $\pi^*(2p)$ valence orbital structure between $[1\downarrow 1\downarrow] \rightarrow [1\downarrow 1]$ and B_o of ~ 1.25 .
- Superoxo-oxyl refers a coordinated O_2^x species with covalent-like character, a $\pi^*(2p)$ valence orbital structure between $[1\downarrow 1] \rightarrow [1 1]$ and B_o of ~ 1.75 .
- Oxo-dioxygenyl refers a coordinated O_2^x species with covalent-like character, a $\pi^*(2p)$ valence orbital between $[1 1] \rightarrow [1]$ and B_o of ~ 2.25 .

3.3.2 Peroxo-Superoxyl

Numerous organic covalently bound peroxyls have been shown experimentally and computationally to have strong bands in both Raman and IR ranging from 771 cm⁻¹ (a strong ionic peroxide) to 1,000 cm⁻¹ (a covalent peroxy-superoxyl).^{492,493} Some of these bands were assigned to a variety of O-O and O-C bond stretches, with some C-O, O-O coupling.^{492,493} A series of five different Cr^{III}-superoxo complexes (all bands qualified with O₂¹⁸) have v_{O-O} IR bands ranging from 1,027 cm⁻¹ (a covalent peroxy-superoxyl) to 1,104 cm⁻¹ (an ionic O₂^{·-}) depending heavily on the donor strength of the changing ligand complexing the Cr^{III} metal centre.⁴⁹⁴ Charge contributions to the Cr^{III} metal centre increase as the ligand donor strength increases, subsidising/weakening the Cr^{III}-O₂^{·-} bond producing a higher v_{O-O} value indicative of an ionic-like superoxo-complex. Similarly, for cupric oxides, the ligand shell heavily influences the superoxo Cu^{II}-O₂^{·-} and peroxy Cu^{III}-O₂²⁻ complexes.⁴⁵⁰ Elwell *et al.* reviewed over twenty Cu-O₂ complexes with v_{O-O} bands ranging from essentially covalent peroxy-superoxyl at 961 cm⁻¹ to having ionic O₂^{·-} character at 1,130 cm⁻¹ (all qualified with O₂¹⁸). It is interesting to note that the v_{O-O} bands were usually accompanied by a O-to-Cu stretch vibration (v_{Cu-O}) between the metal centre and oxygen (435-494 cm⁻¹) which are comparable in value to the O-to-surface bond vibrations (v_{O-Surf}) detected at the rAu WE during *in situ* SERS (Table 3. 1). These bonds are analogous to O₂^{·-} electrode surface orientations and can give valuable information on the orientation of the superoxo species in relation to the metal centre, discussed further in the following chapters.

3.3.3 Superoxo-Oxyl

A covalent O₂^x species with a superoxo-oxo valence π*(2p) orbital structure, [1↓ 1] → [1 1], would be expected to have a detectable v_{O-O} bond stretching vibration between that of a relatively well coordinated O₂^{·-} (HO₂: ~1,180 cm⁻¹) and neutral O₂ (1,556 cm⁻¹). Again, this

would be expected to be Raman and IR active. Spectroscopic examples in the literature of these superoxo-oxyl covalent-like species are scarcer than the peroxy-superoxyl suggesting that it is less stable with a tendency to rapidly disproportionate.⁴⁴⁶ The highest ν_{O-O} band found was 1,310 cm⁻¹ for a Fe-superoxo intermediary complex stabilised at -80°C that converted to the Fe-peroxy-bridged intermediate when heated to -60°C (qualified with O₂¹⁸).⁴⁹⁷ This ν_{O-O} suggests a O₂^x species between O₂⁻ and O₂ with significant covalent-like character. Another similar species [Fe^{III}(TAML)(O₂)]²⁻ had an IR ν_{O-O} band at 1,260 cm⁻¹ (qualified with O₂¹⁸).⁴⁹⁸ An example of another relatively covalent species with more superoxo character is the [(Cr^{III})(O₂)(TMC-Im)]²⁺ species dissolved in MeCN which had a ν_{O-O} band at 1,196cm⁻¹ in the IR.⁴⁹⁹ From their respective spectra, these O₂^x species can be assumed to be heavily complexed with significant covalent-like character between the metal centres and O₂^x. The spectroscopic reports of O₂^x complexes in the organic and inorganic chemistry literature is too extensive to list fully here, rather this is intended as an overview of some key complexes that support the discussed trend and the influence of the coordinating environment on the O₂^x bond properties, supporting the variability of the ν_{O-O} based on the coordination strength of the environment.

3.3.4 Oxo-Dioxygenyl

Like the O₂^x anions the ν_{O-O} of the dioxygenyl cation (O₂⁺) is heavily influenced by the counter-anion. A strong counter-anion coordinates and donates electron density into the O₂⁺ orbital, decreasing the effective nuclear charge experienced by the valence electron causing the bond to lengthen slightly which is visible as a lower ν_{O-O} bond vibration (note this is the opposite effect to the anion O₂^x systems were stronger coordinating cations induce bond shortening through the removal of valence bond electron density). Accordingly, over a range of sixteen O₂⁺ species,^{6,487,500,501} the ν_{O-O} varied from partially coordinated at 1,825cm⁻¹ in O₂RhF₆, to weakly coordinated at 1,864cm⁻¹ in O₂Sb₂F₁₁ (much bulkier coordinating anion) and up to free

gaseous O_2^+ at $1,876\text{cm}^{-1}$. With respect to free O_2^+ , $O_2\text{RhF}_6$ has minor oxo-peroxyl covalent character. Hemes (Fe^{2+} centred porphyrin ligand complexes) that were ligand depleted observably took up O_2 and had visible $\nu_{\text{O-O}}$ bands at $1,595\text{cm}^{-1}$ and $1,663\text{cm}^{-1}$ ($1,663\text{cm}^{-1}$ band only visible in asymmetric heme complex)⁵⁰² assigned to the $\nu_{\text{O-O}}$ of an informally dipole bound O_2 molecule (qualified with O_2^{18}). Based on the IR spectra, this would fit with an oxo species that has slight covalent dioxygenyl character, with depletion of the metal donating ligand electron density causing the remaining ligands to withdraw charge from O_2 causing the observed spectral band. Other than this, no other O_2^x species with $\nu_{\text{O-O}}$ bands indicative of oxo-dioxygenyl, $[1\ 1] \rightarrow [1]$, covalent character could be found to date.

All the above discussed $\nu_{\text{O-O}}$ bands in this chapter for various O_2^x species (> 200) have had their estimated bond properties calculated (using eq. 3.4 and Table 3. 7) and have been plotted against their calculated B_o (Fig. 3. 12). O_2^x species with B_o values divisible by 0.5 can be considered ionic or neutral whilst values in between can be considered covalent-like in nature with some level of electron donation occurring between O_2^x and its coordinating environment. Therefore, the B_o is assumed to be on a spectrum and to vary depending on how strongly coordinated the O_2^x diatom is (and therefore, how much of its valence electron it shares).

Experimental data on O-O bond parameters have been reported throughout the scientific literature, particularly measuring the O-O bond distances with X-ray crystallography (XRC) or neutron diffraction techniques. Therefore, the calculated l values using eq. 3.4 can be cross-compared with experimental results to gauge their accuracy. Some of these cross-comparisons are listed in Table 3. 8 with the difference between the measured and calculated bond length values shown as a percentage (the literature is exhaustive and largely disorganised, i.e. individual bond parameters and $\nu_{\text{O-O}}$ values tend to be reported in different chemical,

crystallographic, spectroscopic journals, and would warrant further compilation in future).

Overall, the experimentally reported and calculated bond length values match well with generally a $< 4\%$ difference, supporting correlation. This relationship is useful for analysing experimental result in the following chapters and O-O properties in general.

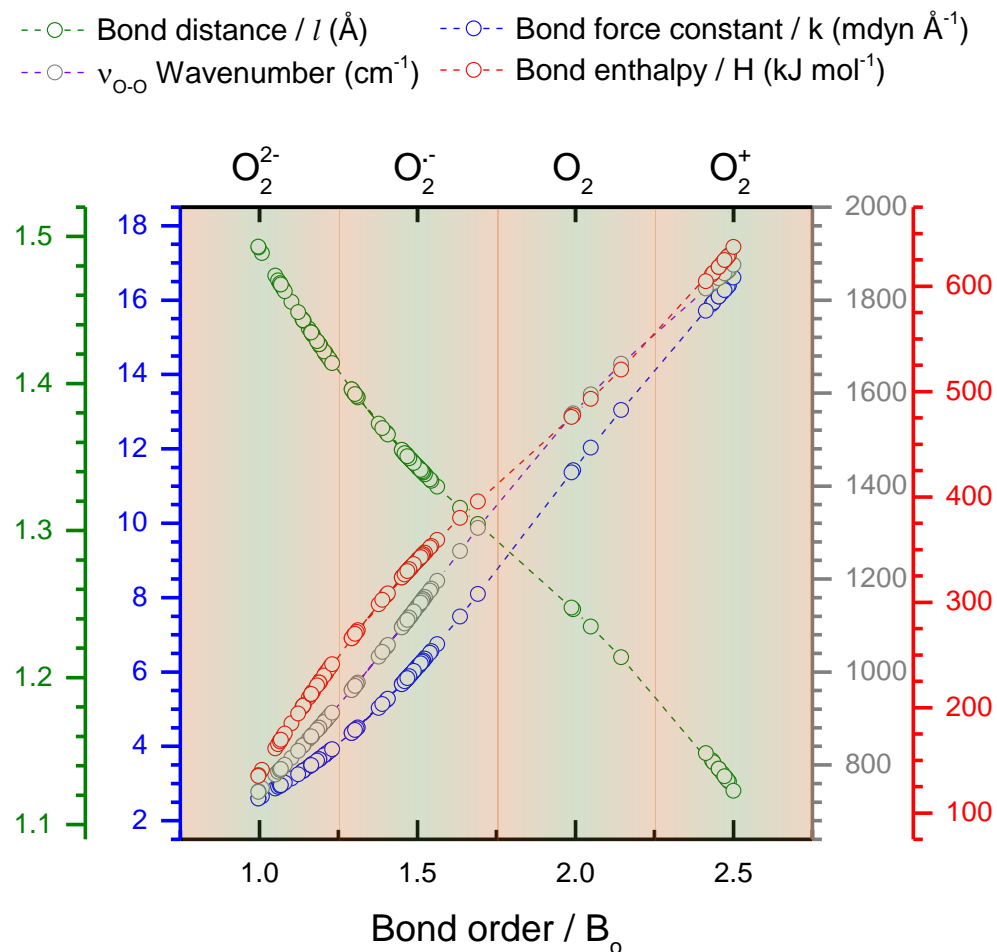


Figure 3. 10. Fitted plots of O_2^x estimated bond parameters calculated from all previously mentioned $\nu_{\text{O-O}}$ values reported in the literature (> 200 species). Light green shaded regions signify covalent O_2^x species where valence bond electrons are concentrated in the $O_2^x \pi_{2p_{x,y}}^*$ orbitals. Light orange regions signify covalent O_2^x species where the outermost valence electron is shared with the coordinating environment. Colour coordinated axis labels are shown above the graph.

Table 3. 8. Some reports of various simple (single atom) and complex (multi-valent, molecular) O₂^x species, using their reported names, where both the v_{O-O} and bond lengths have been reported together. Experimentally observed bond length values using XRC are contrasted with those calculated from their respective v_{O-O} using Table 3. 7 and a percentage difference between the observed and calculated bond lengths generated.

O ₂ ^x species	v _{O-O} (cm ⁻¹)	Bond length / l			Refs.
		Report	Calc.	Δl/%	
[Tp ^{Bu,Me} Cr(pz×H)(O ₂)]BARF	1072	1.327	1.361	2.6	494
1	1112	1.346	1.22	9.4*	8,484
2	961	1.391	1.355	2.6	484
3	1104	1.348	1.325	1.7	484
4	1072	1.357	1.327	2.2	484
6	968	1.389	1.44	3.7	484
7	891	1.417	1.411	0.5	484
9	892	1.417	1.43	0.9	484
(Tp ^{Me²}) ₂ SmO ₂	1124	1.342	1.319	1.8	484
O ₂	1549	1.242	1.208	2.7	484
(SrO ₂) _{0.98} O _{0.02}	865	1.483	1.428	3.7	503
(BaO ₂) _{0.97} O _{0.03}	843	1.493	1.438	3.7	503
(Tp ^{Me²}) ₂ Sm(η ² -O ₂)	1,124	1.319	1.3427	1.8	504
TMPPhAO ₂	1,121	1.332	1.3435	1.6	479
NaO ₂	1,156	1.33	1.337	0.2	504,456
KO ₂	1,145	~1.335	1.345	0.3	505,71

*largest observed difference between calculated and observed bond length values, this anomaly has been noted previously as being an underreported value.⁸

Considering the change in the derived B_o values due to changes in ν_{O-O} between strongly and weakly coordinated O_2^x species, the covalent-like nature (i.e. amount of electron donation) of the interaction between O_2^x and its coordinating environment can be roughly estimated as a percentage (eq. 3. 5). This is another useful/cheap method for estimating the interaction between a O_2^x species and its environment based solely on its experimental ν_{O-O} bond vibration (eq. 3.5 and see examples below). Thus, a value for the coordination strength of the cation (or electrolyte solvent) and the level of electron abstraction/donation from/to the ion by its coordinating environment can be teased out of the ν_{O-O} literature. On a side note, these values are not suggested to be precise as contributions from anharmonicity are excluded; rather they are useful tools for calculating approximate values for O_2^x bond parameters which confirm and enhance the understanding of its spectra. This is particularly useful for helping to understand dynamic systems that are in flux such as at an electrode surface where countless thermodynamic, kinetic and charge transfer processes are occurring simultaneously, allowing for a general understanding of reaction processes to be rationalised with respect to O_2^x in terms of its ν_{O-O} .

$$\% e^- \text{ donation} = \frac{(B_{o,c} - B_{o,i})}{0.25} \times 100 \quad (\text{eq. 3. 5})$$

Where: $B_{o,c}$ = calculated bond order, $B_{o,i}$ = nearest whole B_o to $B_{o,c}$ devisable by 0.5 (if the nearest bond order is less than $B_{o,c}$ then the species is covalent in the opposite direction). A change in bond order of 0.5 is equivalent to adding/removing an electron from O_2^x . A change in bond order of 0.25 is equivalent to adding/removing $\frac{1}{2}$ an electron (i.e. covalent character).

Examples: HO₂ (1,179 cm⁻¹), NaO₂ (1,156 cm⁻¹), TBAO₂ (~1,108), Cu:O₂ complex A (1,033 cm⁻¹),⁴⁵⁰ Cu:O₂ complex B (892 cm⁻¹)⁸ have calculated B_o values of 1.574, 1.549, 1.5, 1.409 and 1.228, respectively. Values greater than 50% can be considered to have significant covalent character.

Therefore:

$\% e^- \text{donation to H}^+ = \left(\frac{(1.579 - 1.5)}{0.25} \right) \times 100$	= 29.5 %	(HO ₂)
$\% e^- \text{donation to Na}^+ = \left(\frac{(1.549 - 1.5)}{0.25} \right) \times 100$	= 19.5 %	(NaO ₂)
$\% e^- \text{donation to TBA}^+ = \left(\frac{(1.5 - 1.5)}{0.25} \right) \times 100$	= 0%	(TBAO ₂)
$\% e^- \text{donation to Cu complex} = \left(\frac{(1.409 - 1.5)}{0.25} \right) \times 100$	= -36.4%	(Cu:O ₂ A)
$\% e^- \text{donation to Cu complex} = \left(\frac{(1.228 - 1)}{0.25} \right) \times 100$	= 91.2 %	(Cu:O ₂ B)

As discussed in detail in the Introduction, it is important for a practical non-aqueous M-O₂ battery electrolyte to provide a chemically stable environment for the cathode reaction and to solvate reaction intermediaries without degrading. The electrolyte's stability in the presence of O₂^{•-} is as important as its compatibility with the metal anode. In the following chapters, O₂^{•-} was generated electrochemically and probed spectroscopically at the roughened gold (rAu) electrode-electrolyte interface with *in situ* SERS in a variety of different IL and novel solvent blended IL electrolytes. Thus, O₂^{•-} can be used as diagnostic molecule to probe electrolyte interactions in more complex heterogeneous electrolyte formulations, significantly aiding the electrolyte selection and tailoring process. This approach to deriving bond properties from the spectral bond vibration of bonds in different coordinating environments will most likely provide comparable results for other bonds (e.g. N-N, N=N etc. or C-C, C=C etc. or C-O, C=O) and provide similar quick approximations from detecting their bond vibrations.

4. *In Situ* SERS of ILs

4.1 Overview

In this chapter OR/ERs at the electrode interface were probed using *in situ* spectroscopic techniques in eight different ILs. Six of the ILs used had the same anion (TFSI^-) and different cations (TES^+ , Pyr_{14}^+ , Pip_{14}^+ , Aze_{14}^+ , N_{1444}^+ , N_{1888}^+) whilst three had the same cation (Pyr_{14}^+) and different anions (TFSI^- , OTf^- , DCA^-), see Figure 4. 1 for chemical structures. $\text{O}_2\cdot^-$ spectral bands ($\nu_{\text{O-O}}$) were detected during ORR at the rAu WE surface in all ILs, except $\text{N}_{1888}\text{TFSI}$, and slight shifts in the $\nu_{\text{O-O}}$ wavenumber were visible between the different ILs. Also, $\nu_{\text{O-O}}$ Stark-shifted by varying amounts with potential, however, the direction of the wavenumber shift, i.e. whether blue (higher) or red (lower), depended on the IL cation. Generally, ILs with large, weak Lewis acid cations (see Table 4. 1) had low $\nu_{\text{O-O}}$ values indicative of a free poorly coordinated $\text{O}_2\cdot^-$ species whilst the reverse was visible for the ILs with small, more Lewis acidic cations, matching observations in the previous Chapter. Changing the anion also influenced the $\nu_{\text{O-O}}$ band positions with lower values detected in ILs containing small, relatively strong Lewis basic anions, likely due to increased coulombic repulsion between $\text{O}_2\cdot^-$ and IL anions and weaker cation- $\text{O}_2\cdot^-$ interactions. Whilst, the reverse was visible for the ILs with large, less Lewis basic anions. The characteristic $\text{O}_2\cdot^-$ -to-surface ($\nu_{\text{O-Surf}}$) bond vibration⁷⁴ was also visible in all ILs where $\nu_{\text{O-O}}$ was present. When $\text{O}_2\cdot^-$ was more strongly coordinated by the IL cation and had high $\nu_{\text{O-O}}$ bond vibrations; $\nu_{\text{O-Surf}}$ values were typically low, indicative of a weak surface interaction. Conversely, when the $\nu_{\text{O-O}}$ bond vibration was low, its $\nu_{\text{O-Surf}}$ was generally high due to stronger surface interactions. This provides direct evidence of the influence of the IL ions on $\text{O}_2\cdot^-$ generated at the surface. Repeated stable quasi-reversible electrochemistry with minimal capacity decay suggests most of the ILs tested had good $\text{O}_2\cdot^-$ stability, whilst using more electron accepting ILs with smaller ions improved the OR/ER reversibility and peak currents. This information helped to guide the electrolyte tailoring process in the following Chapter.

4.2 Introduction

As discussed, O_2^{*-} is the key reaction intermediary formed during the ORR at the cathode in non-aqueous Li-O₂ cells and the electrolyte's propensity to coordinate and solvate it in the presence of dissolved Li⁺ dictates whether a solution or surface reaction mechanism occurs.^{4,41,87} However, O_2^{*-} can cause parasitic side reactions with organic electrolytes or electrodes that limit the capacity and cycle life of the cell, which needs to be better understood and mitigated against. Therefore, understanding the interaction between O_2^{*-} and the electrolyte provides valuable information for selecting and designing a more robust non-aqueous Li-O₂ battery electrolyte. Due to many of their innate properties, ILs are unique for use as non-aqueous electrolytes to support OR/ERs. An ideal electrolyte should have an ‘amphoteric-like’ nature, with both a high DN and AN component capable of effectively stabilising and solvating both positively and negatively charged species and reaction intermediaries, reducing their propensity to react together and increasing their solvation into the bulk electrolyte away from the cathode surface.^{4,41} As discussed, ILs fit this model as they contain ions with both positive and negative formal charges and the Hard-soft nature of the IL ions varies based on their size, Mr etc.

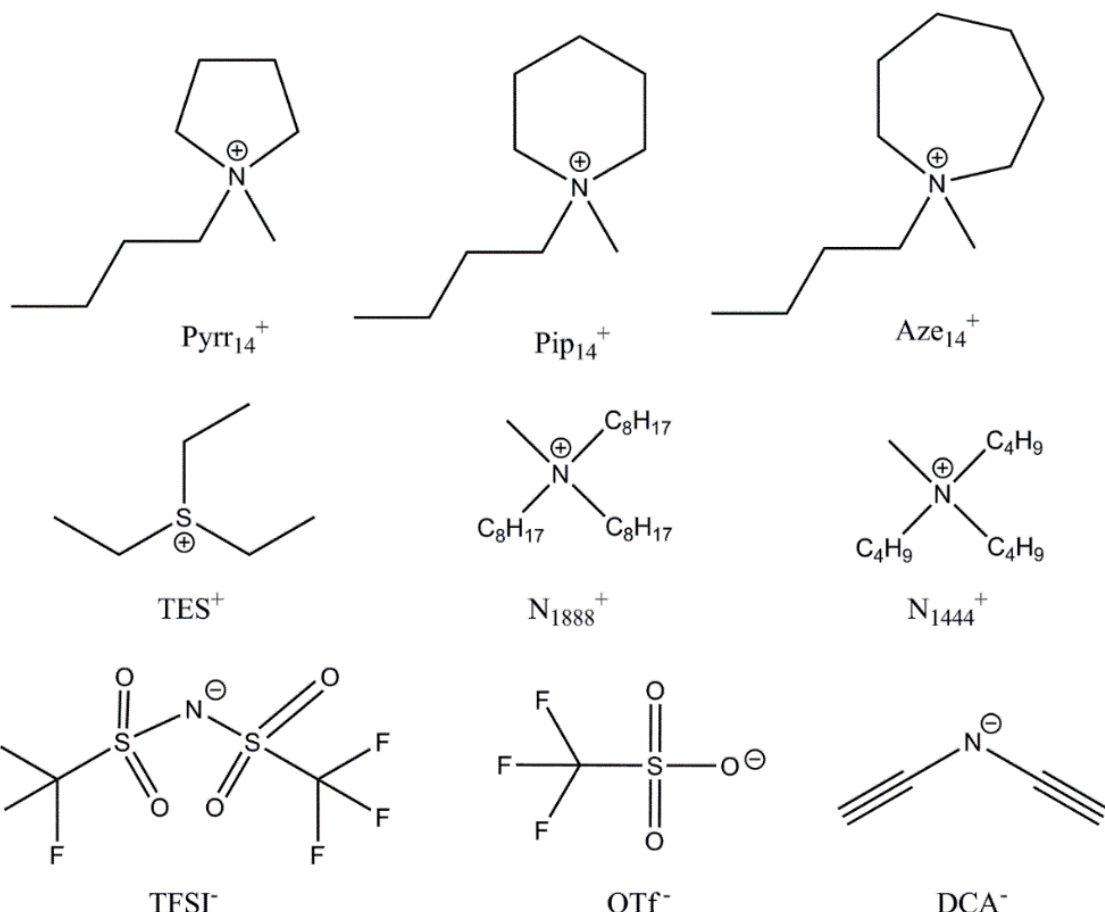


Figure 4. 1. Chemical structures of IL cations, anions used in this work as well with the associated abbreviations for each constituent are presented.

In this chapter $\text{O}_2^{\cdot-}$ was generated electrochemically and probed spectroscopically at the roughened gold (rAu) electrode-electrolyte interphase using *in situ* SERS in a variety of different ionic liquid (ILs). rAu acts as a model electrode to compare the flux of species at the cathode surface during the OR/ERs and the $\text{O}_2^{\cdot-}$ -electrolyte interactions. Recent comparisons between the rAu and catalytically inactive GC planar electrode surfaces using SHINERS, showed rAu has slightly slower reaction kinetics than carbon cathodes, but gives a good approximation of the OR/ER cathode interface overall.⁴⁶² Spectroscopic enhancement techniques are required to detect $\text{O}_2^{\cdot-}$ at the planar electrode surface over bulk electrolyte signal and to ensure observations are localised to the surface as the enhancement diminishes exponentially away from it.

4.3 *In situ* SERS of OR/ER in ILs

4.3.1 Cation Effect

Because of the cation's effect on O_2^\cdot , discussed, and the relationship between the AN of the IL and its substituent cations;⁴⁰⁷ a series of TFSI⁻ anion based ILs with different cyclic amide cations ($Pyrr_{14}^+$, Pip_{14}^+ , Aze_{14}^+ , N_{1444}^+), as well as a relatively small sulphurous cation (TES^+), were selected to investigate the effect reducing the cation size (and \mathcal{K}_{iv}^c) has on O_2^\cdot generated at the electrode surface and its characteristic ν_{O-O} stretch. Two different *in situ* SERS spectral acquisition techniques were employed to probe the flux in vibrational bonds at the surface; (1) dynamic surface potentials and (2) controlled surface potentials.

Dynamic surface potential

As stated in the experimental section, one of the methods for collecting Raman spectra is in rapid succession (~1.4 seconds per spectra) during potential cycling. The inherently short laser exposure times lead to high background noise making enhancement active surfaces essential for detecting reaction products. However, with an optimum SERS electrode substrate, multiple spectra were amassed with excellent signal to noise ratios allowing for detailed time-resolved contour and multi-dimensional plots (Fig. 4. 2) to be generated showing the real-time flux of vibrational bonds at the surface in conjunction with changes in surface potential. Two ILs with significant differences in cation sizes, the relatively hard TES^+ and soft Aze_{14}^+ ($\mathcal{K}_{iv}^c = 17,704.2$ and $36,928.8 \text{ g mol}^{-1} \text{ n}^{-1} \text{ \AA}^3$, respectively), are contrasted in Figure 4. 2. The top section of Figure 4. 2 (a) and (c) shows the variation of potential and current with respect to time during a CV scan of O_2 saturated TESTFSI and Aze_{14} TFSI ILs. The corresponding contour plots (dark-red colour being the most intense and purple the least) of Raman band intensities with respect to time are shown below. Equivalent 3D plots of the Raman data are shown in Figure

4. 2 (b) and (d) with significant bands labelled on the plot. For both TESTFSI and Aze₁₄TFSI several potential dependent bands are observed to emerge and vanish as the potential is swept. As can be seen in the plots (Fig. 4. 2), two spectral characteristic bands for O₂^{•-} appear during ORR and disappear on the OER reverse scan: (1) the v_{O-O} stretch, (ca. 1,097-1,122 cm⁻¹) and (2) the O₂^{•-}-surface bond, (v_{O-Surf}, ca. 459-488 cm⁻¹).⁷⁴ Both O₂^{•-} bands are heavily dependent on the immediate coordinating environment and counter-cation size. Changes in intensity in δCF₃ and ωSO₂ anion bond vibrations of TFSI⁻ with potential are also more clearly visible in the 3D plots than in contour plots. These are associated with reduced anion presence at the surface at lower potentials in TESTFSI (Fig. 4. 2b) that recovers when potentials are returned to positive values and anions repopulate the EDL.^{428,506} Potentials where the v_{O-O} and v_{O-Surf} bands are most intense are highlighted in red and green on the potential/current vs. time plots (Fig. 4. 2a and c).

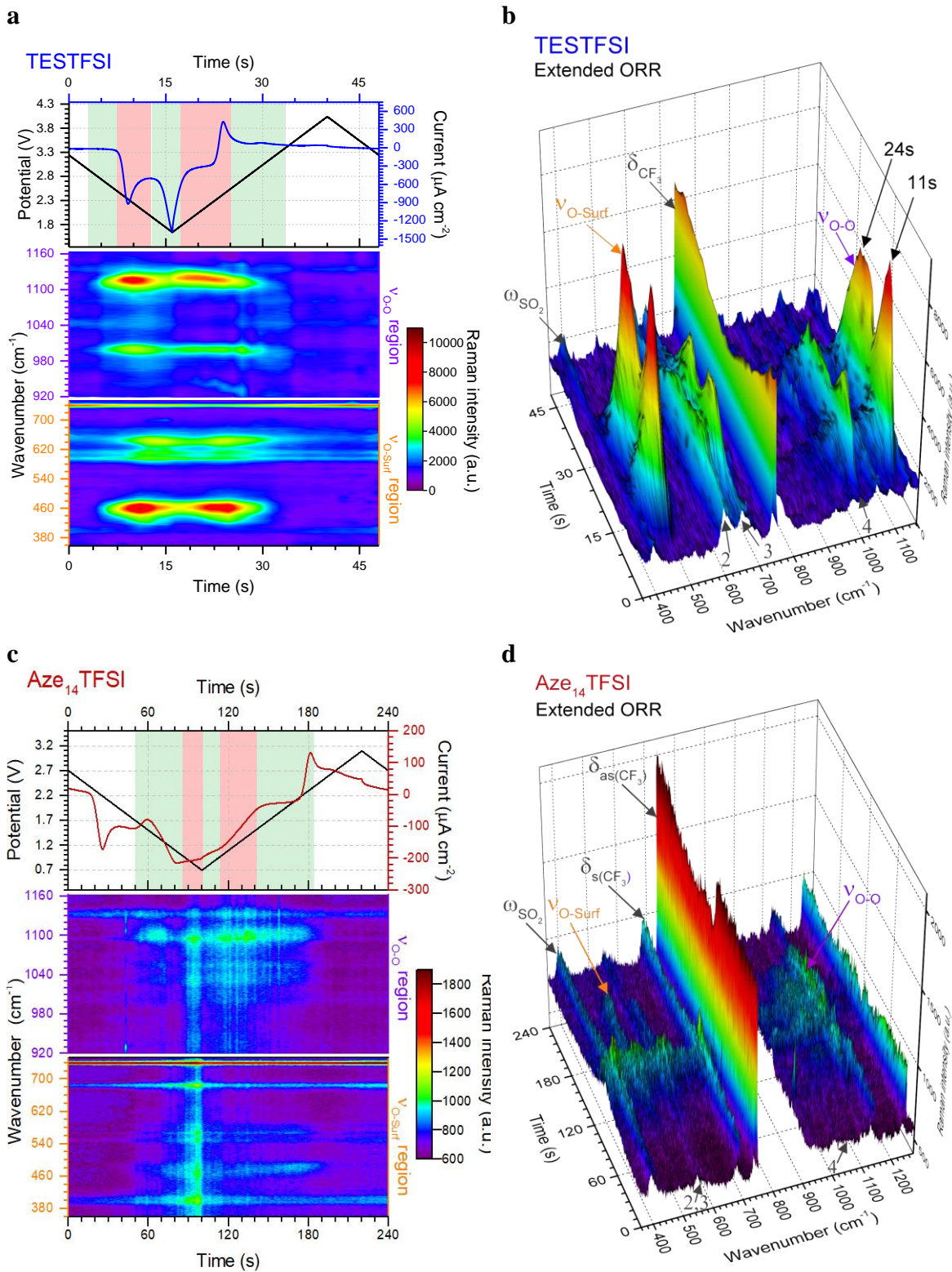


Figure 4.2. Dynamic surface potential *in situ* SERS multi-dimensional **(a)** and **(c)**: plots, Top: Potential (black lines)/current (blue or red lines) vs. time plots of OR/ER in O₂ saturated TESTFSI and Aze₁₄TFSI (analogous with CVs in Figure 4.3 (b) and (d)). Bottom: contour plots of SERS data in v_{O-O} and v_{O-Surf} regions, respectively, at corresponding times with the

electrochemistry. Regions of low and high $\nu_{\text{O-O}}$ and $\nu_{\text{O-Surf}}$ band intensities highlighted in green and red in the electrochemical top plots. **(b)** and **(d)**: 3D visual plot of spectral changes with time. This data has been reproduced from previously published work, ref: ⁴²¹.

Figure 4. 3 (a) and (c) show corresponding selected stacked spectra of the data shown in Figure 4. 2 that were peak fitted. From this plot, band shifts of $\nu_{\text{O-O}}$ and $\nu_{\text{O-Surf}}$ become more apparent. The top half of Figure 4. 3 (b) and (d) show OR/ER CVs of O_2 saturated TESTFSI (relatively hard cation) and $\text{Aze}_{14}\text{TFSI}$ (soft cation) ILs, respectively, during normal (lower potential limit of 2.0 V) and extended (lower potential limit down to either 1.6 or 0.6 V) potential cycling. Normal OR/ER cycles are shown by dashed lines, however, in order to improve visibility and investigate the influence of potential on the $\text{O}_2^{\cdot-}$ bond vibrations, spectra were collected during reduction cycles where the potential was taken to the second reduction maxima generally associated with O_2^{2-} production.⁶⁶ It should be noted within this study no bands pertaining to O_2^{2-} were observed.

During extended potential cycling, rapid spectra of the rAu working electrode surface were continuously collected. The appearance and disappearance of characteristic $\nu_{\text{O-O}}$ and $\nu_{\text{O-Surf}}$ spectral bands (highlighted in grey and light grey) was apparent in both ILs as the potential was swept. However, the signal for $\text{O}_2^{\cdot-}$ bands were almost an order of magnitude weaker in the $\text{Aze}_{14}\text{TFSI}$ than in TESTFSI and were only detected at potentials beyond the ORR current maxima at slower scan rates (20 mV s⁻¹ in $\text{Aze}_{14}\text{TFSI}$ compared with 100 mV s⁻¹ in TESTFSI). Similarly weak $\text{O}_2^{\cdot-}$ bands have been reported previously with alkyl ammonium salts dissolved in MeCN, where the $\nu_{\text{O-O}}$ signal was much stronger in smaller tetraethylammonium (TEA^+) than tetrabutylammonium (TBA^+) based electrolytes.⁷⁰ Both bands were observed to blue or red Stark shift with decreasing potential in TESTFSI or $\text{Aze}_{14}\text{TFSI}$, respectively, and a plot of their peak-fitted band positions and intensities are shown in the bottom half of Figure 4. 3 (b) and (d). Electrolyte peaks labelled 2-4 were observed to vary in intensity, mirroring changes in $\nu_{\text{O-O}}$ and $\nu_{\text{O-Surf}}$, however, they were visible at all potentials and have been tentatively assigned as cation bands that are coupling with $\text{O}_2^{\cdot-}$. Identities of key potential dependent peaks of both

ILs with observations are summarised within Table 4. 2. In TESTFSI, the O_2^{*-} bond vibrations first appeared (weakly) at 2.75 V vs Li⁺/Li in TESTFSI and grew in intensity to a maximum just after the reduction potential current maxima. The top right inset of Figure 4. 3 (b) shows this to be the precise onset point of the exponential decrease in current and beginning of bulk O_2 reduction. This is below the thermodynamic reduction potential of O_2 reduction in lithiated systems (2.97 V vs Li⁺/Li)⁵⁰⁷ but significantly higher than the half-potentials ($E_{1/2}$) of the OR/ER reaction in TESTFSI suggesting the formation of a surface adsorbed Au- O_2^{*-} surface species at 2.75 V vs Li⁺/Li.

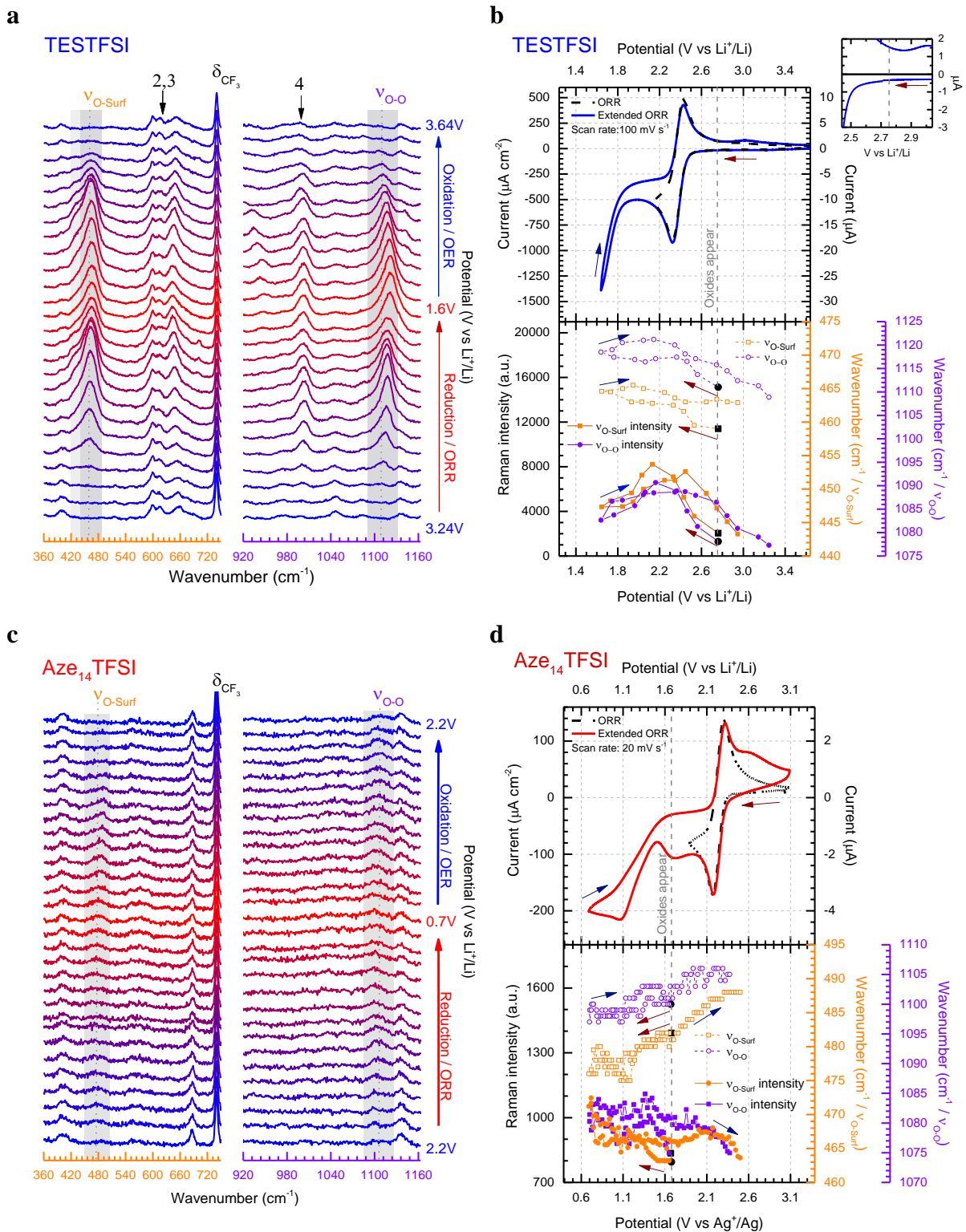


Figure 4. 3. Dynamic surface potential *in situ* SERS. (a) and (c): Selection of stacked SERS spectra of the rAu working electrode surface collected in rapid succession in O₂ saturated TESTFSI and Aze₁₄TFSI, respectively. Left and right are scans of v_{O-O} and v_{O-Surf} wavenumber regions, respectively. (b) Top, CVs of O₂ saturated TESTFSI at 100 mV s⁻¹ with standard

OR/ER cycle (dashed line) and extended reduction cycle (blue line). Top right inset shows potential region where O_2^{*-} bands first appear with small current response due to formation of a O_2^{*-} -surface layer prior to the bulk ORR current response. Bottom, ν_{O-O} (purple dashed lines and dots) and ν_{O-Surf} (orange dashed lines and dots) wavenumber position/intensity vs. potential plots. There is a visible blue-Stark shift and intensity rise then decrease as the potential is lowered. **(d)** Top, CVs of O_2 saturated $Aze_{14}TFSI$ at 20 mV s^{-1} during normal OR/ER cycle (dashed line) and extended reduction cycle (red line). Bottom, ν_{O-O} and ν_{O-Surf} wavenumber positions and intensity plots vs. potential. There is a visible red-Stark shift and intensities increase with decreasing potential. Both **(b)** and **(d)**: starting data points when O_2^{*-} bands appear shown in black, where possible coloured arrows are included as visual aids indicating reduction (dark red) and oxidation (dark blue) directions of potential scanning.

Table 4. 1. Summary of key IL bands. C⁺ refers to cation, either TES⁺ or Aze₁₄⁺ (Note Peak 1 is the designation of the flat conformer of adsorbed O₂^{•-} at ca. 430 cm⁻¹).

	TESTFSI	Aze ₁₄ TFSI
δCF ₃ (TFSI ⁻)	- intensity decreases/increases with potential, anion bands are still present throughout cycling and changes indicate that the anion reorientates at lower potentials from flat to side-on, to balance surface charge.	- intensity does not decrease with potential - intensity changes when potential reversed only - anion remains flat on surface - intensity changes mirror oxide bands
ωSO ₂ (TFSI ⁻)	- intensity decreases/increases with potential - supports anion reorientation at low potentials	- intensity changes mirror δCF ₃ - supports anion remaining flat at low potentials
Peaks 2,3 (C ⁺)	- 590-610 (doublet), 650 cm ⁻¹ - present at all potentials - assigned to cation (match Spartan DFT simulated spectra for TES ⁺) - intensity changes mirror O ₂ ^{•-} bands - cation-O ₂ ^{•-} coupling causes intensity changes - increased cation concentration at surface - stronger cation and cation-O ₂ ^{•-} bond	- 550, 570 cm ⁻¹ - present at all potentials - intensity changes mirror oxide bands - cation-O ₂ ^{•-} coupling - weaker cation and cation-O ₂ ^{•-} bond
Peak 4 (C ⁺)	- 1000 cm ⁻¹ - intensity changes mirror O ₂ ^{•-} bands - S-O, cation-O ₂ ^{•-} coupling bond - changes in coupling intensity correspond with changes in O ₂ ^{•-} concentration at surface	- 1030, 1055 cm ⁻¹ - only present when O ₂ ^{•-} bands present - intensity changes mirror O ₂ ^{•-} bands - N-O, cation-O ₂ ^{•-} coupling bond - changes in coupling intensity correspond with changes in O ₂ ^{•-} concentration at surface

Controlled surface Potential

The second method for collecting Raman spectra was using long laser exposure times (~5 minutes per spectrum) whilst holding the rAu surface at a selected potential for the duration of the spectral acquisition. Holding the potential for a prolonged length of time allowed for scanning over large wavenumber ranges, multiple acquisitions and for extended laser exposure times that significantly improve the signal-to-noise ratio. Once spectra were collected, the potential was cycled back positive and the process repeated at incrementally lower or higher potentials on reduction or oxidation, respectively.

The top half of Figure 4. 4 (b) and (d) show selected OR/ER CVs in TESTFSI and Aze₁₄TFSI ILs, respectively. The current visibly decreases in periods where the potential is held due to the EDL approaching equilibrium with surface potentials. Corresponding spectra of the surface in each IL at specified potentials are shown stacked in Figure 4. 4 (a) and (c) respectively. Characteristic ν_{O-O} and ν_{O-Surf} spectral bands (highlighted in grey and light grey) are visible during OR/ER potentials. Both oxide band positions were observed to blue and red Stark shift (as observed with dynamic surface potentials) in TESTFSI and Aze₁₄TFSI, respectively, and a plot of their peak fitted band positions and intensities are shown in the bottom half of Figure 4. 4 (b) and (d). A summary of all the wavenumber ranges of both ν_{O-O} and ν_{O-Surf} bands in each IL using both technique is shown in Table 4. 3.

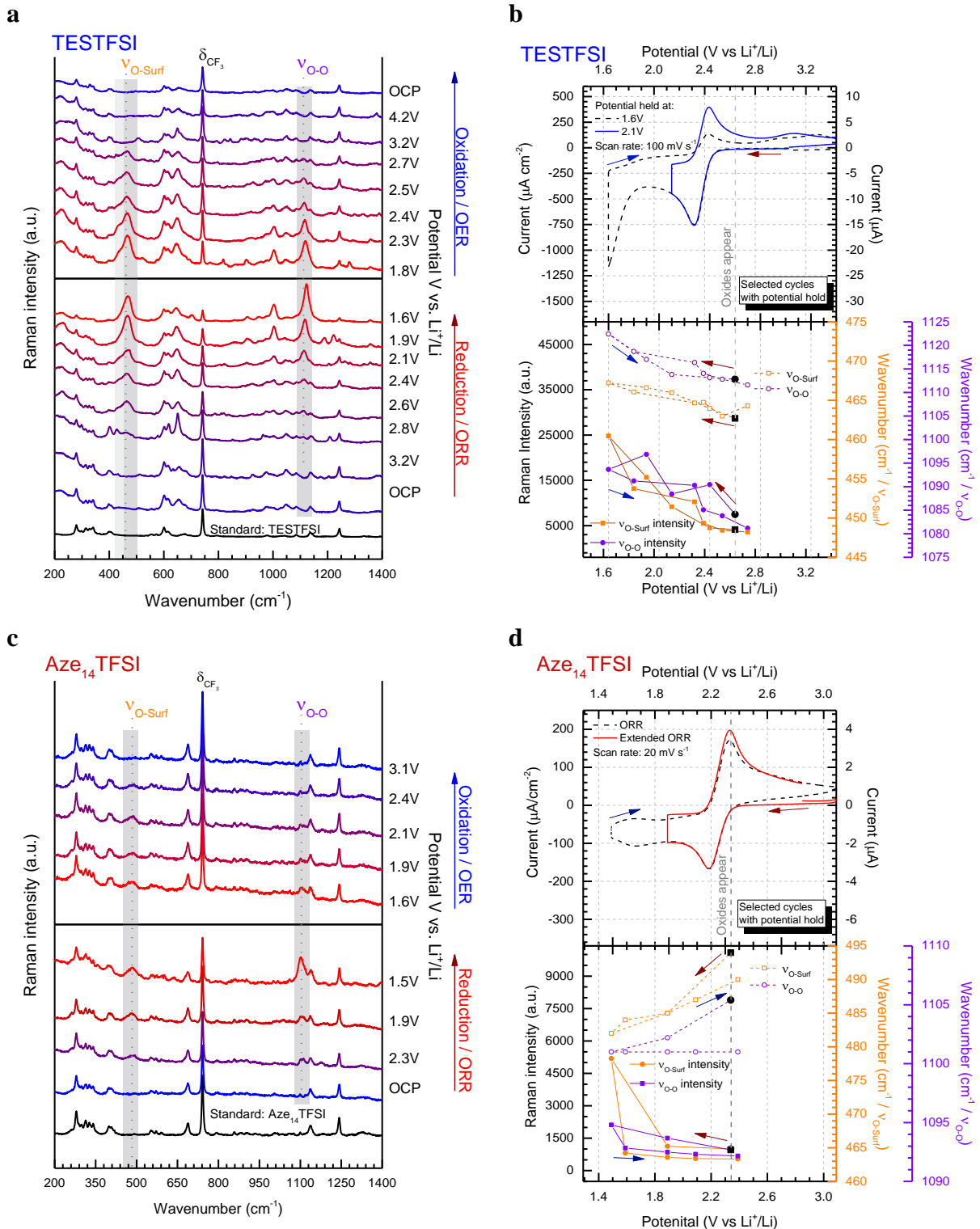


Figure 4. Controlled electrode surface potential *in situ* SERS spectra (**a**) and (**c**): Stacked SERS spectra of rAu working electrode surface at specified held potentials, during reduction (bottom) and oxidation (top) in O₂ saturated TESTFSI (**a**) and Aze₁₄TFSI (**c**), respectively. (**b**) and (**d**): Top: Selected CVs of O₂ saturated TESTFSI (**b**) and Aze₁₄TFSI (**c**), respectively.

Where potential is held a current drop is visible on the CV. Bottom: ν_{O-O} and ν_{O-Surf} wavenumber position and intensity plots vs potential. ν_{O-O} (purple dashed lines and points) and ν_{O-Surf} (orange dashed lines and points) bands both visibly blue and red Stark shift in TESTFSI and Aze14TFSI, respectively. Both (b) and (d): starting points when bands appear shown in black, coloured arrows are visual aids indicating reduction (dark red) and oxidation (dark blue) directions of potential scanning.

Discussion

Peak shifts in ν_{O-O} band positions from lower (red) to higher (blue) wavenumbers generally indicate more ionic or covalent, respectively, interactions between O_2^{*-} and its coordinating environment. A more ionic O_2^{*-} species is a less coordinated, more radical, harder Lewis base with electron density concentrated on the diatom. Whilst a more covalent O_2^{*-} species is a more coordinated, softer Lewis base and has a higher frequency ν_{O-O} band. Likewise, red and blue Stark shifts in ν_{O-O} bands during potential cycling indicate surface potential induced fluctuations in the ionic and covalent character, respectively, of generated O_2^{*-} . The potential induced Stark effect, being consistent with Guoy-Chapman theory, is heavily dependent on the distance of the probe molecule (i.e. O_2^{*-}) from the surface and indicates observation of species bonded, adsorbed or adjacent to the surfaces that can have their bond force constants directly influenced by changes in the surface potential.⁵⁰⁸ For ν_{O-Surf} , differences in band positions between electrolytes and red and blue Stark shifts indicate longer (weaker) and shorter (stronger) adsorption bonds, respectively. Both ν_{O-O} and ν_{O-Surf} bands are closely related appearing on ORR and disappearing on OER in unison; though there were significant differences between the two IL electrolytes which will be discussed. As such, the focus on the effect of the cation on electrochemically generated surface O_2^{*-} by varying the substituent cation in two distinct ILs with either a relatively small, TES^+ , or large charge dissociated, Aze_{14}^+ , cation is given thorough consideration.

Comparing surface oxide bands between the two ILs using both Raman scanning techniques; the ν_{O-O} is visibly much higher (between: 12-23 cm⁻¹) whilst the ν_{O-Surf} is much lower (between: 16-27 cm⁻¹) in TESTFSI than in the $Aze_{14}TFSI$, respectively, independent of which scanning technique is used (Table 4. 2). Therefore, time-resolved *in situ* SERS methods using dynamic surface potentials can be used as effectively as conventional acquisition techniques using

controlled surface potentials to improve visualisation of surface speciation. The ν_{O-O} values agree with the trend in coordinating cation size discussed in the previous chapter, indicating a freer $O_2^{\cdot-}$ species is generated at the surface in $Aze_{14}TFSI$ than TESTFSI due to it being weakly coordinated at the surface by the soft Aze_{14}^+ counter cation in the IL. For the ν_{O-Surf} bands, lower wavenumbers indicate longer, weaker O-to-surface bonds. Therefore, lower ν_{O-Surf} wavenumbers in TESTFSI than $Aze_{14}TFSI$ suggest that the stronger cation is abstracting more electron density from surface $O_2^{\cdot-}$ species which weakens the $O_2^{\cdot-}$ -surface bond, whilst weak cation interactions mean electron density is concentrated on $O_2^{\cdot-}$ and in the $O_2^{\cdot-}$ -surface bond producing a visibly higher wavenumber ν_{O-Surf} peak. Comparing the ranges ($\Delta\nu_x$) over which ν_{O-Surf} and ν_{O-O} shift (Table 4. 3), it is interesting to note that ν_{O-O} is more susceptible to changes in electrode potentials in TESTFSI Whereas, in $Aze_{14}TFSI$ the ν_{O-Surf} is.

Table 4. 2. Summary of ν_{O-Surf} and ν_{O-O} bond vibrations (ν_x) with dynamic and controlled surface potentials (E) at the rAu interface in O_2 saturated TESTFSI and $Aze_{14}TFSI$. Δ denotes difference between highest and lowest spectral values shifting with potential.

		Dynamic E		Controlled E	
		ν_x (cm^{-1})	$\Delta\nu_x$ (cm^{-1})	ν_x (cm^{-1})	$\Delta\nu_x$ (cm^{-1})
TESTFSI	ν_{O-Surf}	459-466	7	463-467	4
	ν_{O-O}	1,109-1120	11	1,111-1,122	11
$Aze_{14}TFSI$	ν_{O-Surf}	475-488	13	482-494	12
	ν_{O-O}	1,097-1105	8	1,101-1,105	4

O-to-Surface bond: The O-to-metal centre bond (O-M) vibrations (ν_{O-M}) in dioxygen (O_2^x) ligand complexes in organometallic chemistry are analogous to ν_{O-Surf} bonds observed here and can be used to help further rationalise the structure and orientation of the surface $O_2^{+/-}$ species. In organometallic complexes, the three most common O_2^x -metal bond structures are side-on (flat), kinked and bent (Fig. 4. 5). The longest/weakest O-M bond is in the side-on O_2^x -metal structure usually associated with peroxy species^{7,509} though side-on superoxo species can also exist.^{495,510} The flat conformation results when the energy of the $O_2^x \pi^*$ levels lie below that of metal d orbitals of the metal centre, and is composed of d-to- π^* bonding with equal bonding between both O atoms and the metal centre.⁵⁰⁹ The conventional superoxo-ligand however is known to be preferentially bent-bonded to metal sites, through ligand-to-metal σ donation, with the possibility of back donation from the metal into the antibonding orbitals. Back bonding from the metal weakens the O-M or adsorption bond and effects the bond force constant producing a longer kinked adsorption bond structure.⁵⁰⁹ A kinked bond has characteristics somewhere between the flat and bent bonded species with both O atoms interacting to differing degrees with the metal centre or surface (Fig. 4. 5). ν_{O-O} and ν_{O-Surf} spectral bands are both visible in the bent and kinked bond orientations, however due to Raman selection rules associated with using a polarised light source, in the flat orientation only the ν_{O-Surf} would be expected to be visibly enhanced due to $O_2^{+/-}$ being parallel with the surface. Thus, the O-O bond will likely have only minor enhancement in the direction perpendicular to the surface.

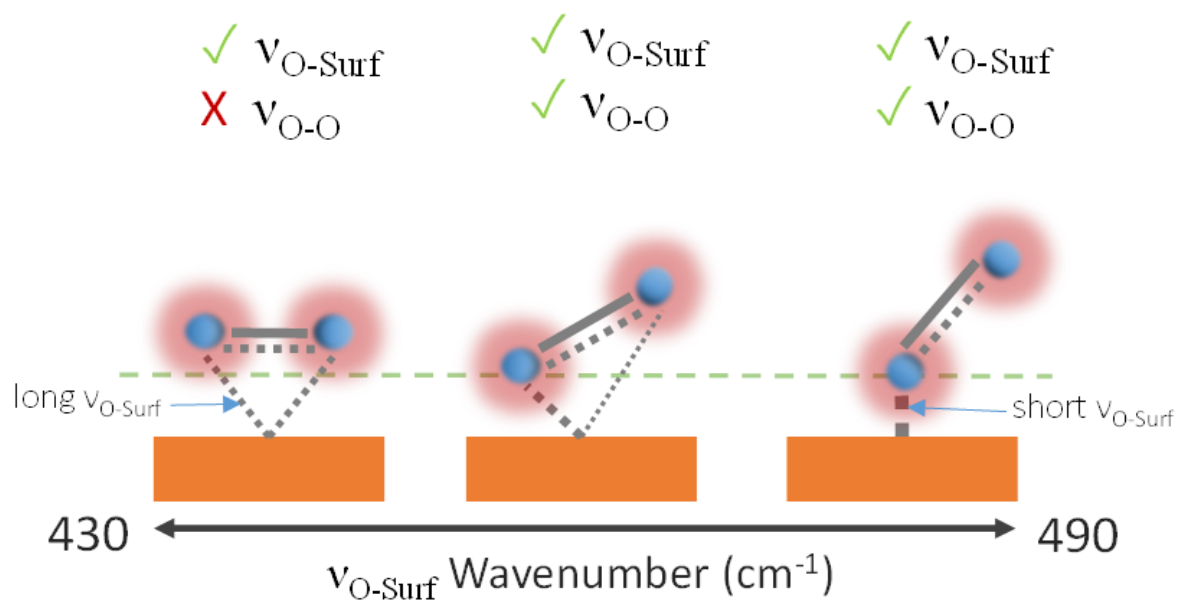


Figure 4. 5. O_2^x -surface bond structures, left to right: flat, kinked and bent. Visible bond vibrations based on the surface selection rule are shown above each structure.^{7,509,511} The tick and cross indicate which band will be observable by Raman.

For $\text{Aze}_{14}\text{TFSI}$, both $\nu_{\text{O-Surf}}$ and $\nu_{\text{O-O}}$ peaks were seen to red-Stark shift with decreasing surface potentials. Shifting the electrode potential negative, increasing the Fermi level of electrode surface, induces Coulombic repulsion between the surface and adsorbed anions and negative dipole moments on molecules in the EDL. Poor electron accepting electrolyte (i.e. $\text{Aze}_{14}\text{TFSI}$), are less effective at balancing excess negative surface charge, and this increased surface electron density will be concentrated in, or transferred to, any free molecular orbitals in surface bonded or adsorbed species that are closest in energy to the surface. In the case of $\text{O}_2^{\bullet-}$ this is the π^* orbital. Therefore, back-bonding increases with decreasing potentials and the bond becomes longer and increasingly kinked. This can also be explained as the increasingly negative surface charge contributes more electron density to surface adsorbed species, reducing the effective nuclear charge experienced by valence bond electrons, causing both the O-O and O-Surf bonds to weaken and lengthen, visible by decreasing frequency $\nu_{\text{O-O}}$ and $\nu_{\text{O-Surf}}$ peaks. Hence the concomitant red-Stark shift occurs in the $\nu_{\text{O-O}}$ bond vibrations of $\text{O}_2^{\bullet-}$ close to the surface at more negative potentials. This charge localisation on $\text{O}_2^{\bullet-}$ at low potentials is indicative of a more Lewis basic species being generated at the surface with a weaker adsorption bond.

For TESTFSI, which is the most electron accepting IL electrolyte investigated herein, $\nu_{\text{O-Surf}}$ is significantly lower than $\text{Aze}_{14}\text{TFSI}$ ($\sim 16\text{-}27 \text{ cm}^{-1}$), suggesting $\text{O}_2^{\bullet-}$ valence electron density interacts more with the electrolyte than the surface and has a weaker adsorption bond with a kinked structure and some surface back bonding. An additional shoulder at $\sim 430 \text{ cm}^{-1}$, labelled peak 1 (see Fig. 4. 6 and area highlighted in light grey on Fig. 4. 3a and 4. 4a), is also present at OR/ER surface potentials above 1.8 V vs. Li^+/Li . Peak 1 has been characterised previously as a conformationally flat $\text{O}_2^{\bullet-}$ surface species on catalytically active Pt and Pd surfaces using SHINERS.⁴⁶² As stated, when the O-O bond is parallel to the surface, the O-surface bond must

be longest and therefore possess the lowest frequency. It is clear from the spectra (Fig 4.6) that the signal from the O-O bond is much reduced when the longer flat O-surface bond (peak 1) is present at $\sim 430\text{ cm}^{-1}$. This implies that the surface normal polarizability component of a surface-parallel O-O is very small. One possible explanation could be that the electric field of the Raman laser needs to be parallel to this bond for maximum Raman signal, but surface-parallel fields do not get enhanced by surface plasmons. Therefore, $\nu_{\text{O-O}}$ would be absent or weak when a conformationally flat species is prominent at the surface. This was indeed the case when holding the potential at onset reduction potentials (Fig. 4. 6). However, at the same potential during cycling only a mixed (predominantly kinked) species is present (Fig. 4. 3a). Therefore, the kinked structure appears to be kinetically more stable during potential cycling when the double layer is in flux, yet when the potential is held, and the double layer equilibrates, the $\text{O}_2^{\bullet-}$ relaxes to a conformationally flat species at ORR onset potentials. Peak 1 was visible at onset potentials in TESTFSI electrolyte, but not in $\text{Aze}_{14}\text{TFSI}$ or any of the other ILs. However, this effect was also present and far more pronounced in other solvent blended electrolytes evaluated in the following chapter. At extremely low potentials, below 1.8 V vs Li^+/Li , peak 1 disappears completely with only the $\nu_{\text{O-O}}$ (kinked) species visible. Blue-Stark shifts in both $\nu_{\text{O-O}}$ and $\nu_{\text{O-Surf}}$ were also present with decreasing potentials. These observations suggest that the flat surface bond becomes less kinked and back bonding with the surface decreases with decreasing potential, the opposite of what was observed in $\text{Aze}_{14}\text{TFSI}$.

Counterintuitively, this would suggest that the π^* orbital is being depleted of charge as the surface becomes increasingly more negative. This may be accounted for by considering changes within the EDL. When the surface potential is decreased the IL EDL becomes increasingly populated with positively charged species⁴²⁸ and, if possible, anions reorientate or are expelled⁵⁰⁶ in order to balance surface charge. TESTFSI is a more accepting electrolyte

with a lower viscosity and faster reaction kinetics (visible by more reversible CVs) than in Aze₁₄TFSI. Therefore, surface charge is well compensated for by the electrolyte and not concentrated on O₂⁻ at low potentials. The increased and decreased presence of cations and anions, respectively, in the EDL produces a better coordinated O₂⁻ species that is more bent bonded with reduced back-bonding.

This was apparent in TESTFSI (Fig. 4. 3a and b) by a continuous decrease in the intensity of characteristic δCF_3 (740 cm⁻¹) and ωSO_2 (400 cm⁻¹) vibrations of the TFSI anion⁵¹² with lowering of potential. Both anion peak intensities increased again when the direction of potential scanning was reversed due to the anion repopulating the double layer. Furthermore, as the potential decreased, a broad Au-S adsorption band from the S in the TES cation (200-300 cm⁻¹) appeared with ORR, indicative cation adsorption and its increased population in the double layer (Fig. 4. 4a and b). In addition, the intensity of electrolyte related peaks 2-4 of TESTFSI mirrored the intensity changes in the v_{O-Surf} bond vibration as discussed. Similar electrolyte conformational changes were present, but much more difficult to observe in Aze₁₄TFSI as shown in the contour plots in Figure 4. 2 c and d, due to the greater signal to noise ratio. That said, reduction of the TFSI⁻ spectral bands with decreasing surface potentials was minimal suggesting poor anion depletion in the EDL.

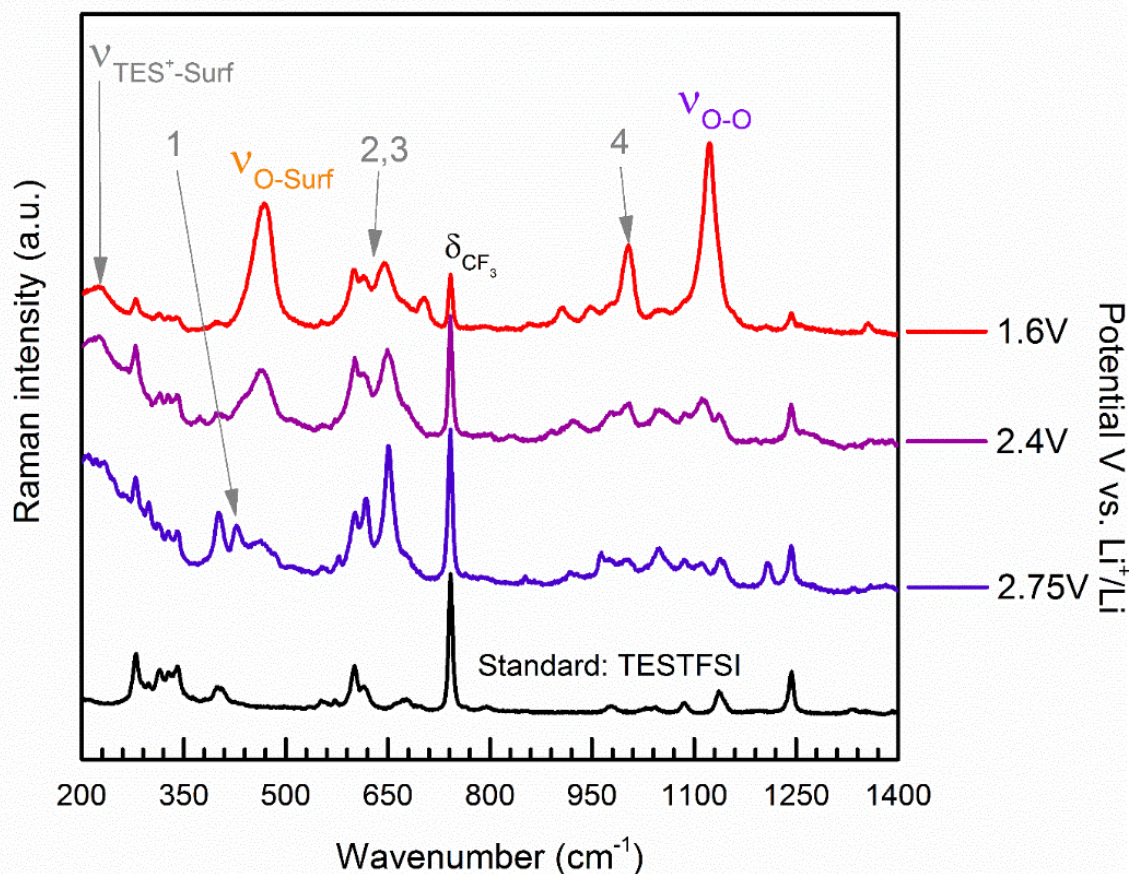


Figure 4. 6. Extended spectra acquired with surface potential control at specified held ORR potentials in O₂ saturated TESTFSI. Standard (black line) refers to TESTFSI at OCP.

Other ILs

Figure 4. 7a shows clearly the appearance of characteristic ν_{O-O} and $\nu_{O-Surf} O_2^{\cdot-}$ spectral bands at ORR potentials detected in all other tested ILs. Comparing the ν_{O-O} band between ILs, there is a shift to lower wavenumbers in the order; $TES^+ > Pyrr_{14}^+ > Pip_{14}^+ > Aze_{14}^+$, correlating well with increases in their respective \mathbb{K}_{iv}^c values ($17,704 > 26,060 > 31,826 > 36,929 \text{ g mol}^{-1} \text{ n}^{-1} \text{ \AA}^3$, respectively). This trend is in accord with the observations of the cation's influence on ν_{O-O} discussed in the previous chapter (ν_{O-O} values summarised in Table 4. 8). One apparent anomaly to the ν_{O-O} trend is the N_{1444}^+ based IL which, compared with the cyclic amine cations, has a high ν_{O-O} value ($\sim 1,108 \text{ cm}^{-1}$) considering its large \mathbb{K}_{iv}^c value ($53,492 \text{ g mol}^{-1} \text{ n}^{-1} \text{ \AA}^3$). This can be accounted for by the partial-symmetry of the cation. N_{1444}^+ and TES^+ both have relatively symmetric structures with an axis of partial-symmetry (Fig. 4. 8a and b) compared with the cyclic amines (Fig. 4. 8c and d) which do not.

All ν_{O-O} values for $O_2^{\cdot-}$ complexes plotted on the charge dispersion line from chapter 3 (Fig. 3. 3b) had symmetrical coordinating-cations. Plotting these values alongside the average ν_{O-O} value for each IL (Fig. 4. 7c), using the respective \mathbb{K}_{iv}^c values of each IL cation, (Fig. 4. 7c and d); two trend-lines are for (A) asymmetric cations ($Pyrr_{14}TFSI$, $Pip_{14}TFSI$ and $Aze_{14}TFSI$) and (B) ILs with partially-symmetric cations ($TESTFSI$ and $N_{1444}TFSI$). The partially-symmetric cations, have a ν_{O-O} trend close-to/parallel with the \mathbb{K}_{iv}^c trend line derived in chapter 3, and are in good agreement with it. However, the asymmetric cyclic amines cations diverge from the trend with lower than expected bands for their respective \mathbb{K}_{iv}^c values indicative of weakly coordinated, more Lewis basic, $O_2^{\cdot-}$ species being generated at the electrode surface. Considering the well-known effect ion asymmetry has on disrupting inter-ion interactions this can account for the weaker cation- $O_2^{\cdot-}$ interactions and lower ν_{O-O} values in line with the overall trend: weak $O_2^{\cdot-}$ coordination \rightarrow more Lewis basic $O_2^{\cdot-}$ species \rightarrow lower ν_{O-O} value.

It is no surprise to see cation symmetry influences on ν_{O-O} as they are well known (especially in the IL literature) to influence inter-ion interactions i.e. asymmetrical ions are less able to coordinate counter ions repetitively and resulting in weaker interactions and lower melting points. Therefore, decreasing the symmetry of the coordinating cation, like increasing its \mathbb{K}_{iv}^c , can weaken the cation-to- O_2^- interaction and produce a freer more ionic, harder Lewis base, O_2^- species at the electrode surface. Quantifying a value that approximates an ion's symmetry and incorporating it into the \mathbb{K} concept may be a useful method for further refining this concept and potentially bring the ν_{O-O} values in the cyclic amine based ILs into alignment with the overall trend.

For the ν_{O-surf} band a slightly different trend is visible (Fig. 4. 7a). All the ammonium-based cations ($Pyrr_{14}^+$, Pip_{14}^+ , Aze_{14}^+ , N_{1444}^+) had similarly high peak positions ($479\text{-}490\text{ cm}^{-1}$) that red-shift with potential, indicating a bent bonded surface species. Whilst the more accepting TES $^+$ had lower bands indicative of a kinked surface species. Therefore, O_2^- has a similar O-to-surface bond structure in the ammonium cation based ILs, suggesting they are all poor at balancing changes in the surface potential and coordinating surface O_2^- . This is supported by lower half-potentials ($E_{1/2}$) and higher OR/ER peak separations (ΔE), indicative of less reversible reactions requiring larger overpotentials in the ammonium cation based ILs compared with TESTFSI (Fig. 4. 7b, Table 4. 4). Thus, O_2^- coordination can be manipulated by the IL electrolytes in a detectable way and can be used as a diagnostic molecule to probe the IL-cation interactions during OR/ER.

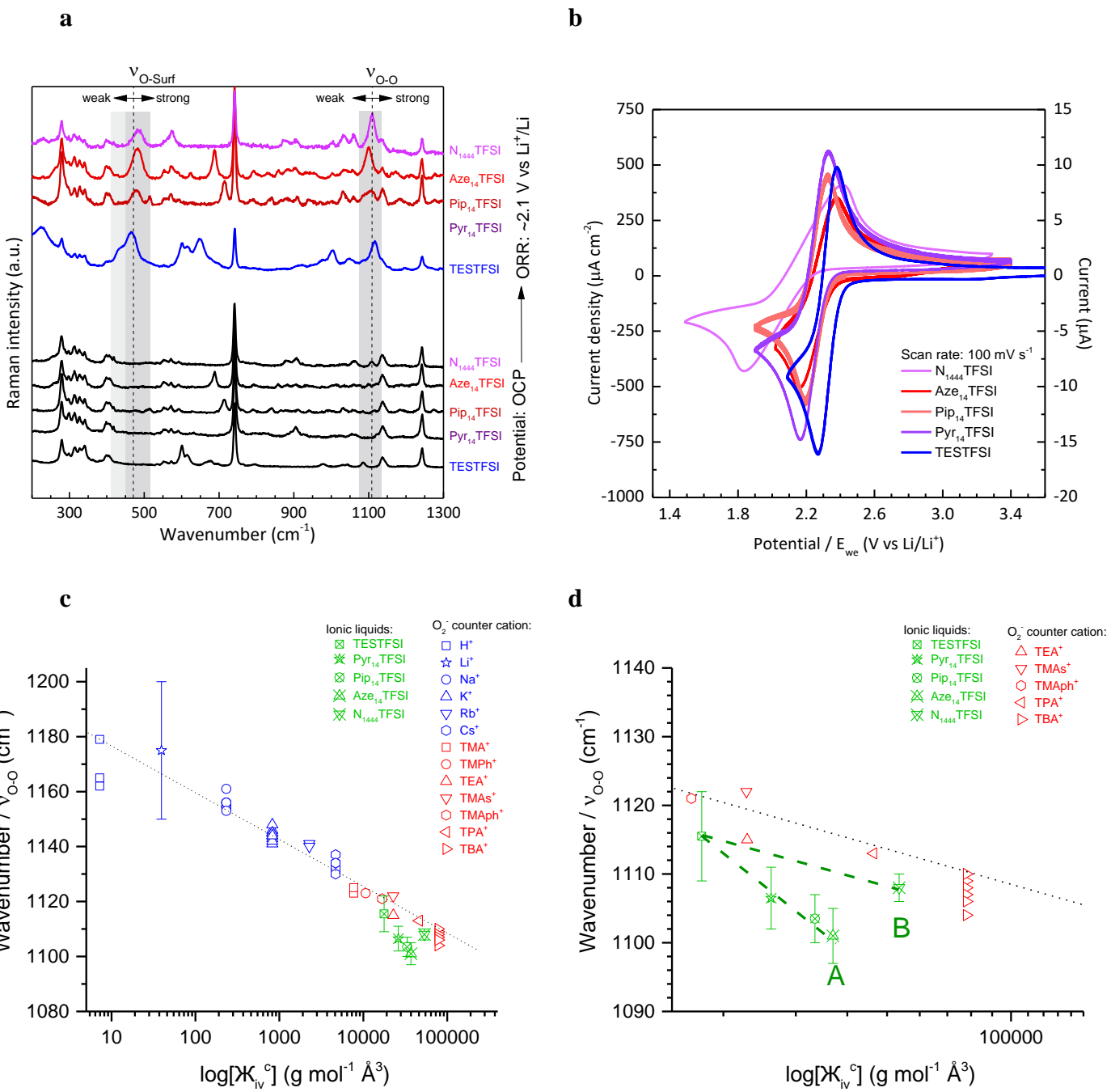


Figure 4.7. (a) Stacked spectra of rAu surface at OCP and ORR potentials in cation-varied ILs. Dashed lines demarcate weak and strong v_{O-O} and v_{O-Surf} bands (light grey and grey). (b) CV comparison of OR/ERs in O_2 saturated cation-varied ILs cycled at 100 mV s^{-1} . (c) Average v_{O-O} values for ILs plotted on Figure 3. 3b. Calculated trend-line shown (black dotted line). Error bars indicate range over which v_{O-O} shifted with potential. (d) Close-up of IL section. Subs-trends (green dashed lines) for asymmetrical and partially-symmetrical cation containing ILs are denoted by A and B, respectively. All spectral bands are summarised in Table 4.8.

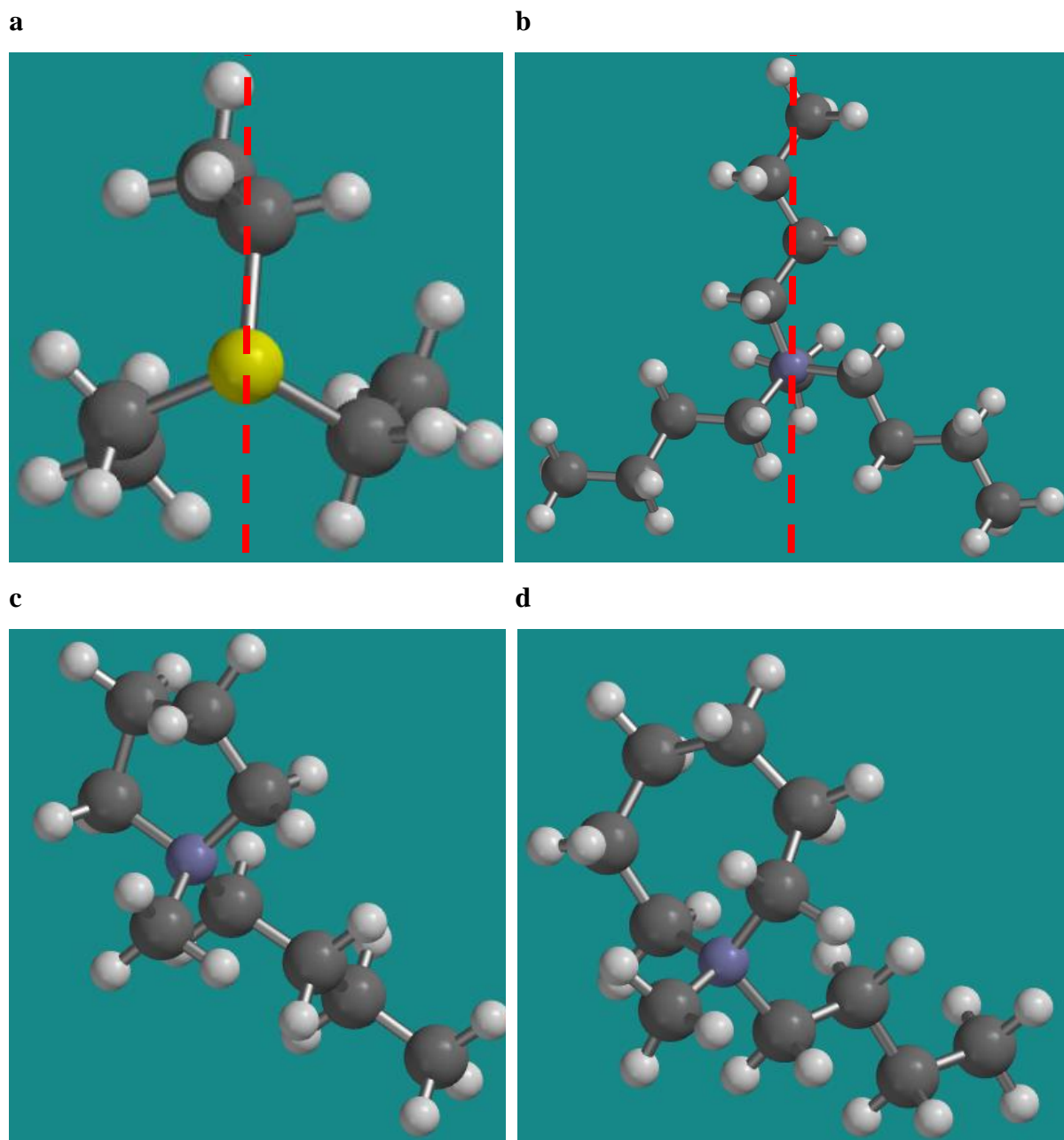


Figure 4.8. Cation structures generated in Spartan 15: (a) TES⁺ (b) N₁₄44⁺ (c) Pyr₁₄⁺ (d) Aze₁₄⁺. Partial-symmetry axis shown by red-dashed line.

Electrochemistry

Comparing the OR/ER CVs at multiple scan rates (20, 50, 100 mV s⁻¹) in each cation varied IL (Fig. 4. 9), electrochemical parameters (Table 4. 4) were elucidated and contrasted with the five diagnostic criteria of an electrochemically reversible system (Table 4. 5).

No IL met criterion 1 of cathodic-anodic potential peak separations (ΔE) of 59 mV for one electron OR/ERs, suggesting the rate of electron transfer is insufficient to maintain equilibrium at the electrode surface and an overpotential is required to drive OR/ERs.⁵¹³ Of the ILs; TESTFSI required the lowest overpotential and N₁₈₈₈TFSI the highest (Table 4. 4). For criterion two, cathodic and anodic current ratios (i_p^c/i_p^a) that diverge from a value of 1 indicate cycling inefficiencies and possible electrolyte instability/irreversible side-reactions. N₁₄₄₄TFSI, Pip₁₄TFSI and Pyr₁₄TFSI matched this criterion and N₁₄₄₄TFSI had a value close to 1, whilst TESTFSI and Aze₁₄TFSI had slightly lower values and were the least electrochemically efficient. However, they still cycled well (+50 cycles) without any noticeable change in their OR/ER CV profiles indicating any side products that may be formed are soluble and not passivating the electrode surface. Criterion three was satisfied by all the ILs as the current for OR/ERs increased proportionally with the square-root of the scan rate. Criterion four was almost met by TESTFSI, though not by any other IL, as OR/ER peak potentials (E_p) were not constant and shifted with increasing scan rates. Criterion five was satisfied by all the ILs, as beyond the OR/ER potential peaks the current falls off proportionally with the square-root of time. Overall, as the ILs cation size increased, the OR/ERs reversibility decreased, also the ORR onset potential and $E_{1/2}$ shifted to lower potentials in agreement with the observed relationship between the electrolytes $E_{1/2}$ for OR/ERs and decreasing electrolyte ANs observed by Kwabi *et al.* further supporting the relationship between the IL cation and its AN.⁶⁷

Due to two or more of the criteria not being met in all the ILs, the OR/ERs cannot be said to be reversible and the Randle-Sevcik relationship does not apply. Although, criteria three and five are met in all ILs, whilst criterion one is approached at lower scan rates in TESTFSI and criterion two is met by most of the ILs, therefore, the electrolytes can be said to be quasi-reversible²³ showing some properties of fast electron transfer kinetics but possibly poor diffusivity of redox species to the electrode surface during cycling due to the large sizes of the IL ions and the high viscosity of the liquids slowing ion diffusivity, or a mixture of both. From the relative symmetry of the current peaks ratios (i_p^a/i_p^c) it can also be assumed that the one electron OR/ERs are occurring. The electrochemical potential window (E_{window}) of all Ar-saturated ILs at 20 mV s⁻¹ (Fig. 4. 9) was also determined (Table 4. 4). All ILs had large (> 3.0 V vs. Li⁺/Li) E_{window} values which support OR/ERs and are much higher than many conventional organic electrolytes. TESTFSI had the smallest E_{window} with a lower anodic limit than the other ILs, indicating TES⁺ is more readily reduced (3.5 V vs. Li⁺/Li) than the larger ammonium cations (> 4.0 V vs. Li⁺/Li). The E_{window} anodic limit of all the ILs due to TFSI⁻ reduction were all similar (0-0.5 V vs. Li⁺/Li). The lack of secondary peaks in OR/ER CVs and the continuous cyclability (> 20 cycles at 20 mV s⁻¹) with minimal capacity loss in all ILs indicates the electrolytes show good electrochemical stability. It should also be noted that ORR peak currents (E_p^c) were markedly lower in ILs with larger (less accepting) cations, indicating a link between the cation and the concentration/solubility of electrochemically generated O₂^{•-}.

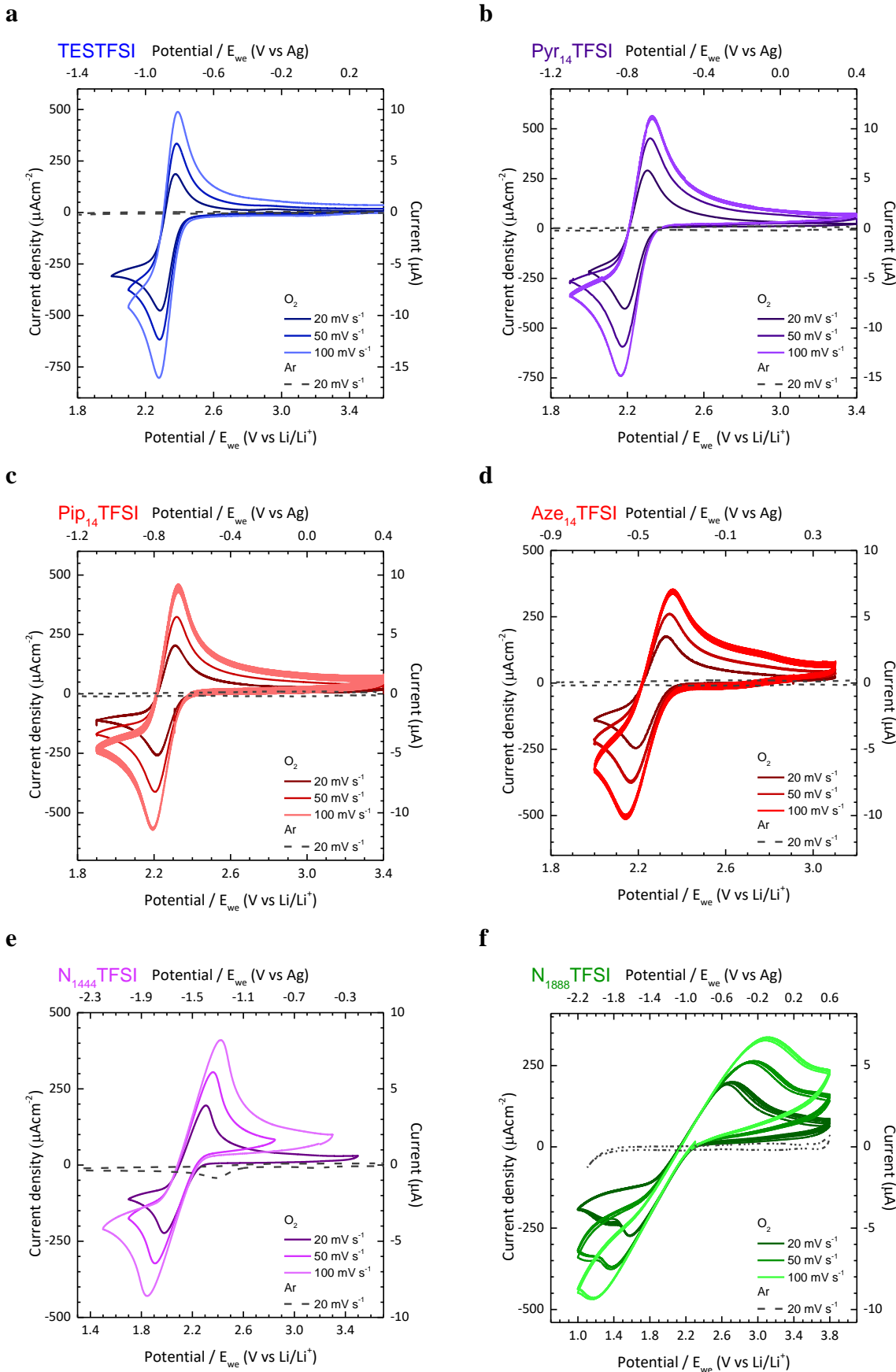


Figure 4. 9. OR/ER CVs at 20, 50 and 100 mV s⁻¹ at an rAu electrode in O₂ saturated ILs: **(a)**

TESTFSI, (b) Pyr₁₄TFSI, (c) Pip₁₄TFSI, (d) Aze₁₄FSI, (e) N₁₄₄₄TFSI, (f) N₁₈₈₈TFSI. Ar-saturated E_{window} also shown (dark grey dashed lines).

Table 4. 3. OR/ER electrochemical parameters from IL CVs in Figures 4. 9. Scan rates: 20/100 mV s⁻¹. Potentials corrected versus ferrocene redox couple.

ILs	E _p ^c (V vs Li/Li ⁺)	E _p ^a (V vs Li/Li ⁺)	E _{1/2} (V vs Li/Li ⁺)	ΔE (mV)	i _p ^c (μA cm ⁻²)	i _p ^a (μA cm ⁻²)	i _c / i _a	E _{window}
N ₁₈₈₈ TFSI	1.57/1.15	2.71/3.10	2.14/2.13	1,140/1,950	-276/-473	264/425	0.96/0.90	3.6
N ₁₄₄₄ TFSI	1.97/1.84	2.39/2.41	2.18/2.13	424/570	227/-434	226/433	1.00/1.00	5.4
Aze ₁₄ FSI	2.19/2.14	2.33/2.36	2.26/2.25	136/215	-519/252	229/425	0.82/0.91	4.3
Pip ₁₄ TFSI	2.22/2.19	2.31/2.33	2.26/2.26	94/132	-265/-576	262/570	0.99/0.99	4.5
Pyr ₁₄ TFSI	2.20/2.18	2.32/2.35	2.25/2.26	117/160	-406/-748	398/732	0.98/0.98	5.7
TESTFSI	2.28/2.28	2.38/2.39	2.33/2.33	90/114	-480/-809	419/706	0.87/0.87	3.35

Table 4. 4. Overview evaluating reversibility of CVs and which diagnostic criteria were met in each ILs in Figure 4. 9.

ILs	(1) ΔE _p = 59/n(mV)	(2) i _p ^a /i _p ^c = 1	(3) i _p ∝ v ^{1/2}	(4) E _p independent of v	(5) beyond E _p , i ∝ t ^{1/2}
N ₁₈₈₈ TFSI	×	≈	✓	≈	✓
N ₁₄₄₄ TFSI	×	✓	✓	✗	✓
Aze ₁₄ FSI	×	✗	✓	✗	✓
Pip ₁₄ TFSI	×	✓	✓	✗	✓
Pyr ₁₄ TFSI	×	✓	✓	✗	✓
TESTFSI	×	✗	✓	✗	✓

Where: ✗ denotes criteria not met, ✓ denotes criteria met and ≈ approximately meets criteria.

4.3.2 Anion Effect

In addition to the IL cation, the influence of the IL anion on OR/ERs has also been investigated. Three different ILs with Pyr_{14}^+ cations and different anions (TFSI^- , OTf^- , DCA^-) are compared to probe the effect reducing the anion size (and K_{iv}^{a}) on O_2^\cdot generated at the electrode surface and its characteristic spectral bands. Schmeisser *et al.* showed a correlation between the IL anion's ability to donate electron pairs and the overall DN of the IL.⁴⁰⁷ Generally, ILs with smaller, more Lewis basic anions, had higher DNs. In addition, the dominant donating atom in the anion also has a strong influence on each respective ILs DN, with the greatest electron donor sites being in order $\text{N} > \text{O} > \text{F}$.⁴⁰⁷ Of the anions tested DCA^- (DN: 32) can be considered an N site donor, OTf^- (DN: 16) an O site donor and TFSI^- (DN: 5) an F site donor (K_{iv}^{a} : 4,295, 12,455 and 43,014 g mol⁻¹ Å³ respectively).⁴⁰⁷

Results and discussion

In the cation study, above, the weakly coordinating TFSI^- anion was present in each IL and any anion interference in $\text{C}^+ \cdots \text{O}_2^\cdot$ coordination was assumed to be negligible. However, smaller, harder Lewis base, IL anions can be expected to either influence O_2^\cdot directly through coulombic repulsion or indirectly by more strongly coordinating the IL cation, in turn, reducing its ability to coordinate O_2^\cdot , producing a more basic O_2^\cdot species at the electrode surface. Compared with $\text{Pyr}_{14}\text{TFSI}$ (1,112-1,105 cm⁻¹), this anion effect on O_2^\cdot was observed with lower $\nu_{\text{O-O}}$ values in both $\text{Pyr}_{14}\text{DCA}$ (1,103-1,094 cm⁻¹) and $\text{Pyr}_{14}\text{OTf}$ (1,104-1086 cm⁻¹) detected during ORR (Fig. 4. 10, Table 4. 8). All three ILs had similar $\nu_{\text{O-Surf}}$ bands (~494-476 cm⁻¹) and both $\nu_{\text{O-O}}$ and $\nu_{\text{O-Surf}}$ bands red Stark-shifted with potential, starting high and decreasing during the reduction scan before returning to higher values again on the oxidation scan, indicating a weakening and lengthening of both O-O and O-Surface bonds with decreasing potential. $\text{Pyr}_{14}\text{DCA}$ had the lowest $\nu_{\text{O-O}}$ value at ORR onset (1,103 cm⁻¹) however,

$\text{O}_2^{\cdot-}$ generated in $\text{Pyr}_{14}\text{OTf}$ was much more susceptible to changes in potential with a $\nu_{\text{O-O}}$ value of $1,089 \text{ cm}^{-1}$ detected at 1.8 V vs Li/Li^+ , indicative of a free, highly ionic $\text{O}_2^{\cdot-}$ species. It is unclear why the potential shift was greater in $\text{Pyr}_{14}\text{OTf}$, however, this may be due to the OTf⁻ having a higher Kamlet-Taft β -parameter value than the other anions.⁴⁰⁷ The Kamlet-Taft β -parameter is an empirically derived value for approximating a solvent's hydrogen bond acceptance. Though DCA⁻ has the highest reported DN of the IL anions tested, the higher β -parameter of OTf⁻ would indicate stronger interactions with C-H bonds on the cation which is more present at the surface at lower potentials, reducing the cations ability to coordinate $\text{O}_2^{\cdot-}$.

It should be noted that $\text{Pyr}_{14}\text{DCA}$ is highly hygroscopic and we were unable to dry our samples below 50 ppm using our drying apparatus, as such a $\nu_{\text{O-O}}$ band at $1,179 \text{ cm}^{-1}$ (marked by an asterisk in Figure 4. 10a), attributed to hydrogen superoxide (HO_2), was present at all ORR potentials in addition to the free $\nu_{\text{O-O}}$.

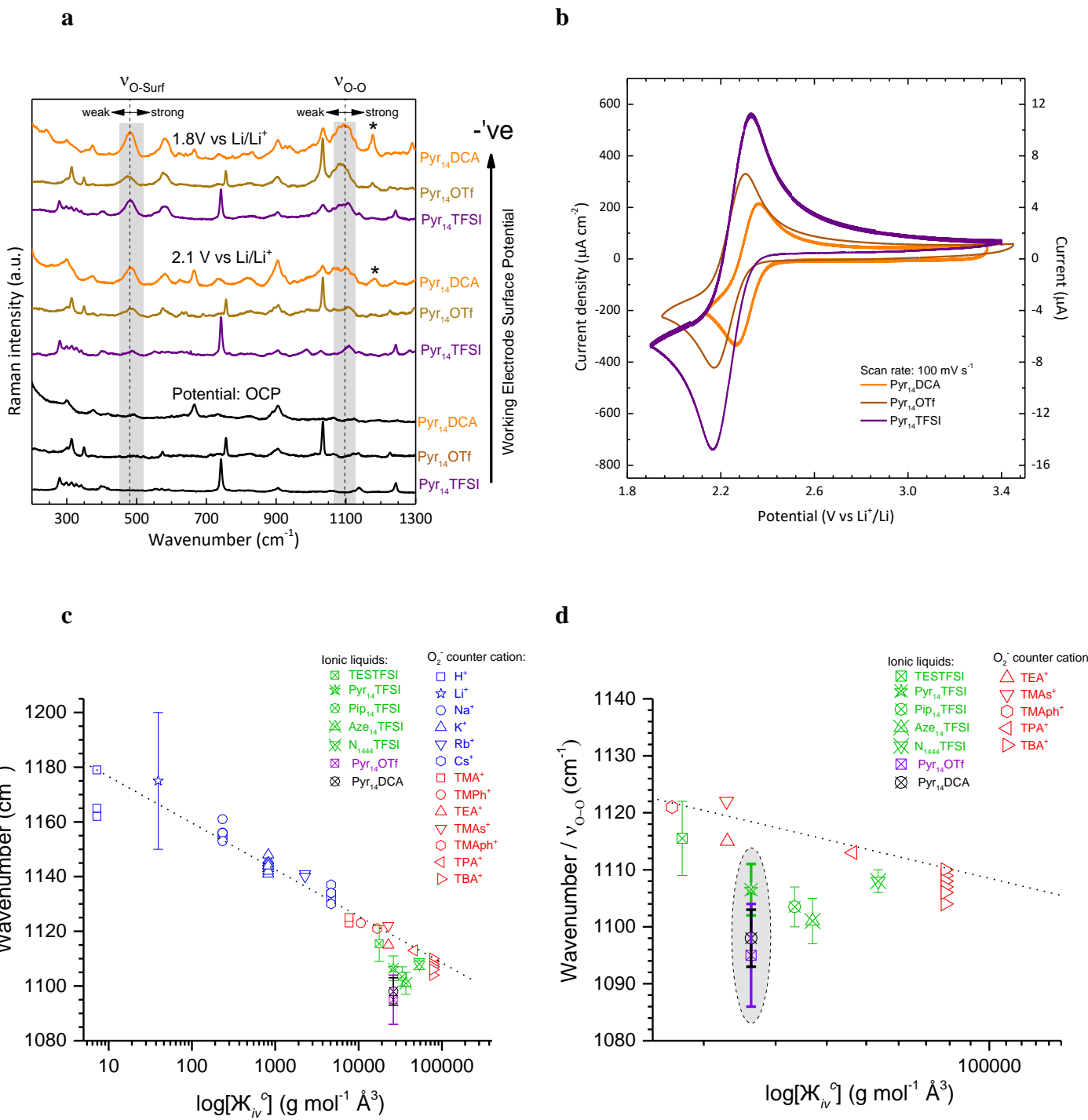


Figure 4. 10. **(a)** Stacked spectra of rAu surface at OCP and ORR potentials (2.1 and 1.8 V vs. Li/Li⁺) in various ILs with different anions. **(b)** CV comparison of OR/ERs in O₂ saturated anion-varied ILs at 100 mV s⁻¹. **(c)** Average v_{O-O} values for ILs plotted on v_{O-O} graph outlined in Figure 3. 3b with the calculated trend line shown (black dotted line). Error bars indicate range over which v_{O-O} shifted with potential in each IL. **(d)** Close-up of the section pertaining to the ILs. Anion based ILs highlighted in grey

Electrochemistry

Comparing the OR/ER CVs at multiple scan rates ($20, 50, 100 \text{ mV s}^{-1}$) in each anion varied IL (Fig. 4. 11), electrochemical parameters (Table 4. 6) were elucidated and contrasted with the five diagnostic criteria of an electrochemically reversible system (Table 4. 7).

OR/ER in all the ILs can be considered quasi-reversible as electrochemical reversibility criteria 2 and 4 were met in all ILs, however, the other criteria varied. The current passed (i_p^c) during ORR is proportional to the concentration and solubility of O_2^{+} generated. It is interesting to note that i_p^c decreased in the order $\text{Pyr}_{14}\text{TFSI} > \text{Pyr}_{14}\text{OTf} > \text{Pyr}_{14}\text{DCA}$ (Fig. 4. 10b). This continues the trend observed in the cation study i.e. as the size of the IL cation increased the i_p^c generally decreased, whereas, here as the anion size increased i_p^c increased, suggesting a relationship between both the cation, anion and O_2^{+} solubility.

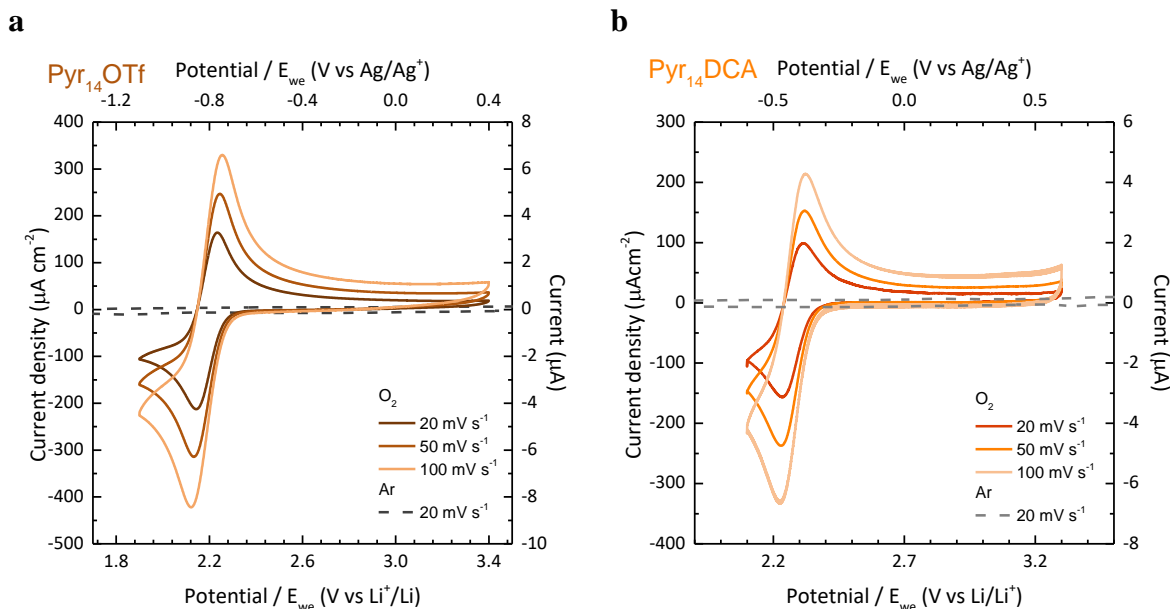


Figure 4. 11. OR/ER CVs at $20, 50$ and 100 mV s^{-1} at an rAu working electrode in O_2 saturated ILs: **(a)** Pyr₁₄OTf and **(b)** Pyr₁₄DCA with different anions. Ar-saturated E_{window} also shown (dark grey dashed lines).

Table 4. 5. OR/ER electrochemical parameters from anion varied IL CVs. Scan rate: 20/100mV s⁻¹. Potentials corrected versus fc⁺/fc redox couple.

ILs	E _p ^c (V vs Li/Li ⁺)	E _p ^a (V vs Li/Li ⁺)	E _{1/2} (V vs Li/Li ⁺)	ΔE (mV)	i _p ^c (μA cm ⁻²)	i _p ^a (μA cm ⁻²)	i _p ^a / i _p ^c	E _{window}
Pyr14TFSI	2.20/2.18	2.32/2.35	2.25/2.26	117/160	-406/-748	398/732	0.98/0.98	5.7
Pyr14OTf	2.19/2.17	2.28/2.30	2.24/2.24	93/133	-216/-426	202/392	0.94/0.92	4
Pyr14DCA	2.27/2.26	2.35/2.36	2.31/2.31	92/98	-158/-337	132/261	0.83/0.77	3.1

Table 4. 6. Table outlining five diagnostic criteria for evaluating reversibility of IL CVs of three anion varied ILs.

ILs	(1) ΔE _p = 59/n(mV)	(2) i _p ^a /i _p ^c = 1	(3) i _p ∝ v ^{1/2}	(4) E _p independent of v	(5) beyond E _p , i ∝ t ^{1/2}
Pyr ₁₄ TFSI	×	✓	✓	×	✓
Pyr ₁₄ OTf	×	≈	✓	×	✓
Pyr ₁₄ DCA	×	×	✓	≈	✓

Where: × denotes criteria not met, ✓ denotes criteria met and ≈ approximately meets criteria.

4.3.3 Summary

Comparing ν_{O-O} in each IL; (1) increasing the IL cation size, (2) decreasing the IL cation symmetry and (3) decreasing the IL anion size and Lewis basicity/DN was observed to reduce the ν_{O-O} spectral band position (due to decreased coordination) of surface O_2^{*-} produced during ORR. Comparing CVs of each IL, ORR i_p^c also generally decreased, as O_2^{*-} coordination and ν_{O-O} values decreased indicating poor coordinating ILs also had weak O_2^{*-} solvation. Characteristic ν_{O-Surf} bands were observed concomitantly with ν_{O-O} during ORR and provided O-to-surface bonding and structural information. High bands ($> 480 \text{ cm}^{-1}$) indicate strong bent O-surf bonds, low values ($< 465 \text{ cm}^{-1}$) indicate kinked bonds and bands below 440 cm^{-1} indicate flat O_2^{*-} surface species. Stark shifts are a surface specific phenomenon indicative of species in the EDL being manipulated by changes in surface potential. All ILs with ammonium-based cations had relatively high ν_{O-Surf} and generally low ν_{O-O} bands that red-Stark shifted with decreasing potentials due to the IL electrolyte's inability to balance surface charge via EDL rearrangement alone, causing increased back-bonding of electrons into the $O_2^{*-} \pi^*$ orbital and increased Coulombic repulsion with the surface, causing both the O-Surf and O-O bonds to lengthen. Blue-Stark shifts in ν_{O-O} and ν_{O-Surf} bands were observed with decreasing potential in TESTFSI due to the increased cation and decreased anion presence in the EDL respectively, balancing surface potential. Depletion of the $O_2^{*-} \pi^*$ orbital via increased cation coordination reduced surface back bonding and caused both O-Surface and O-O bonds to shorten as potentials were decreased. All ILs were also tested for stability versus alkali metals (Li, Na, K) to determine their practicality in a non-aqueous M-O₂ batteries and all were stable after > 1 month with no noticeable change in the metal surface and IL. A summary of all spectral bands in each IL is given in Table 4. 8.

Table 4. 7. Summary of O₂^{•-} spectral bands in different ILs; wavenumber ranges ($\Delta\nu$) between lowest and highest peak fitted values due to potential shifts, full width half-maximum (FWHM) ranges and stability of IL when exposed to alkali metals.

Electrolytes	v _{0-Surf} (cm ⁻¹)	$\Delta\nu_{0-Surf}$ (cm ⁻¹)	FWHM (cm ⁻¹)	v ₀₋₀ (cm ⁻¹) (FWHM / cm ⁻¹)	$\Delta\nu_{0-0}$ (cm ⁻¹)	FWHM (cm ⁻¹)	Li, Na, K metal stability
Cation varied ILs:							
N ₁₄₄₄ TFSI	484-477	15	20-34	1,110-1,106	4	12-26	all stable
Aze ₁₄ TFSI	494-475	19	20-42	1,105-1,097	8	9-28	all stable
Pip ₁₄ TFSI	480-470	10	16-31	1,107-1100	7	20-58	all stable
TESTFSI	467-459	8	12-55	1,122-1,109	13	12-34	all stable
Anion varied ILs:							
Pyr ₁₄ TFSI	486-479	7	20-42	1,111-1,102	9	24-52	all stable
Pyr ₁₄ OTf	488-470	18	16-31	1,104-1,089	15	19-42	all stable
Pyr ₁₄ DCA	494-481	13	14-33	1,103-1,094	12	18-48	all stable

4.4 *In Situ* SEIRAS

To complement the observations of ion flux in the EDL observed using SERS, *in-situ* attenuated total reflection surface enhanced infra-red absorption spectroscopy (ATR-SEIRAS) was performed in a preliminary IL (Pyr₁₄TFSI). Though no O₂^{•-} spectral bands were observed (Fig. 4. 12), bands associated with the anion (1,210 and 1,358 cm⁻¹)⁵¹² visibly leave and appear at the surface at ORR (red) and OER (black) potentials respectively, when compared with spectra at OCP. Two additional weak peaks associated with the cation (1,468 and 2,953 cm⁻¹) also visibly appear at the surface at ORR. These support observations in TESTFSI using SERS (above) of EDL rearrangement; with cations and anions coming to and leaving the surface respectively, at ORR potentials and suggests that even in the weakly coordinating ILs there is still some EDL rearrangement though not to the same extent as in TESTFSI.⁴²⁸

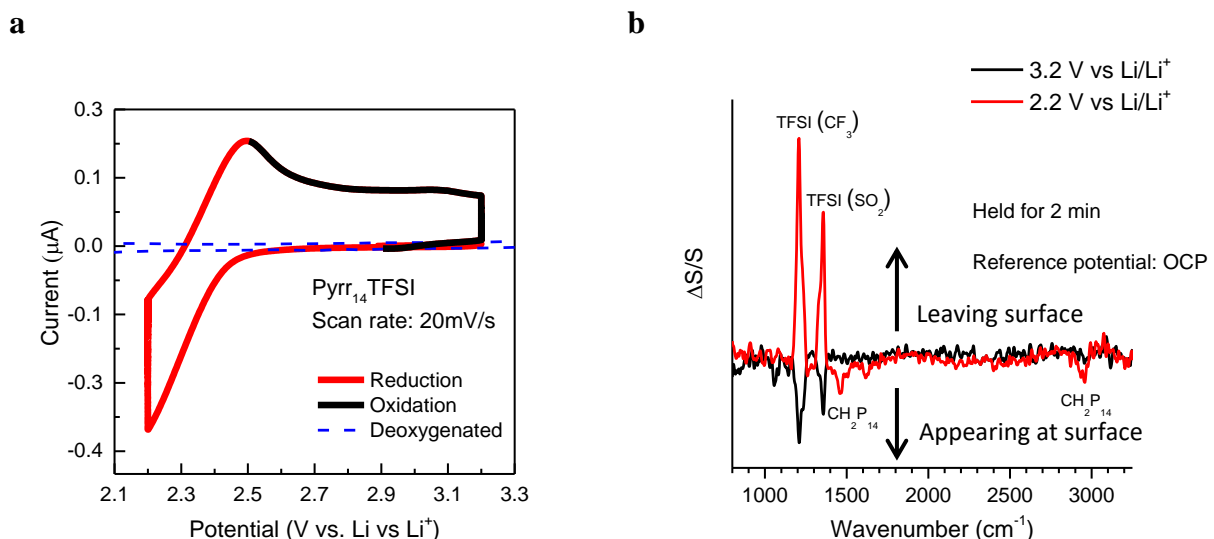


Figure 4. 12. (a) CV of OR/ER at 100 mV s⁻¹ scan rate on Au coated Si-prism, in O₂ saturated Pyr₁₄TFSI. Surface potentials were held at ORR (2.2 V vs Li/Li⁺, red line) and OER (3.2 V vs. Li/Li⁺, black line) potentials. (b) SEIRA spectra recorded for Au thin film at two representative electrode potentials. The reference spectra were taken at the OCP (3.1 V) before the potential sweep started. Work done in collaboration with V. Padmanabhan.

4.5 Conclusion

The one electron OR/ER mechanisms were studied in eight different ILs overall at a rAu electrode and the effect of the cation, anion and potential on surface generated O₂^{•-} was characterised by observing changes in its characteristic spectral bands. In the next chapter the influence of the solvent is probed and more ideal IL:solvent (IL:sol) electrolyte blends were formulated and optimised, using O₂^{•-} as a diagnostic molecule.

The cation, anion and surface potential effect on the radical character of O₂^{•-} was effectively probed in seven ILs using *in situ* SERS. Two ILs with differing properties Aze₁₄TFSI (soft cation), and TESTFSI (relatively hard cation), were investigated in-depth, as well as four ILs with varied cations and two with varied anions. Substantial surface enhancements to the Raman signal permitted the accumulation of a Raman spectra within ca. 1.4 seconds with sufficient signal-to-noise ratio for analysis of the electrode surface. This allowed the flux in surface speciation to be observed in real-time during dynamic potential cycling, for the appearance/disappearance of O₂^{•-} at OR/ER potentials and for the influence of the IL anion and cations at the surface to be evaluated.

The experimental trends provide insight into the nature of O₂^{•-} and its character in non-aqueous purely ionic electrolytes. By contrasting the surface adsorbed O₂^{•-} bands between the two ILs the ν_{O-O} bands were found to occur at a much higher wavenumber for TESTFSI (~1120 cm⁻¹) than in the Aze₁₄TFSI (~1105 cm⁻¹). This indicates that a more Lewis basic O₂^{•-} is generated at the rAu electrode surface in Aze₁₄TFSI than TESTFSI due to it being less strongly coordinated by the Aze₁₄⁺ counter cation. O₂^{•-} can thus be used as a diagnostic molecule to probe the strength of the IL electrolyte interaction and can be used in more complex blended electrolytes to help guide the tailoring process (next chapter). Like ν_{O-O}, there were differences in the ν_{O-}

{Surf} band between TESTFSI than Aze₁₄TFSI (466 cm^{-1} vs. 488 cm^{-1}). Lower $\nu{\text{O-Surf}}$ wavenumbers indicate a longer, weaker O-to-surface adsorption bond. The change in the Lewis basicity of $\text{O}_2^{\bullet^-}$ at the interface depending on choice of IL opens a promising avenue of research, given the chemical flexibility of ILs to be able to ‘design’ an optimum electrolyte system that provides a stable ionic medium to permit long life and reversible cycling of non-aqueous Li-O₂ cells. If such an electrolyte can then also be tailored to provide acceptable levels of O₂ and O₂^{•-} solubility and diffusivity, then progress towards the realisation of practical non-aqueous Li-O₂ cells becomes a step-closer.

5. Tailoring IL Electrolytes

5.1 Overview

For non-aqueous Li-O₂ batteries, IL electrolytes with poor physicochemical properties (e.g. low O₂ solubility and diffusivity, high viscosity and slow OR/ER kinetics) can be improved using organic solvent electrolyte additives, whilst retaining desirable properties of the IL (e.g. good Li-metal stability). OR/ER electrochemistry in IL:sol blended electrolytes composed of a well characterised IL (Pyr₁₄TFSI) mixed with three different solvents: (1) MeCN; (2) DMSO; (3) TEGDME, were investigated to determine the effect the solvent additives have on the chemical nature of O₂^{•-} at the electrode surface. O₂^{•-} was generated electrochemically at the rAu working electrode surface and, using *in situ* SERS, its characteristic v_{O-O} and v_{O-Surf} spectral bands were probed. The DN and AN of the solvent additive was found to influence the spectral band positions and, thus, the character of O₂^{•-} generated at the working electrode surface. The solvent additive's effect on surface O₂^{•-} supports observations in the previous chapter that more electron accepting electrolyte components (whether ionic or molecular) will interact more strongly with O₂^{•-} and can be used to manipulate its Lewis basicity. Inversely, electrolytes with donating solvents generally had much weaker O₂^{•-} interactions.

Using O₂^{•-} as a diagnostic molecule to probe the electrolyte interactions with the understanding gained from the IL and blended electrolytes, more complex multi-component blends were formulated to optimise the electron accepting or donating character of the electrolyte and the Li⁺-OR/ER mechanisms in electrolytes containing Li-salts were investigated. Two optimised electrolyte formulations showed greatly improved electrochemistry compared with pure ILs, whilst retaining the IL's exceptional chemical stability in the presence of pure alkali-metals; both essential characteristics of practical non-aqueous M-O₂ batteries. A further heterogeneous blend (HetBlend) electrolyte, combining both the optimised accepting and donating blends together showed further improvements in performance due to accepting species aiding the

reduction reaction and O₂^{•-} solvation during ORR, whilst the presence of donating species supported the ORR solution mechanism by stabilising Li⁺ in solution.⁴ For selecting electrolyte components, a heuristic method is also outlined for tailoring complex IL/IL:sol blend electrolytes that can help guide future optimisation of the electrolyte for practical Li-O₂ and other M-O₂ batteries. This study provides an important advancement in understanding and formulating or “tailoring” of practical electrolytes.

5.2 Introduction

For the non-aqueous Li-O₂ battery, as discussed in detail previously, organic solvent based electrolytes with either high ANs or DNs have been shown to support a beneficial solution reaction mechanism by solvating O₂^{•-} intermediaries, producing large Li₂O₂ surface deposits and relatively high discharge capacities.^{4,88} Organic solvents have been shown to influence O₂^{•-} coordination and solvation, producing detectable differences in the characteristic v_{O-O} between electrolytes depending on their ANs and DNs.⁴ High AN solvents solvate O₂^{•-} well, evidenced by relatively high v_{O-O} values, whilst high DN solvents keep solvated Li⁺ bound in solution, producing weakly coordinated O₂^{•-} species, with low v_{O-O} values, that are also free to diffuse into solution during discharge. Many organic solvents with desirable electrochemistry that also support the solution mechanism (e.g. DMSO) are unstable in the presence of Li-metal, ruling them out as practical battery electrolyte solvents, which poses a major problem when selecting an electrolyte for non-aqueous Li-O₂ batteries. However, added in small quantities to chemically stable ILs, then organic solvents have the potential to boost the performance of IL electrolytes, whilst retaining the Li-metal stability intrinsic to ILs. Similarly, other organic solvents that may not support the solution mechanism but which have other desirable properties (e.g. MeCN which has high O₂ solvation) can also be used as additives in a similar fashion to further boost specific electrolyte properties and, thus, the overall performance of the electrolyte.

For IL electrolytes, considering the IL cation and anion trends in the previous chapter and work by Schmeisser *et al.*, a high AN IL electrolyte would comprise hard cations and soft anions, whereas a high DN IL electrolyte would comprise soft cations and hard anions. However a slight caveat, ILs with inordinately large ions or high viscosities can have a suppressed electron accepting/donating character, particularly at low temperature, as ions are unable to effectively

interact with one another due to high resistance to motion from large intermolecular forces.⁴⁰⁷

For the AN/DN of the IL cation/anions respectively, to be fully expressed in the electrolyte, low viscosities and fast ion diffusivities are required. However, this incorporates a trade-off into the IL electrolyte selection process as increasing the ion size in the high AN or high DN ILs, respectively, causes IL ion diffusivities to decrease and the melting point to increase etc.. Therefore, care must be taken when selecting the IL ions to constitute a pure high AN or high DN IL electrolyte. Organic solvents provide a convenient way of circumventing some physicochemical limitations inherent to IL electrolytes, which has been investigated in this chapter. O₂^{•-}, generated electrochemically and probed with *in situ* SERS, was used as a diagnostic molecule to track the electrolyte's influence on the relative coordination strength of a variety of different IL:sol blends and a number of optimised multi-component accepting and donating blends were formulated and screened against Li-metal. Li⁺-OR/ERs were also investigated spectroelectrochemically and provide evidence of desired reactions and greatly improved electrochemistry compared with pure ILs.

5.3 Solvent Effect

5.3.1 *In Situ* SERS of OR/ERs

Novel IL:sol (60:40 vol.% ratios, respectively) blend electrolytes were formulated using Pyr₁₄TFSI as the IL and different solvents, (1) MeCN, (2) TEGDME and (3) DMSO, to probe the solvents effect on OR/ERs. Characteristic v_{O-O} and v_{O-Surf} bands were visible in all blends at OR/ER potentials.

Blend (1) with MeCN, a low-DN (14.1) and mid-AN (18.6) solvent,⁶⁷ produced a more coordinated, less Lewis basic, O₂^{•-} surface species (Fig. 5. 1a) than the pure IL. Both v_{O-O} (1,115-1,124 cm⁻¹) and v_{O-Surf} (466-472 cm⁻¹) spectral bands appeared in similar regions to the accepting IL (TESTFSI), and similarly blue-shifted with potential indicating increased cation-O₂^{•-} coordination at the interface at low potentials. Blend (2) with TEGDME, a mid-DN (16.6) and low-AN (10.5) solvent,^{132,514} had similar v_{O-O} (1,107-1,101 cm⁻¹) and v_{O-Surf} (482-474 cm⁻¹) spectral bands to the pure IL that red-shifted with potential indicating minimal change in the strength of electrolyte-O₂^{•-} interactions i.e. a relatively strong Lewis basic O₂^{•-} surface species. Blend (3) with DMSO, a high-DN (29.8) and mid-AN (19.3) solvent,⁶⁷ produced a more strongly coordinated O₂^{•-} species than in the pure IL at ORR onset potentials likely due to its partially accepting character, however, at lower potentials it had similar v_{O-O} (1,117-1,101 cm⁻¹) and v_{O-Surf} (493-480 cm⁻¹) spectral bands to the pure IL which dramatically red-shifted indicating overall weak electrolyte-O₂^{•-} interactions.

Considering, DMSO and MeCN have similar AN values (18.8 and 19.2 respectively)⁶⁷ they would be expected to both interact similarly with O₂^{•-} which could explain the relatively high v_{O-O} (~1,117 cm⁻¹) value at onset ORR potentials in DMSO. However, DMSO has a much

higher DN than MeCN (29 and 14, respectively),⁶⁷ therefore, competes with O₂^{•-} to coordinate Pyr₁₄⁺, reducing the cation's coordination strength and thus indirectly producing a freer O₂^{•-} species, similar to the IL anion effect discussed in the previous chapter and this effect is likely amplified in the EDL at lower, more negative, surface potentials. Reducing the charge shared by O₂^{•-} with its electrolyte environment making it more radical, resulting in the difference in observed Raman peak positions between DMSO and MeCN based blends. Due to the influence of both the AN and DN on OR/ERs, a more detailed scale of the solvent's affinity for coordinating O₂^{•-} may be a AN:DN ratio relative to an accepting or donating standard electrolyte and will provide information on a solvent's overall charge preference.

Comparing CVs (Fig. 5. 1b) of different IL:sol blended electrolytes, ORR onset and E_{1/2} potentials decreased in order; IL:MeCN > IL:DMSO > IL:TEGDME > pure IL. In the IL:sol blend's, this trend in potential shifts correlates with the decreasing solvent ANs, matching previous observations by Kwabi *et al.* using TBA-salt based solvent electrolytes.⁶⁷ Positive shifts in ORR onset potentials indicate more thermodynamically favourable reaction mechanisms. Compared with the pure IL, all solvent blends had > 0.2 V higher ORR onset potentials and higher reduction currents due to higher O₂ concentrations and O₂^{•-} solvation by solvent additives.

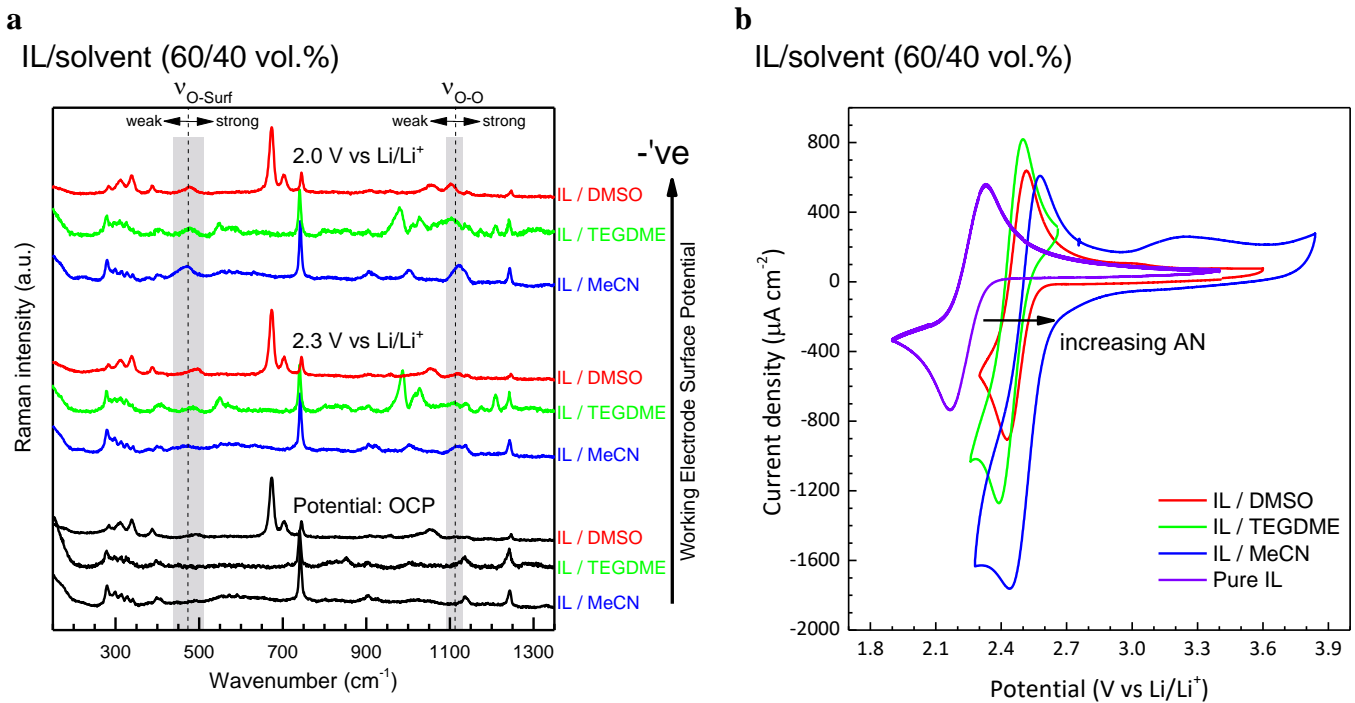


Figure 5.1. (a) Stacked spectra of rAu surface at OCP and ORR potentials (2.3 and 2.0 V vs. Li^+/Li) in O_2 -saturated $\text{Pyr}_{14}\text{TFSI}$ based IL:sol blend electrolytes (60:40 vol.% IL:sol ratio). Dashed lines demarcate weak and strong $\nu_{\text{O-O}}$ and $\nu_{\text{O-Surf}}$ bands **(b)** CVs of OR/ERs in O_2 -saturated IL:sol blends at 100 mV s^{-1} .

Table 5.1. OR/ER electrochemical parameters from IL:sol blend CVs in Figure 5.1. Scan rate: 100 mV s^{-1} . Potentials corrected versus fc^+/fc redox couple.

Pyr ₁₄ TFSI: solvent (60:40 vol%)	E_p^c (V vs Li/Li^+)	E_p^a (V vs Li/Li^+)	$E_{1/2}$ (V vs Li/Li^+)	ΔE (mV)	i_p^c (μA cm^{-2})	i_p^a (μA cm^{-2})	i_p^a/i_p^c	E_{window}
DMSO	2.43	2.51	2.47	85	-909	909	1.0	3.4
TEGDME	2.39	2.50	2.44	109	-1,288	1,192	0.93	3.2
MeCN	2.44	2.58	2.51	141	-1,770	1,158	0.65	3.6

5.3.2 *In Situ* SERS of Lithiated OR/ERs

Practical non-aqueous Li-O₂ batteries require an initial Li⁺ source in the electrolyte to drive Li⁺-OR/ER discharge and charge reactions, producing/dissociating, Li₂O₂ respectively. To explore Li⁺-OR/ER in these novel electrolytes, an Li-salt (LiTFSI) was added to IL:sol blend (3) and investigated using *in situ* SERS to determine reaction mechanisms occurring at the electrode surface. IL:sol blend (3) was investigated due to its high DN.

CVs of O₂-saturated IL:sol blend (3) with 0, 5, and 100 mM LiTFSI are shown in Figure 5.2. All cathodic and anodic peaks are similar to those of Li⁺-OR/ERs in pure DMSO electrolytes.⁴ For the blend with 0 mM LiTFSI (i.e. no Li⁺ in the electrolyte), normal one-electron ORR (A1) and OER (B1) current peaks associated with the O₂/O₂^{•-} (or O₂/Pyr₁₄⁺...O₂^{•-}) redox couple (eq. 5. 1a and 5. 2a) are present (Fig. 5. 2, pink dashed line). Adding 5 mM of LiTFSI salt to blend (3) caused both ORR onset and OR/ER peak potentials (labelled A2 and B2 respectively) to shift positive by ~20 mV (Fig. 5. 2, orange line). Both OR/ER peak currents also decreased and the peak separation (ΔE) increased from 85 mV to 210 mV (Table 5. 2). These changes in the CV profile indicate formation of a partially lithiated free O₂^{•-} (Li⁺...O₂^{•-}) species (redox couple: O₂/Li⁺...O₂^{•-}) during ORR that is slightly more thermodynamically favourable to form than free O₂^{•-} (or Pyr₁₄⁺...O₂^{•-}), but that requires larger overpotentials to dissociate due to thin Li₂O₂ surface passivation films. Blend (3) with 5 mM Li⁺ cycled well with only slight changes in OR/ER peak profiles after +20 cycles. Considering the OR/ER peak current ratio (0.96), most Li⁺...O₂^{•-} formed during one-electron ORR was oxidised via a chemically reversible one-electron mechanism. Therefore, at fast scan rates and relatively low Li⁺ concentrations the Li⁺-OR/ERs favours a one electron O₂/Li⁺...O₂^{•-} mechanism (eq. 5. 1b, 5.2b) as opposed to a two-electron mechanism with Li₂O₂.

At higher LiTFSI concentrations (100 mM); ORR remains unchanged, whilst, OER (B2), associated with $\text{Li}^+ \cdots \text{O}_2^{\bullet-}$ oxidation, was suppressed in favour of a second OER peak, labelled C in Figure 5. 2, associated with two-electron oxidation of Li_2O_2 (eq. 5. 5).⁴ Interestingly, Li^+ concentrations above 50 mM in the electrolytes are usually considered sufficient to suppress the one-electron OER mechanism. However, setting the reduction limit at 2.3 V vs Li/Li⁺ (Fig. 5. 2, dark-red line), a small peak (B2) is visible indicating the presence of some relatively free $\text{O}_2^{\bullet-}/\text{Li}^+ \cdots \text{O}_2^{\bullet-}$ species, even at high Li^+ concentrations, suggesting the solution reaction mechanism was still occurring.¹¹⁰ Lowering the CV reduction limit to 2.1 V vs Li/Li⁺ caused peak B2 to disappear and C to grow. This supports the mechanism outlined by Lee *et al.* that; at high ORR potentials Li_2O_2 is formed via diffusion limited chemical disproportionation reaction mechanism (eq. 5. 3) whilst at lower potentials direct two-electron reduction of any surface $\text{O}_2^{\bullet-}/\text{Li}^+ \cdots \text{O}_2^{\bullet-}$ to Li_2O_2 occurs (eq.5. 4).

Pyr₁₄TFSI/DMSO (60/40 vol.%) + 5 mM mol Li⁺

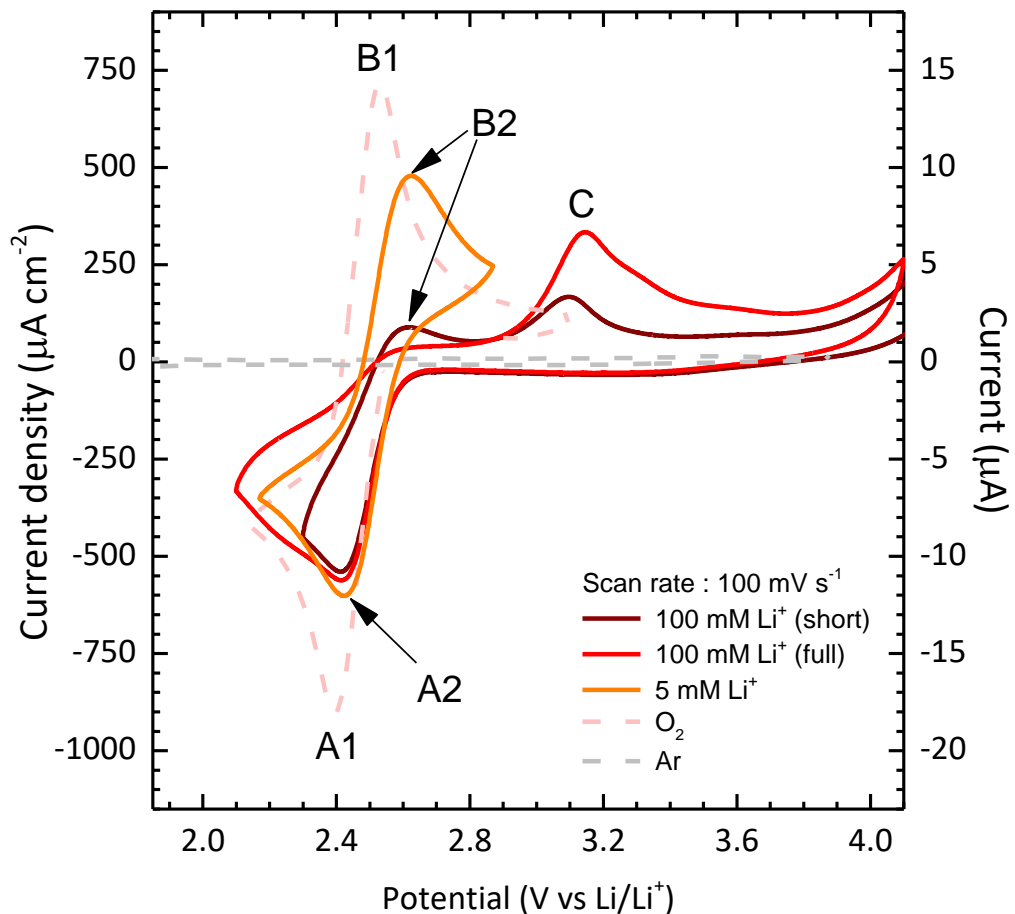


Figure 5. 2. Li⁺-OR/ERs CVs of; 0, 5, 100 mM LiTFSI in O₂-saturated Pyr₁₄TFSI:DMSO IL:sol blend electrolytes (60:40 vol % ratio) at 100 mV s⁻¹. Ar electrochemical window shown (grey dashed line). Reaction mechanism for current peaks A-C are outlined below (eq. 5. 1-5. 3) and their parameters in Table 5. 2.

Table 5. 2. OR/ER electrochemical parameters from IL:sol blend CVs in Figure 5. 1. Scan rate:100 mV s⁻¹. Potentials corrected versus fc⁺/fc redox couple.

Pyr ₁₄ TFSI: solvent (60:40 vol%)	E _p ^c (A) (V vs Li/Li ⁺)	E _p ^a (B) (V vs Li/Li ⁺)	E _p ^a (C) (V vs Li ^{+/Li})	ΔE (mV)	i _p ^c (A) (μA cm ⁻²)	i _p ^a (B) (μA cm ⁻²)	i _p ^a (C) (μA cm ⁻²)	i _p ^a / i _p ^c (B/C)
+0 mM Li ⁺	2.43	2.51	-	85	-909	909	-	1.0
+5 mM Li ⁺	2.42	2.63	-	210	-610	588	-	0.96
+100 mM Li ⁺ (short)	2.41	2.61	3.10	206/690	-560	190	175	0.33/0.31
+100 mM Li ⁺ (full)	2.41	-	3.14	730	-570	-	342	0.6



For *in situ* SERS studies of Li⁺-OR/ER at the rAu working electrode surface in O₂-saturated IL:sol blend (3) containing 5 mM LiTFSI, vo_{surf} and vo_O spectral bands for O-Surface and O-O (Li⁺...O₂^{•-} and Li₂O₂) bond vibrations were all visible during Li⁺-OR/ERs (Fig. 5. 3b and c). However, no discharge products were detected in electrolytes containing 100 mM LiTFSI. A similar Li-salt concentration dependence for Li⁺-OR/ER discharge products (Li_xO_y) was observed by Padmanabhan *et al.* using *in situ* SEIRAS.⁴⁰⁴ This effect was explained as being due to the formation of IR-active Li_xO_y clusters, which lacked large aggregate crystal structures, at the electrode surface in low Li⁺-concentration electrolytes. Whereas the O-O band became IR inactive within the lattices of larger crystalline Li_xO_y surface deposits formed with electrolytes that had higher Li⁺-concentrations. An analogous Li₂O₂ cluster effect could be occurring here also explaining the lack of SERS bands in the 100 mM LiTFSI containing blend. Thick electrically insulating Li₂O₂ deposits produced in high Li⁺-concentration electrolytes will likely also inhibit propagation of surface plasmon resonances, greatly reducing the surface enhancement signal and thus visibility of Li⁺-ORR discharge products.

SER spectra of the rAu working electrode surface were collected under potential control. The prolonged potential hold time (~5 minutes) at more positive (≥ 2.3 V vs. Li/Li⁺) Li⁺-ORR potentials (Fig. 5. 3a) produced visibly larger B2 peak currents than during normal potential cycling due to larger O₂^{•-}/Li⁺...O₂^{•-} concentrations at the electrode surface being oxidised (Fig. 5. 3a, purple lines). Holding at low Li⁺-ORR potentials (≤ 2.2 V vs. Li/Li⁺) caused B2 to decrease and broaden (Fig. 5. 3a, red line) due to the direct two-electron electrochemical reduction reaction occurring, forming thin Li₂O₂ layers on the electrode surface. This resulted in higher Li⁺-OER overpotentials to support electron tunnelling through these layers. Interestingly, holding the surface at positive Li⁺-OER potentials (≥ 3.1 V vs. Li/Li⁺) was sufficient to remove these Li₂O₂ deposits (Fig. 5. 3b). Consecutive cycles after removing Li₂O₂

deposits showed much more reversible CV profiles with larger peak currents (Fig. 5. 3b, blue line). However, without holding at high Li⁺-OER potentials the CV profile always returned to the normal cycling profile in consecutive cycles. This indicates the presence of Li₂O₂ surface deposits, formed via chemical or electrochemical mechanisms, under normal CV cycling. That said from the general CV profile it is clear O₂^{•-}/Li⁺...O₂^{•-} is the main discharge product formed and being oxidised during Li⁺-ORR. As shown in other DMSO electrolytes, O₂^{•-}/Li⁺...O₂^{•-} will dissolve and diffuse away from the cathode surface, as supported by SERS observations below.

The ν_{O-O} of Li₂O₂ at 787 cm⁻¹ was the most prominent discharge product spectral band appearing and diminishing during Li⁺-ORR and Li⁺-OER, respectively (Fig. 5. 2c and d). The characteristic ν_{O-Surf} band was also visible (480-485 cm⁻¹) at all Li⁺-ORR potentials (Fig. 5. 2c). However, it was absent when potentials were reversed during Li⁺-OER (Fig. 5. 2d). Similarly, a faint band for the ν_{O-O} of O₂^{•-} (Li⁺...O₂^{•-}) at 1,112 cm⁻¹ was visible during Li⁺-ORR (Fig. 5. 2c) and absent during Li⁺-OER (Fig. 5. 2d). These observations support the presence of Li₂O₂ deposits on the electrode surface, formed by reaction mechanisms described previously (eq. 5. 3 or 5. 4), as indicated by the electrochemistry. Li₂O₂ deposits are likely not thick enough to inhibit surface enhancement, though they are thick enough to influence Li⁺-OR/ER electrochemistry. The Li₂O₂ band was present at all Li⁺-OER potentials though high potentials (≥ 3.3 V vs. Li/Li⁺) were required for it to be substantially diminished which matches the potential for Li₂O₂ oxidation in Figure 5.2 (peak C). A weak kinked surface bound dioxygen species, either Li₂O₂ or Li⁺...O₂^{•-} is also present, though its immediate disappearance during Li⁺-OER is unclear and possibly suggests surface bound species are the first to be oxidised. The weak O₂^{•-}/Li⁺...O₂^{•-} spectral band suggests it is not present at the surface and is being effectively solvated into the bulk electrolyte. Overall this suggests blend (3) can support a desired Li⁺-OR/ER mechanisms.

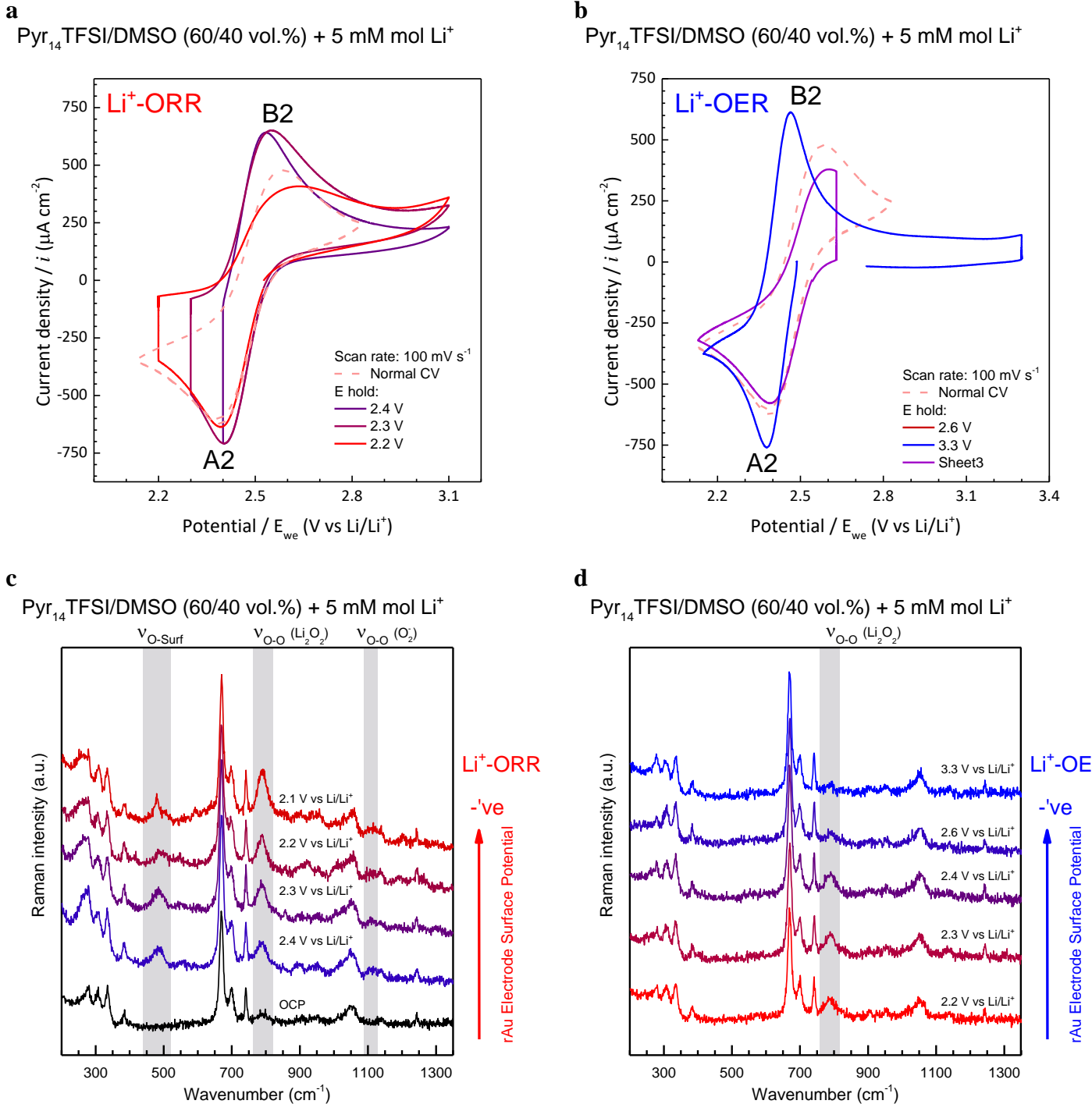


Figure 5. 3. Selected Li⁺-ORR CVs in a O₂-saturated, 5 mM LiTFSI in Pyr₁₄TFSI:DMSO (60:40 vol% IL:sol ratio) blend (3) electrolyte during (a) ORR and (b) OER cycling. SERS spectra were collected whilst potentials were held. Stacked SERS spectra of rAu surface at (c) reduction and (d) oxidation potentials (labelled). Where present $v_{\text{O-surf}}$, $v_{\text{O-O}} (\text{O}_2^{2-})$ and $v_{\text{O-O}} (\text{O}_2^{\cdot-})$ spectral band regions are highlighted in grey.

5.3.3 Li-Metal Stability

It is essential that non-aqueous Li-O₂ battery electrolytes are stable versus Li-metal and can form a Li⁺ permeable SEI layer if Li-anode cycling is to be feasible. As a quick screening method, a piece of clean, untarnished, Li-metal was added to five different organic solvents; (1) MeCN, (2) TEGDME, (3) DMSO, (4) DEGME and (5) m-Pip (Fig. 5. 4, top). All solvents were left for more than 72 hours exposed to the Li-metal inside an Ar glovebox to test their general stability. From Figure 5. 4, solvents (1) and (3) reacted with the Li-metal, solvents (2) and (5) are stable and remained colourless, however, a thick black SEI-layer was formed on the Li-metal surface. Solvent (4) was the only solvent where Li-metal was untarnished and the solvent remained clear, which is no surprise as DEGME is known for its chemical stability even against K-metal. This process was also done in all ILs used in this thesis. All ILs remained colourless and the Li-metal untarnished after > 1 month exposure to Li metal, so can be considered extremely stable. This information helped guide the electrolyte tailoring process in the next section.

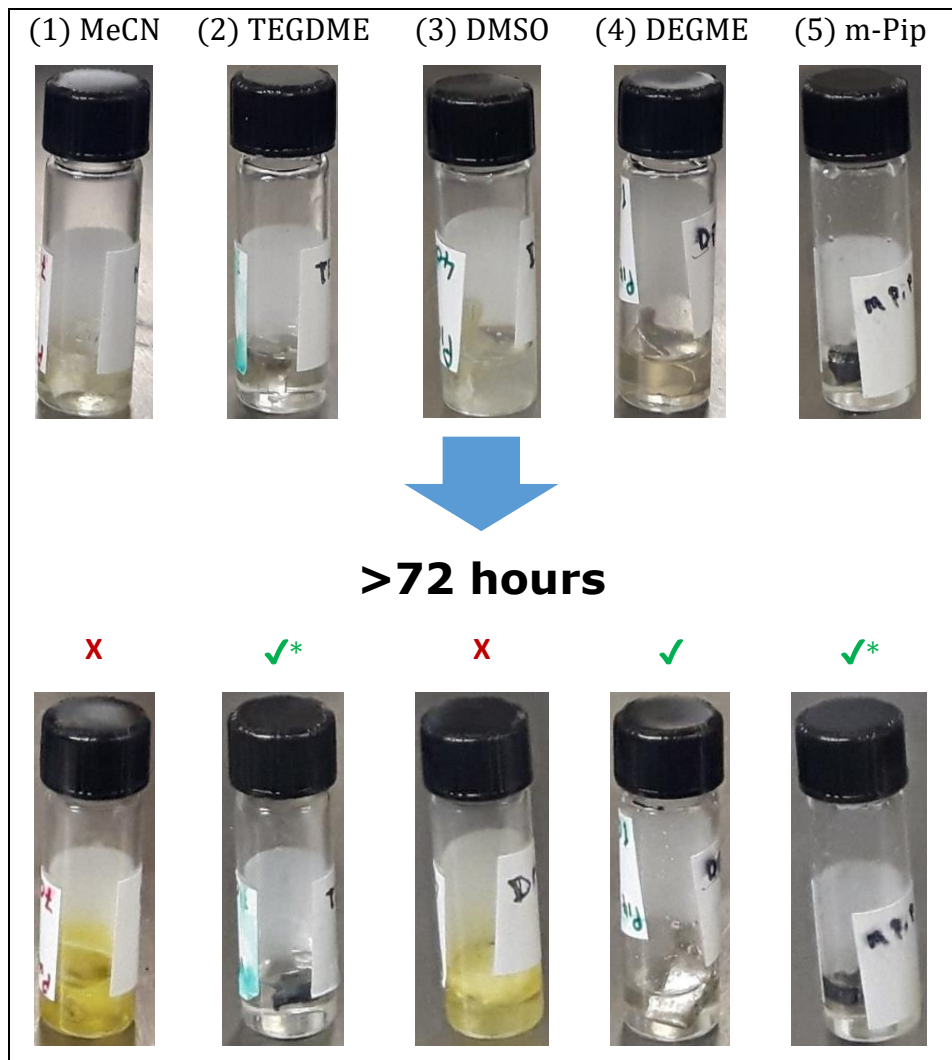


Figure 5.4. Solvent screening versus Li-metal showing visible electrolyte changes after >72 hours exposure. * denote blends that formed an SEI with Li-metal.

5.4 Multi-Component IL:Solvent Blends

Ara *et al.* showed that a heterogeneous IL electrolyte (mix of BMIMTFSI:Pyr14TFSI) can improve Li⁺-OR/ER electrochemistry. Increased disorder in heterogeneous ILs improved ion mobility and likely caused a eutectic lowering of the melting point through increased disorder in the liquid.⁵¹⁵ This suggests some heterogeneous multi-component electrolyte mixtures may be better than pure homogenous electrolytes. To optimise the physicochemical properties and Li-metal stability of the electrolyte, several novel IL:sol blend electrolytes were formulated by combining multiple different ILs and organic solvents into complex multi-component electrolytes. Electrolyte formulations were heuristically guided by selecting components with desirable physicochemical properties and by the cation, anion and solvent trends discussed previously. Using *in situ* SERS, O₂^{•-} was used as a diagnostic molecule to probe electrolyte interactions during OR/ERs, thus providing a reference point to assess the complex multi-component blended electrolytes. Multi-component electrolytes with optimised electron accepting or donating character with improved electrochemistry and excellent Li-metal stability were thus formulated. The electrolyte was further optimised by combining both the optimised accepting and donating electrolytes together into a heterogeneous blend (HetBlend) electrolyte with an amphoteric-like nature desired for non-aqueous Li-O₂ batteries.

5.4.1 Heuristic Electrolyte Tailoring Methodology

Mixed multi-component electrolytes are one way of overcoming the limitations of any one electrolyte component individually, such as poor ion mobility or O₂ solubility or low AN/DN etc., by combining numerous different ILs, salts and organic solvent, each with some characteristics desirable for an ideal electrolyte. Each component was selected to boost a certain electrolyte property whilst the quantity of the component in the electrolyte was determined by its overall chemical stability. Tailoring an IL or IL:sol blend electrolyte is difficult due to the practically infinite number of ion and solvent combinations which increases further in complexity when the number of components is increased. Therefore, it is necessary to have some criteria to help guide IL and organic solvent selection for complex multi-component blends, as well as a quick and cheap methods of screening the practicality of the novel electrolytes for application in a practical non-aqueous Li-O₂ batteries. In general, the electrolyte was split into two main sections; (1) the IL part and (2) the solvent-additive part. As a rule, to ensure Li-metal stability the IL part was always kept in excess (≥ 60 vol.%) and was composed of various IL mixtures in any novel blend formulation. Whilst the additive part comprised numerous different salt, mediators and organic solvent additives with desirable physicochemical properties that would be expected to improve various aspects of the overall electrolyte as well as help solvate Li⁺-OR/ER discharge reaction intermediaries. As discussed in the previous chapters, to enable the solution reaction mechanisms required in a non-aqueous Li-O₂ battery, high AN electrolytes should comprise hard Lewis acid cations, soft Lewis base anions and high AN organic solvents. Whilst high DN electrolytes should comprise soft Lewis acid cations, hard Lewis base anions and high DN organic solvents.

Key parameters

Table 5. 3 shows a list of some key electrolyte parameters that an ideal non-aqueous Li-O₂ battery electrolyte should have. However, it is unlikely any one electrolyte solvent or IL will possess all these characteristics solvents and ILs that fulfil some of these requirements individually can still be selected for blending into a multi-component electrolyte. A solvent matrix was built based on these known parameters. Once several ILs, organic solvents and additive salts were selected as having beneficial properties they were mixed to form a multi-component blend and then tested for good OR/ER electrochemistry and Li-metal stability.

Screening novel multi-component electrolytes

Each novel multi-component electrolyte that was formulated was screened according to the criteria below. If the answer to the question was no, it was discounted if yes, the electrolyte was screened using the next test;

1. Is the electrolyte stable versus Li-metal? (If no discount, if yes continue)
2. Does the electrolyte have stable and quasi-reversible OR/ER and Li⁺ OR/ER chemistry indicative of stability versus radical oxides? (If no discount, if yes continue)
3. Does it have the expected O₂^{•-} electrolyte coordination environment using *in situ* SERS? (If no discount, if yes continue)
4. Does it have stable Li/Li stripping/plating cycling > 200 cycles. (If no discount, if yes continue)

If the electrolyte passed these initial criteria it was considered as a preliminary practical non-aqueous Li-O₂ electrolyte. Based on these criteria several blends, summarised below, were formulated and optimised, however, due to an ongoing international patent application, the exact formulations could not be presented here.

Table 5. 3. Important electrolyte properties for an ideal non-aqueous Li-O₂ battery electrolyte and solvents, ILs and electrolyte additives that fit the criteria, etc.

Properties	Symbol	Units	Ideal	Possible Electrolyte Component/Additive
Viscosity	η	mPa s^{-1}	Low	organic solvents e.g. MeCN, DME, DMSO, m-Pip
Conductivity	σ	S cm^{-1}	High	organic solvents e.g. MeCN, DME, DMSO, m-Pip
DN	DN	-	High	m-Pip, Me-im, DMSO
AN	AN	-	High	H ⁺ (i.e. very low acid concentrations)
O ₂ solubility	[O ₂]	mM	High	MeCN, DMA
O ₂ ^{•-} solubility	[O ₂ ^{•-}]	mM	High	MeCN, DMA,
H ₂ O solubility	[H ₂ O]	mM	Low	ILs with large alkyl chains e.g. N ₁₈₈₈ TFSI
CO ₂ solubility	[CO ₂]	mM	Low	same as H ₂ O solubility additives
Li ⁺ solubility	[Li ⁺]	mM	low	Li ⁺ -saturated electrolytes have good Li-metal stability. ^{228,229}
Li ⁺ diffusivity	D[Li ⁺]	mM	High	-
O ₂ diffusivity	D[O ₂]	cm ² s ⁻¹	High	MeCN
O ₂ ^{•-} diffusivity	D[O ₂ ^{•-}]	cm ² s ⁻¹	High	MeCN
EC window	E _{window}	V	Large	IL
Melting point	T _m	°C	Low	IL/ eutectic IL mixtures
Boiling point	T _b	°C	High	IL/ eutectic IL mixtures
Vapour pressure	V _p	mmHg	High	IL/ eutectic IL mixtures

5.4.2 Li-Metal Stability

Several multi-component electrolytes with accepting (AB1, AB2), donating (DB1, DB2) and mixed (HetB1, HetB2) chemical natures were formulated and screened for stability versus Li-metal in accordance with the first electrolyte screening criteria outlined previously (Figure 5.5). Both accepting blends and HetB1 visibly reacted with Li-metal and were unstable, however, DB1, DB2 and HetB2 remained clear with untarnished Li-metal, indicating good stability after 72 hours. Leaving these for a further 3 weeks in the Ar glovebox, all blends remained clear and Li-metal untarnished and can be considered stable versus Li-metal. This is good considering the large presence of DMSO (> 10 vol.%) in DB1 and DB2 which normally reacts with Li-metal. Therefore, the IL is having the desired effect of chemically stabilising the organic solvent electrolytes. This is particularly interesting in the case of HetB2 which is a 50:50 mix of blends AB2 and DB2 and contains both MeCN (> 10 vol.%) and DMSO (> 5vol.%) which are normally reactive but have been stabilised here.

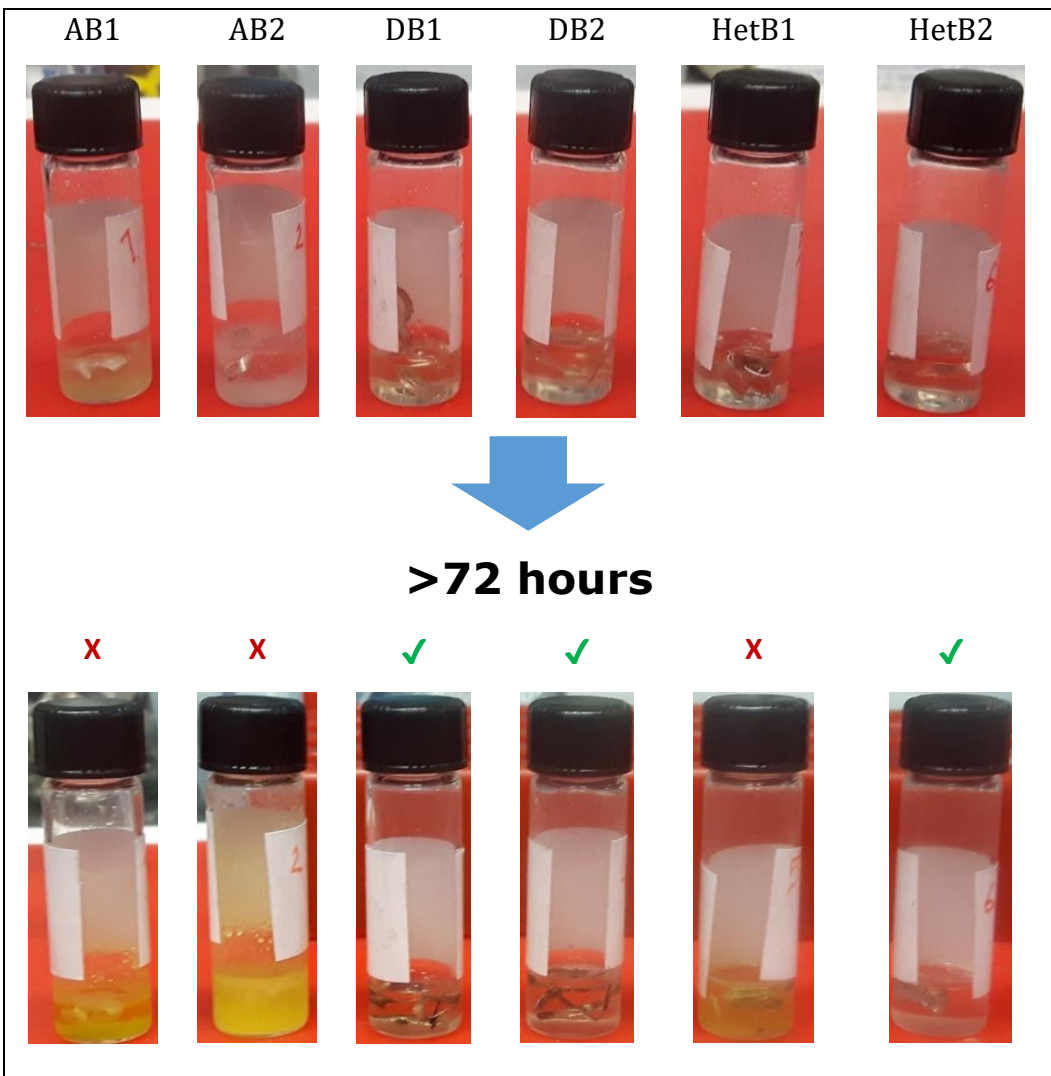


Figure 5.5. Formulate multi-component IL: Red crosses and green ticks indicate unstable and stable electrolytes after 72 hours exposure to Li-metal, respectively.

5.4.3 *In Situ* SERS of OR/ERs

Accepting blend

OR/ERs were investigated in the optimised accepting blend, AB2, using *in situ* SERS to probe the electrolyte-O₂^{•-} coordination (Fig. 5. 6). As expected, ν_{O-O} (1,109-1,127 cm⁻¹) and ν_{O-Surf} (458-464 cm⁻¹) values indicate relatively strong electrolyte-O₂^{•-} interactions and weak kinked O-surf structures analogous to the accepting IL, TESTFSI and IL:sol (1) blend. Both ν_{O-O} and ν_{O-Surf} spectral bands appear before the ORR onset potential and above E_{1/2} though ν_{O-Surf} appears at 200 mV higher potentials (Fig. 5. 7) than ν_{O-O} due to the initial formation of a flat surface-O₂^{•-} species, whose O-O stretch is invisible due to Raman selection rules, discussed in the previous chapter. The appearance of these O₂^{•-} bands at such high potentials is unexpected and will require future work to explain fully. As the potential decreased below ORR onset potentials, the intensity of both ν_{O-O} and ν_{O-Surf} bands increased massively, correlating with ORR current changes. Thus, these high intensity spectral bands can be associated with free and bulk solvated O₂^{•-} near the surface and the low intensity bands with surface bound O₂^{•-}. ν_{O-Surf} bands had much higher intensities compared with ν_{O-O}, which suggest a larger concentration of surface bound O₂^{•-}. These observations show that the general electrolyte-O₂^{•-} interaction strength can be tailored and tracked in complex multi-component electrolytes.

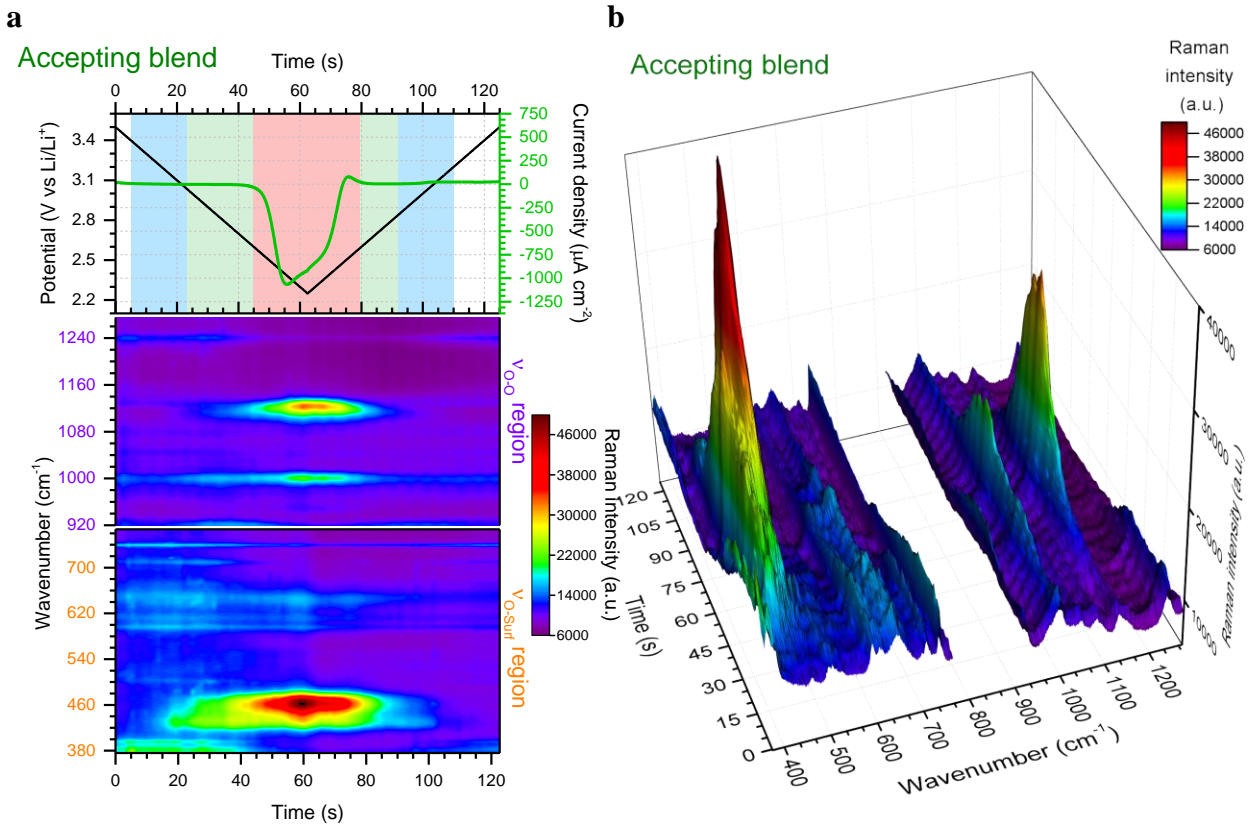


Figure 5.6. Dynamic surface potential *in situ* SERS multi-dimensional: plots, **(a)** Top: potential (black line)/current (green line) vs. time plots of OR/ER in O₂-saturated AB2 electrolyte (analogous with CVs in Fig. 5.7 b). Regions of very low, low and high v_{O-O} and v_{O-Surf} band intensities are highlighted in blue, green and red, respectively (top). Bottom: contour plots of SERS data in v_{O-O} and v_{O-Surf} regions, respectively, at corresponding times with the electrochemistry (analogous with SERS spectra in Fig. 5.7 a). **(b)** 3D visual plot of spectral changes with time.

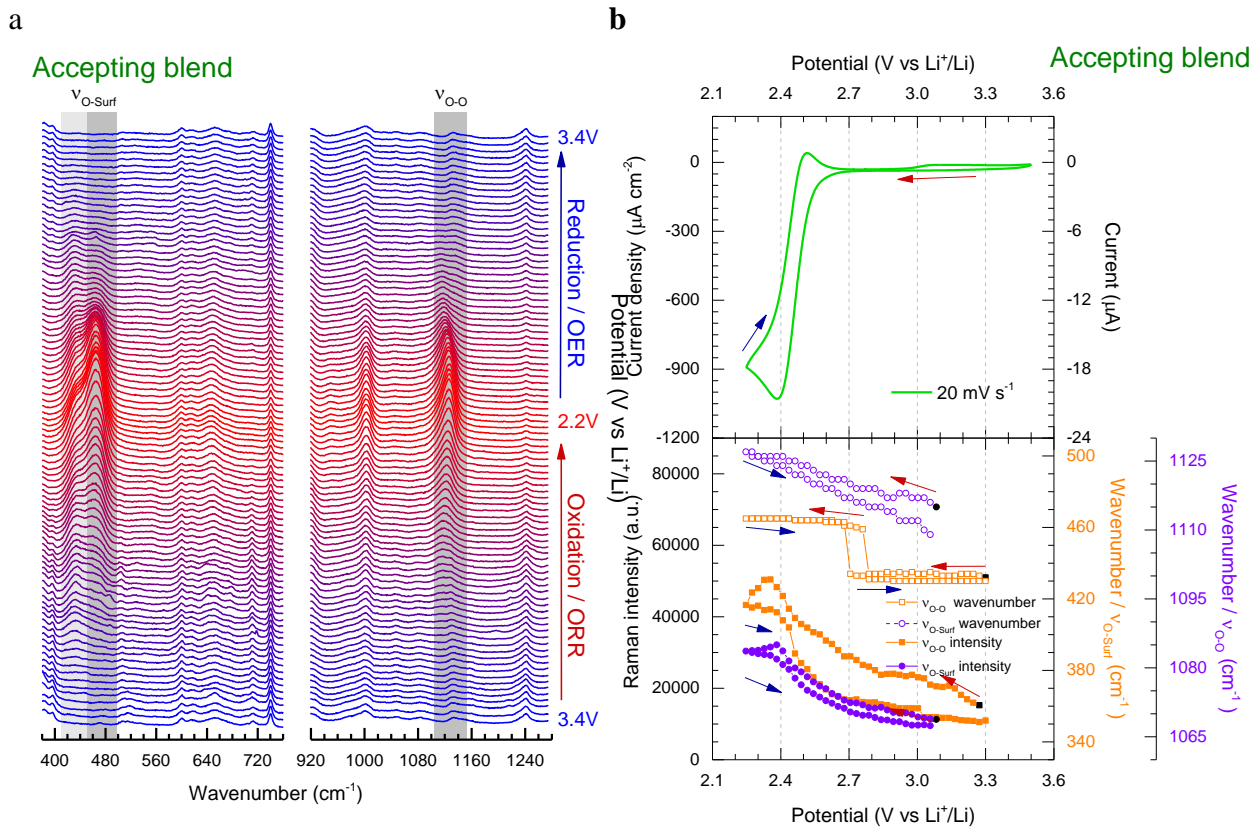


Figure 5.7 **(a)** Selection of stacked SERS spectra of the rAu working electrode surface collected in rapid succession in O₂-saturated AB2 electrolyte. Left and right are scans of v_{O-O} and v_{O-Surf} wavenumber regions, respectively. **(b)** Top, CV of OR/ER in O₂-saturated AB2 at 20 mV s⁻¹ (green line). Bottom, v_{O-O} and v_{O-Surf} wavenumber position/intensity vs. potential plots. Start data points where O₂^{•-} appears shown in black and where possible coloured arrows are included as visual aids indicating reduction (dark red) and oxidation (dark blue) directions of potential scanning. There is a strong visible blue-Stark shift and intensities rise then decrease after the ORR maximum as potential is lowered.

From spectra acquired at controlled surface potentials in AB2 (Fig. 5. 8), the vo-Surf shoulder at 429-433 cm⁻¹, labelled peak 1 (highlighted in light grey in Figure 5. 7c), was visible at all OR/ER surface potentials examined and was much more visible than the same bands were for pure TESTFSI. Peak 1 has been characterised previously as a conformationally flat O₂^{•-} previously and its appearance prior to the ORR onset and above the E_{1/2} potential indicates the formation of a surface O₂^{•-} layer prior to bulk ORR and this layer is much more stable in AB2 than TESTFSI as it is also visible during dynamic surface potential cycling (Fig. 5. 6a and c) independent of vo-o, due to Raman selection rules, bond vibrations perpendicular to the surface are likely less visible than those with vibrational components in the perpendicular direction.

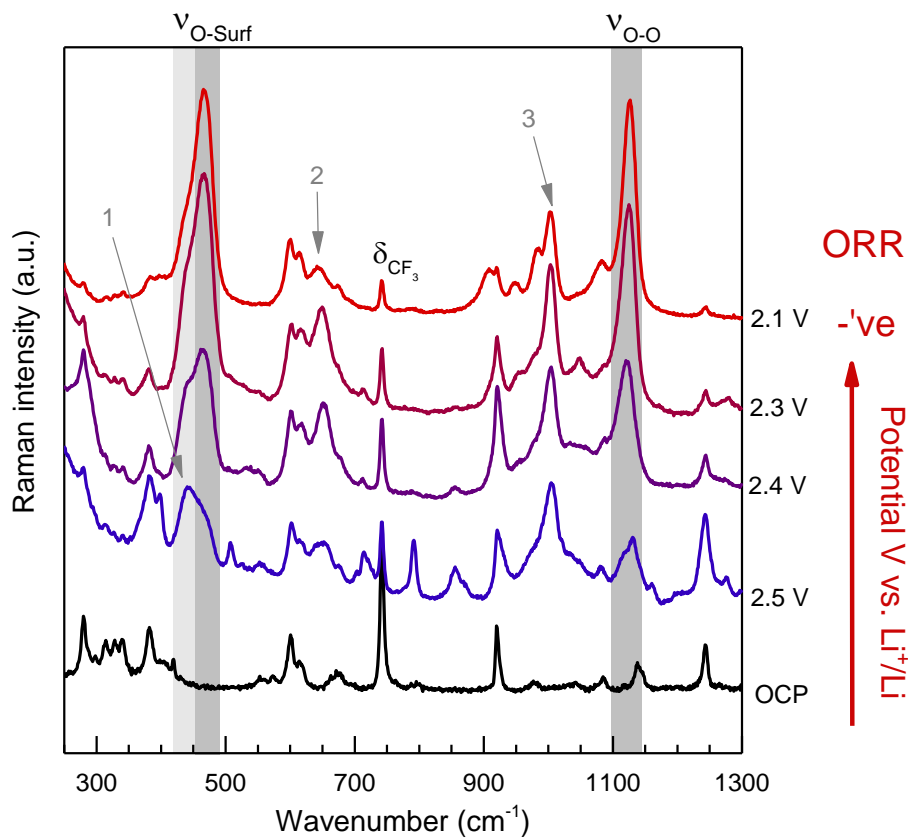
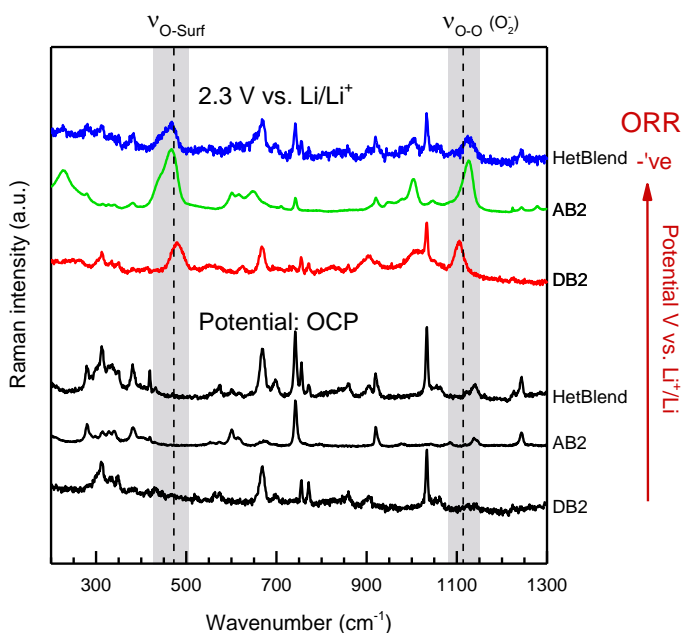


Figure 5. 8. Extended spectra acquired with surface potential control at specified held potentials during ORR in oxygen saturated TESTFSI. v_{O-surf} and v_{O-O} spectral band regions are highlighted in light grey and grey.

5.4.4 Comparing blends

Guided by spectroscopic findings with O_2^{*-} , the accepting (AB2) and donating (DB2) IL:sol based blends with good Li-metal stability were optimised and these two blends were combined together into a complex HetBlend electrolyte. Comparing the *in situ* SERS spectra of OR/ERs (Fig. 5. 9a) in each complex blend shows; a free O_2^{*-} species in DB2 blend (low ν_{O-O} : 1,109 cm^{-1}) as expected. Interestingly, the HetB2 blend had ν_{O-O} bands (1,126 cm^{-1}) more analogous to AB2 than DB2 indicating strong electrolyte... O_2^{*-} interactions despite the presence high DN organic solvents (m-Pip and DMSO) and relatively hard anions (DCA⁻, SO₄²⁻ etc.), which would normally weaken the O_2^{*-} interaction, supporting the desired amphoteric-like nature of the HetB2 electrolyte. This combined with its good Li-metal stability and improved more reversible OR/ER electrochemistry (Fig. 5. 9b) make HetB2 a promising electrolyte for practical applications in non-aqueous Li-O₂ batteries.

a



b

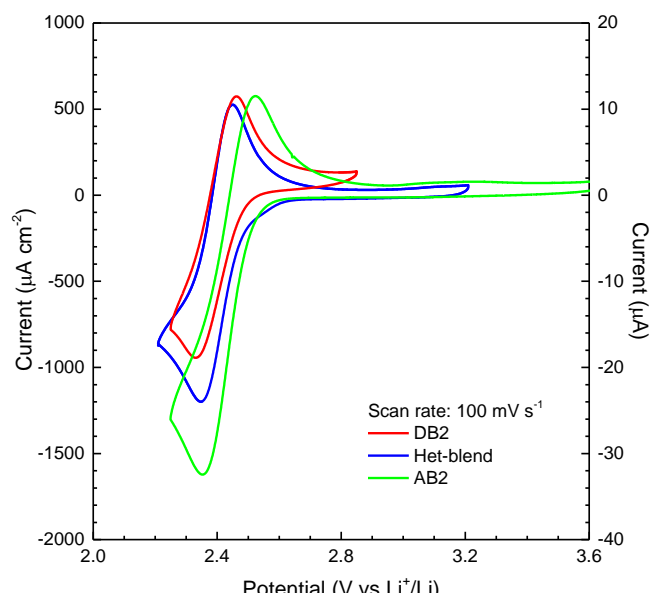


Figure 5. 9. (a) Stacked SERS spectra of rAu surface at OCP and ORR potentials in O_2 -saturated multi-component IL:sol blends. ν_{O-Surf} and ν_{O-O} spectral band regions are highlighted in grey. (b) OR/ER CVs of blended electrolytes at 100 $mV s^{-1}$.

5.5 Electrolyte Practicality

5.5.1 Li-Li Symmetrical Cell Cycling

To test the SEI layer stability and whether the HetB2 electrolyte can support sufficient Li^+ diffusion rates, Li-Li symmetrical cell stripping plating cycles were performed (Fig. 5. 12). Conductive additives Pyr_{14}I and $\text{Pyr}_{14}\text{HSO}_4$ were also added to the electrolyte blend as both H^+ and I^- improve the electrolyte accepting and donating properties and conductivity. HetB2 with the conductive additives showed far better Li-Li cycling with over an order of magnitude lower stripping-plating overpotentials (2 mV) compared with the standard Li-ion battery electrolyte, LP30 (40 mV) after an initial SEI formation process in the first 15 stripping-plating cycles. This suggests a highly stable Li^+ conductive surface layer is formed on the Li-metal even compared with that of the LP30 which is known to be stable. This supports the practicality of heterogeneous IL:sol blends as future battery electrolytes.

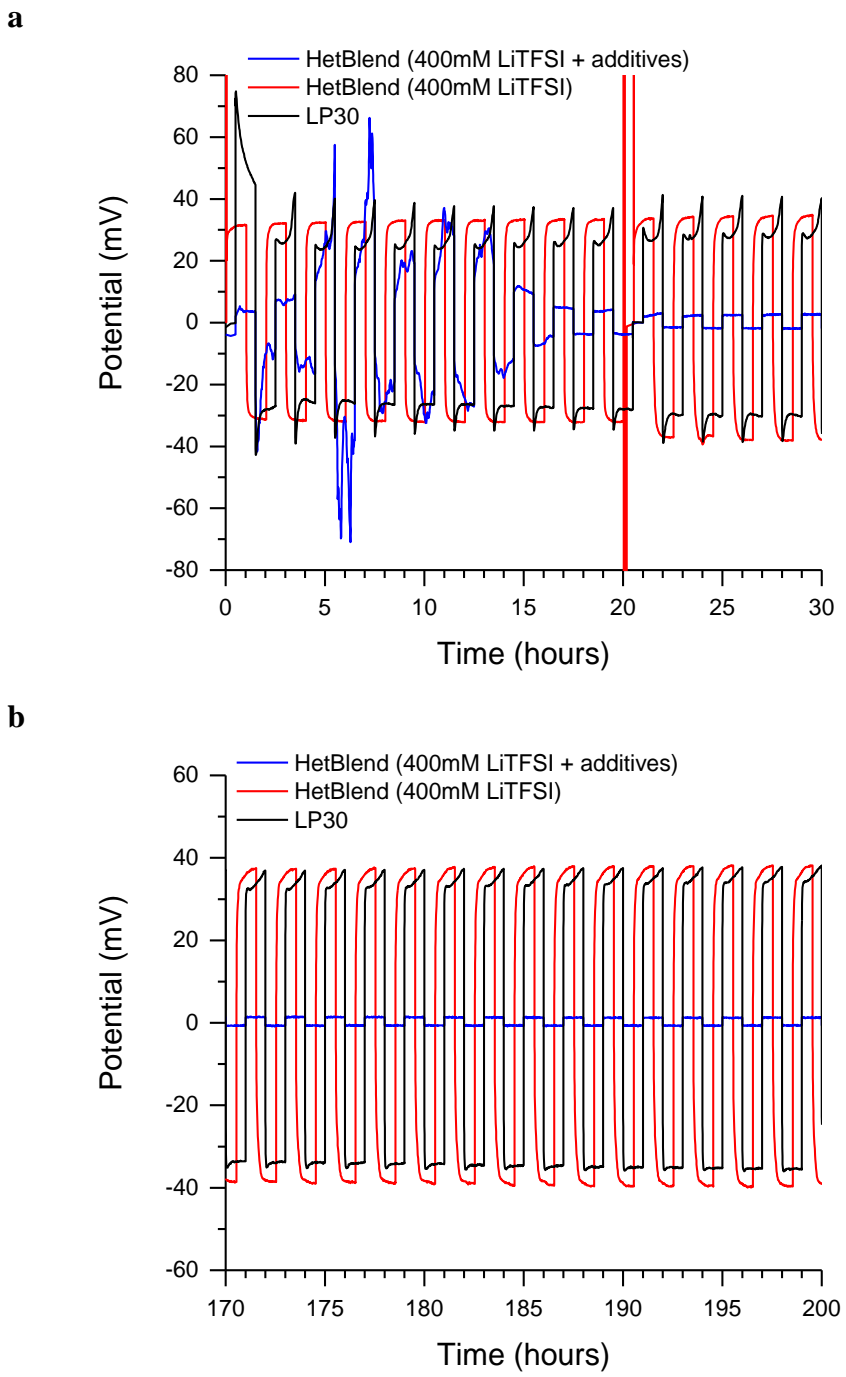


Figure 5.12. Galvanostatic voltage-time curves of 200 Li-Li symmetrical cell plating-stripping cycles with LP30 (black-line) and 400 mM LiTFSI in HetB2 without (red-line) and with conductive additives (green-line). **(a)** First 30 Li-Li symmetrical cell cycles. **(b)** Last 30 Li-Li symmetrical cell cycles after 200 cycles. Low cycling currents of 0.01 C (2 mM diameter Li-metal electrodes) were used to prevent Li-dendrite formation and each stripping and plating cycle lasted an hour.

5.5.2 Li-Metal Reference Electrode

Using Ag reference electrodes for electrochemical measurements is inconvenient as potentials can shift between electrolytes and need to be measured relative to a ferrocene/ferrocinium (fc^+/fc) redox couple to be able to standardise experimental potentials vs. Li^+/Li . To overcome this problem, a custom Li-metal reference electrode was made in-house using the novel HetB2 electrolyte (Fig. 5. 10). A micro-porous frit was attached to the bottom of reference electrode body with PTFE heat shrink (both purchased from IJ Cambria) and a clean strip of Li-metal attached to a silver wire soldered onto a copper rod passed through a screw fitting (electrode easily reassembled) rated for UHV in the top of the reference (Fig. 5. 13a) containing a 20 mM LiTFSI HetB2 electrolyte (Fig. 5. 10b). The whole reference electrode was assembled inside an Ar-atmosphere glovebox.

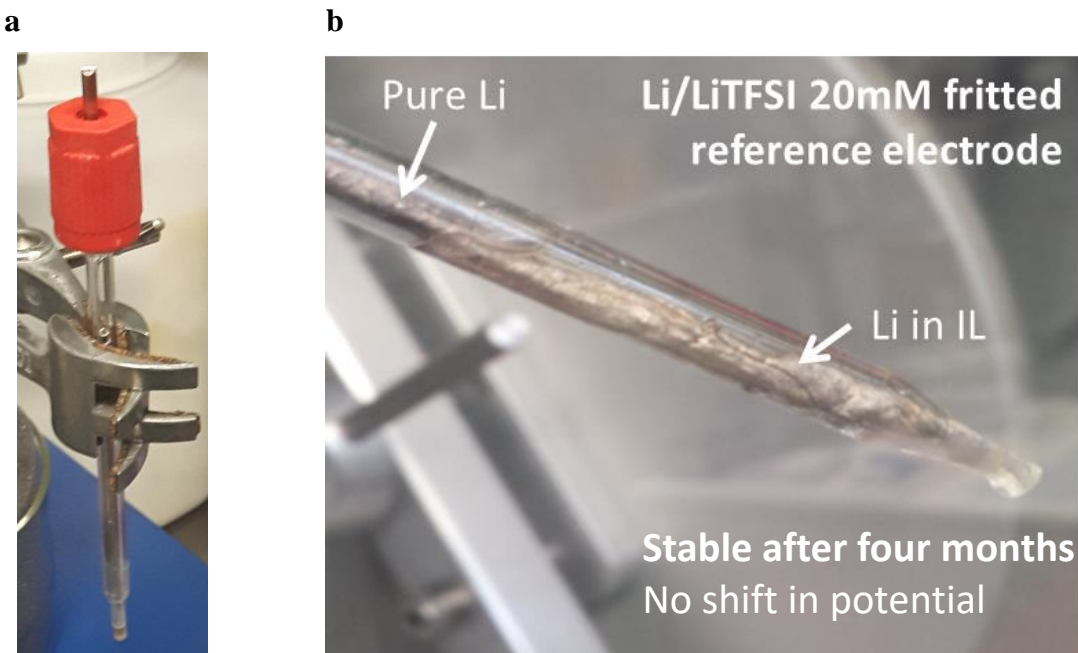


Figure 5. 13. (a) Photo of Li-metal reference electrode. (b) Close-up of reference electrode showing untarnished Li-metal in HetB2 electrolyte.

Using the Li-metal reference electrode the Fc^+/Fc redox couple had a precise $E_{1/2}$ potential of 3.44 V vs. Li^+/Li , exactly as expected, and this remained the same without shifting or tarnishing after > 4 months of use (Fig. 5. 11) proving the precision of the electrode and further showing the exceptional stability of the blended electrolyte.

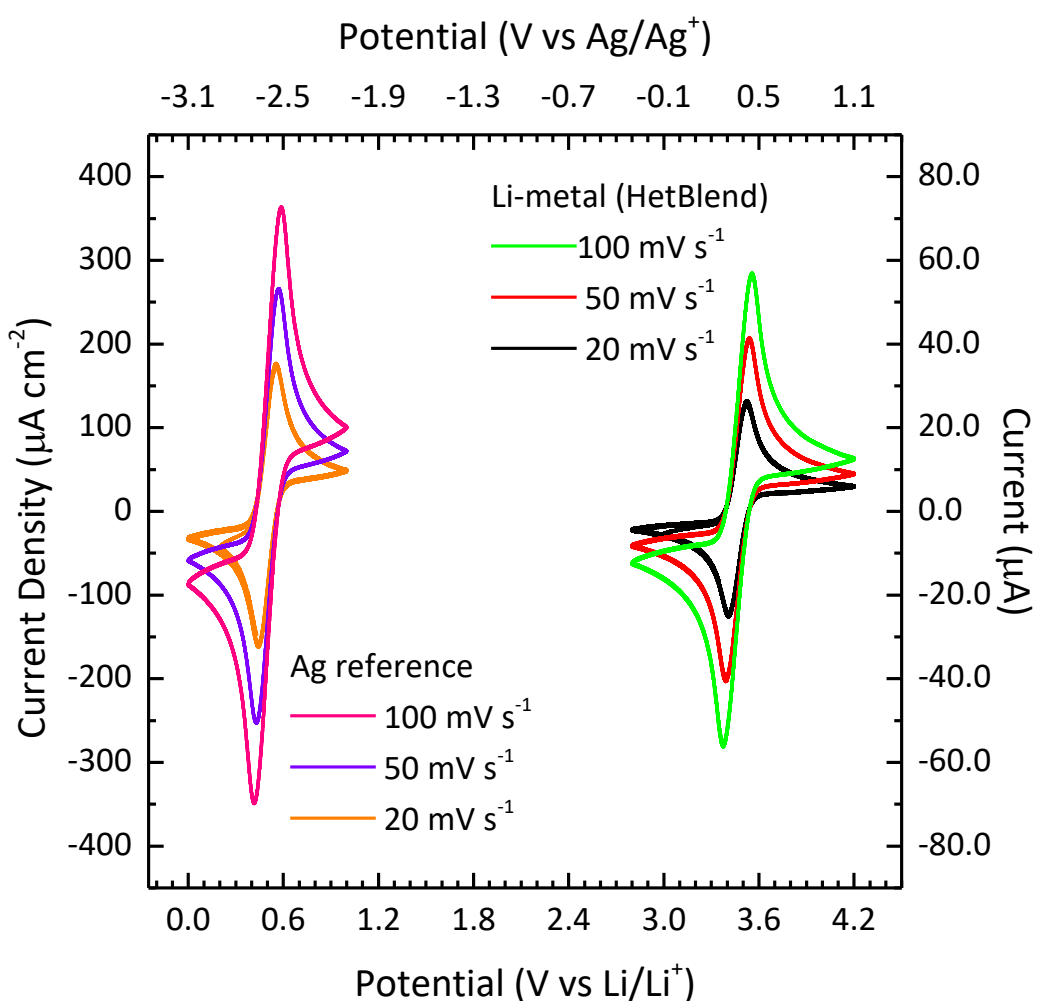


Figure 5. 14. CVs of Fc/Fc^+ redox couple in $\text{Pyr}_{14}\text{TFSI}$ electrolyte, with dissolved ferrocene, using Ag-metal quasi-reference electrode and the custom Li-metal reference electrode.

5.6 Conclusion

A number of novel IL:sol and multi-component IL-solvent blend electrolytes for non-aqueous Li-O₂ batteries were formulated and investigated spectroelectrochemically during OR/ER potential cycling. Guided by O₂^{•-} observations and the trends observed in chapter 3 and 4, these blends were optimised and complex multicomponent HetBlends were formulated which had extremely good Li-metal stability, evidenced by Li-metal plating-stripping experiments with extremely low overpotentials that had an order of magnitude better overpotentials than commercial Li-ion battery electrolytes. These results were particularly surprising as they contained organic solvents known to have good OR/ER electrochemistry but that normally react with Li-metal, however, they were able to be effectively stabilised by the bulk IL. This novel concept shows promise for practical non-aqueous Li-O₂ and could also be exploited in other batteries such as high power Li-ion as well as Na and K-metal based batteries.

6. Conclusion

6. Conclusion

In this thesis, novel ionic liquid (IL)-based electrolytes for non-aqueous Li-O₂ batteries have been investigated and optimised. Due to the electrolyte's key role in stabilising and facilitating discharge-charge reactions and the fact it interacts with every part of the battery, a detailed literature review was carried out to give a sound understanding of the overall system. OR/ER mechanisms in a series of novel IL and solvent blended electrolytes were investigated in detail using *in situ* SERS. Investigating the literature of characteristic v_{O-O} spectral bands for O₂^x species helped to elucidate the strong influence the immediate coordinating environment has on the O-O bond vibrations. This information provided the understanding with which to analyse O₂⁻ spectral bands generated *in situ* in novel electrolytes. Ultimately using O₂⁻ as a diagnostic molecule to probe the electrolytes interactions with OR/ER intermediaries, a series of important electrolyte trends were observed which helped to guide the electrolyte tailoring process culminating in a heuristic design methodology that produced complex multi-component IL:sol blend electrolytes with amphoteric-like character, good OR/ER electrochemistry and exceptional Li-metal stability with an order of magnitude lower Li-Li stripping-plating overpotentials than commercial Li-ion battery electrolytes.

Comparing spectra of the surface at open circuit with spectra at different potentials enabled the flux of species with Raman active bond vibrations to be observed spectroscopically. Differences in spectral band intensities of bands associated with surface O₂⁻ reduction products during potential cycling gave qualitative information on the molecular orientation and strength of electrolyte interactions in the EDL. Differences in v_{O-O} band positions between electrolytes from lower (red) to higher (blue) wavenumbers indicated production of more ionic or covalent, respectively, O₂⁻ species during OR/ER potential cycling at the electrode interface. A more ionic O₂⁻ species corresponds to a less coordinated, more radical, harder Lewis base and a

more covalent O₂^{•-} species to a more coordinated, softer Lewis base. Likewise, red or blue Stark shifts in v_{O-O} bands during potential cycling indicated surface potential induced fluctuations in the ionic or covalent character of generated surface O₂^{•-}.

By studying the OR/ER on rAu electrodes in a series of IL based electrolytes, the effect of the electrolyte (solvent/salt components) on the chemical nature of the O₂^{•-} anion (the key intermediate in the reaction at the non-aqueous Li-O₂ reaction),¹⁻⁴ has been determined. Four parameters were shown to affect the radical character of O₂^{•-} at the interface in IL-based electrolytes; (1) surface potential (Stark shift), (2) electrolyte cation, (3) electrolyte anion and (4) solvent electron acceptor/ donor numbers. Thus, It was shown that the radical nature of O₂^{•-} can be influenced and manipulated by selecting different electrolyte additives (observed experimentally through the Raman shift in the band position of v_{O-O} of O₂^{•-}).

This novel ‘heterogenous blend’ electrolyte concept, which combines accepting and donating multi-component IL:solvent blend electrolytes together to give electrolytes with amphoteric-like character capable of interacting strongly and coordinating both solvated anions and cations, shows significant practical promise. The optimised HetBlend had extremely good stability using lithium as evidenced by extremely low Li-metal plating/stripping overpotentials. This was particularly suprising as the HetBlends used solvents with good electrochemical properties, which normally react with Li-metal. However, they were able to be stabilised using ILs. This concept shows practical promise for application in non-aqueous Li-O₂ and other batteries such as high power Li-ion and alternative metal-air cells such as Na and K-O₂. Due to a number of successful grant applications and an ongoing patent application, the work into the HetBlend concept proposed herein will continue and the IL tailoring process will be further refined to optimise electrolyte properties for practical battery application.

7. Bibliography

7. References

- 1 J. Lu, Y. Jung Lee, X. Luo, K. Chun Lau, M. Asadi, H.-H. Wang, S. Brombosz, J. Wen, D. Zhai, Z. Chen, D. J. Miller, Y. Sub Jeong, J.-B. Park, Z. Zak Fang, B. Kumar, A. Salehi-Khojin, Y.-K. Sun, L. A. Curtiss and K. Amine, *Nature*, 2016, **529**, 377–382.
- 2 P. Hartmann, C. L. Bender, M. Vračar, A. K. Dürr, A. Garsuch, J. Janek and P. Adelhelm, *Nat. Mater.*, 2013, **12**, 228–32.
- 3 X. Ren and Y. Wu, *J. Am. Chem. Soc.*, 2013, **135**, 2923–2926.
- 4 L. Johnson, C. Li, Z. Liu, Y. Chen, S. a. Freunberger, P. C. Ashok, B. B. Praveen, K. Dholakia, J.-M. Tarascon and P. G. Bruce, *Nat. Chem.*, 2014, **6**, 1091–1099.
- 5 J. C. McLennan and J. H. McLeod, *Nature*, 1929, **123**, 160–160.
- 6 A. J. Edwards, W. E. Falconer, J. E. Griffiths, W. A. Sunder and M. J. Vasile, *J. Chem. Soc. Dalt. Trans.*, 1974, 1129.
- 7 L. Vaska, *Acc. Chem. Res.*, 1976, **9**, 175–183.
- 8 L. M. Mirica, X. Ottenwaelder and T. D. P. Stack, *Chem. Rev.*, 2004, **104**, 1013–1045.
- 9 UN - Department of Economic and Social Affairs., *World Economic and Social Survey 2011*, 2011.
- 10 D. Attias, *Automobile revolution : towards a new electro mobility paradigm*, Springer, 2017.
- 11 US EPA - Office of Transportation & Air Quality, <http://www.fueleconomy.gov/feg/atv.shtml>, 2015.
- 12 D. K. et al. Bellman, *Work. Doc.*, 2007.
- 13 G. Girishkumar, B. McCloskey, a. C. Luntz, S. Swanson and W. Wilcke, *J. Phys. Chem. Lett.*, 2010, **1**, 2193–2203.
- 14 Freedonia, *World Batteries - Industry Study*, 2015.
- 15 T. Nagaura and K. Tozawa, *Prog. Batter. Sol. cells*, 1990, **209**.
- 16 J. B. Goodenough and K. S. Park, *J. Am. Chem. Soc.*, 2013, **135**, 1167–1176.
- 17 B. Scrosati, M. Bottini and T. Mustelin, *Nat. Nanotechnol.*, 2007, **2**, 598–599.
- 18 T. Krisher, *The Seattle Times*, 2015.
- 19 W. W. Do, *U.S. Dep. Energy*, 2015, 49–50.
- 20 JMBS, [http://www.jmbatterysystems.com/technology/cells/nickel-metal-hydride-\(nimh\)](http://www.jmbatterysystems.com/technology/cells/nickel-metal-hydride-(nimh)), 2016.
- 21 JMBS, [http://www.jmbatterysystems.com/technology/cells/nickel-cadmium-\(nicd\)](http://www.jmbatterysystems.com/technology/cells/nickel-cadmium-(nicd)), 2016.
- 22 J. Maples, *U.S. Energy Inf. Adm.*, 2013.
- 23 Ivan Cowie, *EE Times*, 2014.
- 24 P. Patel, *ACS Cent. Sci.*, 2015, **1**, 161–162.
- 25 A. Poullikkas, *Renew. Sustain. Energy Rev.*, 2013, **27**, 778–788.
- 26 P. Adelhelm, P. Hartmann, C. L. Bender, M. Busche, C. Eufinger and J. Janek, *Beilstein J. Nanotechnol.*, 2015, **6**, 1016–1055.
- 27 J. O. G. Posada, A. J. R. R. Rennie, S. P. Villar, V. L. Martins, J. Marinaccio, A. Barnes, C. F. Glover, D. A. Worsley and P. J. Hall, *Renew. Sustain. Energy Rev.*, 2017, **68**, 1174–1182.
- 28 E. Peled, D. Golodnitsky, H. Mazor, M. Goor and S. Avshalomov, *J. Power Sources*, 2011, **196**, 6835–6840.
- 29 N. Nitta, F. Wu, J. T. Lee and G. Yushin, *Mater. Today*, 2015, **18**, 252–264.
- 30 M. M. O. Thotiyil, S. A. Freunberger, Z. Peng, Y. Chen, Z. Liu, P. G. Bruce and M. M. Ottakam Thotiyil, *Nat. Mater.*, 2013, **12**, 1050–6.
- 31 Z. Peng, S. a Freunberger, Y. Chen and P. G. Bruce, *Science*, 2012, **337**, 563–566.

- 32 T. Zhang and H. Zhou, *Nat. Commun.*, 2013, **4**, 1817.
- 33 I. Gunasekara, S. Mukerjee, E. J. Plichta, M. a. Hendrickson and K. M. Abraham, *J. Electrochem. Soc.*, 2014, **161**, A381–A392.
- 34 <https://oxisenergy.com>, 2017.
- 35 Y.-S. Su, Y. Fu, T. Cochell and A. Manthiram, *Nat. Commun.*, 2013, **4**, 2985.
- 36 P. G. Bruce, S. A. Freunberger, L. J. Hardwick and J.-M. Tarascon, *Nat. Mater.*, 2011, **11**, 19–29.
- 37 I. M. Aldous and L. J. Hardwick, *Angew. Chemie Int. Ed.*, 2016, **55**, 8254–8257.
- 38 C. Li, O. Fontaine, S. a. Freunberger, L. Johnson, S. Grueon, S. Laruelle, P. G. Bruce and M. Armand, *J. Phys. Chem. C*, 2014, **118**, 3393–3401.
- 39 A. C. Luntz and B. D. McCloskey, *Chem. Rev.*, 2014, **114**, 11721–11750.
- 40 T. Liu, M. Leskes, W. Yu, A. J. Moore, L. Zhou, P. M. Bayley, G. Kim and C. P. Grey, *Science (80-.).*, 2015, **350**, 530–533.
- 41 J. S.-Jirkovsky, R. Subbaraman, D. Strmcnik, K. L. Harrison, C. E. Diesendruck, R. S. Assary, O. Frank, L. Kobr, G. K. H. H. Wiberg, B. Genorio, J. G. Connell, P. P. Lopes, V. R. Stamenkovic, L. A. Curtiss, J. S. Moore, K. R. Zavadil and N. M. Markovic, *ACS Catal.*, 2015, **5**, 6600–6607.
- 42 G. Vardar, J. G. Smith, T. Thompson, K. Inagaki, J. Naruse, H. Hiramatsu, A. E. S. Sleighholme, J. Sakamoto, D. J. Siegel and C. W. Monroe, *Chem. Mater.*, 2016, **28**, 7629–7637.
- 43 N. Akhtar and W. Akhtar, *Int. J. Energy Res.*, 2015.
- 44 X. Ji and L. F. Nazar, *J. Mater. Chem.*, 2010, **20**, 9821.
- 45 H. J. Hwang, W. S. Chi, O. Kwon, J. G. Lee, J. H. Kim and Y. G. Shul, *ACS Appl. Mater. Interfaces*, 2016, acsami.6b07841.
- 46 Y. Li and H. Dai, *Chem. Soc. Rev.*, 2014, **43**, 5257–5275.
- 47 P. Pei, K. Wang and Z. Ma, *Appl. Energy*, 2014, **128**, 315–324.
- 48 S. S. Shinde, C.-H. Lee, A. Sami, D.-H. Kim, S.-U. U. Lee and J.-H. Lee, *ACS Nano*, 2017, **11**, 347–357.
- 49 H. Wang, D. Y. C. Leung, M. K. H. Leung and M. Ni, *Energy & Fuels*, 2010, **24**, 3748–3753.
- 50 M. Mokhtar, M. Z. M. Talib, E. H. Majlan, S. M. Tasirin, W. M. F. W. Ramli, W. R. W. Daud and J. Sahari, *J. Ind. Eng. Chem.*, 2015, **32**, 1–20.
- 51 X. Zhang, X.-G. Wang, Z. Xie and Z. Zhou, *Green Energy Environ.*, 2016, **1**, 4–17.
- 52 G. Vardar, E. G. Nelson, J. G. Smith, J. Naruse, H. Hiramatsu, B. M. Bartlett, A. E. S. Sleighholme, D. J. Siegel and C. W. Monroe, *Chem. Mater.*, 2015, **27**, 7564–7568.
- 53 P. Reinsberg, C. J. Bondue and H. Baltruschat, *J. Phys. Chem. C*, 2016, acs.jpcc.6b06674.
- 54 H. Yadegari, Q. Sun and X. Sun, *Adv. Mater.*, 2016, **28**, 7065–7093.
- 55 I. Landa-Medrano, C. Li, N. Ortiz-Vitoriano, I. Ruiz de Larramendi, J. Carrasco and T. Rojo, *J. Phys. Chem. Lett.*, 2016, acs.jpclett.5b02845.
- 56 A. Manthiram and L. Li, *Adv. Energy Mater.*, 2014, n/a-n/a.
- 57 K. F. Burton and A. F. Sammells, *J. Power Sources*, 1979, **4**, 263–279.
- 58 K. M. Abraham and Z. Jiang, *J. Electrochem. Soc.*, 1996, **143**, 1.
- 59 T. Ogasawara, A. Débart, M. Holzapfel, P. Novák and P. G. Bruce, *J. Am. Chem. Soc.*, 2006, **128**, 1390–3.
- 60 H.-G. Jung, J. Hassoun, J.-B. Park, Y.-K. Sun and B. Scrosati, *Nat. Chem.*, 2012, **4**, 579–85.
- 61 Y. Shen, D. Sun, L. Yu, W. Zhang, Y. Shang, H. Tang, J. Wu, A. Cao and Y. Huang, *Carbon N. Y.*, 2013, **62**, 288–295.
- 62 D. T. Sawyer and E. T. Seo, *Inorg. Chem.*, 1977, **16**, 499–501.

- 63 X. Li and A. a. Gewirth, *J. Am. Chem. Soc.*, 2005, **127**, 5252–5260.
- 64 C. Song and J. Zhang, in *PEM Fuel Cell Electrocatalysts and Catalyst Layers*, Springer London, London, 2008, pp. 89–134.
- 65 C. Pozo-Gonzalo, A. A. J. Torriero, M. Forsyth, D. R. MacFarlane and P. C. Howlett, *J. Phys. Chem. Lett.*, 2013, **4**, 1834–1837.
- 66 A. W. Lodge, M. J. Lacey, M. Fitt, N. Garcia-Araez and J. R. Owen, *Electrochim. Acta*, 2014, **140**, 168–173.
- 67 D. G. Kwabi, V. S. Bryantsev, T. P. Batcho, D. M. Itkis, C. V. Thompson and Y. Shao-Horn, *Angew. Chemie - Int. Ed.*, 2016, **55**, 3129–3134.
- 68 B. D. McCloskey and D. Addison, *ACS Catal.*, 2017, **7**, 772–778.
- 69 C. J. Allen, J. Hwang, R. Kautz, S. Mukerjee, E. J. Plichta, M. a. Hendrickson and K. M. Abraham, *J. Phys. Chem. C*, 2012, **116**, 20755–20764.
- 70 I. M. Aldous and L. J. Hardwick, *J. Phys. Chem. Lett.*, 2014, **5**, 3924–3930.
- 71 D. T. Sawyer, T. S. Calderwood, K. Yamaguchi and C. T. Angelis, *Inorg. Chem.*, 1983, **22**, 2577–2583.
- 72 D. Zheng, D. Y. Qu, X. Q. Yang, H. S. Lee and D. Y. Qu, *ACS Appl. Mater. Interfaces*, 2015, **7**, 19923–19929.
- 73 A. Lande, *Zeitschrift fur Phys.*, 1920, **1**, 191–197.
- 74 Z. Peng, S. A. Freunberger, L. J. Hardwick, Y. Chen, V. Giordani, F. Bard??, P. Nov??k, D. Graham, J.-M. M. Tarascon, P. G. Bruce, F. Bardé, P. Novák, D. Graham, J.-M. M. Tarascon and P. G. Bruce, *Angew. Chemie Int. Ed.*, 2011, **50**, 6351–6355.
- 75 C. L. Bender, P. Hartmann, M. Vračar, P. Adelhelm and J. Janek, *Adv. Energy Mater.*, 2014, **4**, 2–11.
- 76 R. H. Snow, *Contrails*, 1965, 34.
- 77 V. S. Bryantsev, M. Blanco and F. Faglioni, *J. Phys. Chem. A*, 2010, **114**, 8165–9.
- 78 N. Seriani, *Nanotechnology*, 2009, **20**, 1–7.
- 79 N. Ortiz-Vitoriano, T. P. Batcho, D. G. Kwabi, B. Han, N. Pour, K. P. C. Yao, C. V. Thompson and Y. Shao-Horn, *J. Phys. Chem. Lett.*, 2015, **6**, 2636–2643.
- 80 A. I. Belova, D. G. Kwabi, L. V. Yashina, Y. Shao-Horn and D. M. Itkis, *J. Phys. Chem. C*, 2017, acs.jpcc.6b12221.
- 81 G. Yang, Y. Wang and Y. Ma, *J. Phys. Chem. Lett.*, 2014, **5**, 2516–2521.
- 82 U. Das, K. C. Lau, P. C. Redfern and L. a Curtiss, *J. Phys. Chem. Lett.*, 2014, 140210184746002.
- 83 J. Lu, Y. Jung Lee, X. Luo, K. Chun Lau, M. Asadi, H.-H. Wang, S. Brombosz, J. Wen, D. Zhai, Z. Chen, D. J. Miller, Y. Sub Jeong, J.-B. Park, Z. Zak Fang, B. Kumar, A. Salehi-Khojin, Y.-K. Sun, L. A. Curtiss and K. Amine, *Nature*, 2016, **529**, 1–7.
- 84 J. K. Papp, J. D. Forster, C. M. Burke, H. W. Kim, A. C. Luntz, R. M. Shelby, J. J. Urban and B. D. McCloskey, *J. Phys. Chem. Lett.*, 2017, **8**, 1169–1174.
- 85 R. Black, S. H. Oh, J. Lee, T. Yim, B. Adams and L. F. Nazar, *J. Am. Chem. Soc.*, 2012, **134**, 2902–5.
- 86 C. L. Bender, D. Schröder, R. Pinedo, P. Adelhelm and J. Janek, *Angew. Chemie - Int. Ed.*, 2016, **55**, 4640–4649.
- 87 C. O. Laoire, S. Mukerjee, E. J. Plichta, M. A. Hendrickson and K. M. Abraham, *J. Electrochem. Soc.*, 2011, **158**, A302.
- 88 N. B. Aetukuri, B. D. McCloskey, J. M. García, L. E. Krupp, V. Viswanathan and A. C. Luntz, *Nat. Chem.*, 2014, **7**, 50–56.
- 89 C. Xia, R. Fernandes, F. H. Cho, N. Sudhakar, B. Buonacorsi, S. Walker, M. Xu, J. Baugh and L. F. Nazar, *J. Am. Chem. Soc.*, 2016, **138**, 11219–11226.
- 90 Y. Xu and W. a. Shelton, *J. Electrochem. Soc.*, 2011, **158**, A1177–A1184.
- 91 Z.-L. Wang, D. Xu, J.-J. Xu and X.-B. Zhang, *Chem. Soc. Rev.*, 2013, **43**, 7746–7786.

- 92 J.-J. Xu, Z.-W. Chang, Y. Wang, D.-P. Liu, Y. Zhang and X.-B. Zhang, *Adv. Mater.*, 2016, **28**, 9620–9628.
- 93 L. D. Griffith, A. E. S. Sleightholme, J. F. Mansfield, D. J. Siegel and C. W. Monroe, *ACS Appl. Mater. Interfaces*, 2015, **7**, 7670–7678.
- 94 B. D. Adams, C. Radtke, R. Black, M. L. Trudeau, K. Zaghib and L. F. Nazar, *Energy Environ. Sci.*, 2013, **6**, 1772.
- 95 B. M. Gallant, D. G. Kwabi, R. R. Mitchell, J. Zhou, C. V. Thompson and Y. Shao-Horn, *Energy Environ. Sci.*, 2013, **6**, 2518.
- 96 S. Wu, J. Tang, F. Li, X. Liu, Y. Yamauchi, M. Ishida and H. Zhou, *Adv. Funct. Mater.*, 2016, **26**, 3291–3298.
- 97 T. Zhang and N. Imanishi, in *Nanoscale Technology for Advanced Lithium Batteries*, eds. T. Osaka and Z. Ogumi, Springer New York, New York, NY, 2014, pp. 227–241.
- 98 D. Capsoni, M. Bini, S. Ferrari, E. Quartarone and P. Mustarelli, *J. Power Sources*, 2012, **220**, 253–263.
- 99 H. Ohkuma, I. Uechi, M. Matsui, Y. Takeda, O. Yamamoto and N. Imanishi, *J. Power Sources*, 2014, **245**, 947–952.
- 100 I. Kowalczyk, J. Read and M. Salomon, *Pure Appl. Chem.*, 2007, **79**, 851–860.
- 101 N. Kamaya, K. Homma, Y. Yamakawa, M. Hirayama, R. Kanno, M. Yonemura, T. Kamiyama, Y. Kato, S. Hama, K. Kawamoto and A. Mitsui, *Nat. Mater.*, 2011, **10**, 682–6.
- 102 Y. Wang and H. Zhou, *J. Power Sources*, 2010, **195**, 358–361.
- 103 R. Black, B. Adams and L. F. Nazar, *Adv. Energy Mater.*, 2012, **2**, 801–815.
- 104 H. Zhou, Y. Wang, H. Li and P. He, *ChemSusChem*, 2010, **3**, 1009–19.
- 105 P. He, T. Zhang, J. Jiang and H. Zhou, *J. Phys. Chem. Lett.*, 2016, **7**, 1267–1280.
- 106 M. A. Rahman, X. Wang and C. Wen, *J. Appl. Electrochem.*, 2014, **44**, 5–22.
- 107 N. Imanishi, A. C. Luntz and P. Bruce, *The Lithium Air Battery : Fundamentals*, .
- 108 J. Hassoun, F. Croce, M. Armand and B. Scrosati, *Angew. Chemie - Int. Ed.*, 2011, **50**, 2999–3002.
- 109 Y.-C. Lu, H. a. Gasteiger, M. C. Parent, V. Chiloyan and Y. Shao-Horn, *Electrochem. Solid-State Lett.*, 2010, **13**, A69.
- 110 V. S. Dilimon, D.-G. Lee, S.-D. Yim and H.-K. Song, *J. Phys. Chem. C*, 2015, 150206130617001.
- 111 R. Cao, E. D. Walter, W. Xu, E. N. Nasybulin, P. Bhattacharya, M. E. Bowden, M. H. Engelhard and J.-G. Zhang, *ChemSusChem*, 2014, **7**, 2436–40.
- 112 V. Gutmann, *Coord. Chem. Rev.*, 1976, **18**, 225–255.
- 113 D. Y. Kim, M. Kim, D. W. Kim, J. Suk, O. O. Park and Y. Kang, *Carbon N. Y.*, 2015, **93**, 625–635.
- 114 F. Soavi, S. Monaco and M. Mastragostino, *J. Power Sources*, 2013, **224**, 115–119.
- 115 C. Y. Jung, T. S. Zhao and L. An, *J. Power Sources*, 2015, **273**, 440–447.
- 116 Y. Yin, C. Gaya, A. Torayev, V. Thangavel and A. A. Franco, *J. Phys. Chem. Lett.*, 2016, **7**, 3897–3902.
- 117 B. Horstmann, B. Gallant, R. Mitchell, W. G. Bessler, Y. Shao-Horn and M. Z. Bazant, *J. Phys. Chem. Lett.*, 2013, **4**, 4217–4222.
- 118 A. Kushima, T. Koido, Y. Fujiwara, N. Kuriyama, N. Kusumi and J. Li, *Nano Lett.*, 2015, **15**, 8260–8265.
- 119 R. A. Wong, A. Dutta, C. Yang, K. Yamanaka, T. Ohta, A. Nakao, K. Waki and H. R. Byon, *Chem. Mater.*, 2016, **28**, 8006–8015.
- 120 B. D. McCloskey, C. M. Burke, J. E. Nichols and S. E. Renfrew, *Chem. Commun.*, 2015, **51**, 12701–12715.
- 121 D. Aurbach, B. D. McCloskey, L. F. Nazar and P. G. Bruce, *Nat. Energy*, 2016, **1**, 16128.

- 122 D. Sharon, D. Hirsberg, M. Afri, F. Chesneau, R. Lavi, A. a. Frimer, Y.-K. Sun and D. Aurbach, *ACS Appl. Mater. Interfaces*, 2015, **7**, 16590–16600.
- 123 R. Black, J.-H. Lee, B. Adams, C. a Mims and L. F. Nazar, *Angew. Chem. Int. Ed. Engl.*, 2013, **52**, 392–6.
- 124 C. M. Burke, V. Pande, A. Khetan, V. Viswanathan and B. D. McCloskey, *Proc. Natl. Acad. Sci.*, 2015, **112**, 9293–9298.
- 125 J. Scheers, D. Lidberg, K. Sodeyama, Z. Futera and Y. Tateyama, *Phys. Chem. Chem. Phys.*, 2016, **18**, Ahead of Print.
- 126 D. G. Kwabi, M. Tułodziecki, N. Pour, D. M. Itkis, C. V. Thompson and Y. Shao-Horn, *J. Phys. Chem. Lett.*, 2016, **7**, 1204–1212.
- 127 X. Gao, Y. Chen, L. Johnson and P. G. Bruce, *Nat. Mater.*, 2016, **15**, 882–888.
- 128 M. Olivares-Marín, P. Palomino, E. Enciso and D. Tonti, *J. Phys. Chem. C*, 2014, **118**, 20772–20783.
- 129 P. Tan, W. Shyy, Z. H. Wei, L. An and T. S. Zhao, *Electrochim. Acta*, 2014, **147**, 1–8.
- 130 J. Bao, W. Xu, P. Bhattacharya, M. Stewart, J.-G. Zhang and W. Pan, *J. Phys. Chem. C*, 2015, **119**, 14851–14860.
- 131 J. Xiao, D. Mei, X. Li, W. Xu, D. Wang, G. L. Graff, W. D. Bennett, Z. Nie, L. V Saraf, I. a Aksay, J. Liu and J.-G. Zhang, *Nano Lett.*, 2011, **11**, 5071–8.
- 132 C. O. Laoire, S. Mukerjee, K. M. Abraham, E. J. Plichta and M. A. Hendrickson, *J. Phys. Chem. C*, 2010, **114**, 9178–9186.
- 133 F. De Giorgio, F. Soavi and M. Mastragostino, *Electrochem. commun.*, 2011, **13**, 1090–1093.
- 134 J. T. Frith, A. E. Russell, N. Garcia-Araez and J. R. Owen, *Electrochem. commun.*, 2014, **46**, 33–35.
- 135 A. Khetan, A. Luntz and V. Viswanathan, *J. Phys. Chem. Lett.*, 2015, **6**, 1254–1259.
- 136 B. D. McCloskey, A. Speidel, R. Scheffler, D. C. Miller, V. Viswanathan, J. S. Hummelshøj, J. K. Nørskov and A. C. Luntz, *J. Phys. Chem. Lett.*, 2012, **3**, 997–1001.
- 137 J. P. Vivek, N. G. Berry, G. Papageorgiou, R. J. Nichols and L. J. Hardwick, *J. Am. Chem. Soc.*, 2016, jacs.5b12494.
- 138 C. Xia, R. Black, R. Fernandes, B. Adams and L. F. Nazar, *Nat. Chem.*, 2015, **7**, 496–501.
- 139 K. U. Schwenke, M. Metzger, T. Restle, M. Piana and H. A. Gasteiger, *J. Electrochem. Soc.*, 2015, **162**, A573–A584.
- 140 F. Li, S. Wu, D. Li, T. Zhang, P. He, A. Yamada and H. Zhou, *Nat. Commun.*, 2015, **6**, 7843.
- 141 X.-Z. Yuan, V. Alzate, Z. Xie, D. G. Ivey, E. Dy and W. Qu, *J. Electrochem. Soc.*, 2014, **161**, A458–A466.
- 142 Y. G. Zhu, Q. Liu, Y. Rong, H. Chen, J. Yang, C. Jia, L.-J. Yu, A. Karton, Y. Ren, X. Xu, S. Adams and Q. Wang, *Nat. Commun.*, 2017, **8**, 14308.
- 143 C. M. Burke, R. Black, I. R. Kochetkov, V. Giordani, D. Addison, L. F. Nazar and B. D. McCloskey, *ACS Energy Lett.*, 2016, **1**, 747–756.
- 144 B. D. McCloskey, J. M. Garcia and A. C. Luntz, *J. Phys. Chem. Lett.*, 2014, **5**, 1230–1235.
- 145 I. Gunasekara, S. Mukerjee, E. J. Plichta, M. A. Hendrickson and K. M. Abraham, *J. Electrochem. Soc.*, 2015, **162**, A1055–A1066.
- 146 I. Landa-Medrano, M. Olivares-Marín, B. Bergner, R. Pinedo, A. Sorrentino, E. Pereiro, I. Ruiz de Laramendi, J. Janek, T. Rojo and D. Tonti, *J. Phys. Chem. C*, 2017, **121**, 3822–3829.
- 147 S. Matsuda, Y. Kubo, K. Uosaki and S. Nakanishi, *J. Phys. Chem. Lett.*, 2017, **8**, 1142–1146.

- 148 S. Ganapathy, B. D. Adams, G. Stenou, M. S. Anastasaki, K. Goubitz, X. Miao, L. F. Nazar and M. Wagemaker, *J. Am. Chem. Soc.*, 2014, **136**, 16335–16344.
- 149 C. J. Bondue, P. Reinsberg, A. A. Abd-El-Latif and H. Baltruschat, *Phys. Chem. Chem. Phys.*, 2015, **17**, 25593–25606.
- 150 M. D. Radin and D. J. Siegel, *Energy Environ. Sci.*, 2013, **6**, 2370.
- 151 V. Viswanathan, K. S. Thygesen, J. S. Hummelshøj, J. K. Nørskov, G. Girishkumar, B. D. McCloskey and a C. Luntz, *J. Chem. Phys.*, 2011, **135**, 214704.
- 152 J. Hou, M. Yang, M. W. Ellis, R. B. Moore and B. Yi, *Phys. Chem. Chem. Phys.*, 2012, **14**, 13487–501.
- 153 Z. Li, S. Ganapathy, Y. Xu, J. R. Heringa, Q. Zhu, W. Chen and M. Wagemaker, *Chem. Mater.*, 2017, **29**, 1577–1586.
- 154 F. Marchini, S. Herrera, W. Torres, A. Y. Tesio, F. J. Williams and E. J. Calvo, *Langmuir*, 2015, **31**, 9236–9245.
- 155 V. Giordani, D. Tozier, H. Tan, C. M. Burke, B. M. Gallant, J. Uddin, J. R. Greer, B. D. McCloskey, G. V Chase and D. Addison, *J. Am. Chem. Soc.*, 2016, jacs.5b11744.
- 156 D. Y. Kim, M. Kim, D. W. Kim, J. Suk, J. J. Park, O. O. Park and Y. Kang, *Carbon N. Y.*, 2016, **100**, 265–272.
- 157 B. Horstmann, B. Gallant, R. Mitchell, W. G. Bessler, Y. Shao-Horn and M. Z. Bazant, *J. Phys. Chem. Lett.*, 2013, **4**, 4217–4222.
- 158 V. Viswanathan, J. K. Nørskov, A. Speidel, R. Scheffler, S. Gowda and A. C. Luntz, *J. Phys. Chem. Lett.*, 2013, **4**, 556–560.
- 159 C. Xia, M. Waletzko, L. Chen, K. Peppler, P. J. Klar and J. Janek, *ACS Appl. Mater. Interfaces*, 2014, **6**, 12083–12092.
- 160 Y. Lu and Y. Shao-Horn, *J. Phys. Chem. Lett.*, 2013, **4**, 93–99.
- 161 M. M. Ottakam Thotiyil, S. a Freunberger, Z. Peng and P. G. Bruce, *J. Am. Chem. Soc.*, 2013, **135**, 494–500.
- 162 M. Leskes, A. J. Moore, G. R. Goward and C. P. Grey, *J. Phys. Chem. C. Nanomater. Interfaces*, 2013, **117**, 26929–26939.
- 163 E. N. Nasybulin, W. Xu, B. L. Mehdi, E. Thomsen, M. H. Engelhard, R. C. Massé, P. Bhattacharya, M. Gu, W. Bennett, Z. Nie, C. Wang, N. D. Browning and J.-G. Zhang, *ACS Appl. Mater. Interfaces*, 2014, **6**, 14141–51.
- 164 J.-S. Lee, S. Tai Kim, R. Cao, N.-S. Choi, M. Liu, K. T. Lee and J. Cho, *Adv. Energy Mater.*, 2011, **1**, 34–50.
- 165 T. Zhang and H. Zhou, *Angew. Chem. Int. Ed. Engl.*, 2012, **51**, 11062–7.
- 166 S. Monaco, A. M. Arangio, F. Soavi, M. Mastragostino, E. Paillard and S. Passerini, *Electrochim. Acta*, 2012, **83**, 94–104.
- 167 F. Cheng and J. Chen, *Chem. Soc. Rev.*, 2012, **41**, 2172–92.
- 168 J. Wandt, P. Jakes, J. Granwehr, H. A. Gasteiger and R.-A. Eichel, *Angew. Chemie Int. Ed.*, 2016, **55**, 1–5.
- 169 K. M. Abraham, *J. Electrochem. Soc.*, 2014, **162**, A3021–A3031.
- 170 V. S. Ijeri, K. Daasbjerg, P. R. Ogilby and L. Poulsen, *Langmuir*, 2008, **24**, 1070–1079.
- 171 A. C. Luntz and B. D. McCloskey, *Nat. Energy*, 2017, **2**, 17056.
- 172 N. Mahne, B. Schafzahl, C. Leypold, M. Leypold, S. Grumm, A. Leitgeb, G. A. Strohmeier, M. Wilkening, O. Fontaine, D. Kramer, C. Slugovc, S. M. Borisov and S. A. Freunberger, *Nat. Energy*, 2017, **17036**, 1–9.
- 173 A. P. Darmanyan, W. S. Jenks and P. Jardon, *J. Phys. Chem. A*, 1998, **102**, 7420–7426.
- 174 Grant D. Smith and O. Borodin, in *Batteries for Sustainability*, 2012, pp. 6093–6124.
- 175 T. Frömling, M. Kunze, M. Schönhoff, J. Sundermeyer and B. Roling, *J. Phys. Chem. B*, 2008, **112**, 12985–90.
- 176 L. Suo, Y.-S. Hu, H. Li, M. Armand and L. Chen, *Nat. Commun.*, 2013, **4**, 1481.

- 177 Y. Shao, F. Ding, J. Xiao, J. J.-G. Zhang, W. Xu, S. Park, Y. Wang and J. Liu, *Adv. Funct. Mater.*, 2013, **23**, 987–1004.
- 178 Y. Cui, Z. Wen, X. Liang, Y. Lu, J. Jin, M. Wu and X. Wu, *Energy Environ. Sci.*, 2012, **5**, 7893.
- 179 Y.-C. Lu, D. G. Kwabi, K. P. C. Yao, J. R. Harding, J. Zhou, L. Zuin and Y. Shao-Horn, *Energy Environ. Sci.*, 2011, **4**, 2999.
- 180 V. S. Bryantsev, V. Giordani, W. Walker, M. Blanco, S. Zecevic, K. Sasaki, J. Uddin, D. Addison and G. V Chase, *J. Phys. Chem. A*, 2011, **115**, 12399–409.
- 181 S. Monaco, F. Soavi and M. Mastragostino, *J. Phys. Chem. Lett.*, 2013, **4**, 1379–1382.
- 182 D. G. Kwabi, T. P. Batcho, C. V. Amanchukwu, N. Ortiz-Vitoriano, P. Hammond, C. V. Thompson and Y. Shao-Horn, *J. Phys. Chem. Lett.*, 2014, **5**, 2850–2856.
- 183 D. Sharon, M. Afri, M. Noked, A. Garsuch, A. A. Frimer and D. Aurbach, *J. Phys. Chem. Lett.*, 2013, **4**, 3115–3119.
- 184 D. Sharon, V. Etacheri, A. Garsuch, M. Afri, A. a. Frimer and D. Aurbach, *J. Phys. Chem. Lett.*, 2013, **4**, 127–131.
- 185 S. Matsuda, K. Uosaki and S. Nakanishi, *J. Power Sources*, 2017, **356**, 12–17.
- 186 A. R. Neale, P. Li, J. Jacquemin, P. Goodrich, S. C. Ball, R. G. Compton and C. Hardacre, *Phys. Chem. Chem. Phys.*, 2016, **18**, 11251–11262.
- 187 N. Imanishi and O. Yamamoto, *Mater. Today*, 2014, **17**, 24–30.
- 188 V. V Chaban, I. V Voroshyllova, O. N. Kalugin and O. V Prezhdo, *Misc.*, 2011, 1–46.
- 189 N. V Plechkova and K. R. Seddon, *Chem. Soc. Rev.*, 2008, **37**, 123–50.
- 190 V. S. Bryantsev, J. Uddin, V. Giordani, W. Walker, D. Addison and G. V. Chase, *J. Electrochem. Soc.*, 2012, **160**, A160–A171.
- 191 K. Xu, *Chem. Rev.*, 2004, **104**, 4303–4418.
- 192 D. Sharon, D. Hirshberg, M. Afri, A. Garsuch, A. A. Frimer and D. Aurbach, *Isr. J. Chem.*, 2015, **55**, 508–520.
- 193 N. Garcia-Araez and P. Novák, *J. Solid State Electrochem.*, 2013, **17**, 1793–1807.
- 194 T. Laino and A. Curioni, *Chemistry*, 2012, **18**, 3510–20.
- 195 S. A. Freunberger, Y. Chen, Z. Peng, J. M. Griffin, L. J. Hardwick, F. Bardé, P. Novák and P. G. Bruce, *J. Am. Chem. Soc.*, 2011, **133**, 8040–7.
- 196 V. S. Bryantsev and M. Blanco, *J. Phys. Chem. Lett.*, 2011, **2**, 379–383.
- 197 W. Xu, K. Xu, V. V. Viswanathan, S. a. Towne, J. S. Hardy, J. Xiao, Z. Nie, D. Hu, D. Wang and J.-G. Zhang, *J. Power Sources*, 2011, **196**, 9631–9639.
- 198 B. G. Kim, J.-N. Lee, D. J. Lee, J.-K. Park and J. W. Choi, *ChemSusChem*, 2013, **6**, 443–8.
- 199 B. D. McCloskey, D. S. Bethune, R. M. Shelby, G. Girishkumar and A. C. Luntz, *J. Phys. Chem. Lett.*, 2011, **2**, 1161–1166.
- 200 S. a Freunberger, Y. Chen, N. E. Drewett, L. J. Hardwick, F. Bardé and P. G. Bruce, *Angew. Chem. Int. Ed. Engl.*, 2011, **50**, 8609–13.
- 201 J. Christensen, P. Albertus, R. S. Sanchez-Carrera, T. Lohmann, B. Kozinsky, R. Liedtke, J. Ahmed and A. Kojic, *J. Electrochem. Soc.*, 2012, **159**, R1.
- 202 Y.-C. Lu, E. J. Crumlin, G. M. Veith, J. R. Harding, E. Mutoro, L. Baggetto, N. J. Dudney, Z. Liu and Y. Shao-Horn, *Sci. Rep.*, 2012, **2**, 715.
- 203 V. S. Bryantsev and F. Faglioni, *J. Phys. Chem. A*, 2012, **116**, 7128–38.
- 204 J. Yang, D. Zhai, H.-H. Wang, K. C. Lau, J. A. Schlueter, P. Du, D. J. Myers, Y. Sun, L. a Curtiss and K. Amine, *Phys. Chem. Chem. Phys.*, 2013, **15**, 3764–71.
- 205 C. O. Laoire, S. Mukerjee, E. J. Plichta, M. A. Hendrickson and K. M. Abraham, *J. Electrochem. Soc.*, 2011, **158**, A302.
- 206 K. U. Schwenke, S. Meini, X. Wu, H. a Gasteiger and M. Piana, *Phys. Chem. Chem. Phys.*, 2013, **15**, 11830–9.

- 207 J. Kim, H.-D. Lim, H. Gwon and K. Kang, *Phys. Chem. Chem. Phys.*, 2013, **15**, 3623–9.
- 208 C. Barchasz, J.-C. Leprêtre, S. Patoux and F. Alloin, *Electrochim. Acta*, 2013, **89**, 737–743.
- 209 W. Xu, J. Hu, M. H. Engelhard, S. a. Towne, J. S. Hardy, J. Xiao, J. Feng, M. Y. Hu, J. Zhang, F. Ding, M. E. Gross and J.-G. Zhang, *J. Power Sources*, 2012, **215**, 240–247.
- 210 B. D. Adams, R. Black, Z. Williams, R. Fernandes, M. Cuisinier, E. J. Berg, P. Novak, G. K. Murphy and L. F. Nazar, *Adv. Energy Mater.*, 2014, 1–11.
- 211 Y.-C. Lu, B. M. Gallant, D. G. Kwabi, J. R. Harding, R. R. Mitchell, M. S. Whittingham and Y. Shao-Horn, *Energy Environ. Sci.*, 2013, **6**, 750.
- 212 D. Xu, Z. Wang, J. Xu, L. Zhang and X. Zhang, *Chem. Commun. (Camb.)*, 2012, **48**, 6948–50.
- 213 M. J. Trahan, S. Mukerjee, E. J. Plichta, M. a. Hendrickson and K. M. Abraham, *J. Electrochem. Soc.*, 2012, **160**, A259–A267.
- 214 H.-K. Lim, H.-D. Lim, K.-Y. Park, D.-H. Seo, H. Gwon, J. Hong, W. a Goddard, H. Kim and K. Kang, *J. Am. Chem. Soc.*, 2013, **135**, 9733–42.
- 215 V. S. Bryantsev, *Theor. Chem. Acc.*, 2012, **131**, 1250.
- 216 R. Younesi, P. Norby and T. Vegge, *ECS Electrochem. Lett.*, 2014, **3**, A15–A18.
- 217 S.-U. Kim and F. a Villamena, *J. Phys. Chem. A*, 2011, **116**, 886–898.
- 218 Q. Yu and S. Ye, *J. Phys. Chem. C*, 2015, **119**, 12236–12250.
- 219 R. Liu, Y. Lei, W. Yu, H. Wang, L. Qin, D. Han, W. Yang, D. Zhou, Y. He, D. Zhai, B. Li and F. Kang, *ACS Energy Lett.*, 2017, **2**, 313–318.
- 220 F. Wang, C.-S. Liang, Y. Pang, Y.-H. Xu and Z.-K. Luo, *Ionics (Kiel)*, 2013, **19**, 1791–1793.
- 221 J. Xie, Q. Dong, I. Madden, X. Yao, Q. Cheng, P. Dornath, W. Fan and D. Wang, *Nano Lett.*, 2015, **15**, 8371–8376.
- 222 M. H. Chakrabarti, F. S. Mjalli, I. M. AlNashef, M. A. Hashim, M. A. Hussain, L. Bahadori and C. T. J. Low, *Renew. Sustain. Energy Rev.*, 2014, **30**, 254–270.
- 223 P. Du, J. Lu, K. C. Lau, X. Luo, J. Bareño, X. Zhang, Y. Ren, Z. Zhang, L. a Curtiss, Y.-K. Sun and K. Amine, *Phys. Chem. Chem. Phys.*, 2013, **15**, 5572–81.
- 224 E. Nasybulin, W. Xu, M. H. Engelhard, Z. Nie, S. D. Burton, L. Cosimbescu, M. E. Gross and J. Zhang, *J. Phys. Chem. C*, 2013, **117**, 2635–2645.
- 225 D. Sharon, D. Hirsberg, M. Salama, M. Afri, A. A. Frimer, M. Noked, W. Kwak, Y. K. Sun and D. Aurbach, *ACS Appl. Mater. Interfaces*, 2016, **8**, 5300–5307.
- 226 G. A. Elia, J.-B. Park, Y.-K. Sun, B. Scrosati and J. Hassoun, *ChemElectroChem*, 2014, **1**, 47–50.
- 227 M. J. Marczewski, B. Stanje, I. Hanzu, M. Wilkening and P. Johansson, *Phys. Chem. Chem. Phys.*, 2014, **16**, 12341–9.
- 228 J. Qian, W. a. Henderson, W. Xu, P. Bhattacharya, M. Engelhard, O. Borodin and J.-G. Zhang, *Nat. Commun.*, 2015, **6**, 6362.
- 229 B. Liu, W. Xu, P. Yan, X. Sun, M. E. Bowden, J. Read, J. Qian, D. Mei, C. M. Wang and J. G. Zhang, *Adv. Funct. Mater.*, 2016, **26**, 605–613.
- 230 Y. Yamada and A. Yamada, *J. Electrochem. Soc.*, 2015, **162**, A2406–A2423.
- 231 J. Lu, Y. Lei, K. C. Lau, X. Luo, P. Du, J. Wen, R. S. Assary, U. Das, D. J. Miller, J. W. Elam, H. M. Albishri, D. A. El-Hady, Y.-K. Sun, L. a Curtiss and K. Amine, *Nat. Commun.*, 2013, **4**, 2383.
- 232 B. D. McCloskey, R. Scheffler, A. Speidel, D. S. Bethune, R. M. Shelby and a C. Luntz, *J. Am. Chem. Soc.*, 2011, **133**, 18038–18041.
- 233 K. P. C. Yao, M. Risch, S. Y. Sayed, Y. Lee, J. R. Harding, A. Grimaud, N. Pour, Z. Xu, J. Zhou, A. Mansour, F. Bardé and Y. Shao-Horn, *Energy Environ. Sci.*, 2015, **8**, 2417–

- 2426.
- 234 S.-M. Xu, Q.-C. Zhu, M. Harris, T.-H. Chen, C. Ma, X. Wei, H.-S. Xu, Y.-X. Zhou, Y.-C. Cao, K.-X. Wang and J.-S. Chen, *Nano Lett.*, 2016, acs.nanolett.6b02805.
- 235 Y. Bae, Y. S. Yun, H.-D. Lim, H. Lee, Y.-J. Kim, J. Kim, H. Park, Y. Ko, S. Lee, H. J. Kwon, H.-T. H. H.-T. Kim, H.-T. H. H.-T. Kim, D. Im and K. Kang, *Chem. Mater.*, 2016, **28**, 8160–8169.
- 236 H. R. Byon, B. M. Gallant, S. W. Lee and Y. Shao-Horn, *Adv. Funct. Mater.*, 2013, **23**, 1037–1045.
- 237 S. J. Kang, T. Mori, S. Narizuka, W. Wilcke and H.-C. Kim, *Nat. Commun.*, 2014, **5**, 3937.
- 238 P. Guan, G. Wang, C. Luo, K. Yan, E. J. Cairns and X. Hu, *Electrochim. Acta*, 2014, **129**, 318–326.
- 239 J. Luo, X. Yao, L. Yang, Y. Han, L. Chen, X. Geng, V. Vattipalli, Q. Dong, W. Fan, D. Wang and H. Zhu, *Nano Res.*, 2017, 1–9.
- 240 Y. Yao and F. Wu, *ACS Appl. Mater. Interfaces*, 2017, acsami.7b09483.
- 241 S. Li, X. Bi, R. Tao, Q. Wang, Y. Yao, F. Wu and C. Zhang, *ACS Appl. Mater. Interfaces*, 2017, **9**, 4382–4390.
- 242 C. V. Amanchukwu, J. R. Harding, Y. Shao-Horn and P. T. Hammond, *Chem. Mater.*, 2015, **27**, 550–561.
- 243 R. R. Mitchell, B. M. Gallant, C. V. Thompson and Y. Shao-Horn, *Energy Environ. Sci.*, 2011, **4**, 2952.
- 244 J.-J. Xu, Z.-L. Wang, D. Xu, L.-L. Zhang and X.-B. Zhang, *Nat. Commun.*, 2013, **4**, 2438.
- 245 E. Yilmaz, C. Yogi, K. Yamanaka, T. Ohta and H. R. Byon, *Nano Lett.*, 2013, **13**, 4679–84.
- 246 C. V. Amanchukwu, H.-H. Chang, M. Gauthier, S. Feng, T. P. Batcho and P. T. Hammond, *Chem. Mater.*, 2016, acs.chemmater.6b03718.
- 247 X. Xin, K. Ito and Y. Kubo, *Carbon N. Y.*, 2016, **99**, 167–173.
- 248 D. Y. Kim, M. Kim, D. W. Kim, J. Suk, J. J. Park, Oo. Park and Y. Kang, *Carbon N. Y.*, 2016, **100**, 265–272.
- 249 C. V. Amanchukwu, M. Gauthier, T. P. Batcho, C. Symister, Y. Shao-Horn, J. M. D'Arcy and P. T. Hammond, *J. Phys. Chem. Lett.*, 2016, acs.jpclett.6b01986.
- 250 C. Yang, R. A. Wong, M. Hong, K. Yamanaka, T. Ohta and H. R. Byon, *Nano Lett.*, 2016, **16**, 2969–2974.
- 251 M. He, P. Zhang, S. Xu and X. Yan, *ACS Appl. Mater. Interfaces*, 2016, **8**, 23713–23720.
- 252 Z. L. Wang, D. Xu, J. J. Xu, L. L. Zhang and X. B. Zhang, *Adv. Funct. Mater.*, 2012, **22**, 3699–3705.
- 253 S. Liu, Z. Wang, C. Yu, Z. Zhao, X. Fan, Z. Ling and J. Qiu, *J. Mater. Chem. A*, 2013, **1**, 12033.
- 254 H. Nie, C. Xu, W. Zhou, B. Wu, X. Li, T. Liu and H. Zhang, *ACS Appl. Mater. Interfaces*, 2016, **8**, 1937–1942.
- 255 G. Zhao, R. Mo, B. Wang, L. Zhang and K. Sun, *Chem. Mater.*, 2014, **26**, 2551–2556.
- 256 Q.-C. Liu, J.-J. Xu, D. Xu and X.-B. Zhang, *Nat. Commun.*, 2015, **6**, 7892.
- 257 F. Wang, Y.-H. H. Xu, Z.-K. K. Luo, Y. Pang, Q.-X. X. Wu, C.-S. S. Liang, J. Chen, D. Liu and X. H. Zhang, *J. Power Sources*, 2014, **272**, 1061–1071.
- 258 Y. Q. Li, Y. A. Samad, K. Polychronopoulou and K. Liao, *ACS Sustain. Chem. Eng.*, 2015, **3**, 1419–1427.
- 259 H. Qi, E. Mäder and J. Liu, *J. Mater. Chem. A*, 2013, **1**, 9714.
- 260 J. Jiang, P. He, S. Tong, M. Zheng, Z. Lin, X. Zhang, Y. Shi and H. Zhou, *NPG Asia*

- Mater.*, 2016, **8**, e239.
- 261 X. Gao, X. Wang, X. Ouyang and C. Wen, *Sci. Rep.*, 2016, **6**, 27207.
- 262 C. Ruan, K. Ai, X. Li and L. Lu, *Angew. Chem. Int. Ed. Engl.*, 2014, 5556–5560.
- 263 Y. Chang, S. Dong, Y. Ju, D. Xiao, X. Zhou, L. Zhang, X. Chen, C. Shang, L. Gu, Z. Peng and G. Cui, *Adv. Sci.*, 2015, **2**, 1–6.
- 264 A. Kraytsberg and Y. Ein-Eli, *J. Power Sources*, 2011, **196**, 886–893.
- 265 X. B. Zhu, T. S. Zhao, Z. H. Wei, P. Tan and L. An, *Energy Environ. Sci.*, 2015, **8**, 3745–3754.
- 266 F. Li, D.-M. Tang, T. Zhang, K. Liao, P. He, D. Golberg, A. Yamada and H. Zhou, *Adv. Energy Mater.*, 2015, **5**, 1500294.
- 267 C. Shen, Z. Wen, F. Wang, T. Wu and X. Wu, *ACS Catal.*, 2016, acscatal.6b00676.
- 268 M. S. Park, S. B. Ma, D. J. Lee, D. Im, S.-G. Doo and O. Yamamoto, *Sci. Rep.*, 2014, **4**, 3815.
- 269 G. Zheng, S. W. Lee, Z. Liang, H.-W. Lee, K. Yan, H. Yao, H. Wang, W. Li, S. Chu and Y. Cui, *Nat. Nanotechnol.*, 2014, 1–6.
- 270 R. Younesi, M. Hahlin and K. Edström, *ACS Appl. Mater. Interfaces*, 2013, **5**, 1333–41.
- 271 G. Zhou, F. Li and H.-M. Cheng, *Energy Environ. Sci.*, 2014.
- 272 X. Cheng, R. Zhang, C.-Z. Zhao and Q. Zhang, *Chem. Rev.*, 2017, **117**, acs.chemrev.7b00115.
- 273 A. Basile, A. F. Hollenkamp, A. I. Bhatt and A. P. O'Mullane, *Electrochim. commun.*, 2013, **27**, 69–72.
- 274 W. Walker, V. Giordani, J. Uddin, V. S. Bryantsev, G. V Chase and D. Addison, *J. Am. Chem. Soc.*, 2013, **135**, 2076–2079.
- 275 J. Uddin, V. S. Bryantsev, V. Giordani, W. Walker, G. V Chase and D. Addison, *J. Phys. Chem. Lett.*, 2013, **4**, 3760–3765.
- 276 J. B. Goodenough and Y. Kim, *Chem. Mater.*, 2010, **22**, 587–603.
- 277 C. Liu, Z. G. Neale and G. Cao, *Mater. Today*, 2016, **19**, 109–123.
- 278 E. Peled, *J. Electrochem. Soc.*, 1979, **126**, 2047.
- 279 M. B. Pinson and M. Z. Bazant, *J. Electrochem. Soc.*, 2012, **160**, A243–A250.
- 280 E. Peled, *J. Electrochem. Soc.*, 1997, **144**, L208.
- 281 S. Choudhury and L. A. Archer, *Adv. Electron. Mater.*, 2016, **2**, 1500246.
- 282 B. Wang, T. J. Richardson and G. Chen, *J. Electrochem. Soc.*, 2014, **161**, A1039–A1044.
- 283 R. Tao, X. Bi, S. Li, Y. Yao, F. Wu, Q. Wang, C. Zhang and J. Lu, *ACS Appl. Mater. Interfaces*, 2017, **9**, 7003–7008.
- 284 F. Ding, W. Xu, G. L. Graff, J. Zhang, M. L. Sushko, X. Chen, Y. Shao, M. H. Engelhard, Z. Nie, J. Xiao, X. Liu, P. V. Sushko, J. Liu and J. G. Zhang, *J. Am. Chem. Soc.*, 2013, **135**, 4450–4456.
- 285 C. K. Lee and Y. J. Park, *ACS Appl. Mater. Interfaces*, 2016, acsami.6b01775.
- 286 P. Knauth, *Solid State Ionics*, 2009, **180**, 911–916.
- 287 K. Liu, A. Pei, H. R. Lee, B. Kong, N. Liu, D. Lin, Y. Liu, C. Liu, P. Hsu, Z. Bao and Y. Cui, *J. Am. Chem. Soc.*, 2017, **139**, 4815–4820.
- 288 D. J. Lee, H. Lee, Y.-J. J. Kim, J. K. Park and H. T. Kim, *Adv. Mater.*, 2016, **28**, 857–863.
- 289 J. Wu, H. Chen, I. Byrd, S. Lovelace and C. Jin, *ACS Appl Mater Interfaces*, 2016.
- 290 R. Teranishi, Q. Si, F. Mizukoshi, M. Kawakubo, M. Matsui, Y. Takeda, O. Yamamoto and N. Imanishi, *J. Power Sources*, 2015, **273**, 538–543.
- 291 J. Hassoun, H. G. Jung, D. J. Lee, J. B. Park, K. Amine, Y. K. Sun and B. Scrosati, *Nano Lett.*, 2012, **12**, 5775–5779.
- 292 Z. Lu, N. Liu, H. W. Lee, J. Zhao, W. Li, Y. Li and Y. Cui, *ACS Nano*, 2015, **9**, 2540–

- 2547.
- 293 X. Li, Z. Yang, Y. Fu, L. Qiao, D. Li, H. Yue and D. He, *ACS Nano*, 2015, **9**, 1858–1867.
- 294 N. E. Drewett, I. M. Aldous, J. Zou and L. J. Hardwick, *Electrochim. Acta*, 2017, **247**, 296–305.
- 295 T. Wang, R. Villegas Salvatierra, A. S. Jalilov, J. Tian and J. M. Tour, *ACS Nano*, 2017, acsnano.7b05874.
- 296 J. Kim and A. A. Gewirth, *J. Phys. Chem. B*, 2006, **110**, 2565–2571.
- 297 X. hui Yang, P. He and Y. yao Xia, *Electrochem. commun.*, 2009, **11**, 1127–1130.
- 298 E. Y. and H. Zhou, *ACS Nano*, 2011, 3020–3026.
- 299 C. Tran, J. Kafle, X.-Q. Q. Yang and D. Qu, *Carbon N. Y.*, 2011, **49**, 1266–1271.
- 300 M. L. Thomas, K. Yamanaka, T. Ohta and H. R. Byon, *Chem. Commun.*, 2015, **51**, 3977–3980.
- 301 K. Zhang, L. Zhang, X. Chen, X. He, X. Wang, S. Dong, L. Gu, Z. Liu, C. Huang and G. Cui, *ACS Appl. Mater. Interfaces*, 2013, **5**, 3677–3682.
- 302 B. G. Kim, C. Jo, J. Shin, Y. Mun, J. Lee and J. W. Choi, *ACS Nano*, 2017, **11**, acsnano.6b07635.
- 303 W. Weng, C. J. Barile, P. Du, A. Abouimrane, R. S. Assary, A. A. Gewirth, L. A. Curtiss and K. Amine, *Electrochim. Acta*, 2014, **119**, 138–143.
- 304 O. Oloniyo, S. Kumar and K. Scott, *J. Electron. Mater.*, 2012, **41**, 921–927.
- 305 Y. Zhu, S. Liu, C. Jin, S. Bie, R. Yang and J. Wu, *J. Mater. Chem. A*, 2015, **3**, 13563–13567.
- 306 X. Hu, J. Wang, Z. Li, J. Wang, D. H. Gregory and J. Chen, *Nano Lett.*, 2017, **17**, 2073–2078.
- 307 Y. F. Xu, Y. Chen, G. L. Xu, X. R. Zhang, Z. Chen, J. T. Li, L. Huang, K. Amine and S. G. Sun, *Nano Energy*, 2016, **28**, 63–70.
- 308 W. Ni, S. Liu, Y. Fei, Y. He, X. Ma, L. Lu and Y. Deng, *ACS Appl. Mater. Interfaces*, 2017, **9**, 14749–14757.
- 309 Y. Cui, Z. Wen and Y. Liu, *Energy Environ. Sci.*, 2011, **4**, 4727.
- 310 Y. Cui, Z. Wen, S. Sun, Y. Lu and J. Jin, *Solid State Ionics*, 2012, **225**, 598–603.
- 311 C. Jin, Z. Yang, X. Cao, F. Lu and R. Yang, *Int. J. Hydrogen Energy*, 2014, **39**, 2526–2530.
- 312 C. Cao, Y. Yan, H. Zhang, J. Xie, S. Zhang, B. Pan, G. Cao and X. Zhao, *ACS Appl. Mater. Interfaces*, 2016, **8**, 31653–31660.
- 313 J. Wang, R. Gao, D. Zhou, Z. Chen, Z. Wu, G. Schumacher, Z. Hu and X. Liu, *ACS Catal.*, 2017, acscatal.7b02313.
- 314 D. Oh, J. Qi, B. Han, G. Zhang, T. J. Carney, J. Ohmura, Y. Zhang, Y. Shao-Horn and A. M. Belcher, *Nano Lett.*, 2014, **14**, 4837–4845.
- 315 G. Zhao, L. Zhang, B. Wang and K. Sun, *Electrochim. Acta*, 2015, **184**, 117–123.
- 316 Y. Lu, H. Ang, Q. Yan and E. Fong, *Chem. Mater.*, 2016, **28**, 5743–5752.
- 317 Y. Lu, Z. Wen, J. Jin, Y. Cui, M. Wu and S. Sun, *J. Solid State Electrochem.*, 2012, **16**, 1863–1868.
- 318 D. Oh, K. Virwani, L. Tadesse, M. Jurich, N. Aetukuri, L. E. Thompson, H. Kim and D. S. Bethune, *J. Phys. Chem. C*, 2017, **121**, 1404–1411.
- 319 M. Hong, H. C. Choi and H. R. Byon, *Chem. Mater.*, 2015, **27**, 2234–2241.
- 320 K. P. C. Yao, Y.-C. Lu, C. V. Amanchukwu, D. G. Kwabi, M. Risch, J. Zhou, A. Grimaud, P. T. Hammond, F. Bardé and Y. Shao-Horn, *Phys. Chem. Chem. Phys.*, 2014, **16**, 2297–304.
- 321 P. Li, W. Sun, Q. Yu, M. Guan, J. Qiao, Z. Wang, D. Rooney and K. Sun, *Mater. Lett.*, 2015, **158**, 84–87.

- 322 C. Li, Z. Guo, Y. Pang, Y. Sun, X. Su, Y. Wang and Y. Xia, *ACS Appl. Mater. Interfaces*, 2016, **8**, 31638–31645.
- 323 L. Li, L. Shen, P. Nie, G. Pang, J. Wang, H. Li, S. Dong and X. Zhang, *J. Mater. Chem. A*, 2015, **3**, 24309–24314.
- 324 H. S. Jadhav, R. S. Kalubarme, A. H. Jadhav and J. G. Seo, *J. Alloys Compd.*, 2016, **666**, 476–481.
- 325 Y. Cao, S.-R. Cai, S.-C. Fan, W.-Q. Hu, M.-S. Zheng and Q.-F. Dong, *Faraday Discuss.*, 2014, **172**, 215–21.
- 326 S. Song, W. Xu, J. Zheng, L. Luo, M. H. Engelhard, M. E. Bowden, B. Liu, C. Wang and J.-G. Zhang, *Nano Lett.*, 2017, acs.nanolett.6b04371.
- 327 J.-H. Kim, A. G. Kannan, H.-S. Woo, D.-G. Jin, W. Kim, K. Ryu and D.-W. Kim, *J. Mater. Chem. A*, 2015, **3**, 18456–18465.
- 328 F. Wu, Y. Xing, L. Li, J. Qian, W. Qu, J. Wen, D. J. Miller, Y. Ye, R. Chen, K. Amine and J. Lu, *ACS Appl. Mater. Interfaces*, 2016, **8**, 23635–23645.
- 329 J. Han, X. Guo, Y. Ito, P. Liu, D. Hojo, T. Aida, A. Hirata, T. Fujita, T. Adschari, H. Zhou and M. Chen, *Adv. Energy Mater.*, 2016, **6**, 1501870.
- 330 H. Wang, X. Liao, Q. Jiang, X. Yang, Y. He and Z. Ma, *Chinese Sci. Bull.*, 2012, **57**, 1959–1963.
- 331 X. Zhang, Y. Gong, S. Li and C. Sun, *ACS Catal.*, 2017, acscatal.7b02153.
- 332 W. Fan, X. Guo, D. Xiao and L. Gu, *J. Phys. Chem. C*, 2014, **118**, 7344–7350.
- 333 V. R. Chitturi, M. Ara, W. Fawaz, K. Y. S. Ng and L. M. R. Arava, *ACS Catal.*, 2016, acscatal.6b01016.
- 334 B. G. Kim, H.-J. Kim, S. Back, K. W. Nam, Y. Jung, Y.-K. Han and J. W. Choi, *Sci. Rep.*, 2015, **4**, 4225.
- 335 R. Gao, X. Liang, P. Yin, J. Wang, Y. L. Lee, Z. Hu and X. Liu, *Nano Energy*, 2017, **41**, 535–542.
- 336 H. G. Jung, Y. S. Jeong, J. B. Park, Y. K. Sun, B. Scrosati and Y. J. Lee, *ACS Nano*, 2013, **7**, 3532–3539.
- 337 D. W. Su, S. X. Dou and G. X. Wang, *J. Mater. Chem. A*, 2015, **3**, 18384–18388.
- 338 F. Li, Y. Chen, D.-Mi. Tang, Z. Jian, C. Liu, D. Golberg, A. Yamada and H. Zhou, *Energy Environ. Sci.*, 2014, **7**, 1648–1652.
- 339 M. a Schroeder, A. J. Pearse, A. C. Kozen, X. Chen, K. Gregorczyk, X. Han, A. Cao, L. Hu, S. B. Lee, G. W. Rubloff and M. Noked, *Chem. Mater.*, 2015, **27**, 5305–5313.
- 340 W. H. Ryu, F. S. Gittleson, M. Schwab, T. Goh and A. D. Taylor, *Nano Lett.*, 2015, **15**, 434–441.
- 341 S. Ma, Y. Wu, J. Wang, Y. Zhang, Y. Yan, Y. Wei, P. Liu, J. Wang, K. Jiang, S. Fan, Y. Xu and Z. Peng, *Nano Lett.*, 2015, **15**, 8084–8090.
- 342 Z. Jian, P. Liu, F. Li, P. He, X. Guo, M. Chen and H. Zhou, *Angew. Chem. Int. Ed. Engl.*, 2014, **53**, 442–6.
- 343 W. Zhou, Y. Chen, X. Yang, B. Wu, H. Nie, H. Zhang and H. Zhang, *J. Mater. Chem. A*, 2015, **3**, 14556–14561.
- 344 S. Zhang, Z. Huang, Z. Wen, L. Zhang, J. Jin, R. Shahbazian-Yassar and J. Yang, *Nano Lett.*, 2017, **17**, acs.nanolett.7b00603.
- 345 K. Scott, U. Sahapatsombut and H. Cheng, *ECS Trans.*, 2014, **61**, 23–29.
- 346 J. Zhu, M. Metzger, M. Antonietti and T.-P. Fellinger, *ACS Appl. Mater. Interfaces*, 2016, **8**, 26041–26050.
- 347 H. Gong, H. Xue, T. Wang, H. Guo, X. Fan, L. Song, W. Xia and J. He, *ACS Appl. Mater. Interfaces*, 2016, **8**, 18060–18068.
- 348 X. Zeng, C. You, L. Leng, D. Dang, X. Qiao, X. Li, Y. Li, S. Liao and R. R. Adzic, *J. Mater. Chem. A*, 2015, **3**, 11224–11231.

- 349 L. Yu, Y. Shen and Y. Huang, *J. Alloys Compd.*, 2014, **595**, 185–191.
- 350 L. Wang, M. Ara, K. Wadumesthrige, S. Salley and K. Y. S. Ng, *J. Power Sources*, 2013, **234**, 8–15.
- 351 Y. Cao, M. Zheng, S. Cai, X. Lin, C. Yang, W. Hu and Q. Dong, *J. Mater. Chem. A*, 2014, **2**, 18736–18741.
- 352 S. H. Oh, R. Black, E. Pomerantseva, J.-H. Lee and L. F. Nazar, *Nat. Chem.*, 2012, **4**, 1004–10.
- 353 Y. Hu, T. Zhang, F. Cheng, Q. Zhao, X. Han and J. Chen, *Angew. Chemie Int. Ed.*, 2015, **54**, 4338–4343.
- 354 B. Sun, P. Munroe and G. Wang, *Sci. Rep.*, 2013, **3**, 2247.
- 355 J. Zhu, F. Wang, B. Wang, Y. Wang, J. Liu, W. Zhang and Z. Wen, *J. Am. Chem. Soc.*, 2015, 151005161920000.
- 356 M. Asadi, B. Kumar, C. Liu, P. Phillips, P. Yasaee, A. Behranginia, P. Zapol, R. F. Klie, L. A. Curtiss and A. Salehi-Khojin, *ACS Nano*, 2016, **10**, 2167–2175.
- 357 H. Xue, S. Wu, J. Tang, H. Gong, P. He, J. He and H. Zhou, *ACS Appl. Mater. Interfaces*, 2016, **8**, 8427–8435.
- 358 D. Mei, X. Yuan, Z. Ma, P. Wei, X. Yu, J. Yang and Z. F. Ma, *ACS Appl. Mater. Interfaces*, 2016, **8**, 12804–12811.
- 359 Y.-J. Kim, H. Lee, D. J. Lee, J.-K. Park and H.-T. Kim, *ChemSusChem*, 2015, **8**, 2496–2502.
- 360 J. Tang, S. Wu, T. Wang, H. Gong, H. Zhang, S. M. Alshehri, T. Ahamad, H. Zhou and Y. Yamauchi, *ACS Appl. Mater. Interfaces*, 2016, **8**, 2796–2804.
- 361 J. Li, W. Weiwei, M. Zou, L. Guan and Z. Huang, *J. Alloys Compd.*, 2015, **639**, 428–434.
- 362 D. Sun, Y. Shen, W. Zhang, L. Yu, Z. Yi, W. Yin, D. Wang, Y. Huang, J. Wang, D. Wang and J. B. Goodenough, *J. Am. Chem. Soc.*, 2014, **136**, 8941–6.
- 363 D. Kundu, R. Black, B. Adams and L. F. Nazar, *ACS Cent. Sci.*, 2015, **1**, 510–515.
- 364 J. Han, G. Huang, Y. Ito, X. Guo, T. Fujita, P. Liu, A. Hirata and M. Chen, *Adv. Energy Mater.*, 2017, **7**, 1601933.
- 365 A. Y. Tesio, D. Blasi, M. Olivares-Marín, I. Ratera, D. Tonti and J. Veciana, *Chem. Commun.*, 2015, **51**, 17623–17626.
- 366 Y. Qiao and S. Ye, *J. Phys. Chem. C*, 2016, **120**, 15830–15845.
- 367 Y. Chen, S. A. Freunberger, Z. Peng, O. Fontaine and P. G. Bruce, *Nat. Chem.*, 2013, **5**, 489–94.
- 368 K. P. C. Yao, J. T. Frith, S. Y. Sayed, F. Bardé, J. R. Owen, Y. Shao-Horn and N. Garcia-Araez, *J. Phys. Chem. C*, 2016, **120**, 16290–16297.
- 369 W. R. Torres, S. E. Herrera, A. Y. Tesio, M. Del Pozo and E. J. Calvo, *Electrochim. Acta*, 2015, **182**, 1118–1123.
- 370 C. Yang, J. Han, P. Liu, C. Hou, G. Huang, T. Fujita, A. Hirata and M. Chen, *Adv. Mater.*, 2017, **1702752**, 1702752.
- 371 J. Zhang, B. Sun, Y. Zhao, K. Kretschmer and G. Wang, *Angew. Chemie - Int. Ed.*, 2017, **56**, 8505–8509.
- 372 B. J. Bergner, A. Schürmann, K. Peppler, A. Garsuch and J. Janek, *J. Am. Chem. Soc.*, 2014, **136**, 15054–15064.
- 373 D. Grübl, B. J. Bergner, D. Schröder, J. Janek and W. G. Bessler, *J. Phys. Chem. C*, 2016, **120**, acs.jpcc.6b07886.
- 374 B. J. Bergner, C. Hofmann, A. Schürmann, D. Schröder, K. Peppler, P. R. Schreiner and J. Janek, *Phys. Chem. Chem. Phys.*, 2015, **17**, 31769–31779.
- 375 Y. G. Zhu, X. Wang, C. Jia, J. Yang and Q. Wang, *ACS Catal.*, 2016, **6**, 6191–6197.
- 376 W. Zhang, Y. Shen, D. Sun, Z. Huang, J. Zhou, H. Yan and Y. Huang, *Nano Energy*,

- 2016, **30**, 43–51.
- 377 T. Zhang, K. Liao, P. He and H. Zhou, *Energy Environ. Sci.*, 2015, **9**, 1024–1030.
- 378 H.-D. Lim, H. Song, J. Kim, H. Gwon, Y. Bae, K.-Y. Park, J. Hong, H. Kim, T. Kim, Y. H. Kim, X. Lepró, R. Ovalle-Robles, R. H. Baughman and K. Kang, *Angew. Chemie Int. Ed.*, 2014, **53**, 3926–3931.
- 379 W.-J. Kwak, D. Hirshberg, D. Sharon, H.-J. Shin, M. Afri, J.-B. Park, A. Garsuch, F. F. Chesneau, A. a. Frimer, D. Aurbach and Y.-K. Sun, *J. Mater. Chem. A*, 2015, **3**, 8855–8864.
- 380 M. Tułodziecki, G. M. Leverick, C. V. Amanchukwu, Y. Katayama, D. G. Kwabi, F. Bardé, P. T. Hammond and Y. Shao-Horn, *Energy Environ. Sci.*, 2017, **10**, 1828–1842.
- 381 Y. Qiao, S. Wu, Y. Sun, S. Guo, J. Yi, P. He and H. Zhou, *ACS Energy Lett.*, 2017, **2**, 1869–1878.
- 382 W.-J. Kwak, D. Hirshberg, D. Sharon, M. Afri, A. A. Frimer, H.-G. Jung, D. Aurbach and Y.-K. Sun, *Energy Environ. Sci.*, 2016, **9**, 2334–2345.
- 383 Z. Liang and Y. C. Lu, *J. Am. Chem. Soc.*, 2016, **138**, 7574–7583.
- 384 S. H. Lee, W.-J. Kwak and Y.-K. Sun, *J. Mater. Chem. A*, 2017, **5**, 15512–15516.
- 385 X. Xin, K. Ito and Y. Kubo, *ACS Appl. Mater. Interfaces*, 2017, **9**, 25976–25984.
- 386 S. H. Lee, J. Park, H. Lim and Y. Sun, *Adv. Energy Mater.*, 2017, **7**, 1602417.
- 387 W.-J. Kwak, H.-G. Jung, D. Aurbach and Y.-K. Sun, *Adv. Energy Mater.*, 2017, **1701232**, 1701232.
- 388 L. Yang, J. T. Frith and J. R. Owen, *Chem. Commun.*, 2015, **51**, 1705–1708.
- 389 M. J. Lacey, J. T. Frith and J. R. Owen, *Electrochem. commun.*, 2013, **26**, 74–76.
- 390 B. G. Kim, S. Kim, H. Lee and J. W. Choi, *Chem. Mater.*, 2014, **26**, 4757–4764.
- 391 X. Gao, Z. P. Jovanov, Y. Chen, L. R. Johnson and P. G. Bruce, *Angew. Chemie Int. Ed.*, 2017, **56**, 6539–6543.
- 392 N. Feng, X. Mu, X. Zhang, P. He and H. Zhou, *ACS Appl. Mater. Interfaces*, 2017, **9**, 3733–3739.
- 393 S. Matsuda, K. Hashimoto and S. Nakanishi, *J. Phys. Chem. C*, 2014, **118**, 18397–18400.
- 394 S. Matsuda, S. Mori, K. Hashimoto and S. Nakanishi, *J. Phys. Chem. C*, 2014, **118**, 28435–28439.
- 395 W.-H. Ryu, F. S. Gittleson, J. M. Thomsen, J. Li, M. J. Schwab, G. W. Brudvig and A. D. Taylor, *Nat. Commun.*, 2016, **7**, 12925.
- 396 D. Sharon, P. Sharon, D. Hirshberg, M. Salama, M. Afri, L. J. W. Shimon, W. J. Kwak, Y. K. Sun, A. A. Frimer and D. Aurbach, *J. Am. Chem. Soc.*, 2017, **139**, 11690–11693.
- 397 W. Li, H. Yao, K. Yan, G. Zheng, Z. Liang, Y.-M. Chiang and Y. Cui, *Nat. Commun.*, 2015, **6**, 7436.
- 398 J. E. Park, G.-H. Lee, H.-W. Shim, D. W. Kim, Y. Kang and D.-W. Kim, *Electrochem. commun.*, 2015, **57**, 39–42.
- 399 M. Mehta and P. Andrei, *ECS Trans.*, 2014, **61**, 39–55.
- 400 C. P. Grey and J. M. Tarascon, *Nat Mater.*, 2017, **16**, 45–56.
- 401 Y. Li, X. Wang, S. Dong, X. Chen and G. Cui, *Adv. Energy Mater.*, 2016, **6**, 1600751.
- 402 N. Mozhzhukhina, L. P. Méndez De Leo and E. J. Calvo, *J. Phys. Chem. C*, 2013, **117**, 18375–18380.
- 403 G. S. Hutchings, J. Rosen, D. Smiley, G. R. Goward, P. G. Bruce and F. Jiao, *J. Phys. Chem. C*, 2014, **118**, 12617–12624.
- 404 J. P. Vivek, N. G. Berry, J. Zou, R. J. Nichols and L. J. Hardwick, *J. Phys. Chem. C*, 2017, **121**, 19657–19667.
- 405 Y. Katayama, H. Onodera, M. Yamagata and T. Miura, *J. Electrochem. Soc.*, 2004, **151**, A59.

- 406 K. Ghandi, *Green Sustain. Chem.*, 2014, **4**, 44–53.
- 407 M. Schmeisser, P. Illner, R. Puchta, A. Zahl and R. van Eldik, *Chemistry*, 2012, **18**, 10969–82.
- 408 C. V. Amanchukwu, H.-H. Chang and P. T. Hammond, *J. Phys. Chem. C*, 2017, acs.jpcc.7b05322.
- 409 R. G. Evans, O. V. Klymenko, S. a. Saddoughi, C. Hardacre and R. G. Compton, *J. Phys. Chem. B*, 2004, **108**, 7878–7886.
- 410 M. Hayyan, F. S. Mjalli, M. A. Hashim, I. M. AlNashef, S. M. Al-Zahrani and K. L. Chooi, *J. Electroanal. Chem.*, 2012, **664**, 26–32.
- 411 M. A. H. M. Hayyan, Farouq S. Mjalli and M. Hayyan, *J. Appl. Sci.*, 2010, **10**, 1176–1180.
- 412 M. Deetlefs, M. Fanselow and K. R. Seddon, *RSC Adv.*, 2016, **6**, 4280–4288.
- 413 A. S. Fisher, M. B. Khalid, M. Widstrom and P. Kofinas, *J. Power Sources*, 2011, **196**, 9767–9773.
- 414 H. Matsumoto, T. Matsuda and Y. Miyazaki, *Chem. Lett.*, 2000, 1430–1431.
- 415 T. Kuboki, T. Okuyama, T. Ohsaki and N. Takami, *J. Power Sources*, 2005, **146**, 766–769.
- 416 K. U. Schwenke, J. Herranz, H. A. Gasteiger and M. Piana, *J. Electrochem. Soc.*, 2015, **162**, A905–A914.
- 417 H. Nakamoto, Y. Suzuki, T. Shiotsuki, F. Mizuno, S. Higashi, K. Takechi, T. Asaoka, H. Nishikoori and H. Iba, *J. Power Sources*, 2013, **243**, 19–23.
- 418 S. Higashi, Y. Kato, K. Takechi, H. Nakamoto, F. Mizuno, H. Nishikoori, H. Iba and T. Asaoka, *J. Power Sources*, 2013, **240**, 14–17.
- 419 Z. J. Chen, T. Xue and J.-M. Lee, *RSC Adv.*, 2012, **2**, 10564.
- 420 J. Reiter, E. Paillard, L. Grande, M. Winter and S. Passerini, *Electrochim. Acta*, 2013, **91**, 101–107.
- 421 P. M. Radjenovic and L. J. Hardwick, *Faraday Discuss.*, 2018, **206**, 379–392.
- 422 T. Tsuda and C. L. Hussey, *Electrochem. Soc.*, 2007, 42–49.
- 423 W. Xu, J. Wang, F. Ding, X. Chen, E. Nasybulin, Y. Zhang and J.-G. Zhang, *Energy Environ. Sci.*, 2014, **7**, 513.
- 424 D. Larcher and J. Tarascon, *Nat. Publ. Gr.*, 2014, **7**.
- 425 E. Markevich, R. Sharabi, V. Borgel, H. Gottlieb, G. Salitra, D. Aurbach, G. Semrau and M. a. Schmidt, *Electrochim. Acta*, 2010, **55**, 2687–2696.
- 426 T. Fujimori, K. Fujii, R. Kanzaki, K. Chiba, H. Yamamoto, Y. Umebayashi and S. Ishiguro, *J. Mol. Liq.*, 2007, **131–132**, 216–224.
- 427 M. Castriota, T. Caruso, R. G. Agostino, E. Cazzanelli, W. a Henderson and S. Passerini, *J. Phys. Chem. A*, 2005, **109**, 92–6.
- 428 K. Motobayashi, K. Minami, N. Nishi, T. Sakka and M. Osawa, *J. Phys. Chem. Lett.*, 2013, **4**, 3110–3114.
- 429 Z. Tian, B. Ren and D. Wu, *J. Phys. Chem. B*, 2002, **106**, 9463–9483.
- 430 D. C. Harris and M. D. Bertolucci, *Symmetry and Spectroscopy: An Introduction to Vibrational and Electronic Spectroscopy*, Dover Books, 1989, vol. 11957.
- 431 A. Campion, P. Kambhampati and C. Harris, 1998, **27**, 241–250.
- 432 G. McNay, D. Eustace, W. E. Smith, K. Faulds and D. Graham, *Appl. Spectrosc.*, 2011, **65**, 825–37.
- 433 G. C. Schatz, R. P. Van Duyne, J. M. Chalmers and P. R. G. Editors, 2002.
- 434 W. Commons, *Wikimedia Commons*.
- 435 M. Osawa, M. Kuramitsu, A. Hatta, W. Suëtaka and H. Seki, *Surf. Sci.*, 1986, **175**, L787–L793.
- 436 M. Osawa, in *Near-Field Optics and Surface Plasmon Polaritons*, Springer Berlin

- Heidelberg, Berlin, Heidelberg, 2001, vol. 81, pp. 163–187.
- 437 V. Augustyn, J. Come, M. a Lowe, J. W. Kim, P.-L. Taberna, S. H. Tolbert, H. D. Abruña, P. Simon and B. Dunn, *Nat. Mater.*, 2013, **12**, 518–22.
- 438 K. Song, D. A. Agyeman, M. Park, J. Yang and Y.-M. Kang, *Adv. Mater.*, 2017, **1606572**, 1606572.
- 439 G. a. Snook, a. S. Best, a. G. Pandolfo and a. F. Hollenkamp, *Electrochem. commun.*, 2006, **8**, 1405–1411.
- 440 A. E. Russell, Q.-P. L. and Z.-Q. T. Bin Ren,* Xiao-Bing Lian, Jian-Feng Li, Ping-Ping Fang and A. E. Russell, *Faraday Discuss.*, 2009, **140**, 155–165.
- 441 M. Moskovits, *Rev. Mod. Phys.*, 1985, **57**, 783–826.
- 442 M. Namazian, C. Y. Lin and M. L. Coote, *J. Chem. Theory Comput.*, 2010, **6**, 2721–2725.
- 443 A. Lewandowski, L. Waligora and M. Galinski, *Electroanalysis*, 2009, **21**, 2221–2227.
- 444 E. I. Rogers, D. S. Silvester, D. L. Poole, L. Aldous, C. Hardacre and R. G. Compton, *J. Phys. Chem. C*, 2008, **112**, 2729–2735.
- 445 A. M. O'Mahony, D. S. Silvester, L. Aldous, C. Hardacre and R. G. Compton, *J. Chem. Eng. Data*, 2008, **53**, 2884–2891.
- 446 D. T. Sawyer, *Oxygen chemistry*, Oxford University Press, 1991.
- 447 M. Hayyan, M. A. Hashim and I. M. AlNashef, *Chem. Rev.*, 2016, acs.chemrev.5b00407.
- 448 O. Warburg, *Science (80-)*, 1956, **123**, 309–314.
- 449 L. C. Greaves, A. K. Reeve, R. W. Taylor and D. M. Turnbull, *J. Pathol.*, 2012, **226**, 274–86.
- 450 C. E. Elwell, N. L. Gagnon, B. D. Neisen, D. Dhar, A. D. Spaeth, G. M. Yee and W. B. Tolman, *Chem. Rev.*, 2016.
- 451 TCReuter, *Wikimedia Commons*, 2016.
- 452 J. A. Creighton and E. R. Lippincott, *J. Chem. Phys.*, 1964, **40**, 1779.
- 453 B. J. C. Evans, *Chem. Commun.*, 1969, **202**.
- 454 J. B. Bates, M. H. Brooker and G. E. Boyd, *Chem. Phys. Lett.*, 1972, **16**, 391–395.
- 455 F. J. Blunt, P. J. Hendra and J. R. Mackenzie, *J. Chem. Soc. D Chem. Commun.*, 1969, **242**, 278.
- 456 M. B. W. Kanzig, *Phys. Kondens. Mater.*, 1973, **112**, 107–112.
- 457 H. H. Eysel and S. Thym, *Zeitschrift fur Anorg. und Allg. Chemie*, 1975, **411**, 97–102.
- 458 D. a Hatzenbuhler, *J. Chem. Phys.*, 1972, **56**, 3398.
- 459 R. R. Smardzewski and L. Andrews, *J. Phys. Chem.*, 1973, **77**, 801–804.
- 460 L. Andrews and R. R. Smardzewski, *J. Chem. Phys.*, 1973, **58**, 2258–2261.
- 461 W. Holzer, W. F. Murphy, H. J. Bernstein and J. Rolfe, *W. Holzer, W. F. Murphy, H. J. Bernstein, J. Rolfe*, 1968, **26**, 543–545.
- 462 T. A. Galloway and L. J. Hardwick, *J. Phys. Chem. Lett.*, 2016, **7**, 2119–2124.
- 463 P. Vandebaele, *Practical Raman Spectroscopy - An Introduction ALS Catalog*, John Wiley & Sons, Ltd, Chichester, UK, 2013.
- 464 I. Janik and G. N. R. Tripathi, *J. Chem. Phys.*, 2013, **139**, 14302.
- 465 T. A. Galloway, L. Cabo-Fernandez, I. Aldous, F. Braga and L. Hardwick, *Faraday Discuss.*, 2017.
- 466 I. Aldous, *Thesis*, 2016.
- 467 F. S. Gittleson, W. Ryu and A. D. Taylor, *ACS Appl. Mater. Interfaces*, 2014, **6**, 19017–19025.
- 468 D. Zhai, H.-H. Wang, J. Yang, K. C. Lau, K. Li, K. Amine and L. a Curtiss, *J. Am. Chem. Soc.*, 2013, **135**, 15364–72.
- 469 D. Zhai, H. Wang, K. C. Lau, J. Gao, P. C. Redfern, F. Kang, B. Li, E. Indacochea, U.

- Das, H.-H. H. H.-H. Sun, H.-H. H. H.-H. Sun, K. Amine and L. A. Curtiss, *J. Phys. Chem. Lett.*, 2014, **5**, 2705–2710.
- 470 D. Zhai, K. C. Lau, H. Wang, J. Wen, D. J. Miller, J. Lu, F. Kang, B. Li, W. Yang, J. Gao, E. Indacochea, L. A. Curtiss and K. Amine, *Nano Lett.*, 2015, **15**, 1041–1046.
- 471 I. Landa-Medrano, R. Pinedo, X. Bi, I. Ruiz de Laramendi, L. Lezama, J. Janek, K. Amine, J. Lu and T. Rojo, *ACS Appl. Mater. Interfaces*, 2016, **8**, 20120–20127.
- 472 N. Zhao and X. Guo, *J. Phys. Chem. C*, 2015, **119**, 25319–25326.
- 473 I. I. Abate, L. E. Thompson, H.-C. Kim and N. B. Aetukuri, *J. Phys. Chem. Lett.*, 2016, **7**, 2164–2169.
- 474 J. Kim, H. Park, B. Lee, W. M. Seong, H.-D. Lim, Y. Bae, H. Kim, W. K. Kim, K. H. Ryu and K. Kang, *Nat. Commun.*, 2016, **7**, 10670.
- 475 S. A. Hunter-Saphir and J. A. Creighton, *J. Raman Spectrosc.*, 1998, **29**, 1997–1999.
- 476 P. D. C. Dietzel, R. K. Kremer and M. Jansen, *Chem. - An Asian J.*, 2007, **2**, 66–75.
- 477 J. Li and R. J. Davis, *J. Phys. Chem. B*, 2005, **109**, 7141–7148.
- 478 A. Band, A. Albu-Yaron, T. Livneh, H. Cohen, Y. Feldman, L. Shimon, R. Popovitz-Biro, V. Lyahovitskaya and R. Tenne, *J. Phys. Chem. B*, 2004, **108**, 12360–12367.
- 479 P. D. C. Dietzel, R. K. Kremer and M. Jansen, *J. Am. Chem. Soc.*, 2004, **126**, 4689–4696.
- 480 R. R. Smardzewski, *J. Chem. Phys.*, 1972, **57**, 1327.
- 481 R. Boča, *Coord. Chem. Rev.*, 1983, **50**, 1–72.
- 482 L. Popović, D. De Waal and J. C. a Boeyens, *J. Raman Spectrosc.*, 2005, **36**, 2–11.
- 483 E. A. Robinson and M. W. Lister, *Can. J. Chem.*, 1963, **41**, 2988–2995.
- 484 C. J. Cramer, W. B. Tolman, K. H. Theopold and A. L. Rheingold, *Proc. Natl. Acad. Sci.*, 2003, **100**, 3635–3640.
- 485 T. Livneh, A. Band and R. Tenne, *J. Raman Spectrosc.*, 2002, **33**, 675–676.
- 486 C. E. Housecroft and E. C. Constable, *Chemistry : An introduction to organic, inorganic and physical chemistry*, Prentice Hall/Pearson Education, 2010.
- 487 G. W. E. Nathan Kornblum, J. Shamir, J. Binenboym, H. H. Claassen, G. W. E. Nathan Kornblum, J. Shamir, J. Binenboym and H. H. Claassen, *J. Am. Chem. Soc.*, 1968, **90**, 6223–6224.
- 488 P. A. Giguére and T. K. K. Srinivasan, *J. Raman Spectrosc.*, 1974, **2**, 125–132.
- 489 A. Weber and E. A. McGinnis, *J. Mol. Spectrosc.*, 1960, **4**, 195–200.
- 490 V. V Pushkarev, V. I. Kovalchuk and J. L. D’Itri, *J. Phys. Chem. B*, 2004, **108**, 5341–5348.
- 491 T. Shibahara and M. Mori, *Bull. Chem. Soc. Jpn.*, 1978, **51**, 1374–1379.
- 492 J. Oxley, J. Smith, J. Brady, F. Dubnikova, R. Kosloff, L. Zeiri and Y. Zeiri, *Appl. Spectrosc.*, 2008, **62**, 906–915.
- 493 D. Lin-Vien, N. B. Colthup, W. G. Fateley and J. G. Grasselli, in *The Handbook of Infrared and Raman Characteristic Frequencies of Organic Molecules*, 1991, pp. 68–72.
- 494 K. Qin, C. D. Incarvito, A. L. Rheingold and K. H. Theopold, *Angew. Chemie - Int. Ed.*, 2002, **41**, 2333–2335.
- 495 L. M. Mirica, X. Ottenwaelder and T. D. P. Stack, *Chem. Rev.*, 2004, **104**, 1013–1046.
- 496 E. I. Solomon, D. E. Heppner, E. M. Johnston, J. W. Ginsbach, J. Cirera, M. Qayyum, M. T. Kieber-Emmons, C. H. Kjaergaard, R. G. Hadt and L. Tian, *Chem. Rev.*, 2014, **114**, 3659–3853.
- 497 A. Mukherjee, M. A. Cranswick, M. Chakrabarti, T. K. Paine, K. Fujisawa, E. Münck, L. Que, E. Münck and L. Que, *Inorg. Chem.*, 2010, **49**, 3618–3628.
- 498 S. Hong, K. D. Sutherlin, J. Park, E. Kwon, M. a Siegler, E. I. Solomon and W. Nam, *Nat. Commun.*, 2014, **5**, 5440.

- 499 Y. R. Goo, A. C. Maity, K. Bin Cho, Y. M. Lee, M. S. Seo, Y. J. Park, J. Cho and W. Nam, *Inorg. Chem.*, 2015, **54**, 10513–10520.
- 500 J. E. Griffiths, D. Distefano and W. A. Sunder, *J. Raman Spectrosc.*, 1980, **9**, 67–68.
- 501 J. E. Griffiths and W. A. Sunder, *J. Chem. Phys.*, 1982, **77**, 1087–1092.
- 502 H. Fuchsmanta, C. H. Barlow and W. S. Caughey, *Biochem. Biophys. Res. Commun.*, 1974, **61**, 635–643.
- 503 D. de Waal, K. Range, M. Konigstein and W. Kiefer, *J. Raman Spectrosc.*, 1998, **29**, 109–113.
- 504 X. Zhang, G. R. Loppnow, J. Takats and R. McDonald, *J. Am. Chem. Soc.*, 1995, **117**, 7828–7829.
- 505 F. Halverson, *J. Phys. Chem. Solids*, 1962, **23**, 207–214.
- 506 S. Baldelli, *Acc. Chem. Res.*, 2008, **41**, 421–431.
- 507 Y.-C. Lu, Z. Xu, H. a Gasteiger, S. Chen, K. Hamad-Schifferli and Y. Shao-Horn, *J. Am. Chem. Soc.*, 2010, **132**, 12170–1.
- 508 V. Oklejas, C. Sjostrom and J. M. Harris, *J. Phys. Chem. B*, 2003, **107**, 7788–7794.
- 509 M. R. Albert and J. T. Yates, *The surface scientist's guide to organometallic chemistry*, American Chemical Society, 1987.
- 510 K. Fujisawa, M. Tanaka, Y. Moro-oka and N. Kitajima, *J. Am. Chem. Soc.*, 1994, **116**, 12079–12080.
- 511 C. H. Barlow, J. C. Maxwell, W. J. Wallace and W. S. Caughey, *Biochem. Biophys. Res. Commun.*, 1973, **55**, 91–95.
- 512 L. J. Hardwick, J. a. Saint, I. T. Lucas, M. M. Doeffer and R. Kostecki, *J. Electrochem. Soc.*, 2009, **156**, A120.
- 513 R. Nichols, in *Electrochemistry course*, 2014.
- 514 K. M. Abraham, in *ECS Transactions*, 2012, vol. 41, pp. 27–34.
- 515 M. Ara, T. Meng, G.-A. Nazri, S. O. Salley and K. Y. Simon Ng, *J. Electrochem. Soc.*, 2014, **161**, A1969–A1975.

